Probabilistic Seismic Hazard Assessment for Lebanon

Sarah El Kadri

THÈSE

Pour obtenir le grade de

DOCTEUR DE L'UNIVERSITÉ GRENOBLE ALPES

École doctorale : STEP - Sciences de la Terre de l'Environnement et des Planètes
Spécialité : Sciences de la Terre et de l'Environnement
Unité de recherche : Institut des Sciences de la Terre

Estimation de l'aléa sismique probabiliste au Liban

Probabilistic Seismic Hazard Assessment for Lebanon

Présentée par :

Sarah EL KADRI

Direction de thèse :

Céline BEAUVAL directrice de recherche, Université Grenoble Alpes	Directrice de thèse
Marleine BRAX CNRSL	Co-encadrante de thèse
YANN KLINGER	Co-encadrant de thèse

Rapporteurs :

Martin MAI
PROFESSEUR, King Abdullah University of Science and Technology (KAUST)
Francesco VISINI
CHARGE DE RECHERCHE, The National Institute of Geophysics and Volcanology

Thèse soutenue publiquement le **22 mars 2024**, devant le jury composé de :

Céline BEAUVAL DIRECTRICE DE RECHERCHE, IRD	Directrice de thèse
Yann KLINGER DIRECTEUR DE RECHERCHE, CNRS	Co-directeur de thèse
Martin MAI PROFESSEUR, King Abdullah University of Science and Technology (KAUST)	Rapporteur
Francesco VISINI CHARGE DE RECHERCHE, The National Institute of Geophysics and Volcanology	Rapporteur
Anne SOCQUET PHYSICIENNE, Université Grenoble Alpes	Présidente
Wassim RAPHAEL PROFESSEUR, Université Saint Joseph	Examinateur

Invités :

Marleine BRAX
SENIOR SCIENTIST, Centre National de Recherches Geophysiques

Acknowledgments

As I reach the completion of my PhD journey, I would like to thank all the people who have contributed, whether closely or indirectly, to this significant accomplishment. Your support has been invaluable, and I am truly grateful.

I would like to take this opportunity to extend my utmost appreciation and gratitude to my supervisor, Celine Beauval, for her exceptional guidance and unwavering support throughout my PhD journey. From the very beginning, she played a pivotal role in helping me secure my PhD scholarship, ensuring that I had the best possible environment to conduct my studies. Her unwavering belief in my abilities has had a profound impact on my academic and personal growth. She consistently pushed me to reach my full potential and encouraged me to explore new avenues of knowledge. Her expertise and guidance not only shaped the direction of my research but also instilled in me a deep sense of responsibility, diligence, and integrity. Thank you for being an exceptional supervisor and for helping me become the researcher I am today.

I would also like to extend my heartfelt appreciation to my co-PhD advisors, Yann Klinger and Marleine Brax, whose guidance, support, and expertise were invaluable throughout this journey. Their mentorship and encouragement have been instrumental in shaping this thesis and my academic growth. Their commitment to my success and their willingness to share their expertise have been invaluable assets throughout this journey. I am honored to have had the opportunity to work with such exceptional advisors.

I am profoundly thankful to the members of my jury for agreeing to review and discuss my manuscript. Their expertise and critical analysis will undoubtedly contribute significantly to the advancement of this research and its ultimate contribution to the academic community. I eagerly look forward to incorporating their feedback and suggestions to refine and enhance the quality of this work.

I would also like to thank the IRD (Institut de Recherche pour le Developpement), Labex OSUG@2020 (Investissements d'avenir –ANR10 LABX56) and the CNRS-L for funding this research. Their financial support has been instrumental in enabling me to carry out this study and has provided me with the necessary resources to pursue my scientific endeavors.

To my cherished friends and colleagues from ISTerre, I could not have got this far without the constant support. Thank you for making this place a truly wonderful and inspiring environment to pursue knowledge while having some fun.

Above all, a special thanks go to my family, who have been a source of encouragement, boundless patience, and selfless sacrifices throughout these years. Their presence and support have been vitally important, providing me with the motivation and strength to persevere even during moments of doubt and uncertainty.

And a last huge final thanks to my husband Mhamad, for being an incredible pillar of support throughout this journey. His attentive listening, support, and understanding have been instrumental in helping me

bring forth my very best. His presence and encouragement have made a significant difference in my ability to navigate the challenges and triumphs of this academic pursuit.

Finally, I acknowledge the support and inspiration from all those whose names might not appear here but have played a pivotal role in shaping my academic and personal endeavors.

Thank you, everyone, for being a part of this remarkable chapter in my life.

Table of Contents

Abstract

The necessity for Probabilistic Seismic Hazard Assessment (PSHA) in civil engineering emerges from the need to design structures that can endure varying degrees of ground motion while maintaining acceptable performance. The Levant Fault System (LFS) stands out as one of the active plate boundary strike-slip faults globally, experiencing an estimated deformation of 4 to 5 mm/yr. This region witnessed devastating historical earthquakes with magnitudes above 7 causing significant casualties and destruction. However, the last century appears relatively quiet based on instrumental recordings, posing challenges for seismic hazard assessment.

Lebanon, along with neighboring countries Jordan, Palestine, and Syria, lies along the LFS, making seismic hazard assessment critical due to the dense population in these regions. Our main goal was to evaluate the seismic hazard levels in Lebanon, a region that has not undergone a comprehensive hazard assessment, with a particular focus on a thorough examination and exploration of uncertainties.

As a first step, we constructed a fault-based source model integrating available geomorphological, paleoseismological, and geodetic studies. This model was complemented by a catalog-based smoothed seismicity model to forecast off-fault earthquakes. Three ground-motion models adapted for the Levant region were employed, and uncertainties in hazard input parameters were meticulously traced and incorporated into the final hazard calculations to understand their impact on hazard levels. The resulting seismic hazard maps at Lebanon's scale indicated mean Peak Ground Acceleration (PGA) values exceeding 0.3g over two-thirds of the country, with the most elevated hazard values (>0.5g) concentrated along the primary strand of the Levant fault.

However, real-life seismic events worldwide have demonstrated that fault segments can rupture together across discontinuities, resulting in significantly larger events. A classical fault model implementation, as built in the first step of this thesis, doesn't account for the myriad of potential rupture combinations. Therefore, in a secondary phase, we explore an alternative class of fault models designed to replicate more natural rupturing behaviors within the LFS. These algorithms adopt a system-level approach, allowing sub-fault segments to rupture freely, akin to natural occurrences (e.g., OpenSHA Fault System tool by Field et al. 2014, Milner and Field 2021; as well as SHERIF by Chartier et al. 2019). Applying these methodologies to the LFS unveils significant dependencies on specific input parameters, such as segment definitions, rupture barriers, maximum magnitudes, and the shape of the Magnitude-Frequency Distribution (MFD). Comparing these methods with classical fault models, our analysis demonstrates that the interconnected fault model generally may yields lower hazard levels at a 475-year return period.

These findings serve as a foundation for decision-making concerning potential updates to the Lebanese building code, shedding light on the intricate impacts of various fault modeling approaches on seismic hazard estimations.

Résumé

La nécessité d'une Évaluation Probabiliste de l'aléa Sismique (PSHA) en génie civil découle du besoin de concevoir des structures capables de résister à des degrés variables de mouvements sismiques tout en conservant des performances acceptables. Le Système de Failles du Levant (LFS) se distingue comme l'une des failles décrochantes de frontière de plaques actives à l'échelle mondiale, subissant une déformation estimée de 4 à 5 mm/an. Cette région a connu des tremblements de terre historiques dévastateurs avec des magnitudes supérieures à 7, causant des pertes importantes en vies humaines et des destructions immenses dans la région. Cependant, le dernier siècle semble relativement calme sur le plan sismique selon les enregistrements instrumentaux, posant des défis pour l'évaluation de l'aléa sismique.

Le Liban, ainsi que les pays voisins tels que la Jordanie, la Palestine et la Syrie, se trouvent le long de la faille du Levant, rendant l'évaluation de l'aléa sismique cruciale en raison de la densité de population dans ces régions. Notre objectif principal était d'évaluer les niveaux d'aléa au Liban, une région dépourvue d'évaluations d'aléa complètes en tenant en compte l'exploration approfondi des incertitudes.

Dans un premier temps, nous avons élaboré un modèle de source basé sur les failles, intégrant les études géomorphologiques, paléosismologiques et géodésiques disponibles. Ce modèle a été complété par un modèle de sismicité lissée pour prévoir les séismes hors-failles. Trois modèles de mouvements du sol adaptés à la région du Levant ont été utilisés, et les incertitudes liées aux paramètres d'entrée de l'aléa ont été minutieusement suivies et intégrées dans les calculs finaux de l'aléa pour en comprendre l'impact. Les cartes d'aléa sismique résultantes à l'échelle du Liban indiquaient des valeurs moyennes d'accélération maximale du sol (PGA) dépassant 0,3g sur les deux tiers du pays, avec les valeurs d'aléa les plus élevées (>0,5g) concentrées le long de la faille principale du Levant.

Cependant, les événements sismiques réels dans le monde ont montré que des segments de failles peuvent se rompre ensemble à travers des discontinuités, engendrant des événements beaucoup plus importants. Une implémentation classique du modèle de faille, telle que construite lors de la première étape de cette thèse, ne tient pas compte de la myriade de combinaisons potentielles de rupture. Par conséquent, dans une phase secondaire, nous explorons une autre implémentation de modèles de failles conçus pour reproduire des comportements de rupture plus réalistes au sein de la faille du Levant. Ces algorithmes adoptent une approche à l'échelle du système, permettant aux sous-segments de se rompre librement (e.g., OpenSHA Fault System tool développé par Milner and Field 2021; ainsi que SHERIFS développé par Chartier et al. 2019). L'application de ces méthodologies sur la faille du Levant révèle des dépendances significatives à l'égard de certains paramètres d'entrée spécifiques, tels que les définitions de segments, les barrières de rupture, les magnitudes maximales et la forme de la distribution magnitude-fréquence (MFD). En comparant ces méthodes avec des modèles de failles classiques, notre analyse montre que le modèle de faille interconnecté peut généralement produire des niveaux d'aléa iplus bas pour une période de retour de 475 ans.

Ces résultats servent de base à la prise de décision concernant d'éventuelles mises à jour du code du bâtiment libanais, mettant en lumière les impacts détaillés des différentes approches de modélisation des failles sur les estimations d’aléa sismique.

Introduction

Since the earliest times of human civilization, humans have had to either adapt to their environment or domesticate it in order to settle permanently in a region. Among the various challenges a civilization must overcome, natural disasters rank among the most formidable, specifically earthquakes. There are numerous instances of civilizations being weakened or entirely erased by these phenomena that were too destructive for humans to recover from (e.g. The fall of Mycenae, L. Caskey 1969).

The cause of earthquakes was often attributed to divine or mythical causes due to a lack of scientific understanding. Historical records from China, Greece, Middle east and other regions documented earthquakes and their effects. The XXth centurie saw the beginning of systematic earthquake recording and the emergence of seismology as a scientific discipline. Instrumentation, such as seismometers, started being used to measure seismic waves. In the late XXth century, Richter (1935) introduced the Richter scale for quantifying local magnitudes. Meanwhile, Mercalli (1902) developed intensity scales to assess earthquake effects on structures and people. Mercalli intensity scale was revised and updated by the United States Geological Survey (USGS) and the California Institute of Technology (Caltech) in the 1990s.

Over the last decade, the importance of seismic hazard assessment has grown significantly, due to increased societal awareness and a greater focus on emergency and safety services. Additionally, governmental policies aimed at effectively managing potential crises arising from seismic activity. Probabilistic Seismic Hazard Assessment (PSHA) was first introduced by two authors in the late 60's (Cornell, 1968; Esteva, 1967, 1968). Seismic hazard relies on earthquake occurrence models, which evaluate the probability of earthquake happening in specific regions based on historical data, fault information, and geological studies. In recent decades, advancements in technology, computing power, and data collection have enhanced seismic hazard assessments. Probabilistic methods, incorporating various data sources like historical records, paleoseismology, and geophysical studies, provide a more comprehensive understanding of seismic hazard and risk.

The growing recognition of seismic hazards has influenced building codes, zoning regulations, and infrastructure designs in earthquake-prone areas. Subsequently, these regulations have mandated the assessment of hazards through probabilistic methods. These measures aim to mitigate risks and improve the resilience of communities against seismic events. International collaborations, such as the Global Seismic Hazard Assessment Program (GSHAP; Giardini et al. 1999) and Seismic Hazard Assessment of the Mediterranean Basin (SESAME; Jimenez et al. 2001), have worked toward standardized approaches for assessing seismic hazards on a global scale.

The history of seismic hazard assessment reflects a journey from ancient observations to sophisticated scientific methodologies aimed at understanding, predicting, and mitigating the impact of earthquakes on society and infrastructure. Ongoing research and technological advancements continue to refine our understanding of seismic hazards and improve risk assessment capabilities.

In high seismic regions, such as in California, The Working Group on California Earthquake Probabilities (WGCEP - 1988) made significant contributions to the progress of seismic hazard assessments in the late 1980s. Their research incorporated the inclusion of faults in earthquake source models, offering valuable insights into the seismic risk within the region. However, in low to moderate seismicity regions, despite the growing understanding of faults as earthquake-generating sources, PSHA, till the 80s, relied mainly on historical and instrumental seismicity records and did not incorporate information about faults in their source definition or modeling due to limited studies providing detailed fault parameters essential for hazard assessments, such as earthquake frequency or recurrence (McCalpin 2009).

Earthquake catalogs are essential to build source models for PSHA, but they typically cover only a few centuries to over a thousand of years. This timeframe is insufficient to capture the longer seismic cycles of most faults (Schwartz and Coppersmith 1984). This limitation becomes especially problematic in regions with low seismic activity, where faults have recurrence periods much longer than the duration covered by the available catalogs, as seen in areas like France.

Fault-based seismic hazard assessment gained prominence as seismic science advanced and researchers recognized the critical role faults play in generating earthquakes. Currently, paleoseismology stands as a primary method for acquiring fault parameters crucial for seismic hazard assessments. It typically provides information regarding slip rates, earthquake recurrence intervals, and maximum magnitude associated with fault activity. In areas prone to frequent seismic activity, this method is extensively utilized and it is often combined with fault data obtained from other techniques like geodetic or geophysical methods to comprehensively characterize the sources of seismic activity (Field et al. 2014 in California, Stirling et al. 2012 in New Zealand).

Lebanon is considered as a high seismic region, located along the Levant fault system (LFS), a plate boundary between the Arabian plate and the Sinai-African plate. Historical, archaeological and paleoseismological studies underscore major destructive earthquakes along this fault system. Three notable seismic events mark Lebanon's recorded seismic history: the AD 551, an earthquake struck Lebanon on July 9 with an estimated moment magnitude (Mw) of around 7.5, accompanied by a subsequent tsunami (Elias et al. 2007). The earthquake that occurred on May 20, AD 1202 estimated to have an equivalent moment magnitude (Mw) of about 7.5 (Daëron et al. 2005; Elias et al. 2007). In the year AD 1759, two significant seismic events occurred on October 30 and November 25, with estimated equivalent moment magnitudes (Mw) of approximately 6.7 and 7.4, respectively (Daëron et al. 2005). All of these earthquakes are believed to have been triggered by the known and identified active faults within the Levant Fault System (LFS).

The historical activity of the LFS sparked interest in conducting paleoseismic studies in this area to enhance the understanding of seismic hazards. Numerous seismic hazard assessments were perfomed in Jordan, Palestine, Syria and Lebanon (Arieh et al. 1985; Yucemen 1992; Tarazi 1999; Malkawi et al. 1995; Tarazi et al. 2007; Jimenez et al. 2008; Harajli et al. 2002; Huijer et al. 2011). All these studies primarily relied on area sources. However, Huijer et al. (2016) revised their source model, incorporating major faults in their analysis. However, they did not integrate geomorphological or paleoseismological data; in their case, on-fault earthquake recurrence rates were obtained from the seismicity catalog.
The integration of faults into PSHA in the Levant region is still in its developmental stage. The latest seismic hazard maps were provided by the Earthquake Model of the Middle East project, spanning from Turkey to Pakistan (Danciu et al. 2018). Due to the extensive coverage of the region, the epistemic uncertainties related to the source model were not thoroughly investigated. Additionally, faults are often

regarded as separate and non-interacting sources, which might not align with numerous observations in nature showing interconnected ruptures during earthquakes (e.g., Wei et al. 2011; Zhang et al. 2012).

Hence, this thesis is primarily driven by three key motivations. Firstly, the need for developing an updated hazard model, making use of all the knowledge related to the generation of earthquakes, considering the uncertainty in parameters and assumptions used in constructing the source model, and the selection of ground motion models. Secondly, existing publications that incorporate faults into the source model do not utilize the available geodetic and paleoseismic data for the LFS, a step that should be taken. Specifically, in Lebanon, a compact nation riddled with faults positioned in close proximity, approximately 20km apart. Moreover, the aim is to enhance the source model by incorporating fault connectivity to simulate potential real-life scenarios.
Lastly, a specific study on the Yammouneh fault is done where enough data are available to incorporate time dependency and its impact on the hazard.
This thesis aims to establish a robust foundation for updating Lebanon's current building codes.

Content of the thesis

In Chapter 1, we offer a comprehensive overview of seismic hazard encompassing its diverse forms, including both deterministic and probabilistic approaches. Given our primary objective of creating hazard maps specific to the country, our emphasis lies on the probabilistic methodology. We provide a succinct exploration of the various components integral to the conventional probabilistic hazard assessment method.

Chapter 2 delivers a concise introduction to the tectonic environment within our study area. We delve into the region's historical seismicity, outlining notable seismic events and their impact. Additionally, we shed light on the essential tools pivotal for constructing the seismic source model. These tools, such as paleoseismology and geodesy, are presented in detail, highlighting their significance in delineating seismic sources and understanding seismic activity within the study region. Finally, an overview of past international, regional, and local seismic hazard studies conducted for Lebanon has been provided.

Chapter 3 is presented as a published manuscript to the peer reviewed journal of the Bulletin of Earthquake Engineering. This chapter presents a comprehensive probabilistic seismic hazard study for the Lebanese region. Our methodology involves developing a set of smoothed seismicity models based on instrumental data to forecast off-fault seismicity, combined with a set of moment-balanced fault models that account for best-characterized faults. Both the Gutenberg-Richter model and the characteristic model are considered for forecasting earthquakes on the faults, with earthquake frequencies inferred from geological and geodetic slip rates. Uncertainties at every step are tracked and a sensitivity study is led to identify which parameters and decisions most influence hazard estimates. We establish a source model logic tree populated with the key parameters, and combine this logic tree with three ground-motion models (GMMs) potentially adapted to the Levant region. The study provides detailed information on the hazard levels to expect in Lebanon, with the associated uncertainties, constituting a solid basis that may help taking decisions in the perspective of future updates of the Lebanese building code.

Chapter 4 is presented as an article in preparation for submission to a peer reviewed journal. This chapter consists of building a more reslistic fault based source model for the whole Levant region based on fault interaction. In this study, we test one of the methodologies designated to include these kind of

ruptures in the source model, the SHERIFS (Seismic hazard and earthquake rate in fault systems) algorithm developed by Chartier et al. (2019). Application to the LFS unveils significant dependencies on specific input parameters, such as segment definitions, rupture barriers, maximum magnitudes, and the shape of the Magnitude-Frequency Distribution (MFD).

Finally, Conclusion and Perspectives. In this section, the primary findings from these comparative analyses are outlined, emphasizing a detailed discussion on the key methodological challenges. Additionally, it proposes overarching conclusions and outlines perspectives for enhancements and future endeavors

CHAPTER 1

Probabilistic Seismic Hazard Assessment (PSHA)

Contents

List of Figures

1.1 Overview

The primary goal of this work is to offer a realistic fault-based seismic hazard assessment for the Levant Fault System (LFS). We will start by providing a concise explanation of seismic hazard. This will encompass its deterministic and probabilistic approaches, key components, resulting outputs, and practical applications. In the next step, we will explore various methods of implementing faults into seismic hazard, elucidating their concepts and examining their influence on the hazard.

Throughout history, human existence has consistently been threatened by natural hazards, and among these, earthquakes stand out as one of the most devastating natural disasters. Earthquakes, in particular, have proven to be both costly and deadly, accounting for approximately one-fifth of all economic losses and contributing to an annual average of around 20,000 fatalities (Silva et al. 2019).

The main driving force behind the development of quantitative methods for assessing seismic hazard has been the need for civil engineering to design structures that are capable to withstand any level of ground motion while maintaining a desired level of performance.

1.2 Deterministic versus probabilistic approaches

To assess earthquake hazard, scientists strive to forecast and model the future earthquakes' location, magnitude, and ground shaking. Deterministic and probabilistic seismic hazard assessment are the two approaches used to do so. However, when assessing the hazard, analysts often feel pressured to choose between both methods (Reiter 1990, Krinitzsky et al. 1993, Kramer 1996). Boomer (2002) states that the choice of the suitable method must align with the application's requirements and take into account the nature of seismic activity in the region as well as its correlation.

1.2.1 Deterministic calculation

First, deterministic seismic hazard assessment (DSHA) consists in identifying a "worst-case" ground motion scenario. So, one could simply look for the maximum magnitude that could occur on the closest possible fault (McCalpin 2009).
However, this approach proves to be challenging and carries large uncertainties. To start with, accurately estimating a single, realistic maximum earthquake event is a difficult task. Also, the consideration of a unique and close very rare earthquake magnitude leads to gross over estimation of the potential hazard. Additionally, to estimate the amplitude of ground motion at a specific frequency, ground motion models take into account factors such as earthquake magnitude, distance from the seismic source, and site-specific characteristics. Therefore, even if "the maximum magnitude" is selected, it may not necessarily result in the maximum spectral acceleration amplitudes across all frequencies. As well, ground motion prediction models can only predict a distribution for the ground-motion, not a single value. The choice of a “worst-case” earthquake can be difficult and subjective.

Yet, there is no single, established, and universally accepted approach to DSHA, partly due to the lack of a conventional point of reference. The deterministic approach is still widely used in the nuclear field. For example, the French and Japanese nuclear authorities continue to adopt this approach in defining regulations for nuclear facilities (Scotti et al. 2014)

1.2.2 Probabilistic calculation

The probabilistic seismic hazard assessment (PSHA) has gained prominence due to its ability to provide a more comprehensive and statistically rigorous assessment of seismic hazards. PSHA method made its initial appearance in the late 60's (Esteva 1967, 1968; Cornell 1968). Since then, it has become the established methodology adopted by regulations around the world for establishing reference ground motions (e.g. Petersen et al. 2014; Grünthal et al. 2018; Beauval and Bard 2021). In essence, PSHA offers an estimate of the likelihood that a specific ground motion level will be surpassed at a given location within a future time frame.

Ultimately, both analyses are conducted, but the decision on which one to choose is influenced by the purpose of the hazard assessment, the level of seismic risk (low, moderate or high) and the scope of the project (Fig. 1.1) (McGuire 2001, Boomer 2002).

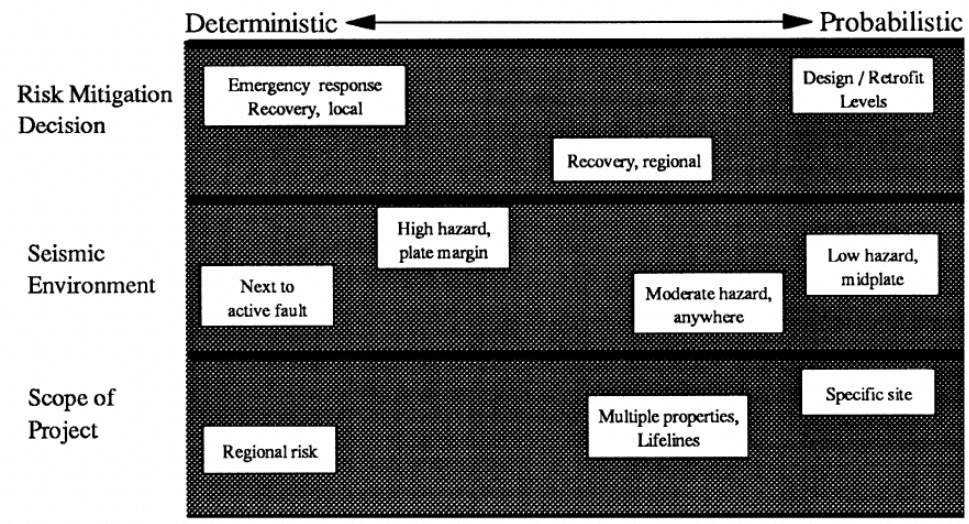

Fig. 1. 1 Applications of seismic risk along the spectrum of deterministic and probabilistic approaches, from McGuire (2001).

Instead of disregarding the inherent uncertainties within the problem, such as the potential seismic sources, the range of magnitudes that could impact a particular site, and the models used to predict ground motion, the probabilistic approach integrates them into the calculations of the annual rates of occurrence for ground motion parameters. For a given acceleration A*, the annual exceedance rate is calculated as follows:

$$\lambda_{A*} = \sum_{i=1}^{N} \lambda_i \int_{m=M_{min}}^{M_{max_i}} \int_r P[A > A* \mid m,r]\, f_{M_i}(m)\, f_{R_i}(r)\, dmdr \qquad (1.1)$$

Where,

- λ_i is the annual rate of earthquakes with a magnitude greater than or equal to the chosen minimum magnitude M_{min} for source zone i.
- f_{M_i}(m) and f_{R_i}(r) are the probability density functions for magnitude and distance of source i, and they are assumed to be independent.
- P[A > A*|m, r] is the probability that an earthquake with magnitude m at distance r from the site generates an acceleration greater than A*. This probability is calculated using the attenuation relationship.
- N is the number of source zones.

Seismic events are typically expected to follow a Poisson process over time, where the likelihood of an earthquake occurring is independent of the time elapsed since the previous one. For a Poisson process with an average annual rate represented as λ, the probability P of the event occurring at least once during a time interval t can be calculated using the formula provided by Ang & Tang 1975:

$$P=1-e^{-\lambda t} \tag{1.2}$$

The return period (RP) is the inverse of the annual rate $T=\frac{1}{\lambda}$. For instance, 10% probability (P) of exceedance over a 50-year time frame (equivalent to an annual rate of 0.0021) implies a 475-year return period. When we design a building to withstand the acceleration associated with a 475-year return period, we are essentially ensuring that the building can endure an acceleration that has a 10% chance of being surpassed within the next 50 years (or a 90% probability of not being exceeded). This 50-year span corresponds to the typical lifespan of conventional buildings.

However, according to Reid's elastic rebound theory (Reid 1911) earthquake occurrences are not independent of each other. Basically, the probability of another earthquake happening at the same place is relatively low immediately after an event, and it gradually increases as tectonic stresses accumulate along the fault (Matthews et al. 2002; Field 2015; Wong & Thomas 2020). However, in order to incorporate time-dependent calculations, it is necessary to specify the date of the last earthquake on the fault along with its return period. Obtaining this information can be particularly challenging in regions with low to moderate seismicity due to the scarcity of paleoseismic and geological data. As a result, this approach is not widely implemented.

1.3 Components of PSHA

1.3.1 Source Model

PSHA relies on a source model that describes the occurrence of future earthquakes, in terms of locations and magnitudes. There are two primary categories of source models utilized in seismic hazard assessment:

1. Area source models in regions with moderate seismicity (e.g., France; Danciu et al. 2021, Australia; Allen et al. 2020, Canada; Adams&Atkinson 2003, Allen et al. 2015) that do not have sufficiently detailed data of geological settings, causative faults and paleoseismic information. In this case, source areas are represented as polygons in which earthquakes may occur anywhere. In the case of the Levant Fault System (LFS), this approach was adopted even where the fault zone is clearly delineated both geologically and seismologically, because of the inherent uncertainty associated with determining hypocenter locations and fault geometry. An illustration of this type of source model for the LFS is provided in Fig. 1.2. Within each area source, it is crucial that the seismic potential and tectonic settings are consistent and uniform (Erdik, 1984).

2. Fault-based source model in regions characterized by significant seismic activity (e.g., California; Field et al. 2014, Taiwan; Chan et al. 2020, Japan; Fujiwara et al. 2009, HERP, 2014) where detailed information is available from past historical earthquakes, geological or geodetic information, see Stirling et al. (2012). Indeed, the LFS offers a distinctive historical record, comprising numerous earthquake testimonies complemented by paleoseismological

investigations (Guidoboni et al. 1994, Zohar et al. 2016). These models require the inclusion of essential fault details, encompassing geometric aspects and slip rates (Fig. 1.3).

When comprehensive data regarding the geometry, mechanics, historical activity, and velocities (geodetic/geologic) of faults are accessible, opting for a fault-based source model has become a common practice. This is rooted in the fact that earthquakes predominantly stem from fault movements, rendering fault source models a more faithful representation of seismic hazards. Additionally, the meticulous consideration of fault geometry and orientation is indispensable for precise ground shaking estimations and facilitates the accurate estimation of earthquake magnitudes and specific rupture characteristics, ultimately enhancing the overall precision of hazard assessments.

Nevertheless, it has been observed globally that neighboring faults can rupture simultaneously, leading to more significant seismic events. The complexity of understanding interactions between various faults and their collective seismic potential is essential for creating realistic forecasts of future earthquakes. Recent advancements in fault-based estimates have incorporated features like multifault ruptures, as well as partial ruptures along faults, as outlined by Field et al. (2014). In such instances, the seismic moment for the entire system is partitioned and distributed among different rupture combinations with varying magnitudes to represent a comprehensive range of potential ruptures. Each of these methodologies employs distinct approaches to calculate on-fault earthquake rates.

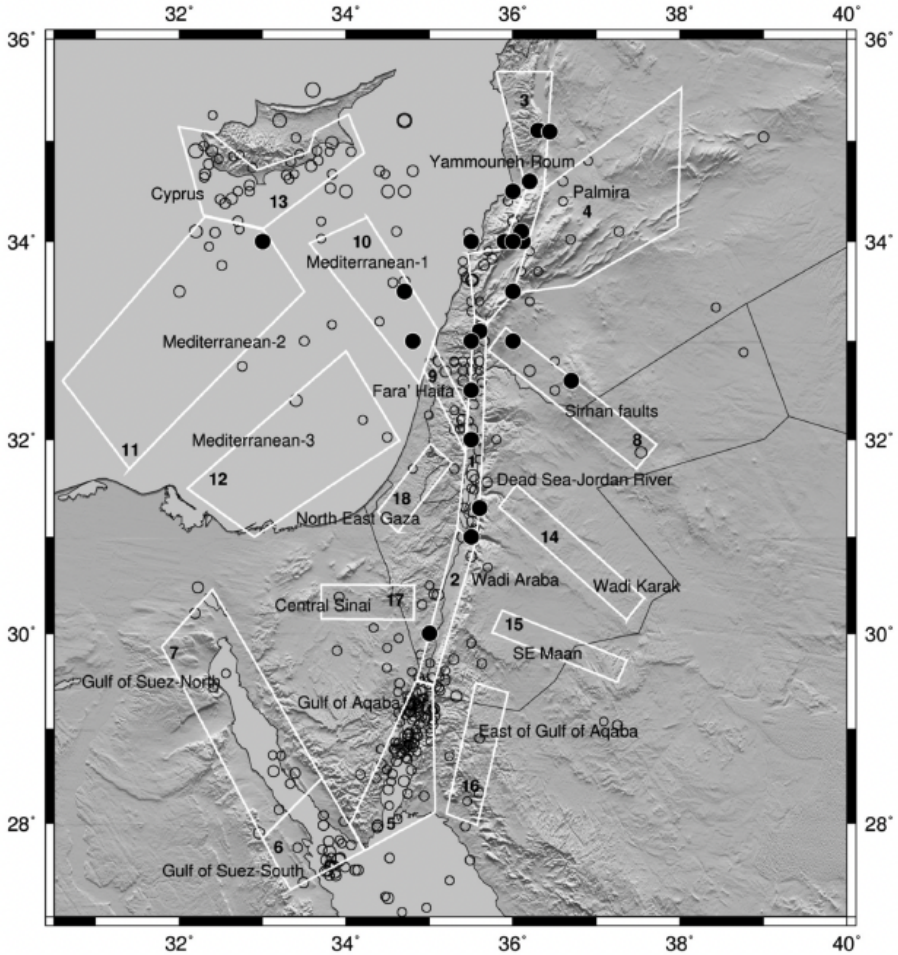

Fig. 1. 2 18 area sources represented by white polygons for the Levant region enclosed by latitudes 27.0°N and 35.5°N and longitudes 32.0°E and 39.0°E, from Jimenez et al. (2008)

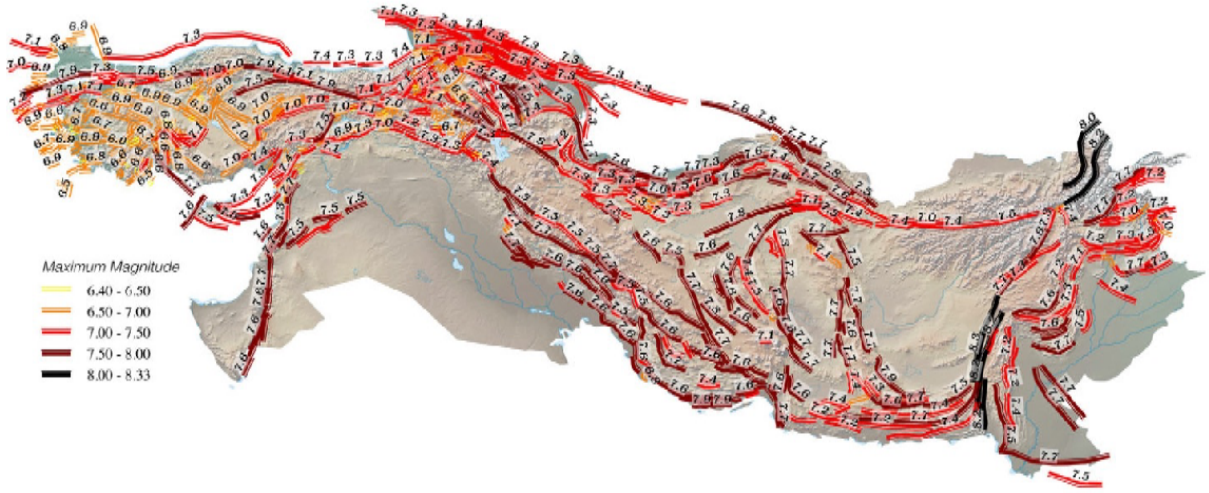

Fig. 1. 3 Fault-based source model incorporating the most thoroughly characterized faults, utilizing their geological and geometrical parameters, from Danciu et al. (2018).

1.3.2 Recurrence Model

For each seismic source, a recurrence law is modeled either based on the seismicity catalog of the zone for the area sources or based on the available moment rate for the fault sources. This recurrence law provides, for a magnitude m, the annual number of earthquakes with a magnitude greater than or equal to m, denoted as λ_m.

1.3.2.1 Area sources

An earthquake catalog first is needed. Then a declustering is usually applied in order to separate the mainshocks from the aftershocks to prevent biasing the expected long-term earthquake forecast. A set of completeness periods associated with a range of magnitudes must be determined. (M_c) is the minimum magnitude above which all earthquakes within a certain region are reliably recorded. Inside each area source zone, earthquakes with magnitude ≥ Mc are used to build the Magnitude Frequency Distribution (MFD).

1.3.2.2 Fault sources

The seismic moment rates based on fault slip rates are being used to constrain the occurrences of earthquakes. Typically, slip rates are established through two primary means: geological analysis involving the examination of displaced geological markers like sedimentary layers or faulted features, or paleoseismic trenches when there's sufficient data on slip variability across successive earthquakes. Alternatively, slip rates can also be derived from geodetic data obtained through satellite systems. Thus, the annual seismic moment rate on the fault can be estimated as:

$$\dot{M}_0 = \mu A S \tag{1.3}$$

with μ the shear modulus (usually estimated to be ~ 3×10^{10} N/m^2), A the total rupture area, and S the average slip rate.

1.3.2.3 Shape of the Magnitude Frequency Distribution

Moreover, it is necessary to make assumptions about how earthquake sizes will be distributed, which is essentially defining the shape of the magnitude-frequency distribution.

Exponential magnitude distribution

Based on an extensive dataset of California earthquakes spanning a considerable duration, Gutenberg and Richter (1944) concluded that λ_m adheres to a linear function when plotted on 10 base logarithmic scale:

$$\log_{10}(\lambda_m) = a\text{-}b(m) \tag{1.4}$$

$$\lambda_m = 10^{a-b(m)} \tag{1.5}$$

with "a" the productivity and "b" the slope of the rate of earthquakes with respect to m.

The truncated exponential model is widely employed and can be identified by its key parameters: the exponential decay coefficient, b, and an upper magnitude limit, M_{max}. Often regions are constrained by the maximum earthquake magnitude determined by the size of the accessible fault systems. Additionally, a minimum magnitude threshold, denoted as M_{min}, is usually defined. The reason behind its prevalence lies in the fact that extremely small magnitudes typically do not pose a significant impact on structures. Hence, we start the calculation with the minimum magnitude that we estimate could affect a specific structure (Fig. 1.4a).
Therefore, the probability density function for M, becomes:

$$f_M(m) = \frac{b\ln(10)10^{-b(m-M_{min})}}{1-10^{-b(M_{max}-M_{min})}}, \qquad M_{min} < m < M_{max} \tag{1.6}$$

Characteristic Distribution

Another alternative distribution is derived from the characteristic earthquake model (Schwartz and Coppersmith 1984), assuming that faults experience repetitive occurrences of maximum earthquakes known as characteristic earthquakes while remaining quiescent during interseismic phase.
However, when we compare the recurrence intervals for characteristic earthquakes obtained from geological sources with those derived from seismicity data, a significant discrepancy is observed. To address this issue, Youngs and Coppersmith (1985) introduce a recurrence model that hinges on the concept of a characteristic earthquake for M_{max}. For lower magnitudes, this recurrence model adopts an exponential distribution (Fig 1.4b). Its probability density function can be written as follows:

$$f_{YC}(m) = \begin{cases} \frac{b\ln(10)\,10^{-b(m-M_{min})}}{1-10^{-b(M_{max}-0.5-M_{min})}} \times \frac{1}{1+c} & (M_{min} \le m \le M_{max}-0.5) \\ \frac{b\ln(10)\,10^{-b(M_{max}-1.5-M_{min})}}{1-10^{-b(M_{max}-0.5-M_{min})}} \times \frac{1}{1+c} & (M_{max}-0.5 \le m \le M_{max}) \end{cases} \tag{1.7}$$

with

$$c = \frac{b \ln(10)\, 10^{-b(M_{max}-1.5-M_{min})}}{1-10^{-b(M_{max}-0.5-M_{min})}} \times 0.5$$

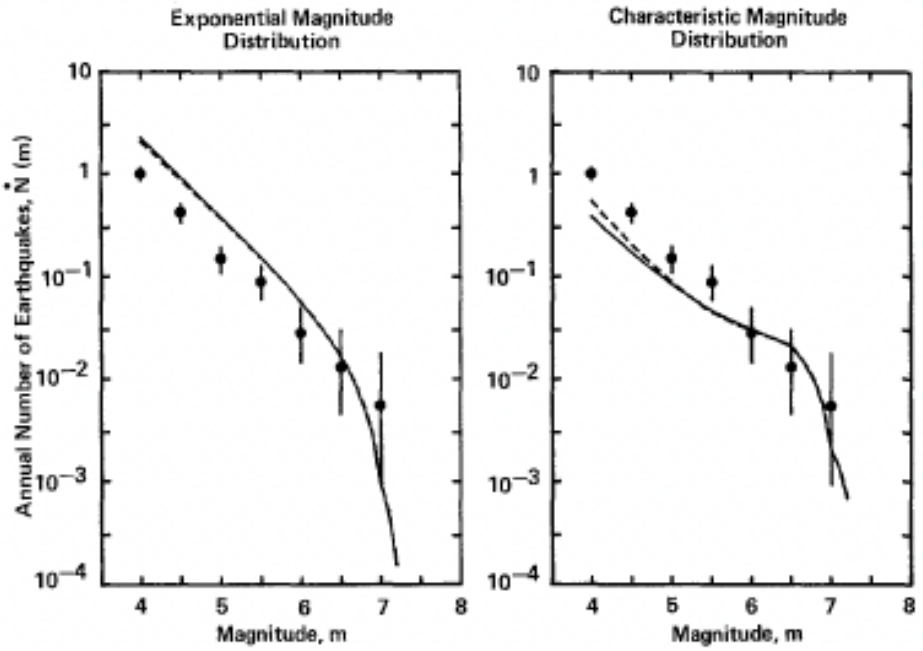

Fig. 1. 4 Comparison of magnitude-frequency distribution models based on slip rate and seismicity. Seismicity data are represented by points and the relative uncertainty by bars. The plot on the left depicts an exponential distribution (i.e., Gutenberg- Richter), while the plot on the right portrays a characteristic earthquake model, from (Youngs&Coppersmith 1985)

1.3.3 Ground Motion Models (GMMs)

The next step is to define the attenuation relations that predict the ground motion levels that these future earthquakes may generate. These models take into account factors such as earthquake magnitude, distance from the earthquake source, faulting mechanism and site conditions (V_{s30}). They are developed using statistical regression on strong-motion databases from different tectonic regions or based on numerical simulations or mixed empirical/simulations data.
GMMs are typically written in the following form:

$$\text{Log}(Y)=f_{source}(M,Mech)+f_{path}(R,M)+f_{site}(V_{s,30},\text{site class},f0,z_{1.0},z_{2.5},Sar) \pm \sigma \qquad (1.8)$$

Y represents the ground motion parameter being predicted (e.g., peak ground acceleration or spectral acceleration).
M is the earthquake magnitude
Faulting Style (Mechanism): Reverse, strike-slip, normal.
R is the distance from the earthquake source (e.g., hypocentral distance or rupture distance).
$V_{S,30}$ is the average shear wave velocity over the top 30m.
Site Class: A, B, C, D, E, S1, S2 for Eurocode 8 base.
Z represents the depth to the earthquake source.

Observed ground motions exhibit a variability in their distribution around the predicted average acceleration or intensity measure. For a given magnitude at a given distance, logarithms of ground-

motions are distributed according to a normal distribution, as depicted in Fig. 1.5. Consequently, ground motion uncertainties are quantified using a statistical framework that involves a mean value (μ) and a standard deviation (σ).
It is crucial to underscore the substantial influence of the GMM's standard deviation on hazard calculations. The larger the sigma, the larger the hazard estimate. The ongoing research focuses on improving the quantification of this parameter.

Four main classes of tectonic regimes are used for developing ground motion models: active crustal region (ACR), stable continental region (SCR), volcanic and subduction.

In situations where ground motion models are unavailable, as is the case in some regions like Lebanon, it is common to import a ground-motion model developed from recordings obtained in tectonically similar areas.

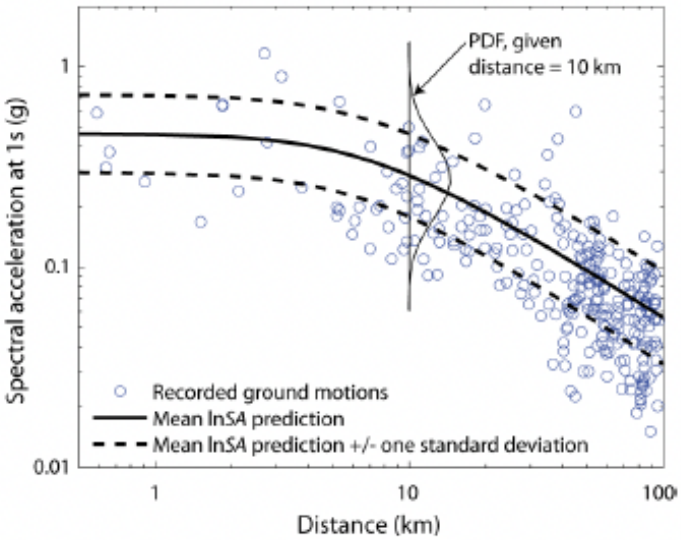

Fig. 1. 5 Observed spectral acceleration values at 1 second from the 1999 Chi-Chi earthquake in Taiwan (M7.6), from Baker (2013)

1.3.4 Logic Tree

A logic tree is set up to account for some of the uncertainties that characterize the models built and propagates them up to the hazard estimates. It was firstly introduced by Kulkarni et al. (1984). The logic tree is divided into multiple branches, with some branches dedicated to exploring distinct earthquake source models. These source models encompass variations in earthquake occurrence rates, fault geometries, maximum magnitudes, and even differing seismicity models. Within each source model, specific parameters are defined, and their levels of uncertainty are quantified. Other branches of the logic tree are concerned with the exploration of various ground motion models.
Each branch within the logic tree represents a distinct model, and each model is assigned a probability or weight. These probabilities are often determined through expert judgment, or other data sources. By combining these diverse branches and their associated probabilities, a distribution is obtained for the hazard estimate. This assessment yields a spectrum of ground motion estimates for different model, encompassing the spectrum of potential seismic hazards.

1.3.5 Seismic Hazard Calculations

Seismic hazard is commonly represented through seismic hazard maps, hazard curves and uniform hazard spectrum (UHS) (Fig. 1.6). Seismic hazard maps display the ground-motions that have the same probability of being exceeded over a given future time window. Additionally, hazard curves illustrate the relationship between ground shaking intensity and the probability of occurrence, as another way to represent seismic hazard. Moreover, the UHS provides a comprehensive view of seismic hazard by illustrating the response spectra, which represent the acceleration response of a structure to ground shaking, over a range of periods. Together, these representations contribute to a thorough understanding of seismic hazard and aid in designing structures resilient to potential ground motions.

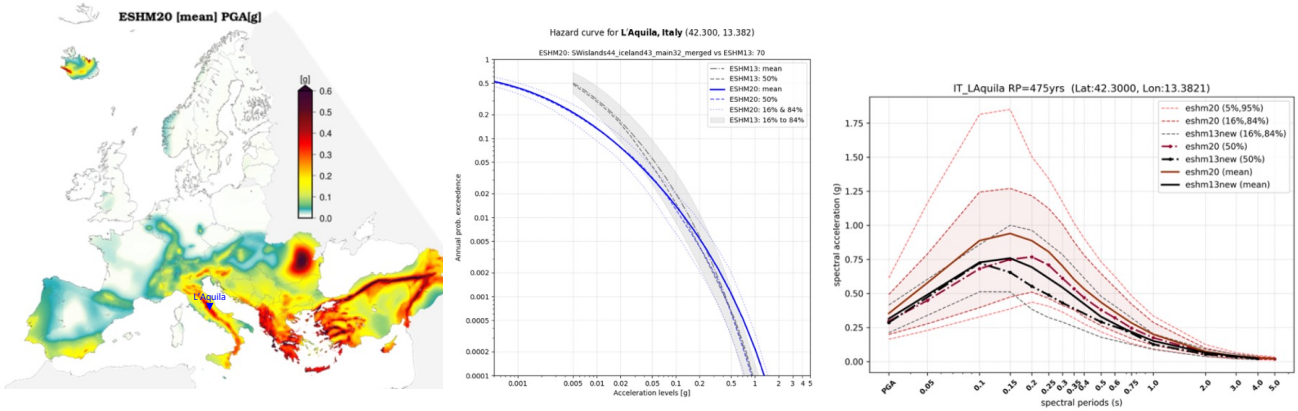

Fig. 1. 6 Representation of various outcomes from a seismic hazard assessment: (a) seismic hazard map illustrating PGA at 475-year return period, (b) hazard curve specific to the l'Aquila site in Italy, and (c) uniform hazard spectrum for the identical site, from Danciu et al. (2021)

CHAPTER 2

Background overview and state of the art

Contents

List of Figures

List of Tables

Overview of the seismic potential of the LFS

This section provides a concise overview of the available paleoseismic, geodetic and seismic hazard studies in the Levant fault region, highlighting the current state of knowledge that forms the basis for the development of this thesis.

2.1 Tectonic Setting

This study focuses on the LFS, a major strike-slip fault that accommodates the northward motion of the Arabian plate relative to the Sinai plate. Roughly 20-25 million years ago, during the Miocene epoch, the Arabian Plate began separating from the Nubian Plate (McQuarrie et al. 2003). This separation set the stage for the formation of the LFS. Over time, the movement and interaction between these tectonic plates caused the fault system to develop its characteristic features, the Lebanese restraining bend, as a link between the northern and southern sections of the LFS. Nubia Plate motion changed and the Sinai Plate became distinct. Other faults within the Lebanese Restraining Bend have developed, Mount Lebanon Thrust, and possibly a late Neogene pulse of contractional reactivation of the Palmyride Fold Belt (PFB) (Fig. 2.1). Based on geological observations, a total post-Miocene, left-lateral motion of 105 km has been documented along this system (Freund et al. 1970; Hatcher et al. 1981; Quennell 1984).

The ~1200 km-long fault can be categorized into three main sections (Gomez et al. 2020). Starting from the southernmost point, it comprises the Araba fault that extends from the Gulf of Aqaba to the dead sea. Continuing from the Dead Sea, it moves in a left step over toward the Hula Basin, passing through the Sea of Galilee, forming the Jordan Valley Fault. In the central part, characterized by the Lebanese restraining bend, the fault splays into 3 branches: the Yammouneh Fault situated in the middle, Rachaya-Serghaya separated by the Mount-Hermon to the east and the Roum fault located to the west. Additionally, a recently discovered offshore thrust is identified as the Mount Lebanon Thrust (Briais et al. 2004; Carton et al. 2009). The northern part, known as the Ghab fault, starts from the El Boquea basin until the Ghab basin featuring the Missyaf fault and a left stepover until the triple junction, where the LFS, the East Anatolian Fault (EAF), and the Cyprus Arc converge (see Fig. 2.2a).

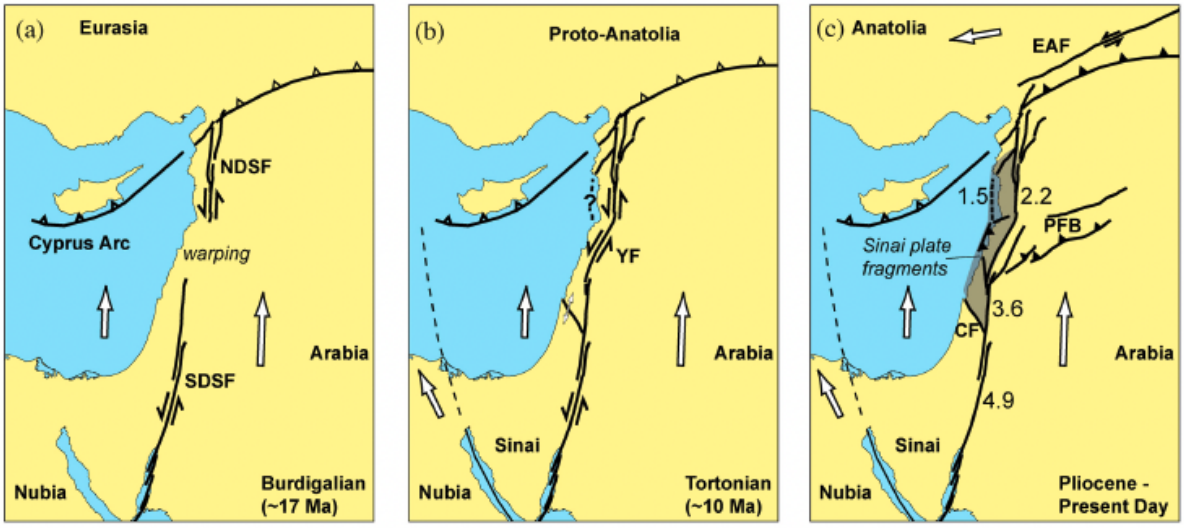

Fig. 2. 1 A visual depiction outlining the progression of the LFS from the Miocene period to the present day, (a) The development of both the northern and southern segments of the LFS during the middle Miocene period, (b)

Around the Late Miocene period, approximately 10 million years ago, the Lebanese restraining bend began to take shape. This involved oblique extension and left-lateral movement along the Carmel fault, indicated by the double-headed arrow. Concurrently, there was a shift in Nubia Plate motion, leading to the distinct separation of the Sinai Plate, (c) Additional faults within the Lebanese Restraining Bend have emerged, potentially accompanied by a resurgence of contractional activity in the Palmyride Fold Belt (PFB) during the late Neogene period, from Gomez et al. (2020)

2.2 Historical seismicity

Historically, this fault system has caused destructive earthquakes with magnitudes exceeding 7 (Fig. 2.2b). Starting from the southern section of the LFS, both the AF and the JVF were sites of significant destructive events. The history of the Gulf of Aqaba bears witness to several impactful seismic events. Notably, significant swarms occurred in 1983, 1990, and 1993. The 1983 sequence, as documented by El-Isa et al. (1984), comprised approximately 500 local earthquakes with a magnitude of ML ≤ 4.85 (the largest reaching ML = 5.2). These seismic activities were largely concentrated within the Aqaba Basin, spanning between latitudes 29° and 29.4° and longitudes 34.5° and 34.75°. The 1990–1991 swarm, with the most substantial magnitude recorded ML = 4.3, primarily affected the southern region of the Aqaba Basin. This period from 1983 to 1991 was notably associated with the Aqaba-Aragonese fault step zone. The most significant earthquake recorded instrumentally in the area occurred on November 22, 1995, within the Gulf of Aqaba, having a magnitude of M_W 7.3. It originated in close proximity to the 1993 swarm area, near the eastern edge of the Aragonese Deep (Klinger et al. 1999).

The main historical events that occurred on the JVF are: the 363 earthquake, it consists of a sequence of two shocks on 18 and 19 May (Ambraseys, 2009) with an estimated magnitude of Ms 7.4±0.3. The 746 (or 747 or 749) that occurred on 18th January in Palestine. The date of this event was poorly constrained. Karcz (2004, p. 778) suggests that discrepancies in ancient texts' multiple-year dates stem from the inconsistent utilization of various calendars and eras in dating this event. Ambraseys (2006) approximated its magnitude to Ms 7±0.3. And the 1033 event with M_W =6 (Guidoboni and Comastri 2005). In more recent times, three moderate earthquakes were documented: 11 July 1927 M_W 6.2; 23 April 1979 Mb 5.2; and 2 February 2004 ML 5.2.

Brax et al. 2019 did a meticulous job to compile a historical and instrumental earthquake catalog for Lebanon. They rigorously reviewed prior studies, handpicking the most trustworthy events to incorporate into this comprehensive catalog. Their coverage spanned from 31 BC to the end of the 19th century, encompassing a geographical area between 31° to 35.5° in latitude and 34° to 37° in longitude. The major earthquakes concentrated in the central part of the LFS are: the 551 Beirut earthquake, Ms=7.3 (Darawcheh et al. 2000); the event on May 20, 1202 with M_W =7.6 (Hough and Avni 2009-2010). This latter earthquake affected two fault segments: the Yammouneh fault, where it originated, and the Jordan gorge fault; there are archaeological and paleoseismic evidence that show a left-lateral offset of 1.6 meters at the walls of the Vadum Jacob castle (Wechsler et al. 2014). The seismic sequence of 1759; October 30, Ms=6.6 (Ambraseys and Barazangi 1989) which ruptured both Rachaya and the JGF; 0.5m offset of the Ottoman Mosque was detected (Ellenblum et al. 1998), and the November 25 with Ms=7.4 (7.2-7.5) (Ambraseys and Barazangi 1989). The 1837 earthquake with Ms=7±0.3 (Ambraseys 2006), seemingly took place along the Roum fault. Seismic records suggest that it was the source of the double shock of the Chim earthquake in 1956. This destructive event comprised two distinct shocks, striking within a span of less than fifteen minutes. The first event was estimated to have a magnitude of M_W 5.3, and the second, M_W 5.5 (ISC-GEM catalog, Di Giacomo et al. 2015). In a more recent event, Lebanon experienced a seismic swarm with a maximum magnitude of M_W 5.1 on March

21, 1997. The Bhannes Seismological Observatory pinpointed the epicenter, noting its proximity to the Roum fault, the same location as the dual seismic occurrence on March 16, 1956. Additionally, early in 2008, a sequence of earthquakes, including a magnitude of M_W 5.1 on February 15, shook parts of South Lebanon (Brax et al. 2019).

In the northern part of the LFS, the seismic activity has been low since 1900, coupled with the limited number of focal mechanisms, contrasting with the history of significant and destructive earthquakes. Among the most important seismic events, the 860 M7-7.5, the 1157 (M7-7.5), 1170 who ruptured Missyaf Fault (M7.3-7.5) and 1408 with M>7.5 or 7.9 (Sbeinati et al. 2009; Khair et al. 2000; Meghraoui et al. 2003). It is worth mentioning, on February 6, 2023, an earthquake with a moment magnitude (M_W) of 7.8 occurred in the southern part of the East Anatolian Fault, just north of its intersection with the LFS. This event was succeeded by another earthquake with a magnitude of 7.6. Numerous aftershocks occurred in the Levant area following these earthquakes (He et al. 2023; Inbal et al. 2023).

Even though the LFS has shown significant historical activity, seismic quiescence in the last century has sparked debates, particularly regarding the present-day activity. The last century appears quiet in comparison to what occurred in the past (Fig. 2.2c). In terms of seismic hazard assessment, the seismic rates inferred from the instrumental catalog are not representative of the true seismic potential in the area. The discrepancy between quiet instrumental period and large historical earthquakes is another challenge for estimating seismic hazard in this area.

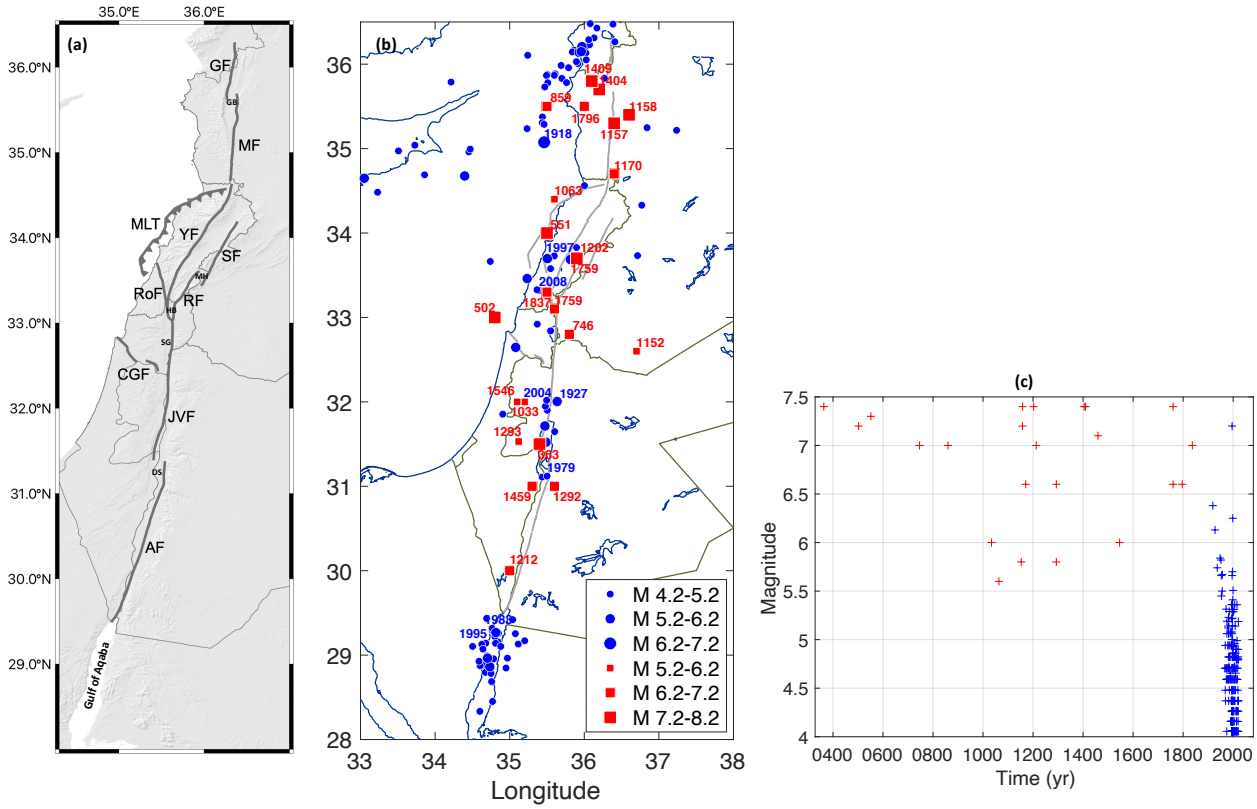

Fig. 2. 2 (a) Active faults of the LFS: Araba Fault (AF), Jordan Valley Fault (JVF), Carmel-Gilboa Fault (CGF), Yammouneh Fault (YF), Rachaya Fault (RF), Serghaya Fault (SF), Roum Fault (RoF), Mount Lebanon thrust (MLT), Missyaf Fault (MF) and Ghab Fault (GF). DS: Dead Sea, SG: Sea of Galilee, HB: Hula Basin, GB: Ghab basin, MH: Mount Hermon (b) Past seismicity along the LFS covering the spatial window from 34.5° to

37° in longitude, and 29° to 37° in latitude, red squares: Historical seismicity, blue circles: instrumental earthquakes 1927-2020 with $M_W \geq 4.2$ using three global sources (ISC-GEM, GCMT and the ISC-reviewed), (c) Magnitude versus Time for the earthquakes shown in the map.

2.3 Paleoseismic studies of the LFS

Given its extensive earthquake history, this fault, stands out as the most suitable and interesting location for conducting paleoseismic and geological studies, as well as testing earthquake behavior models.

Paleoseismic studies are conducted to investigate and understand past seismic activity by examining geological evidence preserved in the Earth's crust, which includes the analysis of features like fault scarps, liquefaction occurrences, offset geological formations, and seismic ruptures within sedimentary layers. Additionally, these studies are used to estimate the recurrence intervals of past seismic events by dating and analyzing earthquake-induced disturbances in sedimentary layers.

The southern and central segments of the LFS have been more extensively investigated compared to the northern section. Therefore, I will discuss the research, moving from the southern end of the system to its northern counterpart.

In 2006, Hayness et al. (2006) excavated a trench at the Tilah site (Ti), identifying four earthquakes believed to have occurred between the seventh century and 1918 A.D (Fig. 2.3). These seismic events were dated to approximately 659/660, 873, 1068, and 1546. They correlated archeoseismic data with historical records to estimate the likely dates for each of these seismic occurrences.

After that, Klinger et al. (2015) trenched at 1 km to the south of the dead sea, at Qatar site (Q). They succeed to present evidence for nine earthquakes that produced surface ruptures during a time period spanning 5000 yr. Only the 5 most recent ones were correlated to historical events which are the 1458 C.E., 1212 C.E., 1068 C.E., one event during the 8th century crisis, and the 363 C.E.

Lefevre et al. (2018) digged a Trench at a site called “Taybeh” (T), 30 km south of the Tilah site and identified 12 events, only the oldest three of them couldn’t be associated with specific historical earthquakes. However, the remaining 8 events they were correlated to the following historical earthquakes: from event 8 (E8) till E6, events were associated to a period of time, mid 8th century BC, 4th century BS and 2nd century BC. For the rest, the observations were stronger and they were able to detect the 31 BC, 114 AD, 1293 AD, 1458AD and the recent one was dated around the 18th century AD.

Ferry et al. (2011) conducted excavation in four trenches across two sites along the Jordan Valley fault (JV). Their results with the investigation of the archeoseismology at Tell Saydiyyeh revealed 12 surface rupturing events occurring approximately every 1160 years, along with an average slip rate of 5 mm per year over the past 25 ka.

Next, along the Jordan Gorge segment (JG), in a site called Beteiha, just north of the sea of Galilee, Wechsler et al. (2014) digged a trench just where Marco et al. (2005) previously did. They succeed to detect eight events that pre-date the 1202 and 1759 earthquakes identified by Marco et al. (2005). Wechsler et al. (2018) improved the accuracy of earthquake history for the past thousand years and assessed displacement for most earthquake ruptures by combining radiocarbon data from Wechsler et al. (2014) with 3D excavations of fluvial channels. The last 1200 years show a notable lack of slip,

raising concerns about a potential increase in future seismic activity. Furthermore, the short-term slip rates over the last two millennia, which have varied by more than a factor of two, suggest a pattern of earthquake clustering in the past.

As stated previously, Lefevre et al. (2018) associated the events depicted in Fig. 2.3 with one or multiple fault segments. However, the proposed catalogue doesn't encompass the same time span for all fault sections due to differing durations covered by various paleoseismological records. Overall, their catalogue indicates irregular seismic activity along the southern part of the LFS (referred to herein as dead sea fault, DSF) over time. There are brief periods, lasting approximately one to two centuries (such as during the 8th and the 12th–13th centuries AD, possibly the 4th century), wherein the entire fault experiences a sequence of earthquakes. These are interspersed with longer periods of roughly 350–400 years characterized by minimal seismic activity. This suggests that temporal clustering might significantly influence seismic activity along the entire DSF, which poses a significant challenge for seismic hazard models.

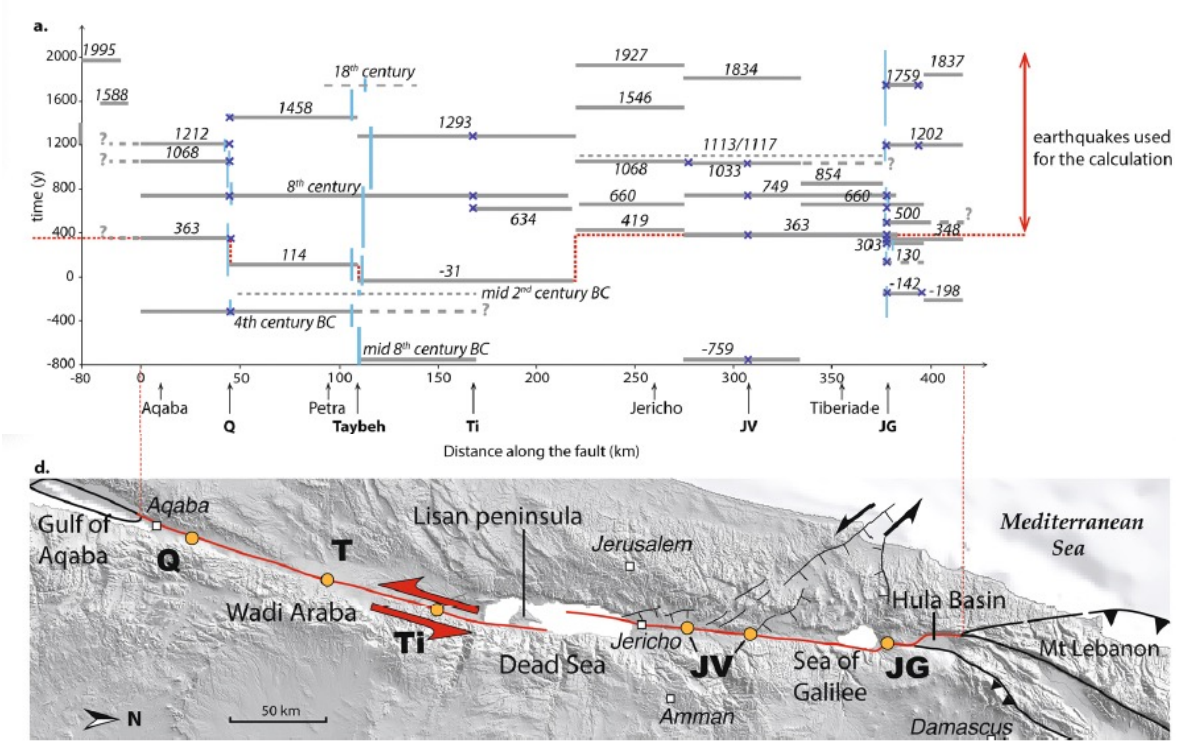

Fig. 2. 3 (a) Spatial and temporal distribution of historical earthquakes: each horizontal bar represents an estimated earthquake location along the Dead Sea fault (DSF). Dashed lines denote uncertain locations or lateral boundaries. Vertical bars correspond to time in intervals linked to paleoearthquakes. Blue crosses represent earthquakes observed in various trench studies, (b) structural map of the southern Dead Sea fault, with the highlighted red branches indicating the studied sections. The locations of prior paleoseismological investigations in the region are marked, including Q for Qatar, Ti for Tilah, JV for the Jordan Valley and JG for Jordan Gorge.

As for the central part of the LFS, the first trench along the Yammouneh fault was done by Daeron et al. (2007) (Fig. 2.4). Ten to thirteen events were identified over ~ 12 ka. Only seven of them could be correlated with historical earthquakes. A mean return period of 1127±135 years was estimated for a ~ M7.5 event (based on scaling relations of Wells&Coppersmith 1994). The paleoseismic analysis conducted by Gomez et al. (2007b) contributes supplementary cosmogenic age constraints and affirms a slip rate ranging between 3.9 and 6.1 mm/yr.

Nemer and Meghraoui (2006) trenched along the Roum fault, at the western edge of the Jarmaq basin, and concluded that it is an active structure. The study shows the occurrence of at least 4-5 large seismic events with surface ruptures during the last 10,000 years.

In the research conducted by Gomez et al. (2003), paleoseismic investigations within the Zabadani basin unearthed indications of five surface-rupture occurrences over the past 6500 years. Each event showed an average left-lateral displacement of about 2 meters, with an average recurrence interval of roughly 1300 years.

Nemer and Meghraoui (2008), performed a paleoseismic investigation along both Rachaya where he excavated a trench at Faqaa ridge scarp and Sergahya fault at the Deir el Achayer site. Results show the existence of shear zones attributed to significant fault movements. This evidence strongly suggests that these faults have served as origins for substantial earthquakes. The Faqaa trench findings indicate the presence of a minimum of two seismic events along the RcF, with an interseismic phase in between. The most recent event possibly aligns with the earthquake sequence of 1759. As well, excavations at Deir-el-Achayer indicated that the younger sample might be associated, albeit with some uncertainty, to the earthquake sequence of 1759.

Meghraoui et al. (2003) also trenched across the northern part of the LFS, along the Missyaf fault, at Al Harif site, and demonstrate a left lateral offset of 13.6±0.2 m also found evidence of three large eartjquakes in the past 2000 years; E1 100-150 AD that may correlate with the 115 earthquake; E2 700-1030 AD and E3 990-1210 AD that may correlate with the 1170 earthquake. Later on, Sbeinati et al. (2010) also studied the faulted Al Harif aqueduct by conducting four archeoseismic excavations and three paleoseismic trenches, suggesting the presence of four events during the last ~3400 yr.

All these paleoseismic studies could be used as a basis for constructing a fault-based source model for PSHA along the LFS.

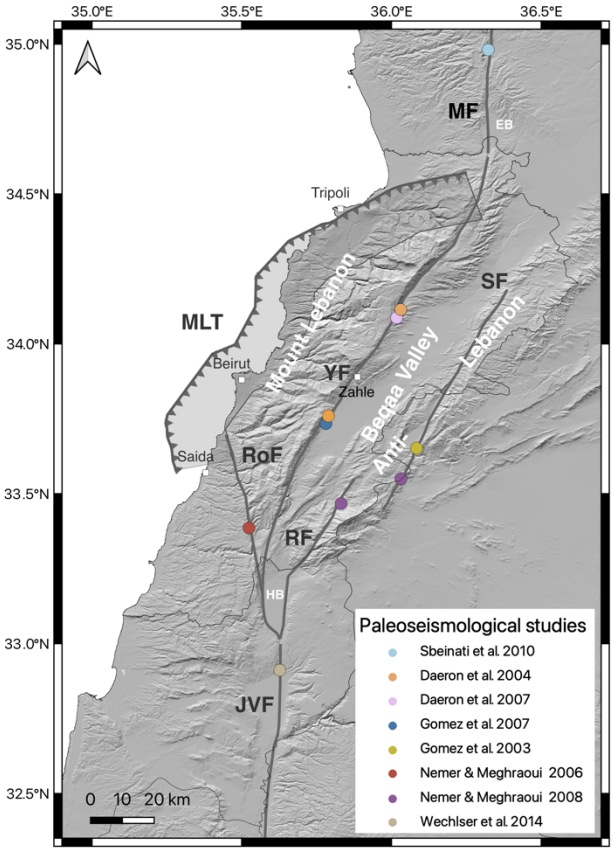

Fig. 2. 4 Sites where paleoseismic studies have been performed (El Kadri et al. 2023)

2.4 Geologic slip rate

Geologic and geomorphologic slip-rate primarily rely on the displacement of geomorphic features (such as stream channels, drainage basins, alluvial fans, and terraces) and the displacement of archaeological piercing points.

For the Araba fault, a slip rate of 4±2 mm/yr was obtained from the analysis of offset geomorphic features of Late Pleistocene to Holocene age (Klinger 1999; Klinger et al. 2000). This slip rate aligns with the 5.4± 2.7 mm/year derived from cosmogenic dating of paleosurfaces displaced by the fault over the past approximately 11,000 years in the southern Wadi Araba (Le Beon et al. 2010).

In the Jordan Valley, plenty of studies provided slip rates along the fault. In the area north of the Sea of Galilee (Fig. 2.3), Marco et al. (2005) approximated a minimum slip rate of 3 mm/year based on a left-lateral offset of a 15-meter stream channel observed over the last 5,000 years. In the same area, Wechsler et al. (2018) estimated later on a slip of $4.1^{+0.4}/_{-1}$ mm/yr over the last 4000 years. Ferry et al. (2007, 2011) indicated an approximate slip rate of ~5 mm/year over the last 47.5 thousand years and 25 thousand years, respectively based on the displacement of stream channels and archaeological features.

Further north, Daeron et al. (2004), studied the geomorphology at two sites along the Yammouneh fault in order to estimate the slip rate and found a late Pleistocene-Holocene slip rate of 5.1±1.3 mm/yr.

By examining stream offsets and conducting paleoseismic trenching along the Roum fault, Nemer and Meghraoui (2006) derived an estimated slip rate ranging from 0.86 to 1.05 mm/year over the past 10,510 years. Along the Serghaya fault, offset stream channels led to a calculated slip rate of 1.4± 0.2 mm/year during the Holocene (Gomez et al., 2003).

As for Mount Lebanon thrust, from shoreline uplifts, Elias et al. (2007) estimated an average slip rate of 1–2 mm/yr.

Sbeinati et al. (2010) also studied the faulted Al Harif aqueduct and suggest the presence of four events and estimate a slip rate ranging between 4.9-6.3 mm/yr.

2.5 Geodetic record

Geodesy history traces back thousands of years, as early civilizations sought to understand the Earth's dimensions and develop methods for navigation, land surveying, and astronomy. Over time, geodesy evolved with technological advancements. Techniques like GPS and Interferometric Synthetic Aperture Radar (InSAR) help monitor the deformation of the Earth's surface caused by tectonic movements before, during, and after seismic events.

- **GPS (Global Positioning System)** renowned as one of the most widely used satellite-based systems in geodesy, offers highly accurate and widespread coverage with real-time measurements. GPS involves a network of satellites that emit signals received by ground-based receivers. By calculating the time it takes for these signals to travel from satellites to receivers, the distances between them can be determined with high accuracy. Despite its effectiveness, this method encounters limitations in urban settings or densely vegetated areas where signal blockage or interference can occur. Additionally, atmospheric conditions may introduce errors, impacting measurement precision.

- **Interferometric Synthetic Aperture Radar (InSAR):** This technique uses radar images captured by satellites to measure ground deformation. By comparing radar images taken at different times, scientists can detect minute changes in the Earth's surface, including movements caused by tectonic activity. It can measure large areas and detect subtle ground deformations over time. Works in various weather conditions and is particularly useful in remote areas. However, it requires complex processing and might be affected by factors like vegetation cover or changes in land cover.

Because the orientation of the LFS aligns parallel with the SAR tracks (essentially perpendicular to the radar line-of-sight), GPS stands out as the most effective method for tracking continuous horizontal deformation along this system, as well monitoring velocities parallel to the LFS and the rate at which strain accumulates in that direction.

Initially, earthquake focal mechanisms, along with geodetic and tectonic observations, validate the left-lateral strike-slip mechanism overall, despite occasional local variations where the primary stress directions might shift, displaying normal or thrust mechanisms (Hofstetter et al. 2007; Palano et al. 2013).

Almost 23 years of dense GPS measurements exist, conducted between 1991 and 2019, and provided estimations for slip rates along various segments of the LFS. Along the Araba fault, an average geodetic velocity of 5 mm/yr is estimated (Al-Tarazi et al. 2011; Gomez et al. 2020; Hamiel et al. 2018; Le Beon et al. 2008; Masson et al. 2015; Sadeh et al. 2012; Saleh & Backer 2015). Moving northward, along the JVF, south of the Carmel-Gilboa fault, a similar slip rate is observed (~ 4.7 mm/yr). However, north of the Carmel-Gilboa fault section, GPS recordings indicate a decrease in the slip rate to around 3.6-4.1 mm/yr (Gomez et al. 2020; Hamiel et al. 2016; Sadeh et al. 2012). It's noteworthy that GPS measurements and late Quaternary tectonic research in the NE-oriented Palmyride fold belt, a division of the LFS in Syria, indicate less than 1 mm/year of active regional shortening along the NNW-SSE axis (Chaimov et al. 1990; Abou Romieh et al. 2009; Alchalbi et al. 2010).
In the central part of the LFS, an average geodetic velocity of approximately 4.7 mm/yr has been estimated. However, in the northern region, the deformation appears to be nearly half of this amount, approximately around 2 mm/yr.

Overall, geodetic data shows a good agreement between the long term slip rate estimates for the southern part of the LFS as well as the faults located inside the Lebanese restraining bend. However, for the northern part of the LFS, estimates from satellite systems (Hamiel and Piatibratova 2021; Alchalbi et al. 2010; Gomez et al. 2020; Li et al. 2024) are almost half of the geologic slip rate (Meghraoui et al. 2003). Addressing this inconsistency has been difficult due to restricted access to the northern LFS in Syria.

Firstly, the high geological slip rate along this segment can be attributed to one earthquake clustering over the past 3500 years (115 AD, 700 AD, 1030 AD and 1170 AD). Secondly, the remaining deformation might be compensated through alternative means.
Several hypotheses have emerged to explain this discrepancy between the geodetic and geologic slip rate along the northern part of the LFS. Alchalbi et al. (2010), proposed that a portion of the strain deficit might be managed by north-south compression within the southwestern area of the Palmyride fold belt in central Syria. However, there's also an evident GPS velocity gradient within the Sinai Plate itself.
Gomez et al. (2020) suggested the presence of subsidiary or branching faults contributing to the overall movement pattern in this area represented in dashed blue in Fig. 2.5. Yet, there is no supporting evidence indicating the existence of such a fault.
Li et al. (2024) alternatively proposed that the presence of widespread seismic activity in the region extending north of Israel, west of Lebanon, toward the Cyprus arc, indicates a diffuse deformation in the eastern Mediterranean. This deformation could potentially accommodate the movement between the primary Sinai plate and its part west of the northern LFS. Their analysis suggests the existence of a separate micro-plate termed "Latakia-Tartus," delineated by the Cyprus arc to the west, the Hatay triple junction to the north, the northern DSF to the east, and the Lebanon restraining bend and the offshore area characterized by diffuse seismicity to the south (Fig. 2.5).

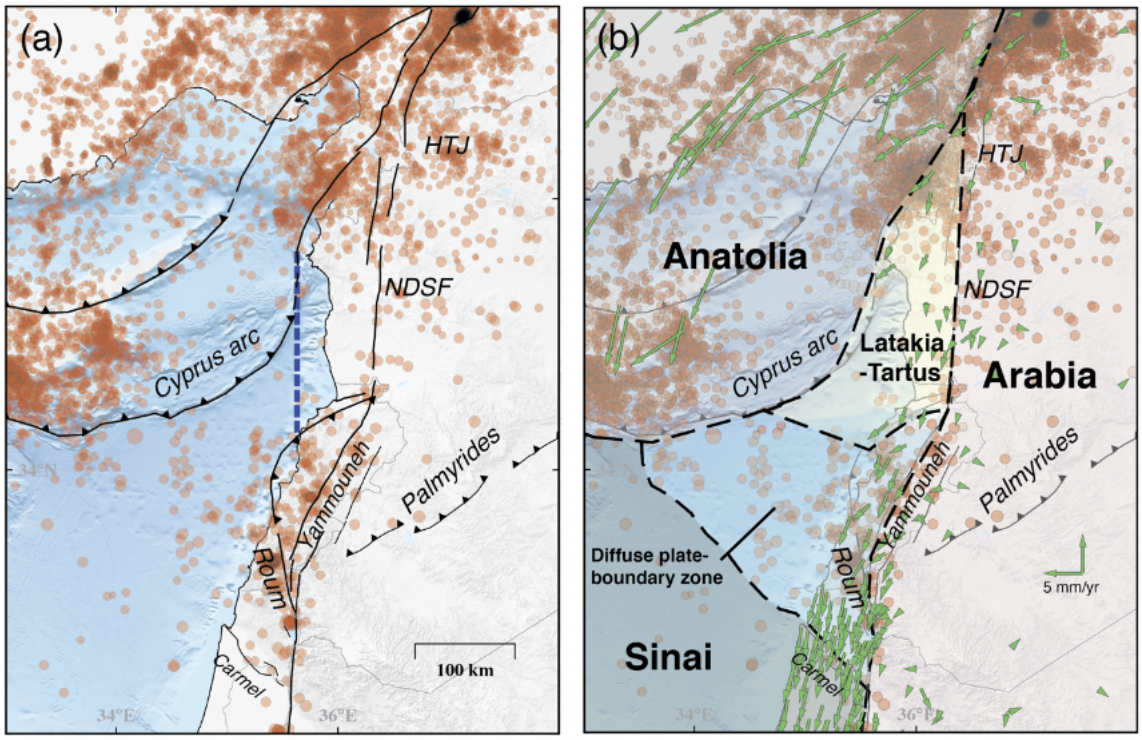

Fig. 2. 5 (a) Seismic activity in the offshore region between Lebanon/Israel and the Cyprus arc is depicted. The blue dashed line denotes the block boundary proposed by Gomez et al. (2020), (b) The Latakia-Tartus microplate, as suggested by Li et al. (2024), is represented with the Cyprus arc bounding it to the west, Hatay triple junction (HTJ) in the north, and the northern LFS in the east.

2.5 Published seismic hazard studies that include Lebanon

The LFS ranks among the world's major continental strike-slip fault systems, having experienced numerous powerful and devastating earthquakes over the years. Many major cities in Syria, Lebanon, Palestine and Jordan are located near or along the LFS which have posed significant threats to human lives due to these seismic events. Consequently, numerous studies focusing on probabilistic seismic hazard assessment (PSHA) have been undertaken in the vicinity of this fault system and its nearby regions. In the following summary, all hazard studies are time independent (Poissonian occurrence of earthquakes).

Please note that I'll be prioritizing the estimation of PGA at 475 years return period on rock sites, as it is the hazard estimate and soil condition most commonly used in the upcoming studies.

2.5.1 Seismic hazard in neighboring regions

Arieh et al. (1989) were the pioneers in conducting seismic hazard assessment for the Levant region. They built upon the prior seismic hazard assessments presented by Shapira (1981, 1983a, b) and Ben Menahem et al. (1982), which had focused on estimating hazard at specific locations. Area source zones were used as seismic sources, going from Araba fault in the south till the Lebanese region in the north with maximum magnitude, M_{max}=7.5, based on historical data (e.g., Ben Menahem1979; Turcotte and Arieh 1986). Parameters of the Gutenberg Richter distribution (GR) for each zone were determined using the available set of instrumental (Arieh et al. 1985 from 1900-1985, and Seismological Division

from 1981-1985) and historical regional earthquake data (M> 6.5 since 1800). Due to the lack of local strong motion records, they applied the ground-motion model of Joyner and Boore (1981) for the hazard calculation. Seismic hazard map for the Peak Ground Acceleration (PGA) at 475 years return period was delivered with maximum estimates located near the dead sea and north of Haifa city on the coast, ranging between 0.2g to 0.25g (Fig. 2.6).

Fig. 2. 6 (a) Source model used for the seismic hazard calculation, (b) Hazard maps for the PGA at 475 years return period (from Arieh et al. 1989)

Throughout the 1990s, several authors conducted studies to estimate seismic hazard levels within Jordan and its surrounding areas (e.g. Yucemen 1992, 1995; Al-Tarazi 1994, 1999; Malkawi et al. 1995). Area sources were also employed to define potential seismic sources in the region. The methodology used to establish seismicity parameters for each seismic source remained consistent, relying on seismicity catalogs. However, these catalogs are adjusted from one study to another to incorporate updates from the instrumental catalog over the years. Seismic hazard maps were delivered for the PGA for different return periods using some chosen ground motion models (Esteva and Villaverde 1973; Esteva 1974). The largest hazard estimates were found along the LFS and decreased moving away from the fault. For the PGA at a 475-year return period, hazard levels derived from Yucemen 1992 closely aligned with those obtained from Al Tarazi (1994), ranging from 0.2g to 0.25g around the dead sea area (Fig. 2.7a). Tarazi (1999) reported seismic hazard values in Syria and Lebanon, for the PGA at 475 years return period, ranging from 0.25g in the eastern part (longitude 39.0°E) and escalating rapidly westward to 0.4g in south Cyprus Island (Fig. 2.7b). The maximum PGA value was delivered by Malkawi et al. (1995), and was identified in the northwestern part of Syria and the Lebanese region, reaching approximately 0.6g for a return period of 475 years (Fig. 2.7c). The variation in hazard estimates among these studies can be attributed to the specific source models adopted in each study, the corresponding earthquake rates, and the selection of ground motion models.

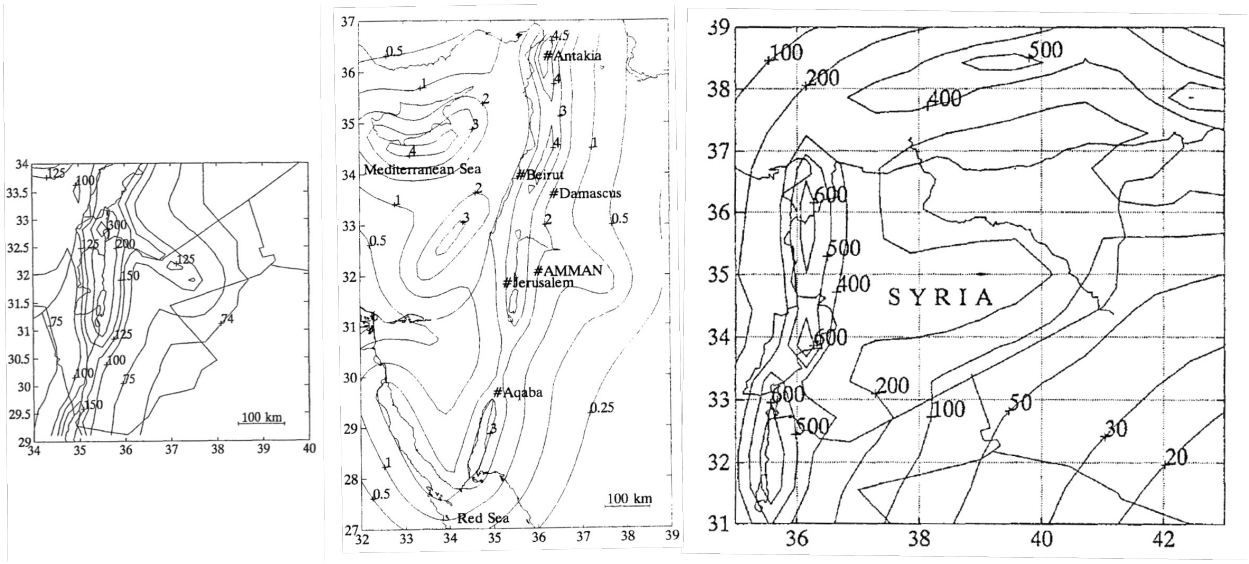

Fig. 2. 7 Hazard maps for the PGA at a 475-year return period corresponding to the study by (a) Al Tarazi 1994, (b) Tarazi 1999 and (c) Malkawi et al. 1995.

Later on, Yücemen et al. (2005) performed probabilistic hazard evaluations for Jordan, focusing on Peak Ground Acceleration and Spectral Acceleration (SA) at 0.2 seconds using the Ambraseys et al. (1996) ground-motion model. The authors incorporated exponential magnitude distribution and characteristic earthquake models, comparing hazard outcomes for four Jordanian cities. The characteristic earthquake model yields PGA and SA values 1.4 to 1.6 times higher than those obtained under the assumption of earthquake magnitudes being exponentially distributed. This notable difference underscores the significance of employing the appropriate recurrence model for faults.

After the 22 November 1995 M_W 7.3 earthquake that happened in the Gulf of Aqaba, Al Tarazi et al. (2007) revised the hazard estimation in this region. Three different source models were employed in the analysis, two smoothed seismicity models and a fault model based on a characteristic distribution for earthquakes. Three different equally weighted GMMs were used, as published by Boore et al. (1997), Sadigh et al. (1997) and Campbell (1997). The mean seismic hazard map obtained indicated that the highest estimates of seismic hazard were concentrated along the Levant Fault System (LFS), covering regions such as the Gulf of Aqaba, Wadi Araba, the Dead Sea, the Jordan Valley, and extending northward into northwestern Syria. The PGA values for major cities, such as Amman and Damascus, ranged between 0.15g and 0.2g, while for Beirut and Jerusalem, the range obtained was 0.2g to 0.25g.

During the same period, Jimenez et al. (2008) proposed a new PSHA study for Jordan, with the objective of revising and updating the national building codes of Jordan. Area source zones were used. Seismic parameters were determined using the Kijko and Sellevol (1989, 1992) methodology based on the catalog compiled by Al-Tarazi (1992). Two ground-motion models were applied: the Ambraseys et al. (1996) and Boore et al. (1997) to test their influence on the hazard estimates. Results were provided for the PGA and a range of Spectral Acceleration (SA) (0.1 s, 0.2 s, 0.3 s, 0.5 s, 1.0 s, and 2.0 s), considering a return period of 475 years for rock sites.
Using the Ambraseys et al. (1996) ground motion model, the highest PGA hazard values (0.3g) were obtained in the northwestern part of the region, in Lebanon, particularly close to the fault trace. As well, high PGA values (0.25g) were found in Jordan, extending from the dead sea to the Sea of Galilee, and around the Gulf of Aqaba. However, employing the hazard estimates based on Boore et al. (1997) results

in a 20% decrease in these hazard estimates. This analysis demonstrated that the choice of the ground motion model is an important factor that can influence hazard outcomes. Therefore, careful consideration of the associated uncertainty is essential when evaluating hazard.

2.5.2 Lebanese seismic hazard studies

Harajli et al. (2002) embarked on one of the first initiatives to evaluate seismic hazard in Lebanon on a national scale. Potential seismic sources were identified and modeled as area sources. Magnitude-frequency distributions of each source were developed from instrumental seismology data and historical records. For area sources outside the Lebanese territory, such as the southern section of the LFS and the mediterranean region including Cyprus arc, information from previous studies were incorporated (Yucemen 1992). The study assessed the sensitivity of the results to varying assumptions concerning seismic sources in the Lebanese region. Notably, they were the first to evaluate the impact of the maximum earthquake magnitude on hazard outcomes. Additionally, the study rigorously examined the influence of the selection of ground motion models. Then in 2010, they updated their seismic source model in response to the discovery of a newly mapped offshore thrust fault system, the Mount Lebanon thrust (MLT), located right underneath the capital city of Beirut (Huijer et al. 2010, 2011). Huijer et al. (2016), re-evaluated their seismic hazard for Lebanon. Seismic hazard maps were calculated for the PGA at different return periods. As well, uniform hazard spectrum for various site classes for the important coastal cities of Beirut, Jbeil, Tripoli, Saida, and Tyre, providing more precise design criteria based on the intended structures or projects. Results show that for a 475 years of return period, PGA varies between 0.2g in the eastern part of the country to 0.3g in the western part which is higher than what was calculated previously when the MLT was not taken into consideration (~0.2g on both the eastern and western boundaries) (Fig. 2.8). This analysis demonstrated that the new mapped offshore fault strongly affects how earthquakes are distributed in Lebanon.

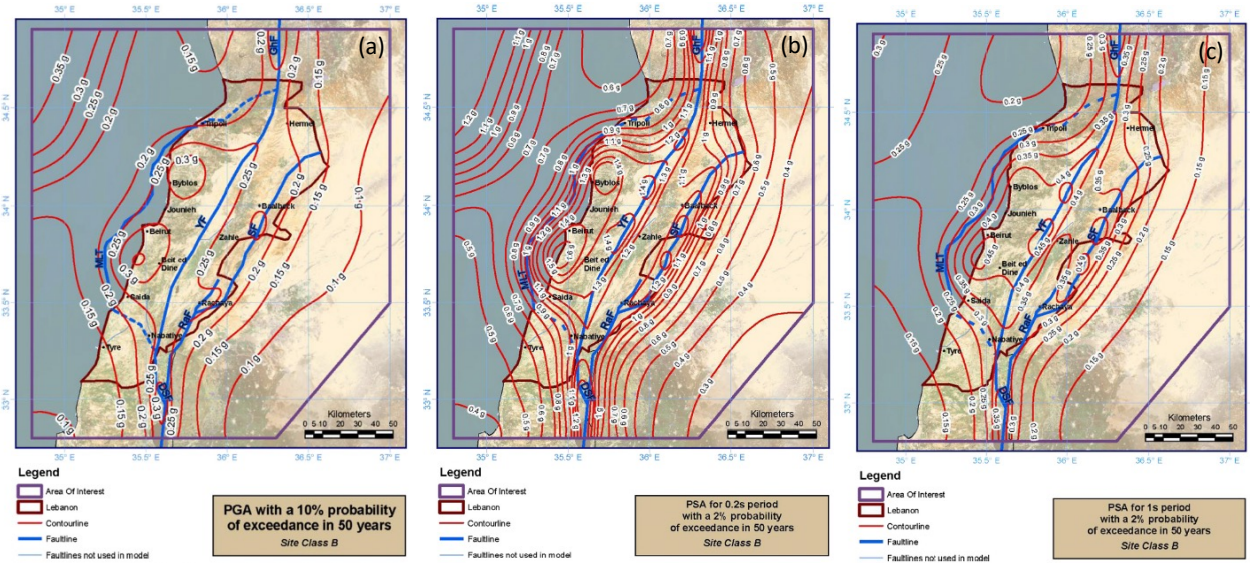

Fig. 2. 8 Hazard map for the (a) PGA with a 10% probability of exceedance in 50 years, (b) SA at 0.2s a 2% probability of exceedance in 50 years, (c) SA at 1s a 2% probability of exceedance in 50 years (from Huijer et al. 2016)

Additionally, several probabilistic seismic hazard studies have been conducted by private consultancies (e.g. Arango and Lubkowski 2012; AMEC 2012; Erdik et al. 2014).

The most recent seismic hazard assessment for the LFS is provided by El Hadidy et al. (2021). They conducted this study in order to support a development plan including the construction of the King Salman Bridge in the Gulf of Aqaba region. Area source models were used as seismic sources combined with smoothed seismicity models. Recurrence parameters for these sources were obtained using their own catalog compiled using the paleo-seismological studies, historical records and instrumental seismicity (Abou Elenean 1997; Ambraseys et al. 1994; CMT online Bulletins; El hadidy 2012; Egyptian National Seismological Network (ENSH catalogue); European Mediterranean Seismological Centre (EMSC online Bulletins); Institute of Petroleum Research and Geophysics (IPRG); ISC online Bulletins)
They generated hazard maps for various return periods and spectral accelerations covering the spatial window going from latitudes 27° to 37° and longitudes 30° to 37°. In Lebanon, PGA values for a 475-year return period, ranged between 0.08g to 0.16g across the whole country except for the area close to the MLT, hazard increased up to 0.16g to 0.24g.

2.5.3 Regional and global seismic hazard

Seismic hazard assessments for the eastern Mediterranean and the Levant region were also conducted as part of regional and international efforts (e.g., GSHAP: Giardini 1999; SESAME: Jiménez et al. 2001; Jiménez et al. 2003; Jiménez 2006; EMME: Danciu et al. 2018**).**

The GSHAP project was the first effort at the global scale to estimate PSHA world-wide, serving as a valuable resource for upcoming national and regional projects. Experts in seismic hazard assessment were enlisted, establishing standardized rules to characterize seismic sources and generating unified regional earthquake catalogs. The final step was to integrate the hazard results from all regions to produce a world-wide map (the Americas: Shedlock & Tanner 1999; Asia, Australia and Oceania: Zhang et al. 1999; McCue 1999; Europe, Africa and the Middle East: Grünthal et al. 1999), as shown in Fig. 2.9. Several iterations of smoothing were needed to render the final map homogenous without significant differences. Overall, higher hazard estimates were found around the location of major plate boundary earthquakes.

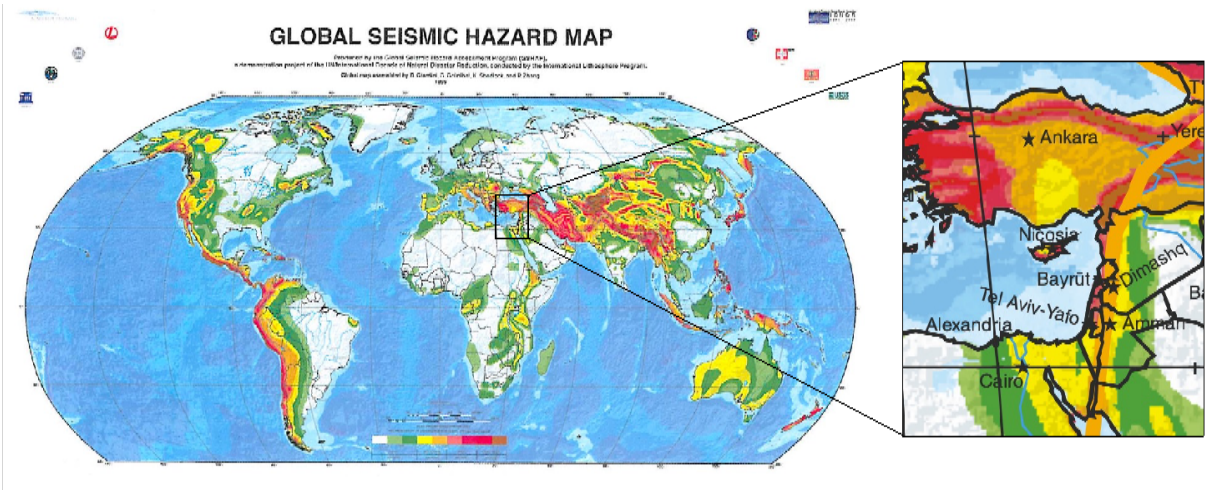

Fig. 2. 9 GSHAP global seismic hazard map for the Peak Ground Acceleration (PGA) at a 475-year return period. Created by combining regional hazard maps developed for various GSHAP regions (Giardini et al. 2003)

Next, the SESAME took place with the aim of performing a harmonized seismic hazard model for the entire Mediterranean basin. The current source zones within each region were combined, and seismic sources in border areas between different regions were redefined to eliminate ambiguities arising from diverse approaches. Every seismic source (all of them areal sources) was defined by its specific seismicity parameters (maximum magnitudes, and earthquake frequency rates) derived on the basis of the seismic catalog. They included 3 ground motion models in a logic tree (some for crustal: Ambraseys et al. 1996, and intermediate-depth: Musson 1999; Papaioannou and Papazachos 2000). Regional hazard maps were produced homogeneously for the PGA, 0.3s and 1s SA on different soil conditions (rock, stiff soil) and different return periods. In Lebanon, for the PGA at 475 years return period, based on rock sites, this study provided the hazard level range between 0.25g to 0.5g (Fig. 2.10).

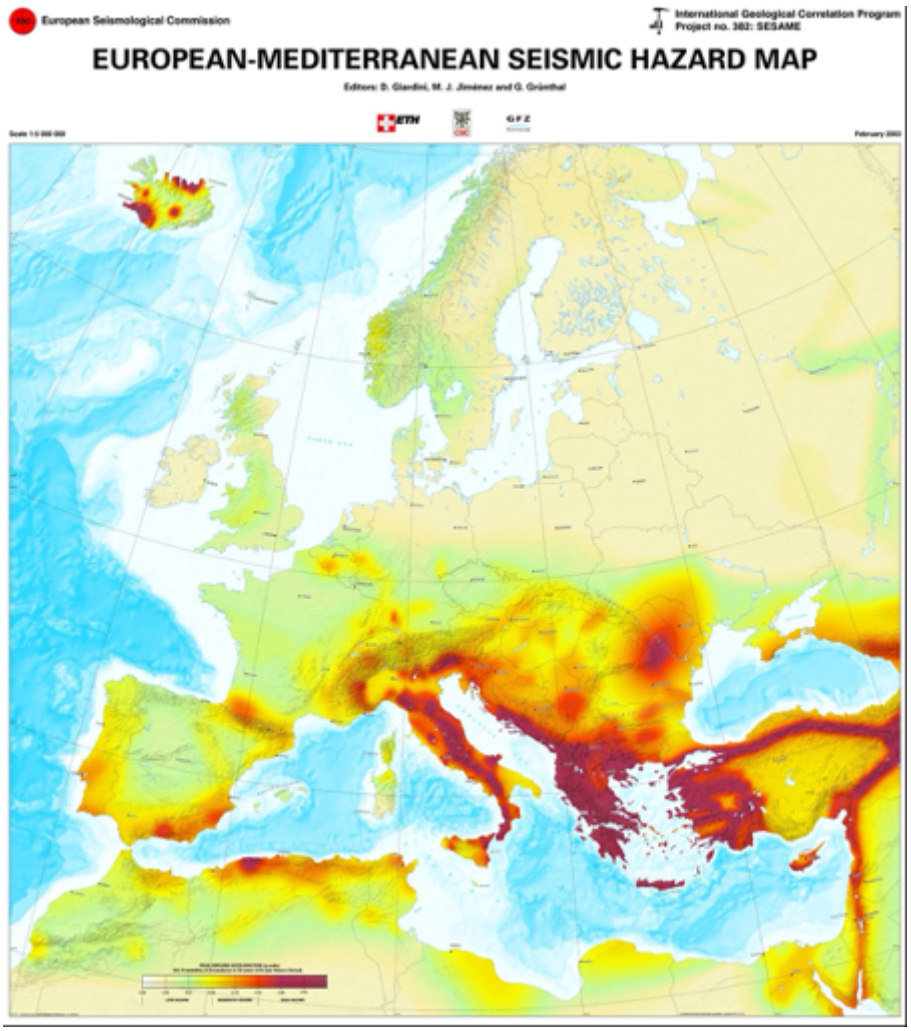

Fig. 2. 10 Probabilistic seismic hazard map of the Mediterranean region for the PGA on stiff soil for 475 years return period.

The Earthquake Model of the Middle East (EMME) project covered eleven countries spanning from Turkey to Pakistan (Fig. 2.11). This project marked the first regional seismic hazard assessment to adopt a fault model for the Levant region based on active tectonic features that were evident during that period (Danciu et al. 2018). The EMME source model was made of two main branches, an area source model where frequency-magnitude distributions (Gutnenberg-Richter) are established from the earthquake catalog (Zare et al. 2014). A fault model combined with smoothed seismicity to account for off-fault earthquakes. Geologic slip-rates were used to characterize moment-balanced earthquake recurrence models. M_{max} was determined using both, scaling relationships and historical seismicity. The selection of the GMMs was determined by considering the comprehensive neotectonic characteristics (Danciu et al. 2016). Among previous projects, EMME stood out in its ability to thoroughly quantify uncertainties associated with hypotheses or parameter values used in the source model (Mmax, b value...) and Ground Motion Models (GMMs) by employing a logic tree.

The seismic hazard results consist of mean values and quantile hazard maps for chosen intensity measures such as Peak Ground Acceleration (PGA) and 5% damped spectral accelerations at various periods. These maps cover multiple return periods. In particular, they computed hazard assessments for Beirut, the capital city of Lebanon, and 13 other locations within their defined spatial region. At a 475-year return period, a mean Peak Ground Acceleration (PGA) of 0.41g was estimated for Beirut (Sesetyan et al. 2018).

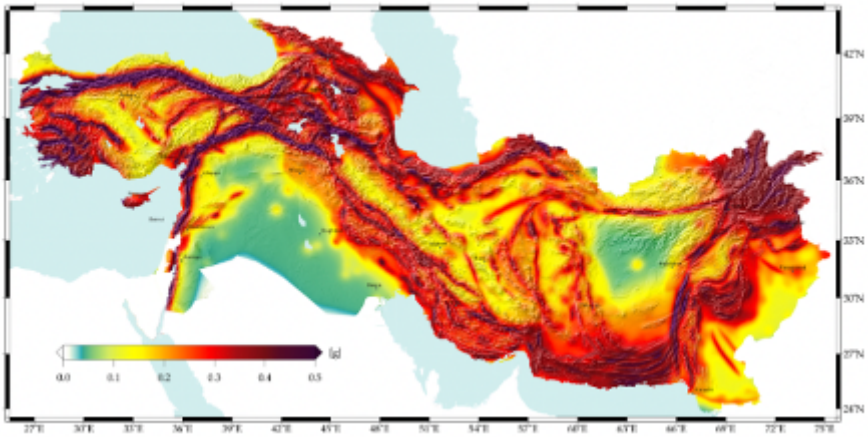

Fig. 2. 11 Probabilistic seismic hazard map depicting the mean PGA distribution for 475-year return period applicable to a reference rock type, Vs30 > 800 m/s (from Sesetyan et al. 2018).

Table 2.1 provides a comparison of the mean hazard values obtained in Beirut, the capital city of Lebanon, by regional and international projects, with respect to studies focused on the country's scale. The inclusion of the MLT in the database of potential seismic sources in Lebanon contributed to an increase in hazard levels at Beirut, situated on the hanging wall of the MLT, from 0.15g to 0.25g.

The results from GSHAP and SESAME exhibit some degree of similarity, suggesting that any differences between them may stem from variations in their respective approaches. GSHAP adopted a regionalized strategy involving the computation of independent regional and national hazard maps, which were subsequently combined. In contrast, SESAME was dedicated to establishing a unified seismic source model encompassing the entire Mediterranean region for consistent hazard assessments.

The EMME estimation for Beirut is the highest, possibly because of the use of a moment-balanced fault model based on available paleoseismic and geodetic slip rate data for the faults.

Yet, pinpointing the exact source of the difference among these studies is not straightforward. All the outcomes hinge on the choice of the source model, the recurrence parameters employed to characterize seismicity for these sources, and the ground motion models applied.

Table 2. 1 Comparison of the hazard levels at Beirut, the capital city of Lebanon, based on regional and local seismic hazard studies

Source	**Mean PGA at 475 years return period**
GSHAP (Giardini et al. 1999)	0.24-0.32g
SESAME (Jimenez et al. 2001)	0.16-0.24g
EMME (Sesetyan et al. 2018)	0.41g
Harajli et al. 2002	0.14-0.15g
Huijer et al. 2016	0.25g

2.6 Seismic Design Requirements

The initial seismic design regulations for Lebanon were introduced during the early 1990s. This code gained authority through governmental decrees N. 646, N. 14293, and N. 7964 that were issued in 2004, 2005, and 2012, respectively. Notably, these decrees exempted constructions under 10 meters in height or comprising fewer than three floors from adhering to any seismic requirements.

As per these decrees, the Lebanese Standards Institution (LIBNOR) released Standard NL135 (NL135), which assumes a uniform seismic hazard across the entire Lebanese territory. NL135 advises designers to reference to (i) the French Norm (PS92), (ii) the Uniform Building Code (UBC), or (iii) the International Building Code (IBC). Furthermore, it announces the exclusive adoption of (iv) Eurocode 8 (EC8) as the sole seismic code applicable in Lebanon. Structures in Lebanon, designed in accordance with Lebanese Standard NL135 and LIBNOR recommendations, have been constructed based on the following set of assumptions:

- Exclusively elastic design response spectra are employed.
- The minimum seismic design level is determined by a single parameter, "a_N", indicating peak ground acceleration. According to Decree 7964 issued on April 7th, 2012, the set value for a_N stands fixed at 0.25g.
- 5% damping ratio is utilized.
- Vertical seismic action is disregarded, as the vertical component of ground motion has a marginal impact on buildings and warrants consideration solely in specific scenarios (e.g., bridges, long-span bays).
- The spectral analysis considers a period range from 0s to 4s.

The elastic design spectrum according to EC8, derived for five different ground types and applicable to horizontal components, are illustrated in Fig. 2.12.

Table 2. 2 Ground types according to EC8, from Gerges et al. 2023

Ground Type	Average Properties at 30 m Depth		
	Shear Wave Velocity	Standard Penetration Resistance	Undrained Shear Strength
	$V_{s,30}$ (m/s)	N_{SPT} (Blows/30 cm)‡	C_u (kPa)*
A	>800	-	-
B	360-800	>50	>250
C	180-360	15-50	70-250
D	<180	<15	<70
E	Soil profile consisting of a surface alluvium layer with V_s values of type C or D and thickness varying between 5 m and 20 m, underlayed by stiffer material with $V_{s,30}$ > 800 m/s		

‡ N_{SPT} stands for "N-value Standard Penetration Test," which is a widely used in-situ test in geotechnical engineering to evaluate the relative density of soils.

* represents the undrained shear strength of soil.

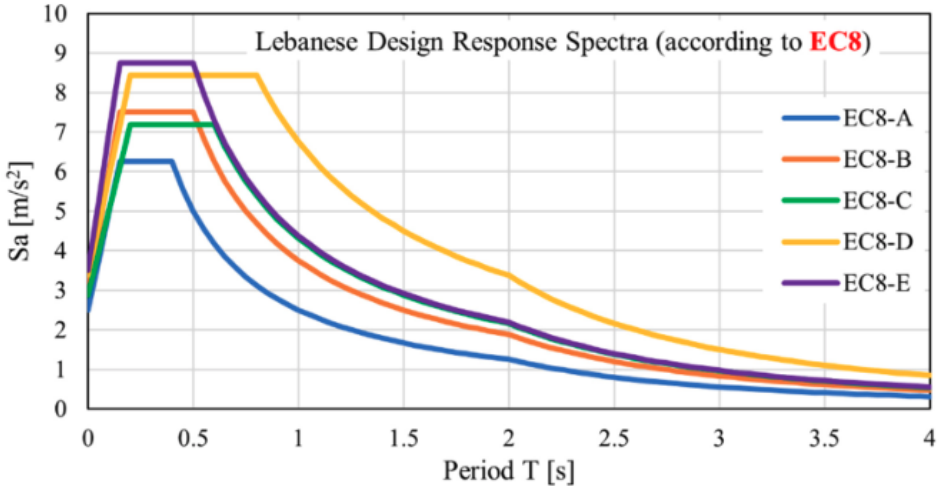

Fig. 2. 12 The Lebanese design spectrum according to EC8, normalized and expressed in terms of acceleration (Sa) as a function of the period (T) for five soil types (A, B, C, D, E) and 5% damping ratio, from Gerges et al. 2023

According to earlier research, Lebanon generally experiences seismic hazard levels surpassing 0.3g across the entire country. As seismic hazard assessments have earned credibility as the foundation for revising building codes, there's a growing demand for a fresh fault based seismic hazard assessment in Lebanon.

CHAPTER 3

A fault-based probabilistic seismic hazard model for Lebanon, controlling parameters and hazard levels

Contents

3.1 General Introduction

This chapter is the subject of an article co-signed by Sarah El Kadri, Celine Beauval, Marleine Brax, Pierre-Yves Bard, Mathilde Vergnolle and Yann Klinger. It was published in the Bulletin of Earthquake Engineering (https://doi.org/10.1007/s10518-023-01631-z) in March 2023. This chapter discusses the implementation of faults into PSHA for Lebanon based on plaeoseismic, geologic and geodetic available information combined with a smoothed seismicity model to account for off-fault seismicity Throughout the process, uncertainties associated with source model parameters, such as slip rate, M_{max} on faults, geometry of the faults, the recurrence model, and its parameters are systematically tracked. A set of GMMs adapted for the LFS is employed. The results show the significant influence of faults on seismic hazard, evident across all return periods. Hazard levels notably increase in regions close to fault traces. Hazard maps for the entire country are delivered for various return periods and spectral accelerations.

3.2 A fault-based probabilistic seismic hazard model for Lebanon, controlling parameters and hazard levels

S. El Kadri[(1,2)] , C. Beauval[(1)], M. Brax[(2)], PY. Bard[(1)], M. Vergnolle[(3)] and Y. Klinger[(4)]

[(1)] Univ. Grenoble Alpes, Univ. Savoie Mont Blanc, CNRS, IRD, Univ. Gustave Eiffel, ISTerre, 38000 Grenoble, France

[(2)] National Council for Scientific Research, CNRS-L P.O. Box 16-5432 Achrafyeh 1100-2040, Beirut, Lebanon

[(3)] Université Côte d'Azur, IRD, CNRS, Observatoire de la Côte d'Azur, Géoazur, Valbonne, France

[(4)] Université de Paris Cité, Institut de physique du globe de Paris, CNRS, 1, rue Jussieu, Paris, France

Corresponding author: sarah.el-kadri@univ-grenoble-alpes.fr

Abstract

The present work develops a comprehensive probabilistic seismic hazard study for Lebanon, a country prone to a high seismic hazard since it is located along the Levant fault system. The historical seismicity has documented devastating earthquakes which have struck this area. Contrarily, the instrumental period is typical of a low-to-moderate seismicity region. The source model built is made of a smoothed seismicity earthquake forecast based on the Lebanese instrumental catalog, combined with a fault model including major and best-characterized faults in the area. Earthquake frequencies on faults are inferred from geological as well as geodetic slip rates. Uncertainties at every step are tracked and a sensitivity study is led to identify which parameters and decisions most influence hazard estimates. The results demonstrate that the choice of the recurrence model, exponential or characteristic, impacts the most the hazard, followed by the uncertainty on the slip rate, on the maximum magnitude that may break faults, and on the minimum magnitude applied to faults. At return periods larger than or equal to 475 years, the hazard in Lebanon is fully controlled by the sources on faults, and the off-fault model has a negligible contribution. We establish a source model logic tree populated with the key parameters, and combine this logic tree with three ground-motion models (GMMs) potentially adapted to the Levant region. A specific study is led in Beirut, located on the hanging-wall of the Mount Lebanon fault to understand where the contributions come from in terms of magnitudes, distances and sources. Running hazard calculations based on the logic tree, distributions of hazard estimates are obtained for selected sites, as well as seismic hazard maps at the scale of the country. Considering the PGA at 475 years of return period, mean hazard values found are larger than 0.3g for sites within a distance of 20 to 30km from the main strand of the Levant Fault, as well as in the coastal region in-between Saida and Tripoli ($\geq$ 0.4g considering the 84th percentile). The study provides detailed information on the hazard levels to expect in Lebanon, with the associated uncertainties, constituting a solid basis that may help taking decisions in the perspective of future updates of the Lebanese building code.

Keywords: Seismic hazard assessment · Active faults · Moment-balanced earthquake recurrence model · Ground-motions · Lebanon

1. Introduction

“Earthquakes don’t kill people, buildings do”, this often repeated saying highlights the importance of building safely in regions exposed to earthquakes. It is not possible to predict the next destructive earthquake, however countries may adopt building codes in order to design structures capable of withstanding given levels of shaking. The probabilistic seismic hazard assessment (PSHA) method was introduced in the late 1960s (Cornell 1968; Esteva 1968) and became the methodology enforced in most regulations worldwide to determine the reference ground-motions (e.g. Petersen et al. 2014; Grünthal et al. 2018; Beauval and Bard 2021). PSHA consists in combining probabilistic earthquake forecasts with ground-motion prediction models, to determine at the sites of interest the probability that a given ground-motion level is exceeded in the future.

Lebanon is a country with high seismic potential since it is located along the Levant Fault System (LFS), a plate boundary that accommodates the northward motion of the Arabian plate relative to the Sinai subplate (Fig. 1). This ~ 1200 km long left-lateral strike-slip fault connects the Red Sea spreading center to the East Anatolian fault system (Garfunkel 2014; Marco and Klinger 2014). Current estimates about the rate at which the fault accommodates horizontal displacement vary between 4 and 6 mm/year, based on a number of geomorphologic, paleoseismic, and geodetic studies (e.g. Gomez et al. 2007a, b; Le Béon et al. 2012; Wechsler et al. 2018). Major destructive earthquakes occurred along this fault system, as demonstrated in numerous historical, archeoseismic and paleoseismic studies (e.g. Guidoboni and Comastri 1994; Daëron et al. 2007; Elias et al. 2007; Ferry et al. 2007; Ambraseys 2009; Wechsler et al. 2014).

In a PSHA study, the source model must include all earthquakes that we believe may occur in the future, with associated probabilities of occurrence. To build this source model, different observations available over different time and space windows may be combined: past earthquakes, e.g. precise instrumental events as well as more uncertain historical events; mapping of active faults with information on the occurrence of historical and paleoearthquakes and on the slip rates, both from geologic and geodetic studies. Considering only the instrumental period, Lebanon would be classified as a country with low-to-moderate seismic potential. In terms of seismic hazard assessment, these low seismicity levels are not representative of the large destructive events that occurred in the past. As a consequence, we believe that in this region, any source model should include faults and that area models relying essentially on earthquake catalogs should not be applied.

The most recent seismic hazard estimates for this area were delivered by a regional-scale project, the Earthquake Model of the Middle East project (EMME), that extends from Turkey to Pakistan (Danciu et al. 2017). The EMME seismic hazard calculations relied on a source model made of two main branches, an area source model where frequency-magnitude distributions are established from the earthquake catalog, and a fault model combined with smoothed seismicity. At the scale of Lebanon, a previous hazard study was performed by Huijer et al. (2016), including area sources and faults. Earthquake recurrence models have been established from past seismicity, however no details are provided on how earthquakes were associated to faults and on the number of events available for each fault. Besides, a number of other probabilistic seismic hazard studies exist, performed within private consultancies (e.g. Arango and Lubkowski 2012; AMEC 2012, Erdik et al. 2014). None of these past studies explore in depth the uncertainties associated to the different steps in the process. The present work aims at establishing a fault-based source model, based on faults’ characterization in the Lebanese region, as well as up-to-date information on past seismicity (newly derived earthquake catalog Brax et al. 2019; GRAL local catalog) and faults characterization in the Lebanese region, applying a strategy for tracking uncertainties, understanding their impact on hazard estimates, and delivering hazard results representative of these uncertainties.

Our source model for Lebanon includes faults and off-fault seismicity. We combine this source model with a set of ground-motion models to evaluate seismic hazard. The first section of the paper describes the past seismicity, the set of active faults in the area, the information on the deformation accumulating along these faults and the potential historical events they generated. The second section details the building of the source model. To forecast off-fault seismicity two alternative smoothed seismicity models are built from the Lebanese instrumental catalog, taking into account uncertainties on the declustering step and on the magnitude range considered to model the recurrence. Then we describe how we build moment-balanced recurrence models for faults based on the available slip rates and assumptions on the geometry of faults. The third section describes the ground-motion models selected. The fourth section aims at identifying which parameters and decisions bearing uncertainties have a strong influence on hazard estimates, at four cities in Lebanon. A logic tree is established for the source model, and the impact of each parameter or decision on hazard is quantified by sampling different branches of the logic tree. To better understand parameters' impacts obtained in Beirut, the capital city, a disaggregation study is conducted. At last, the final section of the paper aims at deriving seismic hazard maps at the scale of the country, exploring the logic tree populated with the controlling parameters.

2. Seismic Potential of the area

2.1 Past Seismicity

Although large historical earthquakes have struck the Lebanese country centuries ago, the seismicity observed since the beginning of the XXth century is moderate. In the instrumental earthquake catalog built from global catalogs by Brax et al. (2019), four earthquakes with a magnitude larger than 5 produced light damages to buildings in some localities, in 1956 (M_W 5.3 and 5.5, Fig. 1a), 1997 (M_W 5.1) and 2008 (M_W 5.1). Much larger magnitude earthquakes occurred in previous centuries. Brax et al. (2019) critically analyzed the published studies available for pre-instrumental events and delivered a list of events with estimated macroseismic epicenters within Lebanon, including the 551 earthquake (M_S ~7.3), 1170 (M_S ~7.3), the 1202 earthquake (M_S ~7.6), the two events in 1759 (M_S ~6.6 in October 30 and M_S ~7.4 in November 25) and the 1837 earthquake (M_S ~7.0) (Fig. 1a).

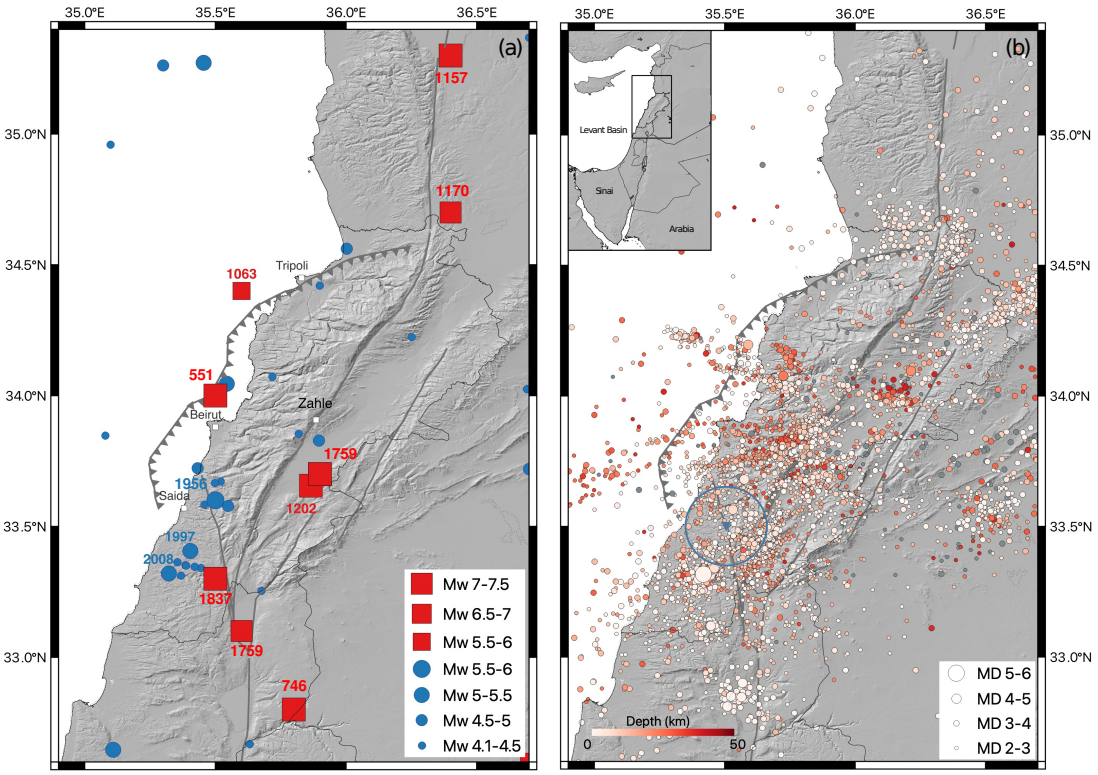

Fig. 1 Past seismicity in Lebanon. a) Earthquake catalog from Brax et al. (2019), circles: instrumental earthquakes 1900-2015 (minimum magnitude in the catalog $M_W = 4.1$, complete for $M_W \geq 4.1$ only since 1985); squares: macroseismic epicenters of historical events (see Table 1 for references). b) GRAL instrumental catalog 2006-2019, duration magnitude M_D.

2.2 Active Faults

The LFS can be divided into two North-South trending sections connected by the Lebanese restraining bend, the Jordan Valley fault to the south and the Ghab fault to the north. The restraining bend comprises two mountain ranges, Mount Lebanon and Anti-Lebanon, separated by the Beqaa Valley. Within the bend, the fault splays into three major strands: the Roum fault on the west, the Yammouneh fault in the center, and the Rachaya and Serghaya faults on the east (Fig. 2). The majority of the strain accumulation is accommodated by the Yammouneh fault (Daëron et al. 2004; Gomez et al. 2007a, b). Another fault has been identified, the Mount Lebanon thrust (MLT), an off-shore east-dipping thrust (Elias et al. 2007; Carton et al. 2009).

In the present work, we will consider only major faults affecting the Lebanese region, secondary fault segments that are not well-characterized are not included in the model (Fig. 2). A fault can be included in the hazard analysis if the fault geometry can be defined and if its seismogenic potential can be quantified.

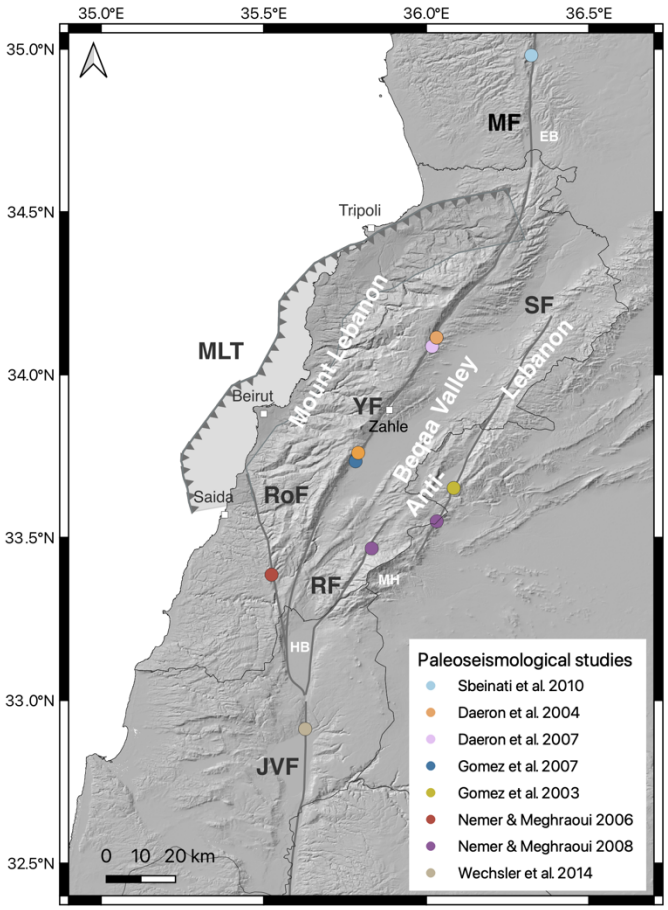

Fig. 2 Active faults in the Lebanese region: Yammouneh Fault (YF), Rachaya Fault (RF), Serghaya Fault (SF), Roum Fault (RoF), Jordan Valley Fault (JVF) and Missyaf Fault (MF, belongs to the Ghab fault system), have a strike-slip mechanism, whereas Mount Lebanon (MLT) is a thrust dipping east (the projection of the fault plane to the surface is displayed, dip 45°, maximum depth 18km). HB: Hula Basin, EB: El Boqueaa basin, MH: Mount Hermon. Sites where paleoseismic studies have been performed are indicated. A larger scale map is provided in the electronic supplement (Fig. S1)

Yammouneh fault

The Yammouneh fault is the throughgoing structure that connects the northern and southern sections of the LFS and forms the eastern boundary of Mount Lebanon. The fault has a left-lateral strike-slip mechanism and extends over ~200km. Daeron et al. (2004) estimated a 25-ka mean slip rate between 3.8 and 6.4 mm/yr, based on cosmogenic dating of offset alluvial fans. Analyzing paleoseismological trenches in lacustrine deposits, Daëron et al. (2005) provide evidence of coseismic slip on this fault corresponding to the A.D. 1202 earthquake (M_S 7-7.8, Ambraseys and Jackson 1998) and show that this segment has remained locked since then. Moreover, Daëron et al. (2007) expanded the trench work across the Yammouneh paleolake and identified ten to thirteen paleo-events (M~7.5), extending back more than ~12 kyr (the latest being the 1202 event). The paleoseismic study of Gomez et al. (2007b) provides additional cosmogenic age constraints and confirms a slip rate between 3.9 and 6.1 mm/yr. Besides, based on the geodetic velocity field and a 1D elastic dislocation model, Gomez et al. (2007a) quantitatively assess an average slip rate of 4.4 mm/year along the fault.

Missyaf fault

To the North of the restraining bend, the Missyaf segment is ~ 90 km long, limited by the Yammouneh Fault to the south and the Ghab basin to the north (Meghraoui et al. 2003). Based on a combined analysis of archaeological excavations and paleoseismic trenches, Sbeinati et al. (2010) establish the occurrence of four faulting events in

the last ~3500 yr (magnitude 7.3-7.5), the last one being the 1170 destructive earthquake, as well as a range of 4.9 to 6.3 mm/yr for the slip rate along this segment. The timing of the most ancient event in the sequence is poorly constrained. Assuming that this ancient event corresponds to an historical earthquake in 1365 BC, they propose a range of 4.9-5.5 mm/year for the slip rate (Sbeinati et al. 2010). On this part of the Levant Fault, a significant discrepancy is observed between slip rates based on geological observations and rates estimated from geodetic measurements or modeling, which are much lower, Alchalbi et al. (2010) finds 2.5±0.7 mm/year; Gomez et al. (2020) 2.2±0.5 mm/year.

Roum fault

The Roum fault is a left-lateral strike-slip fault, that bounds the Mount Lebanon range to the south (Fig. 2). Nemer and Meghraoui (2006) provide a detailed mapping of the fault trace from the western edge of the Hula pull-apart up to the Jarmaq basin (latitude 33.4°). To the north of this basin, they acknowledge that the trace is less clear. We consider the trace of Nemer and Meghraoui (2006) up to latitude 33.5°, and extend the fault towards the north west along a constant strike, based on morphological analyses (Elias 2006; Le Béon et al. 2018). At a paleoseismic site on the southern part of the fault (Fig. 2), Nemer and Meghraoui (2006) establish the occurrence of at least 4 to 5 surface rupture events with magnitude > 6.5 during the last ~10ky. For the most recent event, they provide a lower bound for the date (post A.D. 84-239), and suggest that it might be the 1837 historical earthquake (M_S ~7.0, Ambraseys 2006). Assuming that the stream offsets measured close to the trench correspond to the accumulated coseismic displacements in the last ~10ky, they estimate a range of 0.86-1.05 mm/year for the slip rate.

Mount Lebanon fault

A geophysical survey has shown evidence for submarine seismogenic thrusts off shore central Lebanon that would be responsible for the A.D. 551 earthquake (Elias et al. 2007). This east-dipping thrust system is called Mount Lebanon Thrust (MLT). Its geometry is complex and it is limited to the south and north by oblique lateral ramps. Elias et al. (2007) evaluates a rupture length of at least 100km, possibly 150km, corresponding to an earthquake with magnitude 7.4 to 7.6 according to the scaling relationship of Wells and Coppersmith (1994). From shoreline uplifts, they evaluate an average recurrence time of at least 1500 years for an A.D. 551-type event since the early Holocene, and an average slip rate of 1 to 2 mm/yr for the fault. Here we use the fault trace used in Danciu et al. (2017) prolongated to the south (inclusion of the Saida lateral ramp) and to the north (inclusion of the Tripoli and Aakkar thrusts on land, Elias et al. 2007).

Serghaya fault

The Serghaya fault is located approximately along the Syrian-Lebanese border. This strike-slip fault follows the Anti Lebanon Range east of the Beqaa plain. Meghraoui et al. (2003) and Nemer and Meghraoui (2008) perform a detailed mapping of the fault. The fault trace taken into account here extends from latitude ~33.4° to latitude ~34.2° (Fig. 2). We do not include the segment bordering Mount Hermon to the south, as the fault trace there is less clear. Based on trench excavations (Fig. 2), Gomez et al. (2003) identify five surface rupturing events within the past ~6500 years, with displacement of ~2m and estimated magnitudes larger than or equal to 7.0. The last event postdates A.D. 1650 and may correspond to the 1759 earthquake (M_S ~7.4, the November shock, that destroyed many villages in the Beqaa and ruined Baalbeck (Ambraseys and Barazangi 1989; Daëron et al. 2005). From the buried displaced channels in the trenches, Gomez et al. (2003) estimate a Holocene slip rate of 1.4 ± 0.2 mm/yr.

Rachaya fault

The Rachaya fault extends along the western part of the Anti-Lebanon range for approximately 67 km. Nemer and Meghraoui (2008) provided a detailed mapping for this fault segment as well as geomorphic evidence for recent faulting. Here we consider a trace that splays from the eastern bounding fault of the Hula Basin up to latitude ~33.5°. Nemer and Megrahoui (2008) excavated a trench that revealed the occurrence of at least two

seismic events. The last event belonging to the period 1686-1924 A.D. could thus be correlated to the first 1759 shock (M_S ~6.6, Ambraseys and Barazangi 1989), consistent with the conclusions of Daeron et al. (2005). This fault constitutes the southern continuation of the Serghaya fault. Both faults connect through the compressional jog that forms the Mount Hermon. Hence, we make the hypothesis that they have the same slip rate.

Jordan Valley fault

The fault is limited to the north by the Hula basin and to the south by the Dead Sea pull-apart (e.g. Ferry et al. 2011). Many studies suggest that the Jordan Valley fault slipped during the earthquakes of A.D 363 (M_S ~7.4), 746 (M_S ~7), 1033 (M_S ~6) and 1546 (M_S ~6) (see Fig. 3 and Table S1 in Brax et al. 2019). The Jordan Valley fault has been more studied than the northern part of the LFS and is therefore better characterized. Different segmentations have been proposed (e.g. Ferry et al. 2011; Lefevre et al. 2018). A wealth of paleoseismic data that provided slip rates along the fault (e.g. $4.1^{+0.4}/_{-1}$ mm/yr north of the Sea of Galilee, over the last 4000 years, Wechsler et al. 2018; or 4.9±0.3 mm/yr between the Sea of Galilee and the Dead Sea, for the last 25 ka, Ferry et al. 2011). Slip rates estimated with geodetic models (e.g. 4.7 ± 0.5 mm/yr in Al Tarazi et al. 2011; 4.1 ± 0.8 mm/yr in Hamiel et al. 2016) are overall consistent with the geological slip rates. We consider a unique long segment of ~180km associated with an average slip rate along the fault that ranges from 4 to 5 mm/yr.

Table 1 Characteristics of faults present in the model

Fault	Predominant mechanism	Length L(km) Extension in latitude (°)	Dip (°)	Depth (km)	Slip Rate range (mm/yr)	Slip Rate Alternative values (mm/yr)	Historical event*	Magnitude of historical event& (equivalent M_S or M_W)	M_{max} from L†	M_{max} range used
Missyaf (MF)	SS	75 34.61-35.29	90	10-14-18	4.9-5.5 (Sbeinati et al 2010)	4-5 or 1.7-2.7 (Gomez et al. 2020)	29 June 1170	6.7-7.3 (Ambraseys 2006)	7.1 (6.7-7.5)	7.1-7.5
Yammouneh (YF)	SS	199 32.99-34.62	90	10-14-18	3.9-6.1 (Gomez et al. 2007b)	4-5	20 May 1202	7-7.8 (Ambraseys and Jackson 1998)	7.5 (7.1-7.9)	7.5-7.9
Jordan Valley Fault (JVF)	SS	179 31.4-32.99	90	10-14-18	4-5 (range combining different studies)	4-5	18 Jan 746	7-7.3 (Ambraseys 2009)	7.5 (7.1-7.9)	7.5-7.9
Rachaya (RF)	SS	67 32.99-33.54	90	10-14-18	1.2-1.6	1.2-1.6	30 Oct 1759	6.6 (Ambraseys and Barazangi 1989)	7 (6.7-7.5)	7-7.5
Serghaya (SF)	SS	90 33.45-34.18	90	10-14-18	1.2-1.6 (Gomez et al 2003)	1.2-1.6	25 Nov 1759	7.2-7.5 (Ambraseys and Barazangi 1989)	7.2 (6.8-7.6)	7.2-7.6
Roum (RoF)	SS	61 33.16-33.69	90	10-14-18	0.86-1.05 (Nemer and Meghraoui 2006)	0.86-1.05	1 Jan 1837	6.7-7.3 (Ambraseys 2006)	7 (6.6-7.4)	7-7.4
Mount Lebanon (MLF)	R	159 33.58-34.57	40-45-50	18	1-2 (Elias et al 2007)	1-2	9 July 551	7.1-7.3 (Darawcheh et al 2000)	7.5 (7.1-8)	7.5-8

*Largest historical event potentially associated to the fault
&see Brax et al. (2019) for the selection of earthquake parameters among available studies
† mean M_{max} value and mean ± one standard deviation in parenthesis
scaling relationships of Leonard (2014) are applied, with L and W in m
strike-slip events: $\log_{10}(M_0) = b*\log_{10}(L)+a$, with b=1.5, a=12.45 (11.86-13.03 the one standard deviation range of a),
reverse event: $L= (\frac{W}{C_1})^{1.5}$ with C_1=12, $\log_{10}(M_0) = b*\log_{10}(L)+a$, with b=2.5, a=7.963 (7.31-8.70 the one standard deviation range of a)
M_0 the seismic moment: $\log_{10}(M_0) = 1.5\ M_W + 9.1$

3. Earthquake recurrence model

The source model must describe the locations of future earthquakes, together with their magnitudes and probabilities of occurrence over future time windows. In the Lebanese region, the seismicity in the instrumental period can be qualified as typical of a low-to-moderate seismicity area. In terms of seismic hazard assessment, the seismic rates inferred from the instrumental catalog are not representative of the true seismic potential in the area. We believe that it is not meaningful to derive area source models that heavily rely on earthquake catalogs. On the other hand, faults are rather well characterized and their activity has been demonstrated. We propose here to develop a source model made of faults combined with off-fault seismicity. Occurrences of earthquakes on fault are constrained by the seismic moment rates inferred from the available slip rate estimates. Occurrences of off-fault earthquakes are based on a smoothed seismicity model that relies on the instrumental earthquakes recorded by the local network.

3.1 Modeling Off-Fault Seismicity

To forecast earthquakes in the background, a smoothed seismicity model is developed. Smoothed seismicity models rely on the assumption that future seismicity occurs in areas close to where past seismicity occurred (e.g. Frankel 1995; Stock and Smith 2002). Within Lebanon, the global catalog homogenized in moment magnitude (Brax et al. 2019) contains 23 events with magnitudes $M_W \geq 4.1$ (spatial window: lon 35-36.8 latitude 33-34.7), most of them belong to three earthquake sequences that occurred in 1956, 1997 and 2008 (Fig. 1a). If this catalog is used to establish the smoothed seismicity model, the model will forecast highest probabilities of occurrence at the locations of these sequences. We decided to use instead the Geophysical Research Arrays of Lebanon (GRAL, 2019) local catalog that covers the time window 2006-2019 and includes duration magnitudes down to M_D 2.4 (3677 events within the spatial window of Fig. 1b). These low-magnitude events highlight areas of recent seismic activity. Although the time window is short, we assume that earthquake densities in this low-magnitude range may be a good guide for future off-fault seismicity. Equivalence between duration magnitude and moment magnitude needs to be assumed as there are too few events with both magnitude estimates to establish a correlation (considering M_W from Global Centroid Moment tensor (CMT), Brax et al. 2019).

Historical events are not included in the earthquake catalog used for smoothing for two reasons: the epicentral location of a large magnitude historical event has a limited meaning (in comparison with e.g. the extension of an intensity isoseismal), and most of these large historical events are believed to have been generated on faults (earthquakes in 551, 746, 1157, 1170, 1202, 1759 and 1837, see Fig. 1 and Section 2.2).

Smoothed seismicity rates are estimated from the earthquake catalog applying the algorithm developed by Hiemer et al. (2013, 2014; SEIFA). Seismicity rates account for completeness in time. The density of seismicity in each spatial cell is obtained by smoothing the location of each earthquake with an isotropic variable power-law kernel. We use an adaptive smoothing distance (distance to the second closest neighbor). The b-value is evaluated from the Gutenberg-Richter frequency-magnitude distribution (Gutenberg and Richter 1944) obtained at the scale of Lebanon from the GRAL catalog.

To identify clustered events in the catalog, two well-known and widely applied declustering algorithms are considered. The Gardner and Knopoff (1974, GK74) algorithm relies on simple magnitude-dependent windows in time and space. The Reasenberg (1985, R85) algorithm is a linking algorithm where clusters are allowed to grow in time and space. In time, it is based on the Omori's law, which describes the temporal decrease of the

number of aftershocks after the occurrence of the mainshock. In space, the algorithm assumes a circular rupture radius for each event and searches in this area for clustered events.

We test different parameterizations for the application of these algorithms. For Reasenberg, we consider the original parameters used in California (Reasenberg 1985), as well as three alternative values producing a stronger declustering (see Table 2, range of parameters from Christophersen et al. 2011). Four frequency-magnitude distributions are established based on the declustered catalogs obtained (Fig. 3a). All distributions display two different slopes, below and above M_D 3.3 (respectively ~2.8 and ~1.2). In many places, the analysis of the number of events versus hour of the day shows an abnormal distribution, with many more events during working hours, suggesting the presence of non-tectonic events (examples in Figs. 3c and 3d). These swarms are only partially removed in the declustering (see declustering D4 in Fig. 3d, 46% of earthquakes with $M_D \geq 3.3$ are identified as clustered events). A specific analysis would be required to identify recordings that have a high probability of being anthropogenic events (e.g. quarries and mines); however this is not possible within the timeframe of this project. Besides, we also estimate seismic rates considering only night events (see e.g. Gulia and Gasperini 2021), and observe that the rates above M_D 3.3 remain quite stable (Fig. 3b).

The Gardner and Knopoff algorithm is applied considering two alternative sets of windows in time and space, the original windows from GK74 and the more conservative windows proposed by Burkhard and Grünthal (2009, BG09) for Europe (Fig.4). Gardner and Knopoff algorithm removes many more events than the Reasenberg algorithm. Considering $M_D \geq 2.8$, the GK algorithm removes 62% earthquakes identified as clustered events with the GK74 windows, and 84% with the BG09 windows. Frequency-magnitude distributions are estimated considering all events and night event only. Except for the declustering with BG09 on night events only, these distributions still display two slopes (Fig. 4a). Considering only night events and the BG09 windows, a unique b-value of 1.3 is found over the magnitude range 2.8-4.4; the rates for earthquakes $M_D \geq 3.3$ remain rather stable.

Based on these different tests, we decided to consider two declustered catalogs that lead to two earthquake recurrence models and two alternative smoothed seismicity models to be included in the source model logic tree:

- The catalog declustered with R85 algorithm, set of parameters D4 (Table 2). The frequency-magnitude distribution displays a slope equal to 1.2 from magnitudes 3.3 on. The smoothed seismicity model 1 is established from events with M_D larger or equal to 3.3 (Fig. 4b).
- The catalog declustered with GK74 algorithm applying the windows of BG09, considering only night events. The frequency-magnitude distribution displays a slope equal to 1.3 from magnitudes 2.8 on. The smoothed seismicity model 2 is established from events with M_D larger or equal to 2.8 (Fig. 4b).

These two models rely on rather close annual rates in the magnitude range 3.2-4.2, but provide different spatial densities (Fig. 5). The models are built with a grid of 0.05°x0.05° in space. We allow magnitudes up to 6.5 in the background, which means we assume that such magnitudes can occur anywhere on faults presently unknown.

Table 2 Four sets of parameters required by the Reasenberg (1985) algorithm (see e.g. Christophersen et al. 2011); τ_{min} and τ_{max}: minimum and maximum look-ahead times, P: probability of detecting the next clustered event, x_{eff} : magnitude of completeness, during an earthquake cluster x_{eff} is increased to $x_{eff} + x_k$, r_{fact} : a multiple of the circular crack radius. Uncertainties on the hypocentral location are accounted for in Declustering D2, D3, D4. Declustering D1: original parameters of R85 applied in California

Declustering	D1	D2	D3	D4
τ_{min}	1	1	1	3
τ_{max}	10	10	10	15
P	0.95	0.95	0.95	0.95
x_k	0.5	0.5	0.5	0.5
x_{eff}	2.4	2.4	2.4	2.4
r_{fact}	10	10	20	20
Uncertainty on the hypocentral locations	ignored	Considered 2 km	Considered 2 km	Considered 2 km
Number of Mainshock $M_D \geq 2.8$ out of 3168 events	2838 90%	2174 69%	2110 67%	1818 57%
Number of Mainshock $M_D \geq 3.3$ out of 140 events	98 70%	81 58%	81 58%	75 54%

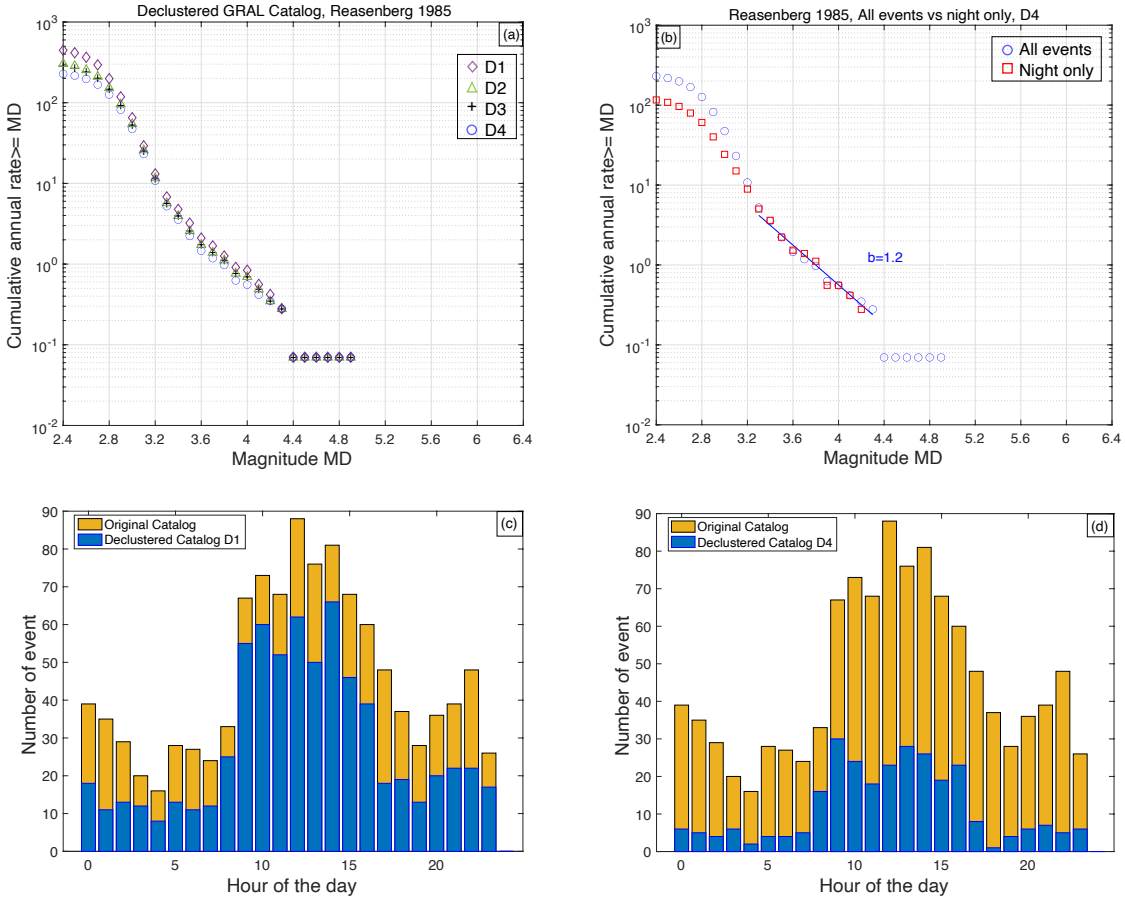

Fig. 3 Declustering on the GRAL earthquake catalog with the Reasenberg (1985) algorithm. a) Frequency-magnitude distributions established on four alternative declustered catalogs, obtained with the parameterizations detailed in Table 2 (D1, D2, D3, D4), spatial window 33° to 34.7° in latitude and 35° to 36.6° in longitude. b) Frequency-magnitude distributions applying D4 parametrization, circles: all events, squares: night periods only (see the text). c) Distribution of events with magnitude $M_D \geq 2.5$ according to the hour of the day, catalog D1, falling within a circle of 15 km radius centered at latitude 33.5° and longitude 35.5° (see Fig. 1b), d) same as c) using catalog D4

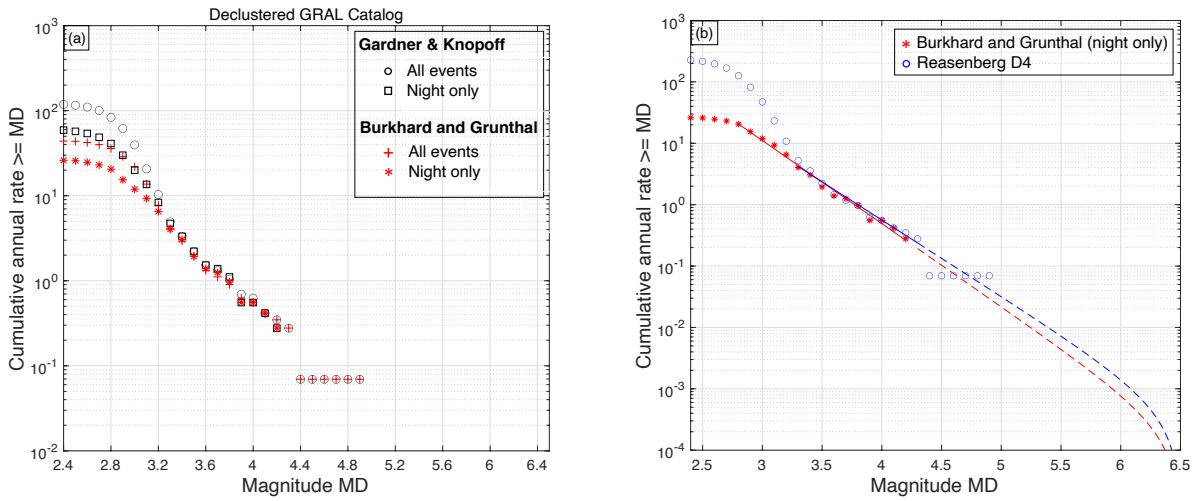

Fig. 4 Frequency-magnitude distributions based on the declustered GRAL earthquake catalog, spatial window 33° to 34.7° in latitude and 35° to 36.6° in longitude. a) Four alternative declustering with the Gardner&Knopoff algorithm, black: window definition of Gardner&Knopoff (1974), all events (circles) and night periods only (squares); red: window definition of Burkhard and Grunthal (2009), all events (crosses) and night periods only (asterisk). b) Final earthquake

recurrence models selected for hazard calculation, based on the catalog declustered with Reasenberg (D4, Table 2) and based on the catalog declustered with the Burkhard and Grunthal (2009) windows applied to night periods only

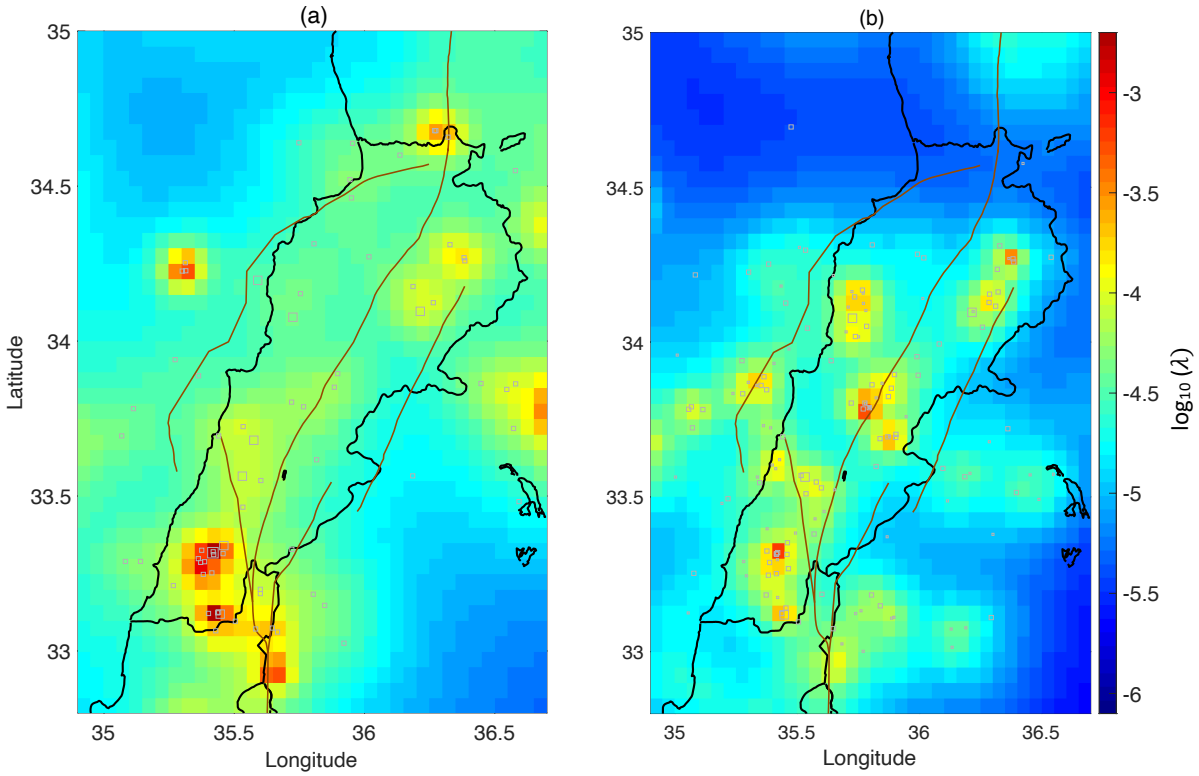

Fig. 5 Annual exceedance rates for magnitude $M_D \geq 4.5$, within a grid cell of 0.05°x0.05°. (a) GRAL catalog declustered with Reasenberg (1985) algorithm, 75 events with $M_D \geq 3.3$ (squares), (b) GRAL catalog declustered with Gardner&Knopoff (1974) algorithms, window parameters from Burkhard and Grünthal (2009), considering only periods at night, 148 events with $M_D \geq 2.8$.

3.2 Earthquake forecast on faults

From the knowledge available on faults, earthquake recurrence models can be derived. We use the average slip rates estimated from geologic studies to determine the seismic moment rates that can be released in earthquakes. Slip rates are determined either from paleoseismic trenches when they document enough earthquakes to allow averaging the slip variability for successive earthquakes (Wechsler et al. 2018), or from offset geomorphological features that provide a slip rate averaged over several thousands of years (Daeron et al. 2004). Paleoseismic studies mostly provide evidence for the large magnitude earthquakes with surface ruptures. Moderate events that rarely produce surface ruptures are often not detected. However, moderate events are more frequent than large events, and they also contribute to seismic hazard assessment (see e.g. Beauval et al. 2006).

To establish a moment-balanced recurrence model, we need to assume how earthquake sizes distribute. For the faults in Lebanon, there are not enough observations available to discriminate between a Gutenberg-Richter exponential decrease of earthquakes with magnitudes and a more characteristic behavior (see e.g. Ishibe and Shimazaki 2012 ; Stirling and Gerstenberger 2018). The GRAL instrumental catalog (14 years) contains many low-magnitude events, but their spatial distribution does not seem aligned with the major fault segments (Fig. 1b). There are not enough historical events associated to the faults (see Fig. 1a) to estimate meaningful mean recurrence times.

We reviewed a number of published seismic hazard models. The decision on which distribution to use for faults is most often not detailed, some studies use the exponential distribution (e.g. Rong et al. 2020; Danciu et al. 2017; Wiemer et al. 2016; Poggi et al. 2020; Meletti et al. 2021); whereas others use a characteristic model (e.g. Stirling et al. 2012; Wang et al. 2020; Demircioğlu et al. 2018). In its simplest form, the characteristic model assumes that each fault source produces a single earthquake magnitude that ruptures the full fault source length (e.g. Stirling and Gerstenberger, 2018). Here we consider both recurrence models, namely the exponential form 2 of Anderson and Luco (1983) and the characteristic model of Youngs and Coppersmith (1985).

The seismic moment rate is estimated from the slip rate assumed constant over the fault area:

$$\dot{M}_0 = \mu A S \tag{1}$$

with S the slip rate per year, μ the rigidity modulus (taken as 3.6 x 10^{10} N/m2), and A the surface of the rupture area.

Using the exponential form 2 of Anderson and Luco (1983), the annual rate N of events with magnitude larger or equal to m can be written as:

$$N(m) = 10^{a-bm} - 10^{a-bM_{max}} \quad \text{for } m \leq M_{max} \tag{2}$$

with b the exponential coefficient and M_{max} the maximum magnitude corresponding to the largest earthquake that may break the fault. We use the universal b-value of 1 (Kagan 1999) for two reasons: the b-values inferred from the instrumental GRAL catalog in duration magnitude are abnormally high; using the Brax et al. (2019) catalog at a regional scale we found a b-value close to 1.
For the model to be moment-balanced, the a-value must be estimated as follows (see e.g. Mariniere et al. 2021):

$$10^a = \dot{M}_0 \frac{c-b}{b} 10^{-d+(b-c)M_{max}} \tag{3}$$

with parameters c and d from the moment-magnitude definition ($log_{10}(\dot{M}_0) = cM_W + d$; with c=1.5 and d=9.1, for moment in units of N.m, Hanks and Kanamori 1979).
The Youngs and Coppersmith (1985) characteristic model combines an exponential model for moderate magnitudes and a characteristic model for large magnitudes, with rates of characteristic earthquakes in the magnitude range M_{max}-0.5 to M_{max} much higher than predicted by the moderate magnitude range. Its probability density function can be written as follows (see e.g. Convertito et al. 2006):

$$f_{YC}(m) = \begin{cases} \frac{b \ln(10)\, 10^{-b(m-M_{min})}}{1-10^{-b(M_{max}-0.5-M_{min})}} \times \frac{1}{1+c} & (M_{min} \leq m \leq M_{max} - 0.5) \\ \frac{b \ln(10)\, 10^{-b(M_{max}-1.5-M_{min})}}{1-10^{-b(M_{max}-0.5-M_{min})}} \times \frac{1}{1+c} & (M_{max} - 0.5 \leq m \leq M_{max}) \end{cases} \tag{4}$$

with

$$c = \frac{b \ln(10)\, 10^{-b(M_{max}-1.5-M_{min})}}{1-10^{-b(M_{max}-0.5-M_{min})}} \times 0.5$$

Then, for the recurrence model to be moment-balanced, the cumulative rate of characteristic magnitude can be calculated according to the following equation (see e.g. Convertito et al. 2006):

$$N_C = \frac{N_{NC} * b * \ln(10) * 10^{-b(M_{max}-M_{min}-1.5)}}{2\left(1-10^{-b(M_{max}-M_{min}-0.5)}\right)} \tag{5}$$

with

$$N_{NC} = \frac{\dot{M}_0 * (1 - 10^{-b(M_{max} - M_{min} - 0.5)}}{K * 10^{(c*M_{max}+d)} * 10^{-b(M_{max} - M_{min} - 0.5)}}$$

$$K = \frac{b * 10^{(-\frac{c}{2})}}{(c - b)} + b * 10^{b} * \frac{1 - 10^{\left(-\frac{c}{2}\right)}}{c}$$

Fault planes need to be defined. A dip of 45° is assumed for Mount Lebanon Thrust (Elias et al. 2007); whereas all strike-slip faults are assumed vertical with a dip of 90°. As the extension at depth of these strike-slip crustal faults is not well constrained, we consider three alternative maximum depths to account for this uncertainty (10,14 and 18 km), according to the range found for locking depths in elastic block modeling studies (e.g. Gomez et al. 2007a). For Mount Lebanon Thrust, the depth is fixed to 18km but the uncertainty on the dip is considered (40, 45 and 50°).

Maximum magnitudes considered for each fault are reported in Table 1. The uncertainty on this parameter is significant. We identify the largest historical earthquake that has been associated to each fault, and its magnitude range inferred from macroseismic intensity data (see Brax et al. 2019). The maximum magnitude M_{max} on the fault must be larger or equal to the magnitude of the historical event, accounting for uncertainties. For strike-slip faults, the Leonard (2014) scaling relationships are applied to infer maximum magnitudes from the total length of the fault (Table 1). Then, we consider the mean value predicted by the scaling relationship, as well as the mean plus one standard deviation. For thrust faults, Leonard (2014) scaling relationships imply that the maximum rupture that the fault can host is limited by its width. Therefore, the length of the maximum rupture is first obtained from the width (applying $L= (\frac{W}{12})^{1.5}$, considering e.g. a width 25km, dip of 45° and depth 18km). Then M_{max} is inferred from the length considering the mean as well as mean plus one standard deviation (see Table 1).

To account for the uncertainty on the slip rates, an interval is considered (Table 1). This interval corresponds to the range provided by the paleoseismic studies available for Missyaf (4.9-5.5 mm/yr, Sbeinati et al. 2010), Yammouneh (3.9-6.1 mm/yr, Gomez et al. 2007b), Roum (0.86-1.05, Nemer and Meghraoui 2006), and Serghaya (1.2-1.6, Gomez et al. 2003). As there is no direct information for Rachaya, the slip rate is assumed to be equal to the slip rate evaluated for Serghaya. The Jordan valley fault has been studied extensively and different slip rate estimates are available along the fault. We infer a mean range from these different estimates that we apply to the whole fault (4 to 5 mm/yr, Table 1).

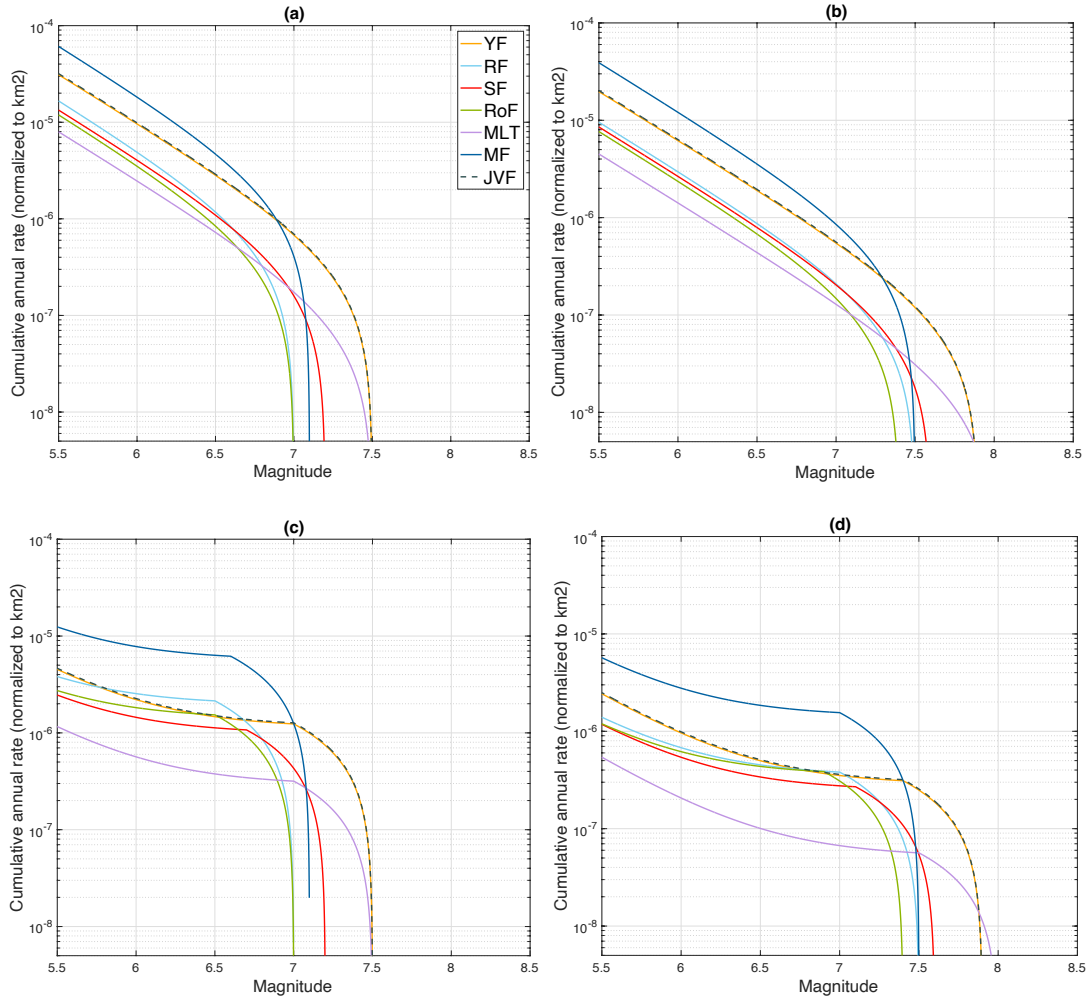

Fig. 6 Moment-balanced frequency-magnitude distributions for the faults included in the model, dependance of seismic rates on the choice of the recurrence model and on M_{max}. a) Exponential Gutenberg-Richter model, minimum bound for M_{max}; b) exponential Gutenberg-Richter model, maximum bound for M_{max}; c) characteristic Youngs and Coppersmith (1985) model, minimum bound for M_{max}; d) characteristic Youngs and Coppersmith (1985) model, maximum bound for for M_{max}. For a given fault, the four models displayed correspond to the same seismic moment rate, estimated considering the minimum bound of the slip rate interval and the fault area (maximum depth 14km for strike-slip faults, dip 45° for MLT). Seismic rates are normalized per km^2. See Table 1 for faults acronyms

Fig. 6 displays the recurrence models obtained for the 7 faults, considering the exponential Gutenberg-Richter model (first row) or the characteristic model (second row). In this example, the total seismic moment rate is inferred from the lower bound of the slip rate estimates applied to the fault area. As expected, the characteristic model leads to larger rates in the upper magnitude range, and lower rates in the moderate magnitude range, with respect to the exponential model. The impact on the rates of the M_{max} choice is also shown. For a moment-balanced recurrence model with fixed moment rate, a decrease of M_{max} leads to an increase of the rates in the moderate magnitude range.

To build the source model, the fault model is combined with the smoothed seismicity model. To avoid double counting earthquakes, a buffer zone of 5 km around the projection of the rupture plane to the surface is considered. Within this buffer zone the frequency-magnitude distributions of the gridded seismicity are truncated at the minimum magnitude taken into account on the fault (following e.g. Danciu et al. 2017; Demircioglu et al. 2018). Here we consider two alternative minimum magnitudes, 5.5 and 6.0. This parameter, which is chosen rather

arbitrarily, has an impact on hazard results. This minimum magnitude considered for the faults varies from one study to the other: M_W 5.5 in Danciu et al. (2017) in the Middle East EMME project, M_W 6.0 in Demiciorglu et al. (2018) in Turkey, M_W 6.4 in Woessner et al. (2015) in Europe, or M_W 6.5 in Rong et al. (2020) in China. Earthquakes on faults contribute to the hazard from this minimum magnitude up to the maximum magnitude attributed to the fault.

4. Ground Motion prediction

There are no ground-motion records available in Lebanon to guide the selection of the ground-motion prediction model. Any site within Lebanon is located within 20 km of a fault, either strike slip for faults inland or thrust offshore (Mount Lebanon). Disaggregation studies show that for the return periods larger than or equal to 475 yrs, most contributions come from source-site distances lower than 50km (see section 5). We select three ground-motion models established from shallow crustal earthquakes, relying on three different datasets, as an attempt to capture the epistemic uncertainty on the prediction of ground motions.

The model of Chiou and Youngs (2014) has been established from the NGA-West2 ground-motion database (Ancheta et al. 2014) complemented by numerical simulations. This database contains mainly California earthquakes, supplemented with recordings from magnitudes M_W 6 to 7.9 events that occurred in other active regions (Iran, Italy, Japan, New Zealand, Taiwan, Turkey, China). These recordings have been used to constrain the magnitude scaling and the aleatory variability for large magnitudes. The functional form accounts for styles of faulting effects, and for the position of the top of rupture. The model has additional terms to account for hanging-wall effects, as well as effects of rupture directivity at large magnitudes. It accounts for magnitude-dependent effects of extended ruptures on distance scaling in the rupture distance range of 0km to approximately 100km. Equations are provided at spectral periods from 0.01 to 10s.

The model of Akkar et al. (2014) relies on a pan-European database including strong-motion recordings obtained in the Mediterranean region and the Middle East. It provides equations for shallow (<30km depth) crustal earthquakes, at spectral periods from 0.01 to 4s. Its distance metric is the Joyner and Boore distance (shortest distance to the surface projection of the rupture). In the database, magnitudes up to roughly M_W 7 are well represented, particularly for normal and strike-slip faulting. For larger magnitudes there are almost no records from reverse-faulting events, the available data are mainly from three large strike-slip earthquakes (largest magnitude M_W7.6). Reverse-faulting earthquakes are quite poorly represented (in contrast with the NGA model for which reverse earthquakes contribute a large proportion of the database).

The third model considered is the Kotha et al. (2020) ground-motion model developed for shallow crustal earthquakes in Europe, with magnitudes M_W up to 7.4. It is based on the new European Strong-Motion datataset (Lanzano et al. 2019). The model includes a region-dependent coefficient of attenuation, and a region-dependent source-scaling factor. However, too few data were available both in the attenuation regionalization and event localization polygons including Lebanon, therefore we apply the ergodic version of the model. Distance measure is Joyner and Boore distance, owing to significant uncertainty in the finite rupture dimensions and hypocentral depths. Events have been categorized into three depth bins (<10km, 10 to 20, and >20km). Equations are provided at spectral periods from 0.01 to 8s.

5. Influence of source model uncertainties on hazard estimates

5.1 Identification of key parameters/key decisions

We start with building a logic tree to explore uncertainties on the source model and understand which parameters, models or decisions, impact hazard estimates. This logic tree is made of the two alternative smoothed seismicity models, lower and upper bounds for the slip rate accumulating on the fault, two alternative earthquake recurrence models for the faults, two alternative b-values (the universal value 1 and an arbitrary value fixed to 0.85, simply to test the sensitivity of the results with respect to this parameter), two alternative minimum magnitude on faults, lower and upper bounds on the maximum magnitude that can break the fault, and three geometries of fault planes (Fig. 7). For strike-slip faults, three alternative maximum depths of fault planes are considered; whereas for Mount Lebanon Thrust three alternative values for the dip are considered. We combine this source model logic tree with the three ground-motion models equally weighted.

Hazard calculations are led considering a minimum magnitude of M_W 4.5, a maximum distance of 150km, the scaling relationship Leonard (2014) for generating extended rupture planes, and a truncation of the gaussian predicted by the ground-motion models at 3 standard deviations above the mean. The OpenQuake engine, developed by the Global Earthquake Model Foundation, is used (Pagani et al. 2014).

Fig. 8 displays the results for four cities in Lebanon (Fig. 2), for the PGA at 475 years return period, considering generic rock site (V_{S30} = 760 m/s). The black distribution is obtained by sampling the full logic tree (2^6x3= 192 source models, combined with 3 GMMs, resulting in 576 hazard estimates). In the capital city Beirut, located on the coast on the hanging-wall of Mount Lebanon Thrust, the mean PGA obtained is 0.3g. In Saida and Tripoli, coastal cities close to the MLT fault but not above it, the mean PGA obtained is around 0.25g. Higher values are obtained in Zahle in the Beqaa Valley (0.42g mean value), located along the Yammouneh strike-slip fault. Besides, the smallest variability on hazard levels is found for Saida (0.17g-0.3g, percentiles 16^{th}-84^{th}), whereas the largest variability is obtained in Zahle (0.28-0.57g) and Beirut (0.17-0.45g).

Following Beauval et al. (2020), different distributions for the acceleration at 475 years (PGA) are displayed, corresponding to different branches of the logic tree sampled (Fig. 8). We choose this representation rather than an impact analysis (as in Beauval and Scotti 2004) or a Tornado diagram (e.g., Anderson 2018), to determine an absolute impact which is not dependent on a specific set of reference parameters. To quantify the impact of the uncertainty on the slip rate, the 576 values are split into two separate distributions, one that relies on the slip rate lower bound (light blue, 288 values), and the other that relies on the slip rate upper bound (dark blue, 288 values). The difference in the mean values of the two distributions corresponds to the impact on hazard of slip rate uncertainty. Similarly, the impact on hazard of the following uncertainties or parameter choices can be evaluated: uncertainty on the geometry of faults, choice of the recurrence model, uncertainty on the maximum magnitude, the decision on the minimum magnitude on faults, decision on the b-value, alternative smoothed seismicity models. The larger the distance between the two mean values of distributions (or the three in case of geometry), the larger the impact the parameter has on hazard.

This analysis shows that the choice of the recurrence model for faults is the decision that impacts the most the hazard values, for all sites. In Beirut, the exponential model leads to hazard values (0.4g) twice as high as the characteristic model (0.2g). The uncertainty on the slip rate and on the M_{max} also impacts significantly hazard estimates (~50% increase in Beirut). Using a minimum magnitude of 5.5 rather than 6 produces an increase of hazard estimates (~20% increase in Beirut). The geometry has a stronger impact in Zahle than in the coastal cities. The uncertainty on the b-value or on the smoothed seismicity model has a negligible impact on hazard. This

hierarchy of parameters' impacts is the same for the four cities, it is also stable considering other spectral periods (0.2s and 1s) and larger return periods (2475 and 4975 yrs) (see Online Resource, Figs. S1 and S2).

It is expected that the hazard levels increase when the slip rate increases, or when the fault area is enlarged, as it leads to larger seismic moment rates to be released in earthquakes. Some impacts are less straightforward. At 475 years, hazard values increase when M_{max} values on faults decrease (at the PGA, increase of 0.36g to 0.5g in Zahle, selecting the M_{max} lower bound rather than the upper bound, Fig. 8). For a fixed moment rate, a decrease of the maximum magnitude leads to an increase of seismicity rates in the moderate magnitude range (Fig. 9a, Yammouneh fault), and an increase in the amplitudes of the hazard spectrum at 475 yrs at a nearby site (Fig. 9b, Zahle city). Similarly, hazard values decrease when the characteristic model is chosen over the exponential model (Fig. 8, PGA at 475 years, decrease of 0.52g to 0.31g in Zahle). For a fixed moment rate, the characteristic model leads to lower seismic rates in the moderate magnitude range with respect to the exponential model (Fig. 9c, Yammouneh fault), and a decrease in the amplitudes of the hazard spectrum at 475 yrs at a nearby site (Fig. 9d, Zahle). However, for the return period 2475 years, at spectral periods larger or equal to 1.0, opposite trends are observed, acceleration levels increase. In this case most contributions come from the upper magnitude range.

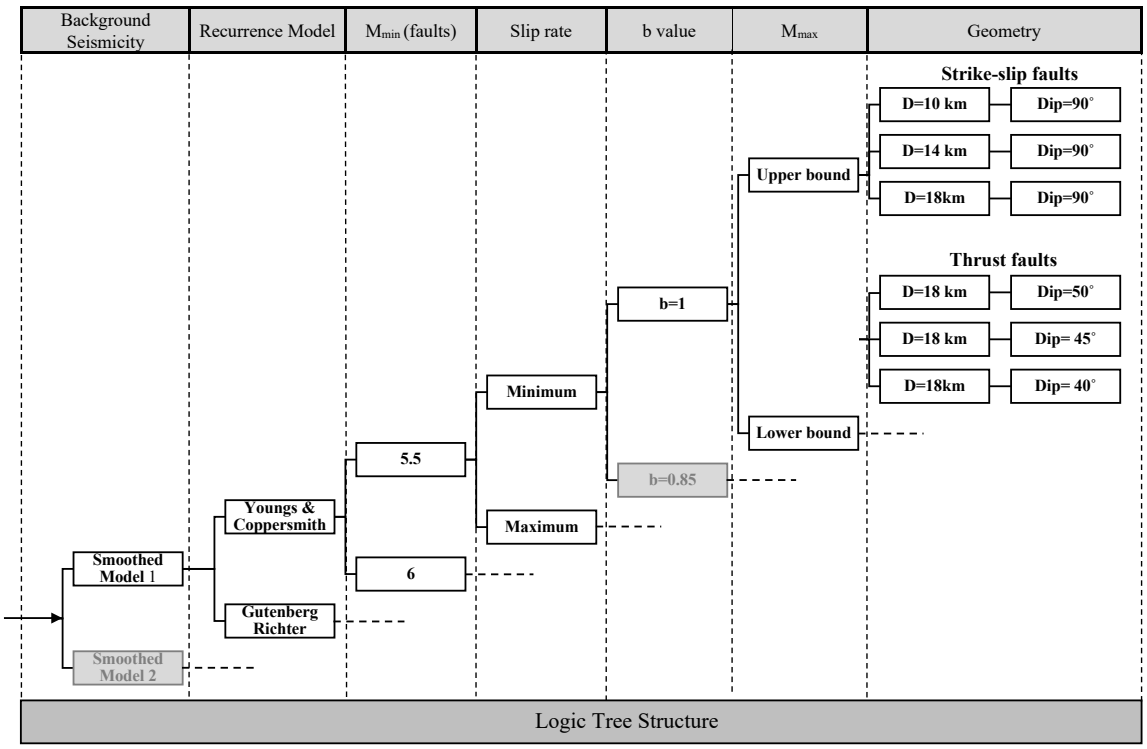

Fig. 7 Source model logic tree. In Section 5, the logic tree is explored considering all branches as equally probable, delivering 2x2x2x2x2x2x3=192 different branches' combinations, combined with 3 ground-motion models, resulting in 576 hazard results. In section 6, the branches in grey are discarded, and 2x2x2x3=48 branches' combinations are kept to derive seismic hazard maps (144 hazard values).

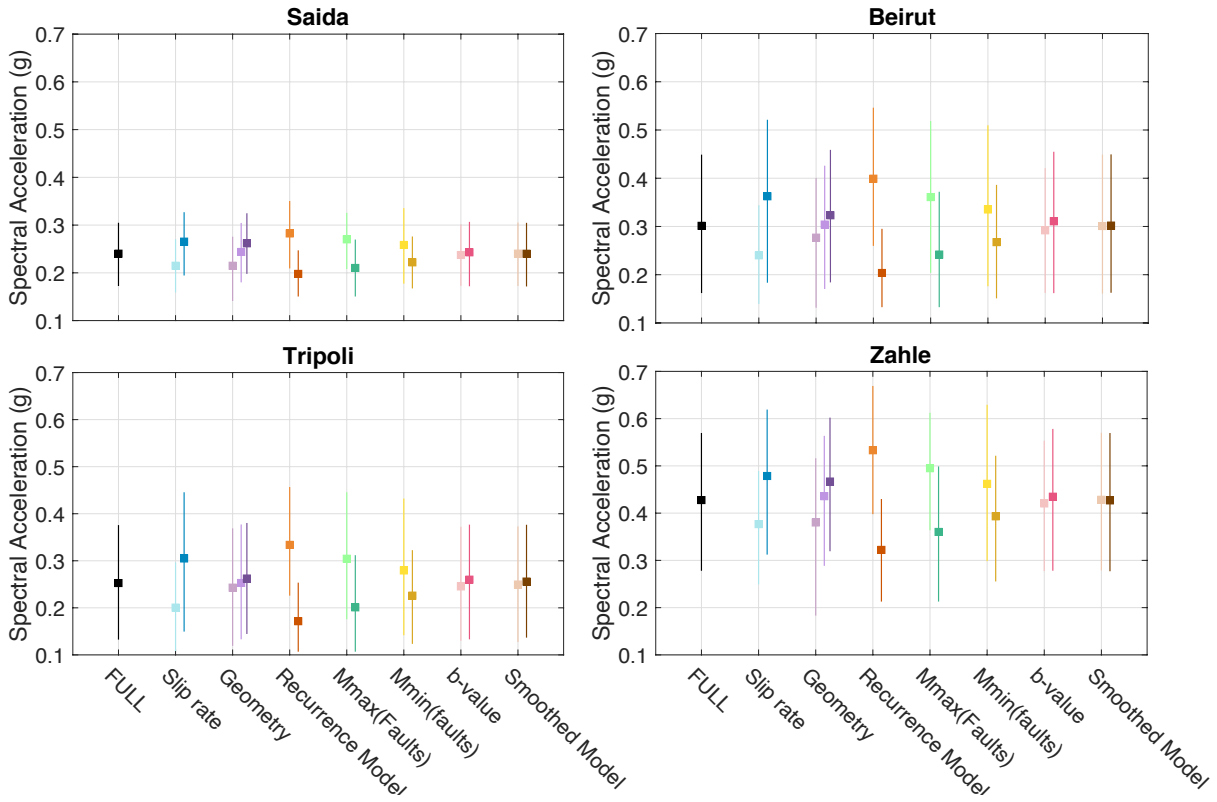

Fig. 8 Hazard level distributions, exploring the source model logic tree, at the PGA and 475 years return period, at 4 Lebanese cities. Mean value (square), percentiles 16th and 84th (vertical bar). 'FULL': full logic tree (576 values). 'Slip rate': choice of the slip rate, lower bound (light blue, 288 values), upper bound (dark blue, 288 values). 'Geometry': 3 alternative fault geometries, light to dark purple (depths 10, 14, 18km SS faults, or dip 40, 45, 50 MLT fault). 'Recurrence model': choice of the recurrence model, exponential (light orange) or characteristic (dark orange). 'M_{max}(faults)': choice of M_{max} on faults, lower bound (light green) or upper bound (dark green). 'M_{min}(faults)': choice of the minimum magnitude on faults, lower bound (light yellow) or upper bound (dark yellow). 'b-value': choice of the b-value, b=1 (light pink) or b=0.85 (dark pink). 'Smoothed Model': choice of the smoothed seismicity model, model 1 (light brown) or model 2 (dark brown). The three ground-motion models are considered in these calculations, equally weighted

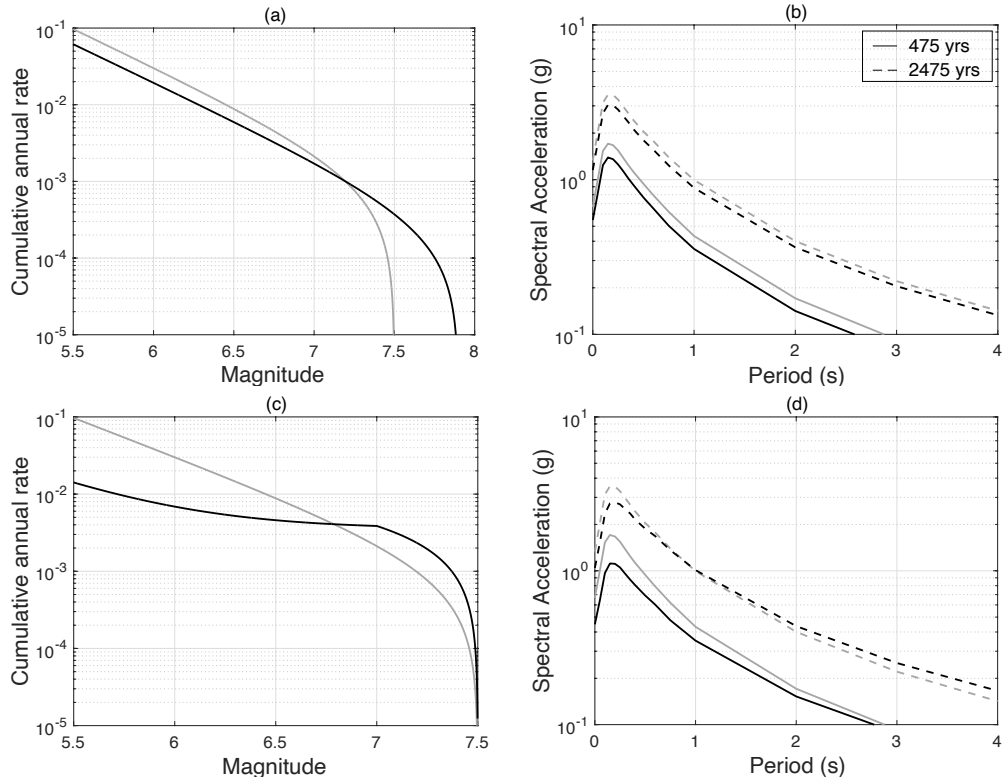

Fig 9 Earthquake recurrence model for Yammouneh fault and associated hazard estimates for Zahle city. (a) Exponential Gutenberg-Richter model, impact of the choice of M_{max} on the earthquake rates, for a fixed moment rate (grey: M_{max} 7.5; black: 7.9), and (b) corresponding impact on the Uniform Hazard Spectrum (UHS) at 475 and 2475 years return period. c) Impact of the choice of the recurrence model on earthquake rates, exponential (grey) or characteristic (black), for a fixed moment rate, and d) impact on the UHS. All recurrence models correspond to the same seismic moment rate, estimated from the slip rate upper bound (6.1 mm/yr) applied to the Yammouneh fault that extends down to 10 km depth

5.2 Beirut, hazard controlled by Mount Lebanon fault

Beirut is the capital city of Lebanon. It is located on the hanging-wall of Mount Lebanon fault, at ~30km from the Yammouneh fault. At 475 years return period, the exploration of the logic tree leads to a mean value of 0.3 and 0.72g, respectively at the PGA and spectral period 0.2s (Fig. 8 and Fig. S3). Considering the percentiles 16 and 84th, PGA values vary between 0.17 and 0.45g. The uncertainty obtained exploring the logic tree results in a large variability of hazard estimates.

It is important to understand where the contributions to hazard come from. Fig. 10 displays the hazard curve obtained in Beirut considering the full model (in red), as well as the hazard curves considering only one source (Mount Lebanon fault, Yammouneh fault, smoothed seismicity model). Considering the exponential Gutenberg-Richter model, for return periods larger than or equal to 475 years (annual rate of exceedance lower or equal to 0.0021), all the contributions come from the Mount Lebanon fault. Considering the characteristic Youngs and Coppersmith model, lower hazard levels are obtained and at 475 years return period, the Yammouneh fault also contributes to hazard in Beirut. The smoothed seismicity has a negligible contribution to hazard. A disaggregation study in magnitude and distance is also useful to understand which earthquakes at which distances contribute to the hazard (Fig. 11). At 475 years, for the PGA, assuming that earthquake occurrence on faults follows an exponential model, most contributions come from sources at less than 20km, with magnitude earthquakes between 5.5 and M_{max}, on Mount Lebanon rupture plane. Assuming instead that earthquake occurrence on faults follow a

characteristic model, there are also contributions from the more distant Yammouneh fault, from magnitude earthquakes both in the moderate and upper magnitude range.

Mount Lebanon is an off-shore fault, much less well characterized than the inland faults (Elias et al. 2007). The slip rate, the fault trace and fault geometry, as well as extension at depth, are less constrained than for the other faults included in the model. The regional EMME project (Şeşetyan et al. 2018; Danciu et al. 2017) obtained a higher mean hazard value in Beirut, close to the percentile 84th we obtain (0.41g, Fig. 12). This difference is due to a combination of decisions. For establishing earthquake recurrences on faults, the exponential Gutenberg-Richter model alone was considered, only the central segment was considered (latitude 33.76° to 34.34°) thus reducing the total length (with a maximum magnitude range 7.3-7.6), and a unique minimum magnitude was considered for faults (MW 5.5). Moreover, a different set of ground-motions has been considered: Chiou & Youngs (2008), Zhao et al. (2006), Akkar et al. (2014) and Akkar and Çağnan (2010), respectively with the weights 0.35, 0.1, 0.35 and 0.2.
If we consider only the exponential model in our logic tree, we get the distribution displayed in Fig. 12, the mean PGA at 475 years increases up to 0.4g. Then, if the segment is reduced to its central part with M_{max} 7.3-7.6, the mean PGA increases up to 0.44g. Next, considering only a minimum magnitude 5.5 for earthquakes on faults, the mean PGA reaches a mean value around 0.5g. At last, applying the EMME ground-motion logic tree, the mean PGA reduces to 0.43g, close to the mean value obtained in EMME. Nonetheless, the EMME source model includes two branches, area source and fault model (Danciu et al., 2017). Using the xml OpenQuake input files, available on the efehr.org website, we have calculated the uniform hazard spectrum in Beirut, considering the mean as well as independently the EMME area model, and the EMME smoothed seismicity and fault model (Fig. S7). Results show that a deeper analysis would be required to understand the differences between the present study and the EMME study.

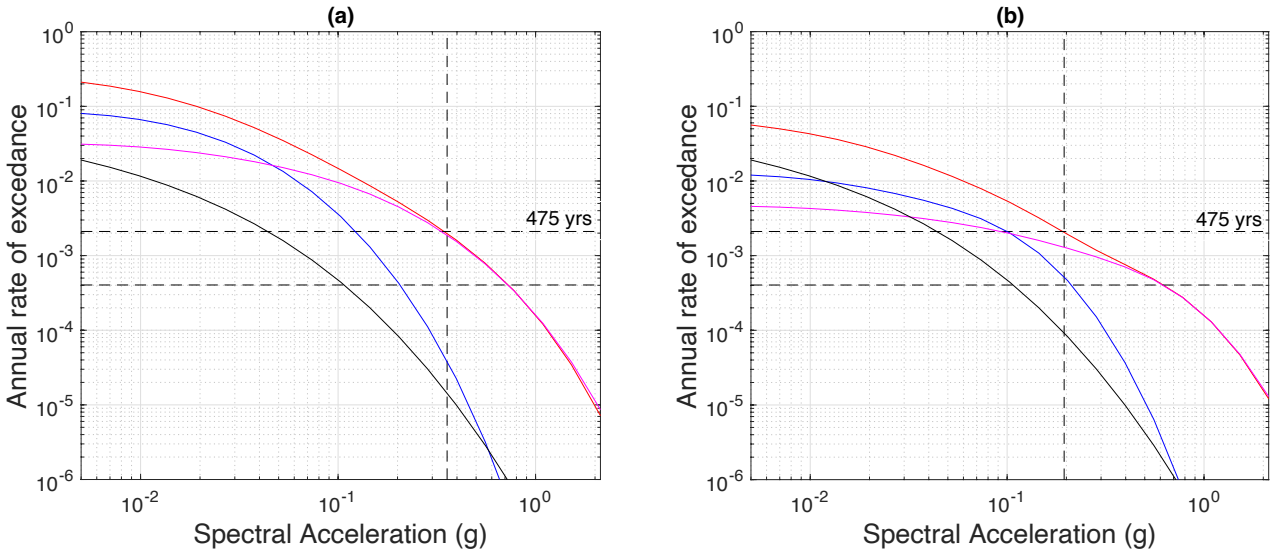

Fig. 10 Hazard curves in Beirut, for the PGA, considering one source model (one combination of branches in the source model logic tree) and one ground-motion model. Red: the full source model is accounted for in the hazard calculations; magenta: only Mount Lebanon Thrust is considered; blue: only the Yammouneh fault; black: only the smoothed seismicity model 1. Model applied to faults: a) exponential; b) characteristic. Earthquake recurrence model based on: lower bound of the slip rate, lower bound of M_{max} (7.5 for the MLT and 7.5 for Yammouneh), M_{min} 5.5 for faults. The Chiou and Youngs (2014) ground-motion model is used

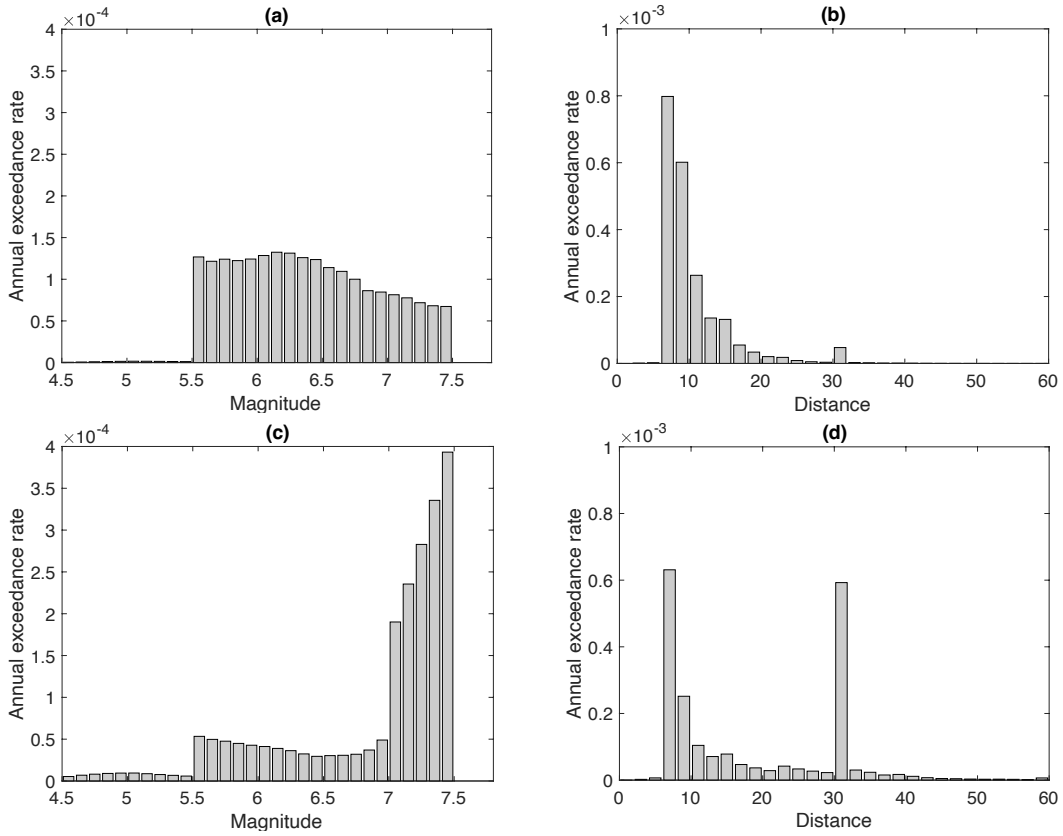

Fig. 11 Beirut site, disaggregation in magnitude (left column) and distance (right column), for the PGA at 475 years return period. First row: exponential model (PGA 0.39g); second row: characteristic model (PGA 0.19g). The source models and hazard calculations used are identical as in Fig. 10. The Chiou and Youngs (2014) ground-motion model is used

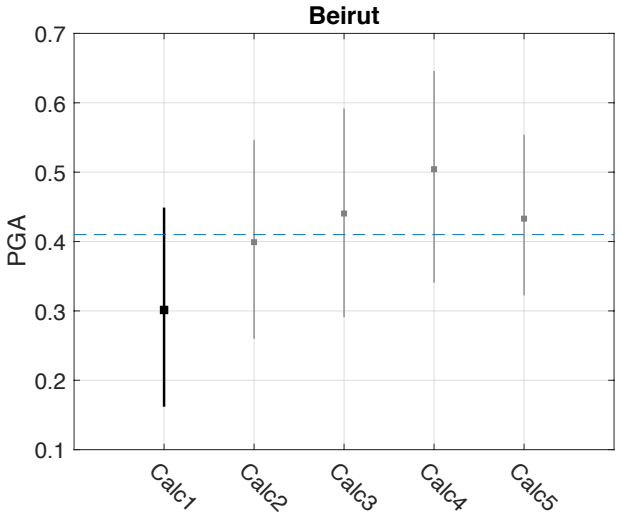

Fig. 12 Hazard estimates in Beirut, distribution of accelerations at the PGA, return period 475 years, mean and percentiles 16th and 84th. Calc1: full logic tree (Fig. 7), hazard results as in Fig. 8. Calc2: only the exponential model is considered. Calc3: one modification with respect to Calc2, Mount Lebanon fault is reduced to the central segment with M_{max} 7.3-7.6 as in EMME. Calc4: one further modification with respect to Calc3, only the minimum magnitude 5.5 is considered on faults. Calc5: same as Calc4 with the GMM logic tree used in the EMME project. The dashed line corresponds to the mean PGA value obtained by EMME for Beirut (0.41g, Sesetyan et al. 2018)

6. Seismic hazard maps

We aim at providing hazard values for the whole country, so that this work can be used in the perspective of future updates of the Lebanese building code. We exclude from the logic tree the branches that have a negligible impact on hazard. A unique b-value of 1.0 is used for the recurrence model on faults; only the smoothed seismicity model 1 is considered. Our aim is to display the range of hazard levels that are obtained, and to show how some decisions on the source model logic tree may impact seismic hazard levels at the scale of the country.

6.1 Hazard maps at the PGA and 475 years, based on our logic tree

A distribution of seismic hazard maps can be obtained from the exploration of the source model logic tree combined with the ground-motion logic tree (48x3=144 different branches' combination, equally weighted). From this distribution, a mean hazard map as well as hazard maps at given percentiles can be displayed, for any return period or spectral period. Fig. 13 displays the mean hazard map (Fig. 13a) and the 84th percentile hazard map (Fig. 13b) obtained at the PGA for the return period 475 years. Mean hazard values are higher than 0.2g throughout most of the country (Fig. 13a). Highest levels are found at sites along the main strand of the Levant fault. South of Lebanon, the 0.3g contour is at a distance of ~10km from the Jordan Valley fault trace. North of 33° latitude, the area with hazard values larger than 0.3g widens, as the contributions of the Rachaya fault and then the Roum fault add onto the contribution of the Yammouneh fault. Hazard values larger than 0.3g are also found along the coast, from north of Saida to south of Tripoli, due to the proximity to the Mount Lebanon fault plane. Levels larger than 0.5g are found for sites nearby the Yammouneh fault. Hazard values on the Missyaf segment exceed 0.6g. The slip rate range associated to this fault (4.9-5.5 mm/yr), combined with an M_{max} of 7.1-7.5 inferred from the length of the segment (75km), lead to rates in the moderate magnitude range that are higher than those estimated for the Yammouneh and Jordan Valley fault (Fig. 5; higher mean slip rate, shorter segment, smaller M_{max}, with respect to Yammouneh fault). As for hazard values corresponding to the 84th percentile, they are larger than 0.3g within most of the country (Fig. 13b), similarly with highest levels along the Yammouneh (>0.6g) and Missyaf (>0.7g) faults. Mean seismic hazard maps have also been produced for the spectral periods 0.2s and 1s, for 475 years and 2475 yrs return periods (see Online Resource, Figs. S5 and S6). To appraise the hazard levels at different spectral periods, the uniform hazard spectra for four cities in Lebanon are displayed, for the return periods 475 and 2475 years (Fig. 14). Also, to appraise the shape of the distribution obtained for a given spectral period, the distribution of hazard levels in Beirut for the PGA and spectral period 0.2s are displayed in the Online Resource (Fig. S8).

The analysis of input parameters' impacts on hazard has shown that the choice of the recurrence model for faults impacts the most the hazard levels (Section 5.1). In many countries, in order to deliver national seismic hazard maps, an expert committee is set up and an elicitation process is led to make the final decisions on the exact input parameters to be used in hazard calculations, as well as branches' weights (e.g. Gerstenberger et al. 2020). Such an expert committee might be established in the future in Lebanon. Decisions on branches weights have obvious consequences on hazard. If the Youngs and Coppersmith characteristic model is favored over the Gutenberg-Richter model, and hazard calculations are led applying e.g. a weight of 80% on the characteristic branch with respect to 20% to the exponential Gutenberg-Richter, final hazard values decrease (Fig. 15a). Mean PGA values at 475 yrs decrease all over the country and the 0.3g contour is now restricted to a strip of 20 to 40 km along the main strand of the Levant fault. Hazard values are still larger than 0.2g in most parts of the country. If instead, a larger weight is applied to the exponential model (80%), with respect to the characteristic model (20%), mean hazard values increase, the whole country is within the contour 0.3g, except for the regions around Tyr and north east of Baalbeck, and hazard values exceed 0.5g along the main strand of the Levant fault (Fig. 15b).

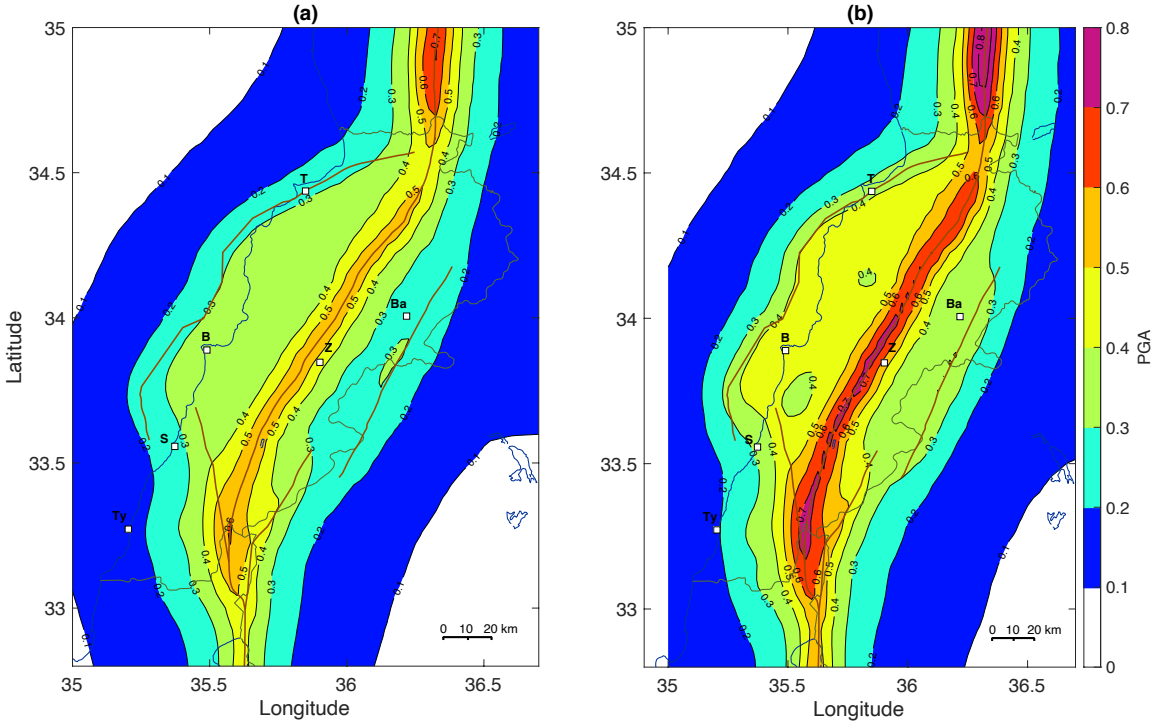

Fig. 13 Mean seismic hazard maps for the PGA at 475 years, generic rock site condition with V_{S30} 760 m/s, considering equal weights on the branches of the source model logic tree combined with the three selected ground-motion models. a) mean hazard values; b) hazard values corresponding to the percentile 84th. B: Beirut; Ba: Baalbeck, Ty: Tyr, T: Tripoli, Z: Zahle, S: Saida

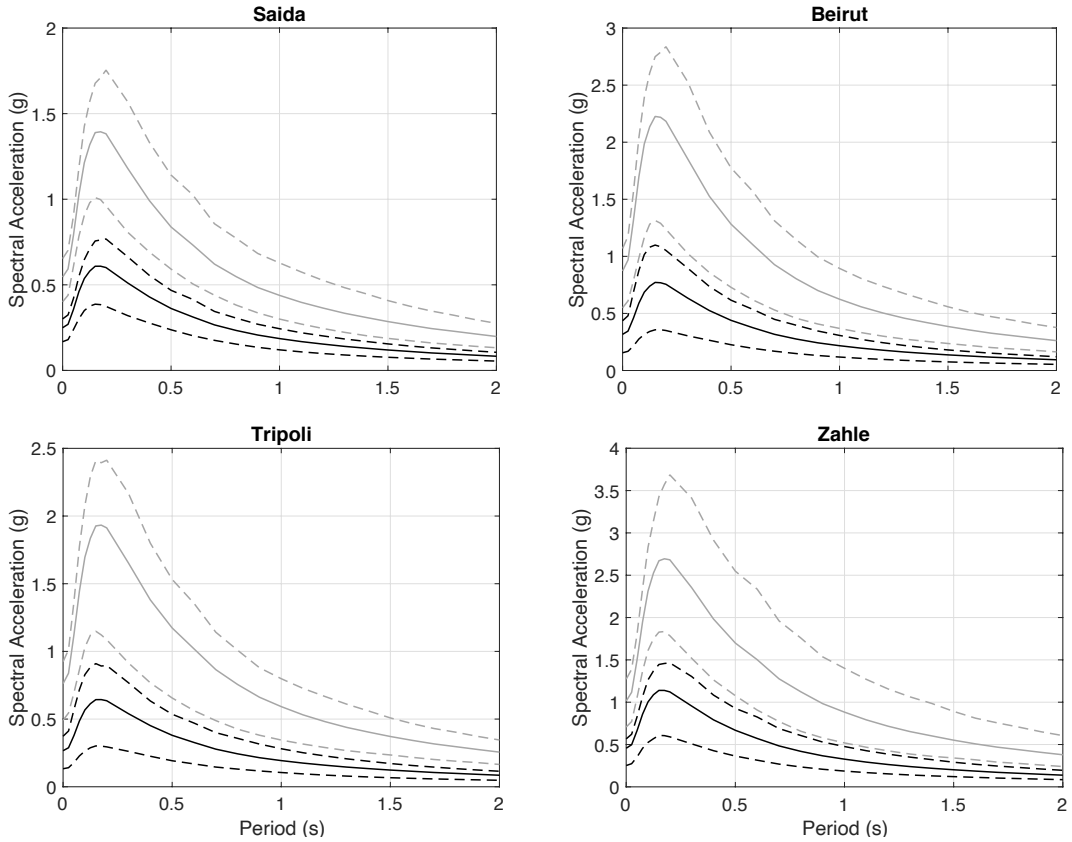

Fig. 14 Distribution of uniform hazard spectra at 4 cities in Lebanon, mean (solid line) and percentiles 16th and 84th (dashed lines). Black: 475 years return period, Grey: 2475 years return period. The source model logic tree is combined with the three alternative ground-

motion models. Average values and percentiles are inferred from a distribution of 144 hazard values (equally weighted), as in Fig. 13 (spectral accelerations are reported in the Online Resource, Table S1)

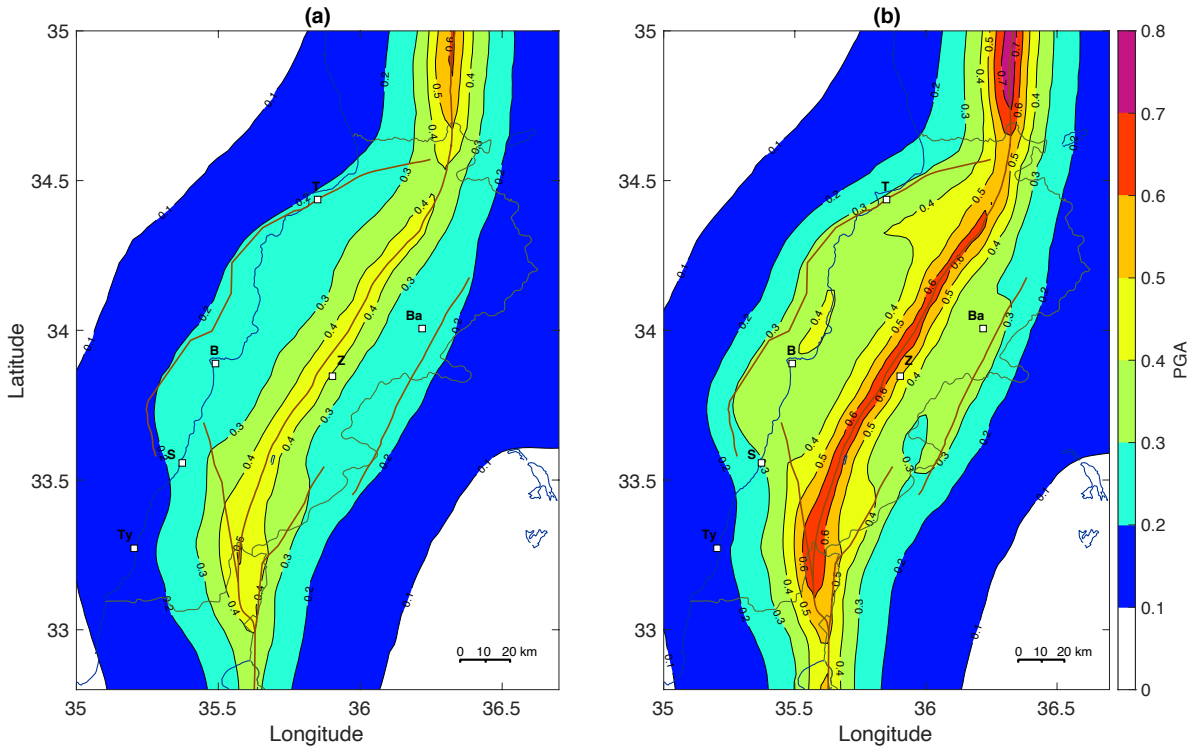

Fig. 15 Mean seismic hazard maps, PGA at 475 years return period, impact of different decisions on the weights associated to the earthquake recurrence model applied to faults. a) 80% weight on the characteristic Youngs and Coppersmith (1985) and 20% weight on the exponential Gutenberg-Richter model branch. b) 20% weight on the characteristic model branch and 80% weight on the exponential model branch. B: Beirut; Ba: Baalbeck, Ty: Tyr, T: Tripoli, Z: Zahle, S: Saida

6.2 Testing different hypotheses for the main strand of the Levant fault

6.2.1 Geodetic versus geologic slip rates on the Missyaf segment

Whereas slip rates inferred from tectonic and geodetic studies are generally consistent for the Jordan Valley fault (e.g. Lefevre et al. 2018), they differ significantly on the northern part of the Levant fault, along the Missyaf segment. Meghraoui et al. (2003) estimated a slip rate of 6.8-7.0 mm/year along this segment, based on the occurrence of three large earthquakes in the past 2000 years identified with archeoseismicity and trenching. The complementary studies by Sbeinati et al. (2010) extended the time window to the last 3500 years, including a fourth event with a very uncertain age (1500 to 900 BC). Assuming that this ancient event corresponds to an historical earthquake in 1365 BC, they propose a range of 4.9-5.5 mm/year for the slip rate (Table 1). However, geodetically derived slip rates obtained for the northern part of the Levant fault are much lower. Alchalbi et al. (2010) derive an average value of 2.5 mm/year (1.8 to 3.3 mm/year), associated with a locking depth of 10km, from GPS sites measured in 2000 and 2008. More recently, Gomez et al. (2020) estimated 2.2 ± 0.5 mm/year, associated to a locking depth of 10km, using a block model with GPS velocities that rely on observations from ~2001 to ~2012. Such a discrepancy between the geologic slip rate (representing an average over a long period of time) and the geodetic slip rate (representing the current state of the fault) would need to be better understood. Both geodetic and geologic slip rates should eventually be included in the source model logic tree, as they represent the epistemic uncertainty on the amount of the deformation that accumulates along the fault and that

can be released in future earthquakes. Fig. 16a displays the mean hazard map at 475 years obtained applying a slip rate range of 1.7 – 2.7 mm/year on the Missyaf segment. As expected, lower hazard levels are found with respect to the hazard calculation that relies on paleoseismic slip rates, with PGA values lower than 0.4 g for sites along the fault trace.

6.2.2 Considering only one long fault for the primary strand of the Levant fault

In our source model, the primary strand of the Levant fault is constituted of three faults, from south to north, the Jordan Valley fault, the Yammouneh fault and the Missyaf fault. The Yammouneh fault stops south of the Hula Basin (Fig. 2, Table 1). This segmentation makes the strong assumption that the Hula Basin and the El Boqueaa pull-apart Basin to the north are major obstacles to a rupture propagation. However, several archeoseismic and paleoseismic studies on the Jordan Gorge section, the northern segment of the Jordan Valley fault, have demonstrated that this segment could rupture during earthquakes originating from the north. One example is the A.D. 1202 event, centered on the Yammouneh fault, that ruptured to the south through this segment (Marco et al. 2005; Wechsler et al. 2014). To understand how this segmentation impacts hazard results, we perform a test where the segmentation is relaxed and a unique long segment is considered that encompasses all segments of the primary strand of the Levant fault. In the hazard calculations, earthquake ruptures are now distributed uniformly along this ~450km-long segment and we consider a unique slip rate interval of 4 to 5 mm/year. We consider a range of 7.5-7.9 for M_{max} (same range as Yammouneh and JVF faults, Table 1). The resulting mean seismic hazard map is displayed in Fig. 16b (PGA, 475 years return period). With respect to Fig. 13a, hazard levels slightly decrease along the Yammouneh fault, and slightly increase south of latitude ~33.3°. The largest impact is obtained for sites along the Missyaf segment with much lower values considering one unique long segment for the Levant fault, as expected (~0.4g rather than ~0.6g).

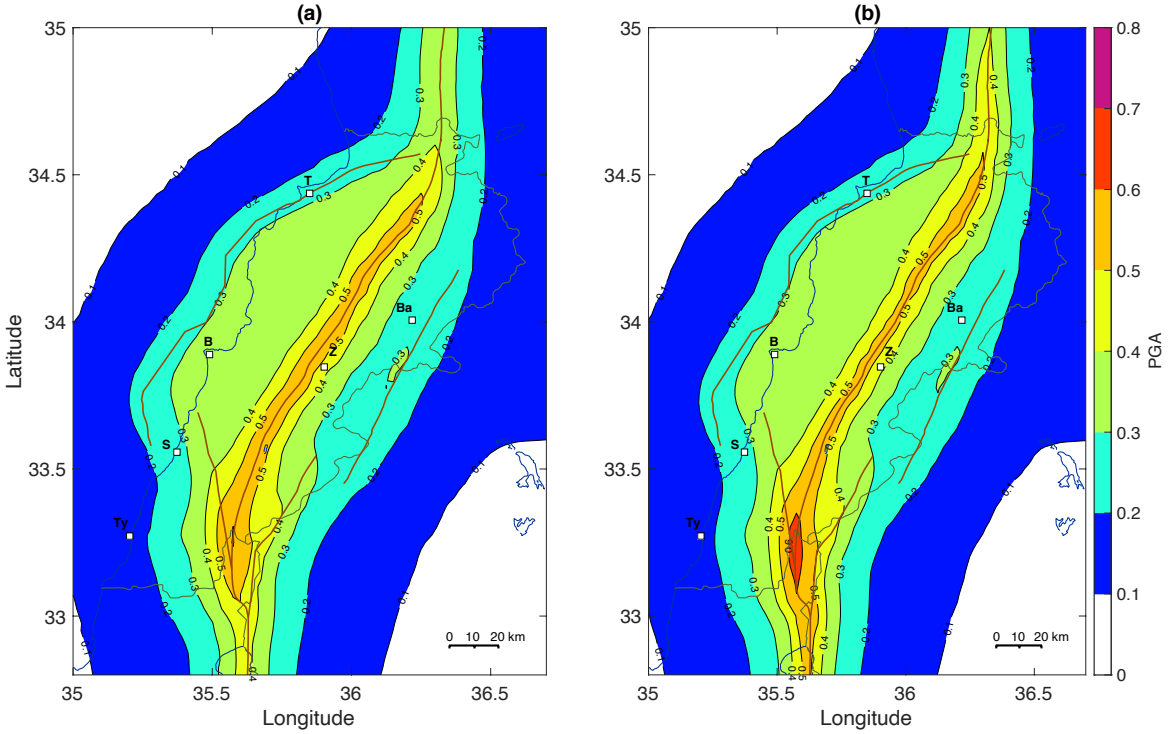

Fig. 16 Mean seismic hazard maps at 475 years return period, for generic rock site conditions (760 m/s). Different assumptions are made on the source model with respect to Fig. 14a: a) the slip rate range applied to Missyaf segment is now inferred from geodetic studies (1.7-2.7 mm/year); b) the main strand of the Levant fault is considered as one unique long segment with slip rate range 4 to 5 mm/year

7. Conclusions

We have built a source model for Lebanon and bordering regions, made of a smoothed-seismicity model (off-fault forecast), combined with a fault model. The fault model relies on the findings of geologic, paleoseismic and geodetic studies in terms of fault traces, fault geometries and the quantification of the deformation that accumulates along faults. Maximum magnitudes on faults are inferred from the magnitude range of historical events associated to the faults, as well as from the application of scaling relationships to lengths and widths of faults. Two sets of alternative moment-balanced earthquake recurrence models are derived for faults, assuming either an exponential Gutenberg-Richter model or a characteristic Youngs and Coppersmith (1985) model. The off-fault seismicity forecast relies on the Lebanese instrumental catalog. To evaluate seismic hazard levels, the source model logic tree is combined with three ground-motion models equally weighted (Akkar et al. 2014; Chiou and Youngs 2014 and Kotha et al. 2020), as an attempt to capture the epistemic uncertainty on the prediction of ground-motion in this area.

We consider four cities, Saida, Beirut (the capital city), Tripoli on the coast and Zahle in the Beqaa plain, where we perform an extensive sensitivity analysis to understand which source model parameters' uncertainties most impact hazard estimates. This analysis demonstrates that:

- the choice of the recurrence model on faults, either exponential or characteristic, impacts the most the hazard levels (up to 100% increase);
- the uncertainties on the slip rate and on M_{max} also impact strongly the hazard (up to 50% increase);
- the minimum magnitude attributed to faults, a parameter that is poorly constrained, has a lower influence on hazard, but still significant (up to 30% increase of the hazard values, reducing M_{min} from 6.0 to 5.5)
- the impact of fault geometry uncertainties depends on the site, it is more significant for sites along the strike-slip faults than for sites close to Mount Lebanon thrust;
- the uncertainty on the b-value for faults has a negligible impact;
- the uncertainty on the smoothed seismicity model (derived only from the short instrumental GRAL catalog, 2006-2019) has no impact on hazard at these four cities; the disaggregation studies show that for most sites in Lebanon, the off-fault model has a negligible contribution to hazard.

We compute mean seismic hazard maps based on the source model logic tree obtained (branches equally weighted), including only the uncertainties that control hazard variability. Our calculations lead to mean PGA values at 475 years larger than 0.3g over two-third of the country, including the coastal region between Saida and Tripoli. Largest hazard values (>0.5g) are obtained along the main strand of the Levant fault. The variability obtained for hazard in the capital city Beirut is quite large, the PGA at 475 years return period varies between 0.16 and 0.45g (16^{th} and 84^{th} percentiles) with a mean around 0.3g. Disaggregation studies show that the hazard estimation in Beirut is mostly controlled by the Mount Lebanon thrust fault located beneath the city. Future studies aimed at characterizing this off-shore fault will be crucial for the hazard assessment of the city as well as within the coastal region.

Our source model relies on annual earthquake frequencies inferred from annual slip rates estimated from geologic, paleoseismologic and geodetic studies. Meanwhile, we ignore part of the information delivered by these studies. Along the Levant fault system, geologic and historical studies have demonstrated that large earthquakes occur in clusters (e.g. the sequence that lasted between the eleventh and thirteen century on the main strand, including the 1033, 1170 and 1202 events). It is not clear yet how this clustering of large events could be accounted for in seismic hazard assessment, but time-dependent models that account for fault interactions are required.

This work delivers a series of alternative source models for Lebanon, with the understanding of which parameters' uncertainties or decisions control hazard values, as well as which sources contribute for given sites, depending on the spectral period and return period. A range for seismic hazard values is obtained, for selected Lebanese cities and at the country scale. The hazard levels obtained in Beirut are compared to the output of the regional EMME project. These results may constitute a basis for discussion and for taking decisions in the perspective of future updates of the Lebanese building code.

8. Acknowledgements

This research benefited from the full support of the laboratory ISTerre, part of Labex OSUG@2020 (ANR10 LABX56) in France, and of the National Center of Geophysics in Lebanon. We are grateful to two anonymous reviewers for their careful and constructive reviews. We are also grateful to John Adams, who read an earlier version of the manuscript, and provided very useful feedbacks.

9. Statements & Declarations

9.1 Funding

S. El Kadri benefitted from a SAFAR scholarship financed by the French Ambassy in Beirut and the Lebanese CNRS.
Her stays in France were also supported by IRD through the ARTS program.

9.2 Conflict of interest

The authors declare no competing interests

10. References

Akkar, S. and Çağnan, Z. (2010) 'A local ground-motion predictive model for Turkey, and its comparison with other regional and global ground-motion models', Bulletin of the Seismological Society of America, 100(6), pp. 2978–2995. doi: 10.1785/0120090367.

Akkar, S., M. A. Sandikkaya, and J. J. Bommer (2014). Empirical ground-motion models for point- and extended-source crustal earthquake scenarios in Europe and the Middle East, Bull. Earthq. Eng. 12, no. 1, 359–387. https://doi.org/10.1007/s10518-013-9461-4

Alchalbi, A., Daoud, M., Gomez, F., et al. (2010), Crustal deformation in northwestern Arabia from GPS measurements in Syria: Slow slip rate along the northern Dead Sea Fault. Geophysical Journal International, 180: 125-135. https://doi.org/10.1111/j.1365-246X.2009.04431.x

Al Tarazi, E., J. Abu Rajab, F. Gomez, W. Cochran, R. Jaafar, and M. Ferry (2011), GPS measurements of near-field deformation along the southern Dead Sea Fault System, Geochem. Geophys. Geosyst., 12, Q12021, doi:10.1029/2011GC003736.

Ambraseys, N. N., and Barazangi, M. (1989). The 1759 earthquake in the Bekaa Valley: implications for earthquake hazard assessment in the Eastern Mediterranean region. Journal of Geophysical Research: Solid Earth, 94(B4), 4007-4013.

Ambraseys, N. N., and Jackson, J. A. (1998). Faulting associated with historical and recent earthquakes in the Eastern Mediterranean region. Geophysical Journal International, 133(2), 390-406.

Ambraseys, N. N. (2006) 'Comparison of frequency of occurrence of earthquakes with slip rates from long-term seismicity data:The cases of Gulf of Corinth, Sea of Marmara and Dead Sea Fault Zone', Geophys. J. Int., 165, pp. 516–256. doi: 10.1111/j.1365-246X.2006.02858.x.

Ambraseys NN (2009) Earthquakes in the Mediterranean and Middle East: a multidisciplinary study of seismicity up to 1900. Cambridge

University Press, Cambridge, United Kingdom, 968 pp. https:// doi. org/10. 1017/ CBO97 81139 195430

AMEC (2012) 'Lebanon Litani risver basin management support program, seismic deformation analysis of Qaraoun Dam, 147 pages (http://www.litani.gov.lb/wp/wp-content/uploads/LRBMS/028-LRBMS-SEISMIC%20DEFORMATION%20ANALYSIS%20OF%20QARAOUN.pdf).'

Ancheta, T. D., Darragh, R. B., Stewart, J. P., et al. (2014). NGA-West2 database. Earthquake Spectra, 30(3), 989-1005. https://doi.org/10.1193/070913EQS197M

Anderson, J. G. and Luco, J. E. (1983) 'Consequences of slip rate constraints on earthquake occurrence relations', Bulletin of the Seismological Society of America, 73(2), pp. 471–496.

Anderson, J. G. (2018) 'Quantifying the Epistemic Uncertainty in the Probabilistic Seismic Hazard from Two Major Faults in Western Nevada. Earthquake Spectra 2018', 34 (2): 54. doi: https://doi.org/10.1193/080717EQS156M.

Arango M.C. and Lubkowski, Z. A. (2012) 'Seismic Hazard Assessment and Design Requirements for Beirut, Lebanon, 15th World Conference on Earthquake Engineering, Lisboa, 10 pages.'

Beauval, C., and Scotti, O. (2004). Quantifying sensitivities of PSHA for France to earthquake catalog uncertainties, truncation of ground-motion variability, and magnitude limits. Bulletin of the Seismological Society of America, 94(5), 1579-1594. https://doi.org/10.1785/012003246.

Beauval, C., Scotti, O., and Bonilla, F. (2006). The role of seismicity models in probabilistic seismic hazard estimation: comparison of a zoning and a smoothing approach. Geophysical Journal International, 165(2), 584-595. https://doi.org/10.1111/j.1365-246X.2006.02945.x.

Beauval C, Bard PY, Danciu L (2020) The influence of source- and ground-motion model choices on probabilistic seismic hazard levels at 6 sites in France. Bull Earthq Eng 18(10):4551–4580. https://doi. org/ 10. 1007/ s10518- 020- 00879-z

Beauval C. and P-Y. Bard (2021). History of probabilistic seismic hazard assessment studies and seismic zonations in mainland France, Comptes Rendus Géoscience, 353, S1, 413-440, https://doi.org/10.5802/crgeos.95.

Brax M, Albini P, Beauval C, Jomaa R, Sursock A (2019) An earthquake catalog for the Lebanese region. Seismol Res Lett 90(6):2236–2249. https:// doi. org/ 10. 1785/ 02201 80292

Burkhard, and M., Grünthal, G. (2009) 'Seismic source zone characterization for the seismic hazard assessment project PEGASOS by the Expert Group 2 (EG1b). Swiss J. Geosci. 102, 149–188 (2009).' doi: https://doi.org/10.1007/s00015-009-1307-3.

Carton, H., Singh, S. C., Tapponnier, P., et al. (2009). Seismic evidence for Neogene and active shortening offshore of Lebanon (Shalimar cruise). Journal of Geophysical Research: Solid Earth, 114(B7). https://doi.org/10.1029/2007JB005391

Chiou, B. J., and Youngs, R. R. (2008). An NGA model for the average horizontal component of peak ground motion and response spectra. Earthquake spectra, 24(1), 173-215.

Chiou, B. S. J., and Youngs, R. R. (2014). Update of the Chiou and Youngs NGA model for the average horizontal component of peak ground motion and response spectra. Earthquake Spectra, 30(3), 1117-1153.

Christophersen A, Gerstenberger MC, Rhoades DA and Stirling MW (2011) Quantifying the effect of declustering on probabilistic seismic hazard. In: Proc of the ninth Pacific conf on earthquake engineering: Building an Earthquake-Resilient Society, Auckland, New Zealand, 14–16 April 2011.Paper number 206, 8 pp

Convertito, V., Emolo, A., and Zollo, A. (2006). Seismic-hazard assessment for a characteristic earthquake scenario: an integrated probabilistic–deterministic method. Bulletin of the Seismological Society of America, 96(2), 377-391. doi: https://doi.org/10.1785/0120050024.

Cornell, C. A. (1968) 'Engineering seismic risk analysis', Bulletin - Seismological Society of America, 58(5), pp. 1583–1606.

Daëron, M., Benedetti, L., Tapponnier, P., Sursock, A., and Finkel, R. C. (2004). Constraints on the post~ 25-ka slip rate of the Yammoûneh fault (Lebanon) using in situ cosmogenic 36Cl dating of offset limestone-clast fans. Earth and Planetary Science Letters, 227(1-2), 105-119. doi: 0.1016/j.epsl. 2004.07.014.

Daëron, M., Klinger, Y., Tapponnier, P., Elias, A., Jacques, E., and Sursock, A. (2005). Sources of the large AD 1202 and 1759 Near East earthquakes. Geology, 33(7), 529-532. doi: 10.1130/G21352.1.

Daëron, M., Klinger, Y., Tapponnier, P., Elias, A., Jacques, E., and Sursock, A. (2007). 12,000-year-long record of 10 to 13 paleoearthquakes on the Yammouneh fault, Levant fault system, Lebanon. Bulletin of the seismological society of America, 97(3), 749-

771. doi: 10.1785/0120060106.

Danciu, L., Şeşetyan, K., Demircioglu, M. et al. (2018). The 2014 Earthquake Model of the Middle East: seismogenic sources. Bull Earthquake Eng 16, 3465–3496. https://doi.org/10.1007/s10518-017-0096-8

Darawcheh, R., Sbeinati, M. R., Margottini, C., and Paolini, S. (2000). The 9 July 551 AD Beirut earthquake, eastern Mediterranean region. Journal of Earthquake Engineering, 4(04), 403-414.

Demircioğlu, M.B., Şeşetyan, K., Duman, T.Y. et al. A probabilistic seismic hazard assessment for the Turkish territory: part II—fault source and background seismicity model. Bull Earthquake Eng 16, 3399–3438 (2018). https://doi.org/10.1007/s10518-017-0130-x

Elias A (2006) Le chevauchement de Tripoli-Saida: Croissance du Mont Liban et risque sismique, These de doctorat. Inst. de Phys. Du Globe de Paris, Paris, 230 pp

Elias, A., Tapponnier, P., Singh, S.C., et al. (2007). Active thrusting offshore Mount Lebanon: Source of the tsunamigenic A.D. 551 Beirut-Tripoli earthquake. *Geology*, 35 (8): 755–758. doi: https://doi.org/10.1130/G23631A.1

Erdik M, Şeşetyan K, Demircioğlu MB, Harmandar E (2014). Assessment of site-specific earthquake hazard for Bisri Dam, Lebanon, report for the Council for development and reconstruction of the Republic of Lebanon, 44p.

Esteva, L. (1968) Bases para la formulacion de decisiones de diseño sismico. Thesis and Report 182, Universidad Autonoma Nacional de Mexico (in Spanish).

Ferry, M., Meghraoui, M., Abou Karaki, N., Al-Taj, M., Amoush, H., Al-Dhaisat, S., and Barjous, M. (2007). A 48-kyr-long slip rate history for the Jordan Valley segment of the Dead Sea Fault. Earth and Planetary Science Letters, 260(3-4), 394-406. doi: 10.1016/j.epsl.2007.05.049.

Ferry, M., Meghraoui, M., Abou Karaki, N., Al-Taj, M., and Khalil, L. (2011). Episodic Behavior of the Jordan Valley Section of the Dead Sea Fault Inferred from a 14-ka-Long Integrated Catalog of Large EarthquakesEpisodic Behavior of the Jordan Valley Section of the Dead Sea Fault. Bulletin of the Seismological Society of America, 101(1), 39-67. doi: 10.1785/0120100097.

Frankel, A. (1995) 'Mapping seismic hazard in the central and eastern United States. Seismological Research Letters, 66(4), 8-21.'

Gardner JK, Knopoff L (1974) Is the sequence of earthquakes in Southern California, with aftershocks removed, Poissonian? Bull Seismol Soc Am 64(5):1363–1367

Garfunkel, Z. (2014) Lateral Motion and Deformation Along the Dead Sea Transform. In: Garfunkel, Z., Ben-Avraham, Z., Kagan, E. (eds) Dead Sea Transform Fault System: Reviews. Modern Approaches in Solid Earth Sciences, vol 6. Springer, Dordrecht. doi: https://doi.org/10.1007/978-94-017-8872-4_5.

Gerstenberger M, Van Houtte C, Abbott ER, Van Dissen RJ, Kaiser AE, Bradley BA, Nicol A, Rhoades DA, Stirling MW, Thingbaijam KKS, NSHM Team (2020) New Zealand national seismic hazard model framework plan. GNS Science, Lower Hutt (NZ), 25 p (GNS Science report; 2020/38). https:// doi. org/ 10. 21420/ NB8W- GA79

Gomez, F., Meghraoui, M., Darkal, A. N., et al. (2003). Holocene faulting and earthquake recurrence along the Serghaya branch of the Dead Sea fault system in Syria and Lebanon. Geophysical Journal International, 153(3), 658-674. https://doi.org/10.1046/j.1365-246X.2003.01933.x
Gomez, F., Karam, G., Khawlie, M., et al. (2007a). Global Positioning System measurements of strain accumulation and slip transfer through the restraining bend along the Dead Sea fault system in Lebanon. Geophysical Journal International, 168(3), 1021-1028.https://doi.org/10.1111/j.1365-246X.2006.03328.x

Gomez, F., Nemer, T., Tabet, C., et al. (2007b). Strain partitioning of active transpression within the Lebanese restraining bend of the Dead Sea Fault (Lebanon and SW Syria). Geological Society, London, Special Publications, 290(1), 285-303. https://doi.org/10.1144/290.10

Gomez, F., Cochran, W. J., Yassminh, R., et al. (2020). Fragmentation of the Sinai Plate indicated by spatial variation in present-day slip rate along the Dead Sea Fault System. Geophysical Journal International, 221(3), 1913-1940. https://doi.org/10.1093/gji/ggaa095

GRAL (2019). Bulletins of Geophysical Research Arrays of Lebanon, National Center for Geophysics, Bhannes, Lebanon (http://www.cnrs.edu.lb/english/research/researchcenters/national-center-for-geophysics---download, last accessed July 2022)

Grünthal, G., Stromeyer, D., Bosse, C., Cotton, F., and Bindi, D. (2018). The probabilistic seismic hazard assessment of Germany—version 2016, considering the range of epistemic uncertainties and aleatory variability. Bulletin of Earthquake Engineering, 16(10), 4339-4395. doi: https://doi.org/10.1007/s10518-018-0315-y.

Guidoboni, E., A. Comastri, and G. Traina (1994). Catalogue of Ancient Earthquakes in the Mediterranean Area up to the 10th Century,

ING, Bologna, Italy, 504 pp.

Gulia, L. and Gasperini, P. (2021) 'Contamination of Frequency–Magnitude Slope (b-Value) by Quarry Blasts: An Example for Italy', Seismological Research Letters, 92(6), pp. 3538–3551. doi: 10.1785/0220210080.

Gutenberg, B. and Richter, C. F. (1944) 'Frequency of earthquakes in California, Bulletin of the Seismological Society of America, 34(4), pp. 185–188.

Hamiel, Y., Piatibratova, O. and Mizrahi, Y. (2016) 'Creep along the northern Jordan Valley section of the Dead Sea Fault', Geophysical Research Letters, 43(6), pp. 2494–2501. doi: 10.1002/2016GL067913.

Hanks, T. C., and Kanamori, H. (1979) 'A moment magnitude scale, J. Geophys. Res., 84(B5), 2348– 2350'. doi: 10.1029/JB084iB05p02348.

Hiemer, S., Jackson, D. D., Wang, Q., Kagan, Y. Y., Woessner, J., Zechar, J. D., and Wiemer, S. (2013). A stochastic forecast of California earthquakes based on fault slip and smoothed seismicity. Bulletin of the Seismological Society of America, 103(2A), 799-810. doi: 10.1785/0120120168.

Hiemer, S., Woessner, J., Basili, R., Danciu, L., Giardini, D., and Wiemer, S. (2014). A smoothed stochastic earthquake rate model considering seismicity and fault moment release for Europe. Geophysical Journal International, 198(2), 1159-1172. doi: 10.1093/gji/ggu186.

Huijer, C., Harajli, M. and Sadek, S. (2016) 'Re-evaluation and updating of the seismic hazard of Lebanon', Journal of Seismology, 20(1), pp. 233–250. doi: 10.1007/s10950-015-9522-z.

Ishibe, T. and Shimazaki, K. (2012) 'Characteristic earthquake model and seismicity around late quaternary active faults in Japan', Bulletin of the Seismological Society of America, 102(3), pp. 1041–1058. doi: 10.1785/0120100250.

Kagan, Y. Y. (1999) 'Universality of the seismic moment-frequency relation, Pure appl. Geophys., 155, 537–573.'

Kotha, S. R., Weatherill, G., Bindi, D., and Cotton, F. (2020). A regionally-adaptable ground-motion model for shallow crustal earthquakes in Europe. Bulletin of Earthquake Engineering, 18(9), 4091-4125. doi: 10.1007/s10518-020-00869-1.

Lanzano, G., Sgobba, S., Luzi, L. et al. (2019). The pan-European Engineering Strong Motion (ESM) flatfile: compilation criteria and data statistics. Bull Earthquake Eng 17, 561–582. https://doi.org/10.1007/s10518-018-0480-z

Le Béon, M., Klinger, Y., Mériaux, A.-S., Al-Qaryouti, M., Finkel, R. C., Mayyas, O., and Tapponnier, P. (2012) 'Quaternary morphotectonic mapping of the Wadi Araba and implications for the tectonic activity of the southern Dead Sea fault, Tectonics, 31, TC5003'. doi: 10.1029/2012TC003112.

Le Béon M, Tseng YC, Klinger Y, et al. (2018) High-resolution stratigraphy and multiple luminescence dating techniques to reveal the paleoseismic history of the central Dead Sea fault (Yammouneh fault, Lebanon). Tectonophysics 738:1–15. https://doi.org/10.1016/j.tecto.2018.04.009

Lefevre, M., Klinger, Y., Al-Qaryouti, M., Le Béon, M., and Moumani, K. (2018). Slip deficit and temporal clustering along the Dead Sea fault from paleoseismological investigations. Scientific reports, 8(1), 1-9. doi: 10.1038/s41598-018-22627-9.

Leonard, M. (2014) 'Self-consistent earthquake fault-scaling relations: Update and extension to stable continental strike-slip faults', Bulletin of the Seismological Society of America, 104(6), pp. 2953–2965. doi: 10.1785/0120140087.

Marco, S., Klinger, Y. (2014) 'Review of On-Fault Palaeoseismic Studies Along the Dead Sea Fault. In: Garfunkel, Z., Ben-Avraham, Z., Kagan, E. (eds) Dead Sea Transform Fault System: Reviews. Modern Approaches in Solid Earth Sciences, vol 6. Springer, Dordrecht.' doi: https://doi.org/10.1007/978-94-017-8872-4_7.

Marco, S., Rockwell, T. K., Heimann, A., Frieslander, U., and Agnon, A. (2005). Late Holocene activity of the Dead Sea Transform revealed in 3D palaeoseismic trenches on the Jordan Gorge segment. Earth and Planetary Science Letters, 234(1-2), 189-205.

Mariniere, J., Beauval, C., Nocquet, J. M., Chlieh, M., and Yepes, H. (2021). Earthquake recurrence model for the Colombia–Ecuador subduction zone constrained from seismic and geodetic data, implication for PSHA. Bulletin of the Seismological Society of America, 111(3), 1508-1528. doi: https://doi.org/10.1785/0120200338.

Meghraoui, M., Gomez, F., Sbeinati, R., et al. (2003). Evidence for 830 years of seismic quiescence from palaeoseismology, archaeoseismology and historical seismicity along the Dead Sea fault in Syria. Earth and Planetary Science Letters, 210(1-2), 35-52. https://doi.org/10.1016/S0012-821X(03)00144-4

Meletti C, Marzocchi W, D'Amico V, Lanzano G, Luzi L, Martinelli F, Pace B, Rovida A, Taroni M, Visini F (2021) The new Italian

seismic hazard model (MPS19). Ann Geophys 64(1):SE112. https:// doi. org/ 110. 4401/ ag- 8579

Nemer, T. and Meghraoui, M. (2006) 'Evidence of coseismic ruptures along the Roum fault (Lebanon): a possible source for the AD 1837 earthquake', Journal of Structural Geology, 28(8), pp. 1483–1495. doi: 10.1016/j.jsg.2006.03.038.

Nemer, T., Meghraoui, M. and Khair, K. (2008) 'The Rachaya-Serghaya fault system (Lebanon): Evidence of coseismic ruptures, and the AD 1759 earthquake sequence', Journal of Geophysical Research: Solid Earth, 113(5), pp. 1–12. doi: 10.1029/2007JB005090.

Pagani M, Monelli D, Weatherill G, et al. (2014) OpenQuake-engine: an open hazard (and risk) software for the global earthquake model. Seismol Res Lett 85:692–702.
https://doi.org/10.1785/0220130087

Petersen, M.D., Moschetti, M.P., Powers, P.M., et al. (2014), Documentation for the 2014 update of the United States national seismic hazard maps: U.S. Geological Survey Open-File Report 2014–1091, 243 p., https://pubs.usgs.gov/of/2014/1091/pdf/ofr2014-1091.pdf

Poggi, V., Garcia-Peláez, J., Styron, R., Pagani, M., and Gee, R. (2020). A probabilistic seismic hazard model for North Africa. Bulletin of Earthquake Engineering, 18(7), 2917-2951. doi: 10.1007/s10518-020-00820-4.

Reasenberg, P. (1985) 'Second-order moment of central California seismicity, 1969–1982', Journal of Geophysical Research: Solid Earth, 90(B7), pp. 5479–5495. doi: https://doi.org/10.1029/JB090iB07p05479.

Rong, Y., Xu, X., Cheng, J., Chen, G., Magistrale, H., and Shen, Z. K. (2020). A probabilistic seismic hazard model for Mainland China. Earthquake Spectra, 36(1_suppl), 181-209. doi: 10.1177/8755293020910754.

Sbeinati, M. R., Meghraoui, M., Suleyman, G., et al. (2010). Timing of earthquake ruptures at the Al Harif Roman aqueduct (Dead Sea fault, Syria) from archaeoseismology and paleoseismology. Ancient earthquakes, 243. https://doi.org/10.1130/2010.2471(20)

Şeşetyan, K., Danciu, L., Demircioğlu Tümsa, M.B. et al. (2018). The 2014 seismic hazard model of the Middle East: overview and results. Bull Earthquake Eng 16, 3535–3566. https://doi.org/10.1007/s10518-018-0346-4

Stirling, M., McVerry, G., Gerstenberger, M., et al. (2012) National seismic hazard model for New Zealand: 2010 update. Bull Seismol Soc Am 102(4):1514–1542. https://doi.org/10.1785/0120110170

Stirling, M. and Gerstenberger, M. (2018) 'Applicability of the Gutenberg-Richter relation for major active faults in New Zealand', Bulletin of the Seismological Society of America, 108(2), pp. 718–728. doi: 10.1785/0120160257.

Stock, C., and Smith, E. G. (2002). Comparison of seismicity models generated by different kernel estimations. Bulletin of the Seismological Society of America, 92(3), 913-922.

Wang, Y. J., Chan, C. H., Lee, Y. T., Ma, K. F., Shyu, J. B. H., Rau, R. J., and Cheng, C. T. (2016). Probabilistic seismic hazard assessment for Taiwan. Terr. Atmos. Ocean. Sci., 27(3), 325-340.

Wechsler, N., Rockwell, T. K., Klinger, Y., Štěpančíková, P., Kanari, M., Marco, S., and Agnon, A. (2014). A paleoseismic record of earthquakes for the Dead Sea transform fault between the first and seventh centuries CE: Nonperiodic behavior of a plate boundary fault. Bulletin of the Seismological Society of America, 104(3), 1329-1347.doi: 10.1785/0120130304.

Wechsler, N., Rockwell, T. K., and Klinger, Y. (2018). Variable slip-rate and slip-per-event on a plate boundary fault: The Dead Sea fault in northern Israel. Tectonophysics, 722, 210-226. doi: 10.1016/j.tecto.2017.10.017.

Wells, D. L. and Coppersmith, K. J. (1994) 'New empirical relationships among magnitude, rupture length, rupture width, rupture area, and surface displacement', Bulletin - Seismological Society of America, 84(4), pp. 974–1002.

Wiemer, S. Danciu, L., Edwards, B., Marti, M., Fah, D., Hiemer, S., Wosssner, J., Cauzzi, C., Kastli, P., Kremer, K. (2016) 'Seismic Hazard Model 2015 for Switzerland (SUIhaz2015)', Swiss Seismological Service (SED) at ETH Zurich, p. 164. doi: 10.12686/a2.

Woessner, J., Laurentiu, D., Giardini, D. et al. (2015). The 2013 European Seismic Hazard Model: key components and results. Bull Earthquake Eng 13, 3553–3596. https://doi.org/10.1007/s10518-015-9795-1

Youngs, R. R. and Coppersmith, K. J. (1985) 'Implications of fault slip rates and earthquake recurrence models to probabilistic seismic hazard estimates', International Journal of Rock Mechanics and Mining Sciences & Geomechanics Abstracts, 23(4), p. 125. doi: 10.1016/0148-9062(86)90651-0.

Zhao, J. X., J. Zhang, A. Asano, et al. (2006). Attenuation relations of strong ground motion in Japan using site classification based on predominant period, Bull. Seismol. Soc. Am. 96, no. 3, 898–913.https://doi.org/10.1785/0120050122

3.3 Electronic Supplement

A fault-based probabilistic seismic hazard model for Lebanon, controlling parameters and hazard levels

S. El Kadri[(1,2)] , C. Beauval[(1)], M. Brax[(2)], PY. Bard[(1)], M. Vergnolle[(3)] and Y. Klinger[(4)]

[(1)] Univ. Grenoble Alpes, Univ. Savoie Mont Blanc, CNRS, IRD, Univ. Gustave Eiffel, ISTerre, 38000 Grenoble, France

[(2)] National Council for Scientific Research, CNRS-L, P.O. Box 16-5432, Achrafyeh, 1100-2040 Beirut, Lebanon

[(3)] Université Côte d'Azur, IRD, CNRS, Observatoire de la Côte d'Azur Géoazur, Geoazur, Valbonne, France

[(4)] Université de Paris Cité, Institut de physique du globe de Paris, CNRS, 1, rue Jussieu, Paris, France

Corresponding author: sarah.el-kadri@univ-grenoble-alpes.fr

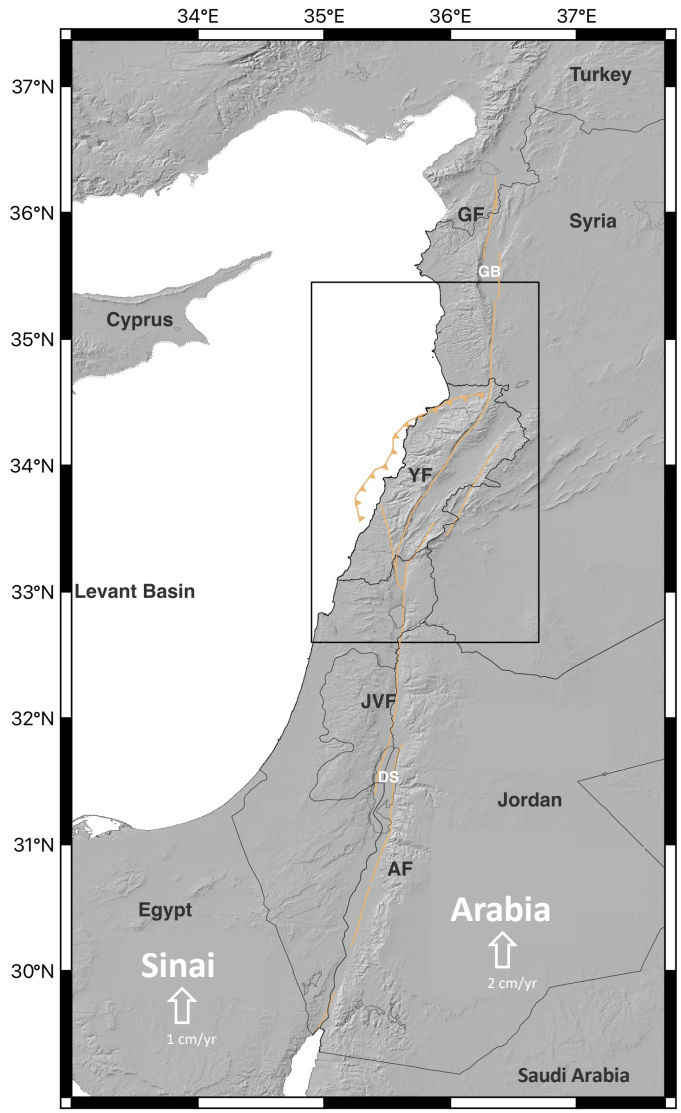

Fig. S1 Levant transform plate boundary. Pull-apart basins: GB, Ghab Basin; DS: Dead Sea. Major fault segments: GF, Ghab fault (that includes Missyaf segment); YF, Yammouneh fault; JVF, Jordan Valley fault; AF, Araba fault. Black frame corresponds to Fig. 1 in the paper

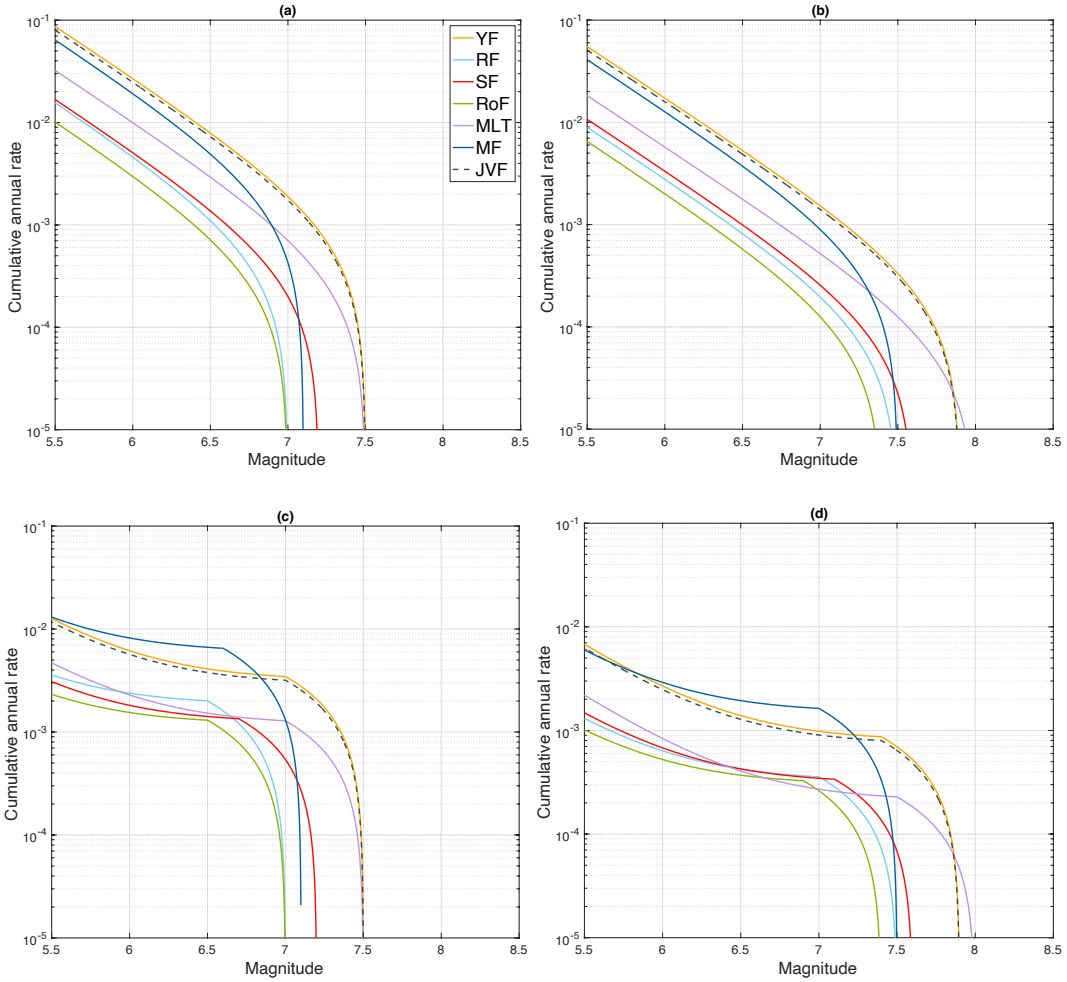

Fig. S2 Moment-balanced frequency-magnitude distributions for the 7 faults included in the model, same legend as Fig. 6 in the paper, the only difference is that the annual occurrence rates have not been normalized per km^2. For example, considering the exponential model and the upper bound of M_{max} (b), the model forecasts a magnitude larger or equal to 6 on average every ~500 years on the Roum fault, every ~170 years on the Mount Lebanon Fault, or every ~60 years on the Yammouneh Fault. Considering the Youngs and Coppersmith model and the upper bound of M_{max} (d), these average recurrence times increase to respectively ~2000 years (Roum), ~1250 years (MLT), and ~350 years (Yammouneh).

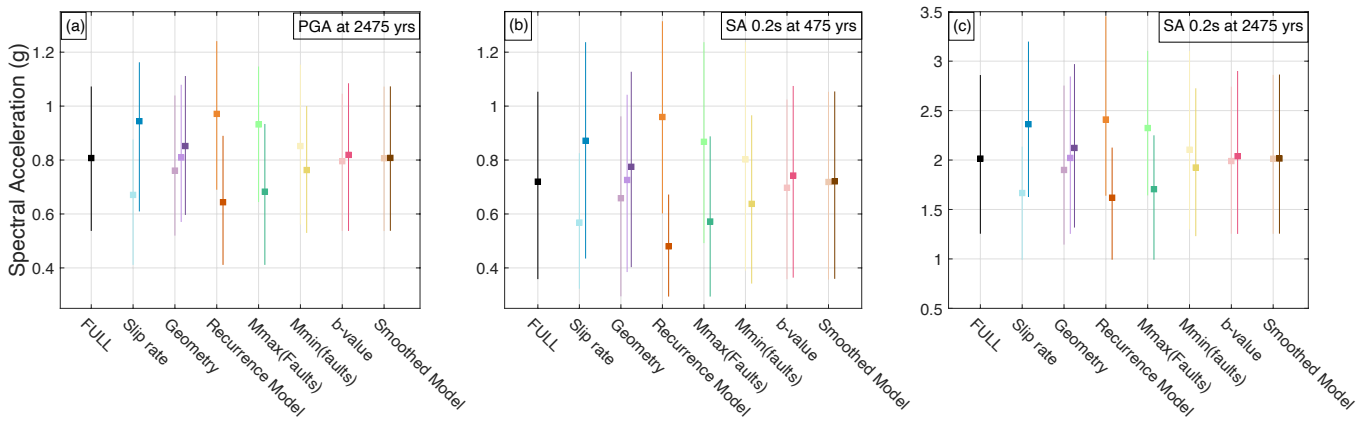

Fig. S3 Distribution of hazard levels in Beirut, for a) PGA at 2475 years return period, b) spectral period 0.2s at 475 years, c) spectral period 0.2 at 2475 years return period. See legend of Fig. 7

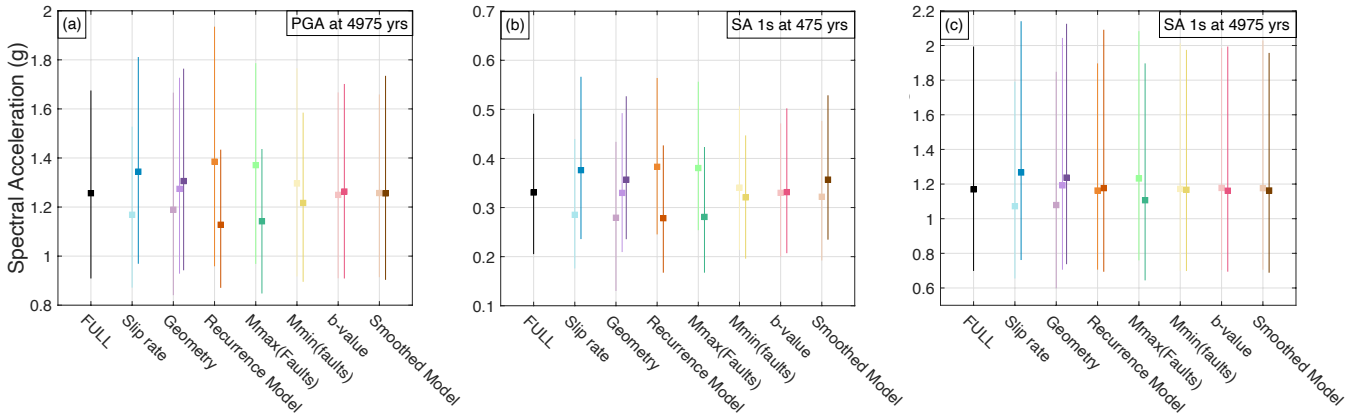

Fig. S4 Distribution of hazard levels in Zahle, for a) PGA at 4975 years return period, b) spectral period 1 at 475 years, c) spectral period 1 at 4975 years return period. See legend of Fig. 7

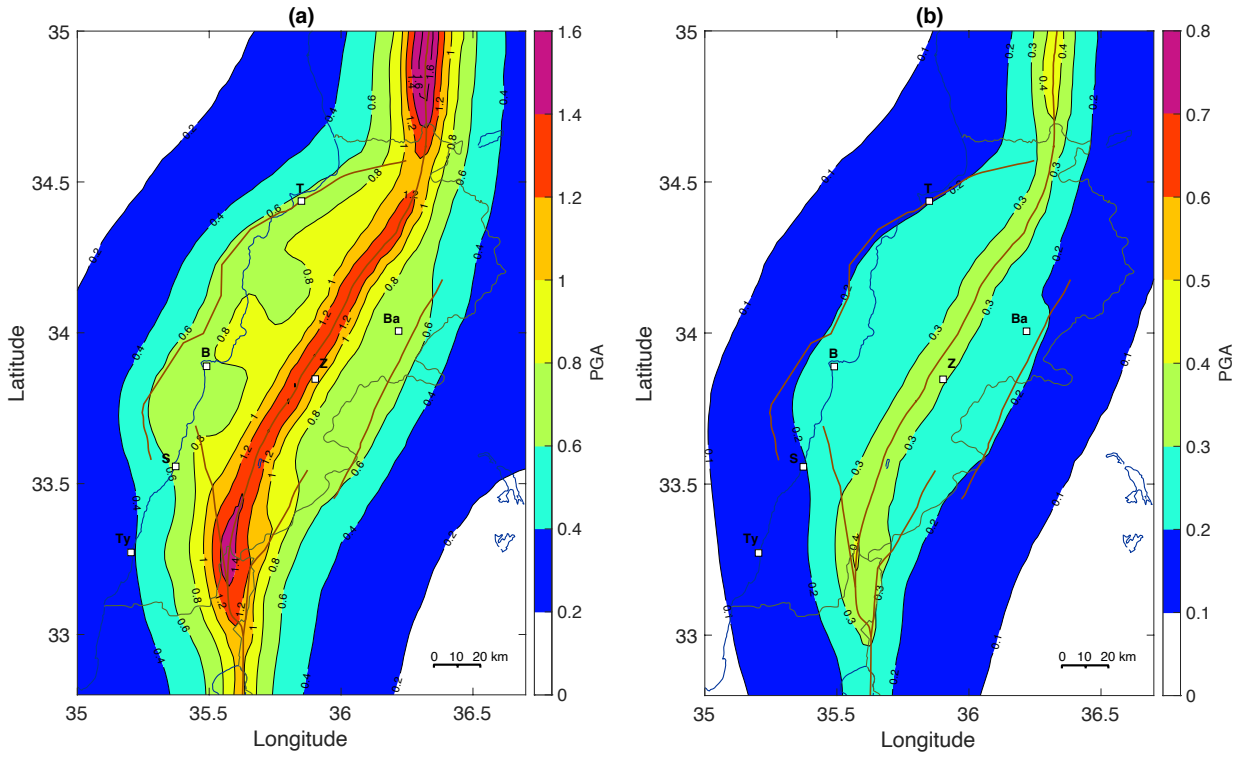

Fig. S5 Mean seismic hazard maps for spectral periods 0.2s (a) and 1s (b), at 475 years, generic rock site condition with V_{S30} 760 m/s. The source model logic tree is combined with the three alternative ground-motion models. Average values and percentiles are inferred from a distribution of 144 hazard values (equally weighted), as in Fig. 13

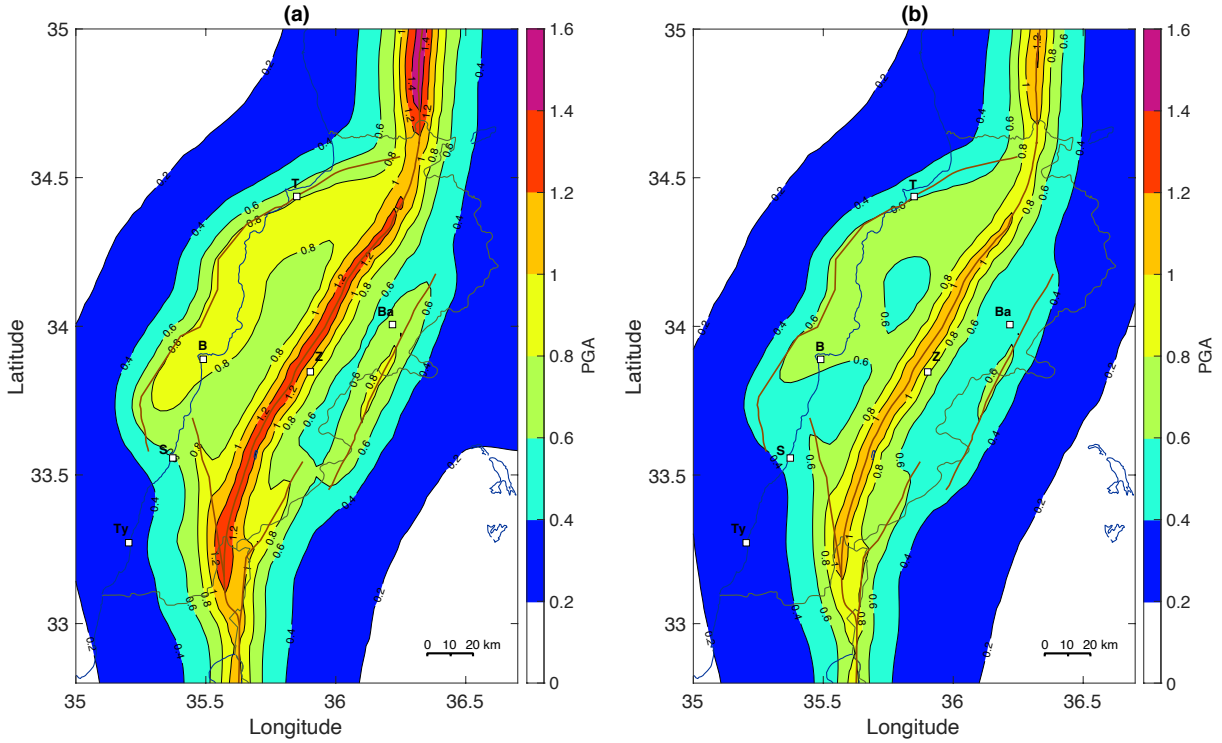

Fig. S6 Mean seismic hazard maps at 2475 years, for the PGA (a) and spectral period 1s (b), generic rock site condition with V_{S30} 760 m/s. The source model logic tree is combined with the three alternative ground-motion models. Average values and percentiles are inferred from a distribution of 144 hazard values (equally weighted), as in Fig. 13

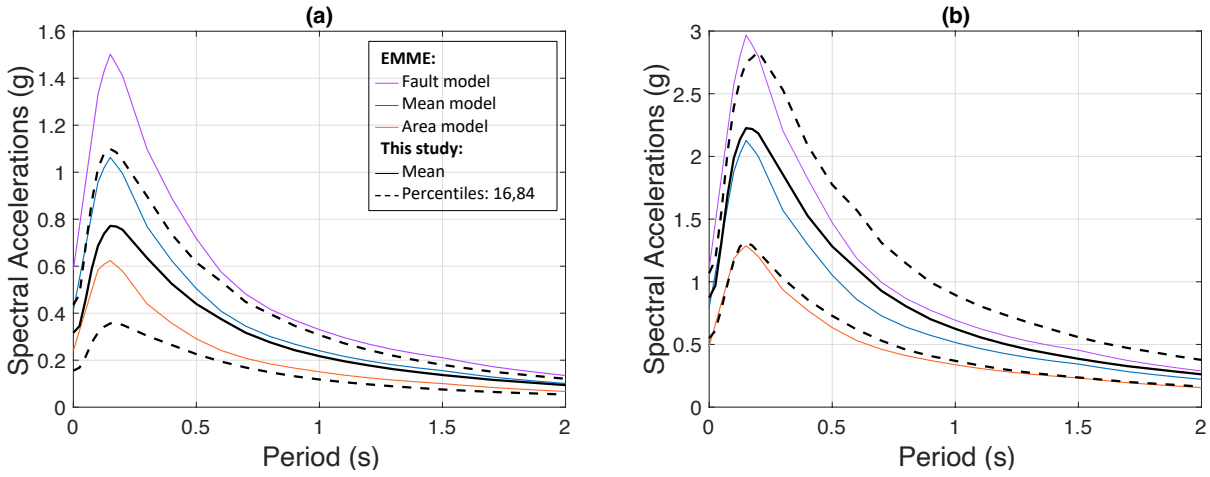

Fig. S7 Distribution of uniform hazard spectra for Beirut, generic rock site condition with V_{S30} 760 m/s. Black: This study results as in Fig. 12 in the paper. EMME results (Danciu et al., 2017), purple: smoothed seismicity and fault model; orange: area model; blue: mean model with 40% weight on the fault model and 60% on the area model. a) at 475 years return period; b) at 2475 years return period. EMME results have been obtained by running the EMME source model and ground-motion model xml input files with OpenQuake

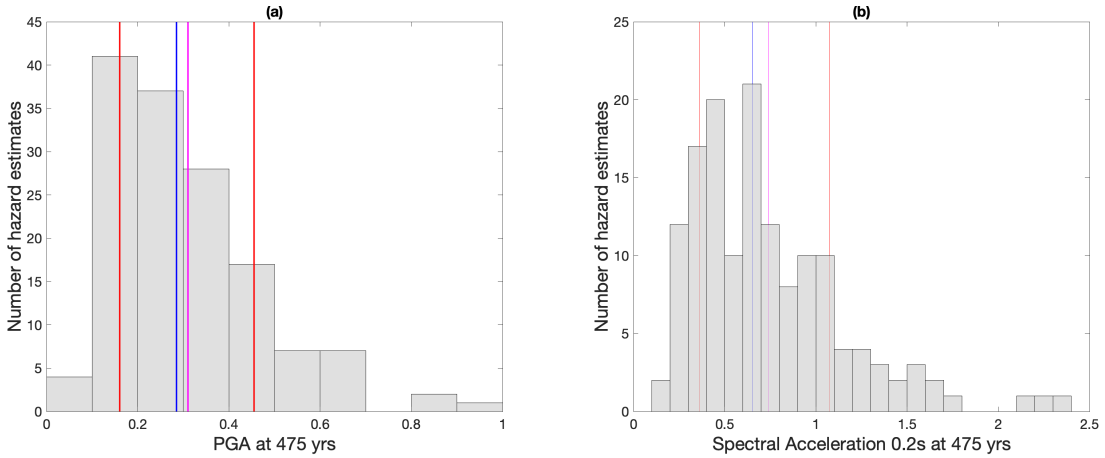

Fig. S8 Distribution of the hazard estimates obtained at Beirut city for a return period of 475 years, in magenta: mean value, in blue: median value and in red: 16th and 84th percentiles. a) for the PGA; b) for the spectral period 0.2s. The final logic tree, with only the parameters influencing the most the hazard, is explored (as in Fig. 14 and Section 6)

Table S1. Acceleration levels obtained for different spectral periods in the cities of Beirut, Zahle, Saida and Tripoli, at 475 and 2475 years return period (corresponding uniform hazard spectra in Fig. 14)

Periods (s)	Beirut		Zahle		Saida		Tripoli	
	475	**2475**	**475**	**2475**	**475**	**2475**	**475**	**2475**
PGA	0.31	0.82	0.44	0.98	0.24	0.53	0.26	0.72
0.025	0.34	0.91	0.48	1.08	0.26	0.58	0.28	0.79
0.05	0.45	1.23	0.64	1.45	0.35	0.78	0.37	1.06
0.1	0.68	1.86	0.96	2.23	0.52	1.19	0.55	1.59
0.2	0.74	2.04	1.08	2.52	0.58	1.33	0.61	1.8
0.5	0.43	1.23	0.65	1.64	0.35	0.81	0.37	1.13
1	0.22	0.62	0.32	0.86	0.18	0.43	0.19	0.58
2	0.09	0.26	0.14	0.37	0.08	0.2	0.08	0.25

The existing model may introduce several limitations in PSHA due to the model's limited capacity to account for the possibility of earthquakes rupturing segments from different faults, as observed in various regions worldwide (1931 MS 7.9 earthquake along the Fuyun fault, Xinjiang, China, Klinger et al. 2011; 2002 Mw 7.9 Earthquake along the Denali fault in Alaska, Eberhart-Phillips et al. 2003; 1957 MW 8.1, Gobi-Altai earquake, Southern Mongolia, Kurtz et al. 2018). Notably, in Lebanon, no prior studies have made an attempt to relax the segmentation and model the occurrence of interconnected fault ruptures. For this reason, one of the methodologies that allows multi-fault rupture, SHERIFS (Seismic Hazard and Earthquake Rate In Fault Systems, Chartier et al. 2017) was tested for the LFS. More discussion can be found in chapter 4.

CHAPTER 4

Implementation of an interconnected fault systems in PSHA, example on the Levant fault

Contents

List of Figures

List of Tables

Implementation of an interconnected fault system in PSHA, example on the Levant fault

Sarah El Kadri, Céline Beauval, Marlène Brax, Yann Klinger

Article in preparation

4.1 Introduction

The Levant Fault System (LFS) stretches approximately along a distance of 1200 km, starting from the Red Sea in the south and reaching the East Anatolian fault system in the north, at the southern fault-rupture termination of the largest of the 6 February 2023 (Mw7.8) Kharamanmaraş earthquakes (Zhang et al. 2023). The system is characterized by left-lateral strike-slip kinematics. Inside the Lebanese restraining bend, the fault splays into several branches: the Roum and Mount Lebanon faults to the west and the Rachaya and Serghaya faults to the east. The main strand accommodates most of the deformation with a mean slip rate ranging between 4 to 5 mm/yr (Gomez et al. 2007a, b; Le Béon et al. 2012; Wechsler et al. 2018), whereas on the secondary faults its estimate is around 1 to 2 mm/yr (Gomez et al. 2003; Nemer and Meghraoui 2006, 2008).

Probabilistic Seismic Hazard Assessment (PSHA) is required to produce seismic hazard maps essential for establishing building codes (e.g. Meletti et al. 2021 in Italy; Danciu et al. 2021 within Europe; Sesetyan et al. 2018 in Turkey or Wang et al. 2016 in Taiwan). In most of the source models built for PSHA, the conceptual representation of faults is rigid. Faults are made of a number of tectonically defined segments. Within a predefined fault, ruptures can occur on individual segments or on a combination of segments. Ruptures that would involve segments from different predefined faults are not included in the model. The source models thus most often include only a subset of the future ruptures that may occur on the fault system.

El Kadri et al. (2023) published a seismic hazard model for Lebanon that integrates in a classical way the major faults in the area. Each fault, as classically described in the literature, has been included separately in the model (Fig. 4.1a). Earthquake frequencies on these faults are inferred from a moment-balanced recurrence model relying on the geologic or geodetic mean slip rate evaluated for the fault. The source model also includes off-fault seismicity, through a catalog-based smoothed-seismicity model. El Kadri et al. (2023) follow the state-of-the-art standards in PSHA and deliver for each site within Lebanon a distribution for the seismic hazard levels, that may be useful for future updates of the Lebanese building code. In the present manuscript, the aim is to understand how the source model and eventually the hazard levels may change if considering an interconnected fault system.

A number of earthquakes that occurred in the last 30 years have shown that in some cases, ruptures can jump over some geometrical discontinuities, previously considered as major obstacles, such as gaps or steps in the fault system, and result in larger magnitudes than anticipated (e.g. 2001 M_W 7.8 Kunlunshan earthquake in China, Fu et al. 2005; 2010 M_W 7.2 El Mayor-Cucapah earthquake in Mexico, Fletcher et al. 2014; 2016 Kaikōura M_W7.8 in New Zealand, Klinger et al. 2018). Therefore,
several research groups have been developing along the years methods to take into account these complex ruptures into hazard models. In 2014, the Working Group on California Earthquake Probabilities (WGCEP) developed a new inversion-based methodology called the “Grand inversion”,

to relax fault segmentation and incorporate multifault ruptures in the Uniform California Rupture Forecast (UCERF, Field et al., 2014; Page et al., 2014). Subsequently, Chartier et al. (2017) implemented the SHERIFS (Seismic Hazard and Earthquake Rate In Fault Systems) algorithm, a method to relax fault segmentation which is simpler than the UCERF framework and that requires less input parameters. A couple of other algorithms were developed, such as the integer-programming optimization by Geist and ten Brink 2021, or the SUNFiSH approach by Visini et al. (2020). In the present work, we focus on the algorithm SHERIFS that has been applied on a several crustal fault systems (in the Corinth rift in Greece, Chartier et al. 2017; along the North Anatolian Fault, Chartier et al. 2019, in the Eastern Betics in southeastern Spain, Gomez Novell et al. 2020; in the southeastern Tibetan Plateau Cheng et al. 2021, as well as in central Italy, Moratto et al. 2023).

Our aim is to develop interconnected fault models for the Levant fault system, applying the algorithm SHERIFS, and estimate the associated hazard levels. We consider the faults described in El Kadri et al. (2023), but rather than including them separately in the hazard calculation, we first go down to the segment scale and then evaluate all possible segment combinations, including the maximum magnitude earthquake. We show how the iterative process in the SHERIFS algorithm builds the set of ruptures and associated occurrence rates, distributing the moment budget over the ruptures with the constraint that earthquake frequencies follow a given distribution at the scale of the system. We show that in order for the maximum magnitude earthquake to be realistic, the connectivity of the fault system must be fully released. Besides, we compare the earthquake forecast with the available observations at a regional scale (earthquake catalog), and at a local scale (paleoseismic trenches). At last, we compare the hazard levels obtained with values based on the El Kadri et al. (2023) more traditional implementation of faults.

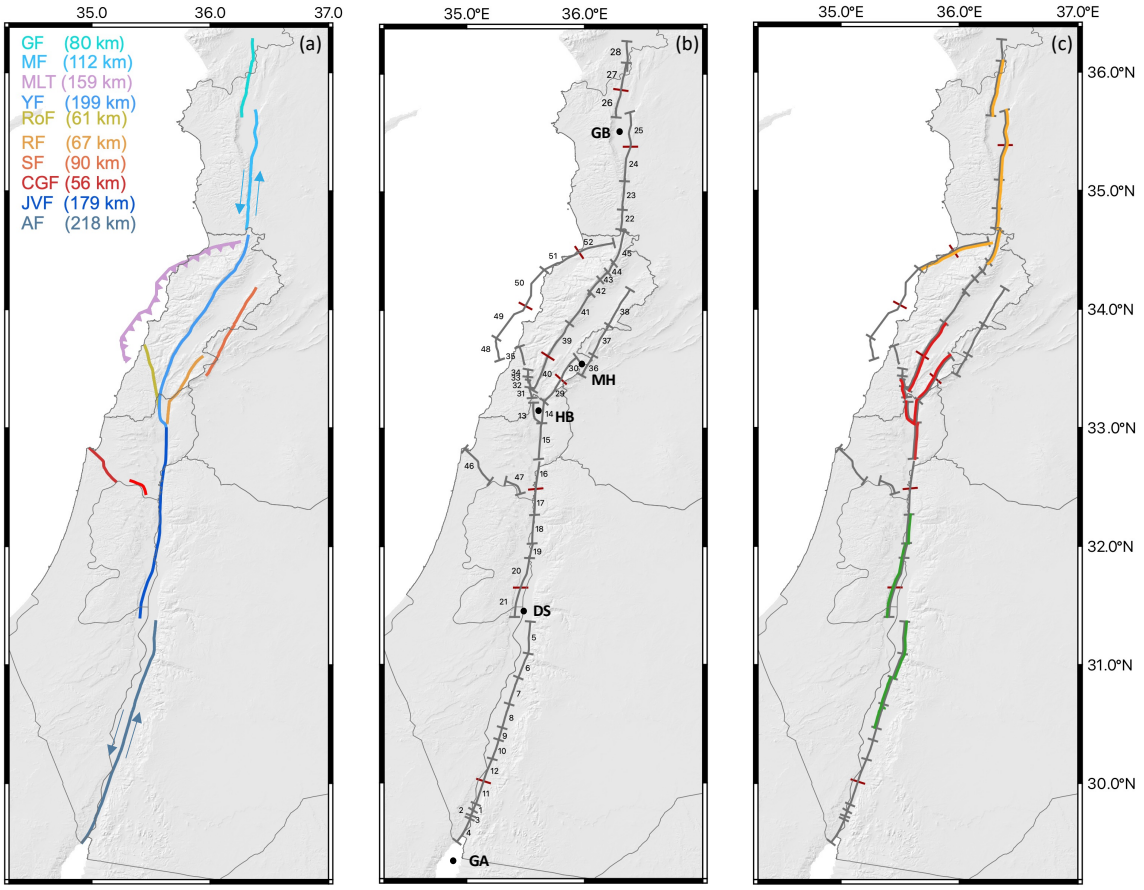

Fig. 4. 1 The Levant Fault System. (a) Classical fault representation, the fault system is made of 10 main faults, GF: Ghab Fault, MF: Missyaf, MLT: Mount Lebanon thrust, YF: Yammouneh, RoF: Roum, RF: Rachaya, SF: Serghaya, CGF: Carmel-Gilboa, JVF: Jordan Valley, AF: Araba. (b) Detailed segmentation of the fault system, gray dash: tectonic discontinuities, red dash: arbitrary subdivision of segments required for homogenizing segments' length; GB: Ghab basin, MH: Mount Hermon, HB: Hula Basin, DS: Dead Sea, GA: Gulf of Aqaba. (c) Examples of possible complex ruptures that are not accounted for in the classical implementation of faults.

4.2 Seismic potential of the Levant Fault System

The Levant Fault System (LFS) has been the source of multiple significant earthquakes (Fig. 4.2), resulting in extensive destruction, surface faulting, and alterations to the landscape. Lefevre et al. 2018 has summarized the known history of major earthquakes along the southern fault section, between the Gulf of Aqaba and the Galilée Sea, over the last ~1200 years, based on tectonic, paleoseismic and historical data. Brax et al. (2019) analyzed the literature on historical events in-between latitudes 31.5° and 35.5° (approximately from the Dead Sea to the Ghab pull-apart). A number of destructive earthquakes occurred, including the 363 earthquake (M~7.3) that may have ruptured segments on the Araba fault or both on the Araba and Jordan Valley fault (Ferry et al. 2011; Klinger et al. 2015), the 551 event (M~7.3) that probably ruptured the off-shore Mount Lebanon thrust (Elias et al. 2007), or the 1202 earthquake (M~7.6) that ruptured the Yammouneh fault (Daeron et al. 2007) as well a segment of the Jordan Valley fault (Jordan Gorge fault, Wechsler et al. 2018). North of Lebanon, strong earthquakes have also occurred along the Missyaf and Ghab faults, in particular the 1170 and 1157 earthquake sequences.

To build the set of ruptures that may occur within the fault system, we need to move away from the usual fault scheme of the LFS (Fig. 4.1a) and go down to the scale of the tectonic segment. Several authors have studied the fault system and analyzed the segmentation. To the south, based on the location of major jogs and bends, Lefevre et al. (2018) proposed to split the Araba and Jordan Valley faults into 9 segments, up to the Hula Basin segment south of Lebanon. Ferry et al. 2011 studied the Jordan Valley section, based on satellite photographs, field investigations, and offset measurements. They mapped in detail the fault trace in-between the Dead Sea and the Galilée Sea and identified six 15 to 30km-long right-stepping segments limited by transpressive relay zones. Within the Lebanese restraining bend, the Roum, Rachaya and Serghaya fault traces were mapped by Nemer and Meghraoui et al. (2006, 2008) through detailed field work and aerial-photograph analysis. Meghraoui (2015) discussed the LFS fault trace and its segmentation, from the Gulf of Aqaba to the Amik Basin in Turkey, identifying the geometrical complexities (large step overs, pull-apart basins, restraining bends) that may act as barriers to earthquake ruptures.

We have built on these works and analyzed satellite images along the whole fault system, looking for distinct steps and bends to define the segments. We have carefully analyzed the geological features and incorporated the relevant local paleoseismic information. The LFS mostly exhibits a transtensional nature, characterized by the significant pull-apart structures of the Gulf of Aqaba, the Dead Sea (~14km) and the Ghab pull-apart (~11km). Another major discontinuity is the compressional jog that forms the Mount Hermon and separates the Rachaya and Serghaya faults. At a smaller scale, the LFS comprises linear strands characterized by left-lateral offsets of drainage systems, right-stepping ruptures exhibiting pressure and shutter ridges, and minor pull-apart basins distributed along its length (such as the Qalaat Al Hosn pull-apart basin at the Syrian/Lebanese border, the Hula Basin, or the Yammouneh basin along the Yammouneh fault). We have also detected some push-up zones indicating an uplift along the Araba Fault. In total, we obtained 43 segments with lengths varying from 5 to 39 km (Fig. 4.1b, Table 4.1). Future ruptures may break along one or several segments. A large earthquake could start in the Dead Sea pull apart, and propagate both to the south on the Araba fault and to the north on the Jordan Valley fault (Fig. 4.1c, green). A large earthquake could also involve in the same event a rupture on the main strand as well as ruptures on the Roum and Sergaya faults (Fig. 4.1c, red). Fault models in PSHA need to include this complexity in order to be more realistic. The level of connectivity in the system will depend on which discontinuities are considered firm barriers for earthquake ruptures.

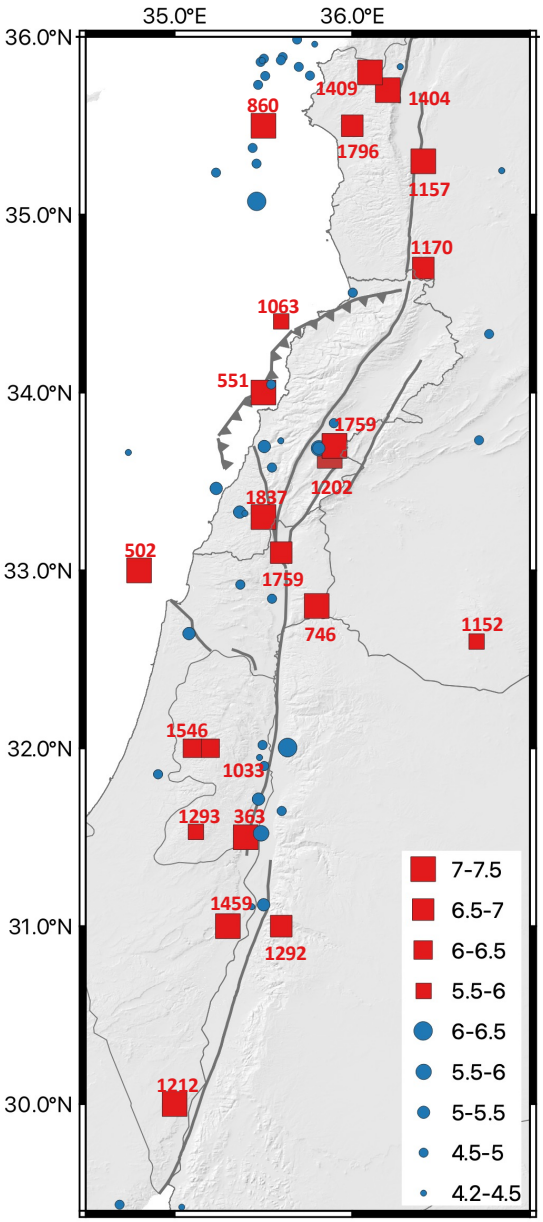

Fig. 4. 2 Seismic activity in the region of the Levant Fault System, historical events (squares, Brax et al. 2019), instrumental events from global datasets (circles, integration of ISC-GEM, GCMT and ISC-reviewed catalogs).

4.3 SHERIFS algorithm applied to the Levant Fault System

4.3.1 The iterative process in SHERIFS: key steps

The algorithm requires as inputs the set of fault segments' traces with dip angles and widths of the segments, the slip rates associated to every segment, an estimate for the maximum magnitude of the system, an assumption on the shape of the magnitude-frequency distribution of the system (here the Gutenberg-Richter with a b-value equal to 1), and the selection of a scaling relationship (here Leonard 2014). If necessary, the algorithm subdivides the longest segments into shorter segments to homogenize segments' length. Nine tectonic segments are arbitrarily subdivided into two segments, resulting in 52 segments in total within the fault system (Fig. 4.1b). Table 1 summarizes the characteristics of the

segments considered. References for the mean slip rates can be found in El Kadri et al. (2023). A set of rules governs the combination of adjacent individual segments into longer ruptures, i.e. the maximum azimuth between two adjacent segments (here 75°) and the maximum distance between segments that a rupture may jump.

At the beginning of the process, based on the scaling relationship, the algorithm establishes all possible ruptures (segment combinations), for magnitudes ranging from a minimum magnitude to the maximum magnitude of the system. The total slip rate budget in the system is estimated by considering the slip rates of all segments. This slip rate budget is spent iteratively in a loop, always the same value/increment (Fig. 4.3). At each iteration, the increment of slip rate must be associated to a given magnitude and a given rupture hosting this magnitude earthquake. The magnitude is randomly picked in a pdf with probability increasing with magnitude, representing the contribution of the magnitude bin in terms of moment rate within the system (assuming a Gutenberg-Richter MFD, Fig. 4.3, see also Chartier et al. 2017). The rupture is selected randomly from the pool of ruptures with areas matching the magnitude, according to the scaling relationship. At last, the moment rate spent in the iteration is calculated using the total area of the rupture (Fig. 4.3), and the seismic rate is eventually obtained dividing this moment rate by the moment associated to the magnitude. Our tests show that the increment in slip rate must be very small to ensure a homogeneous distribution of the slip rate budget over the whole system (here we use 0.0001 mm/year).

To begin with, the maximum jump for ruptures is set to 10km, implying that ruptures cannot pass the major discontinuities (Ghab and Dead sea pull-aparts, Mount Hermon jog). We consider a maximum magnitude of 7.5, corresponding to the maximum magnitude earthquake in the classical implementation of faults (maximum length ~200km and width 18km, Fig. 1a, mean magnitude inferred from the area, Leonard 2014). With a slip rate increment of 0.0001 mm/yr, in total ~1.6 million iterations are required to spend the system slip rate budget. Figure 4 illustrates the process at three different steps. The first column displays, for the iteration n°1500, the moment rate spent (Fig. 4.4a, in blue), earthquake frequencies (Fig. 4.4b, in blue), and the fault segments that still have some budget to spend at this stage (in grey). The second column provides an update at iteration n°685300. At that time, the rates of magnitudes 7.3-7.5 are fixed and the Gutenberg-Richter MFD of the system is anchored to these upper magnitude rates (black straight line). A number of segments have spent entirely their budget (Fig. 4.4f, in orange), others still have some budget (in grey) but no more large magnitudes (7.3-7.5) can be produced. In further iterations, magnitudes are further picked and the remaining slip rate budget is spent until the seismic rates predicted by the system MFD are reached (Fig. 4.4h). Any slip rate increment that would lead to higher rates than predicted (for the magnitude bin picked) are discarded and considered aseismic slip. The third column displays the final iteration: the total moment rate spent (in green), the final magnitude-frequency distribution (in green), and the segments that have either consumed entirely their budget (orange and green), or have part of their slip budget converted into aseismic deformation (dark grey). Overall, in this calculation, 9% of the slip rate budget was not spent into earthquakes. Chartier et al. (2017) call the unused slip rate ‘non-mainshock slip’. We prefer to simply state that part of the slip rate is not used and is considered aseismic slip. This aseismic slip may correspond to creep or afterslip of major events.

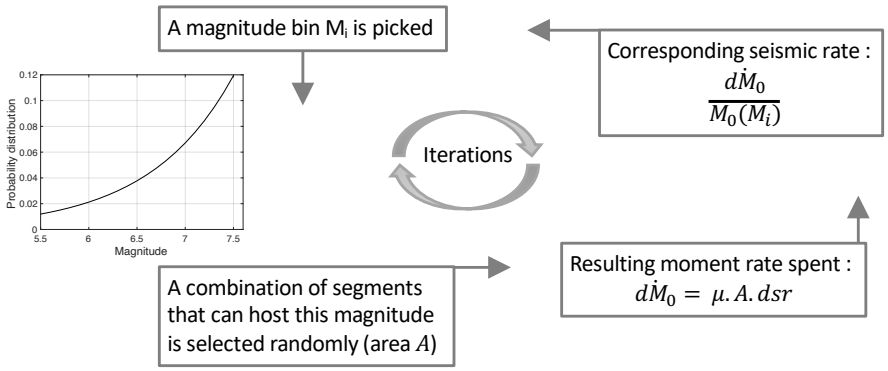

Fig. 4. 3 Scheme illustrating the main steps of the iterative process, in which "dsr" represents the incremental slip rate

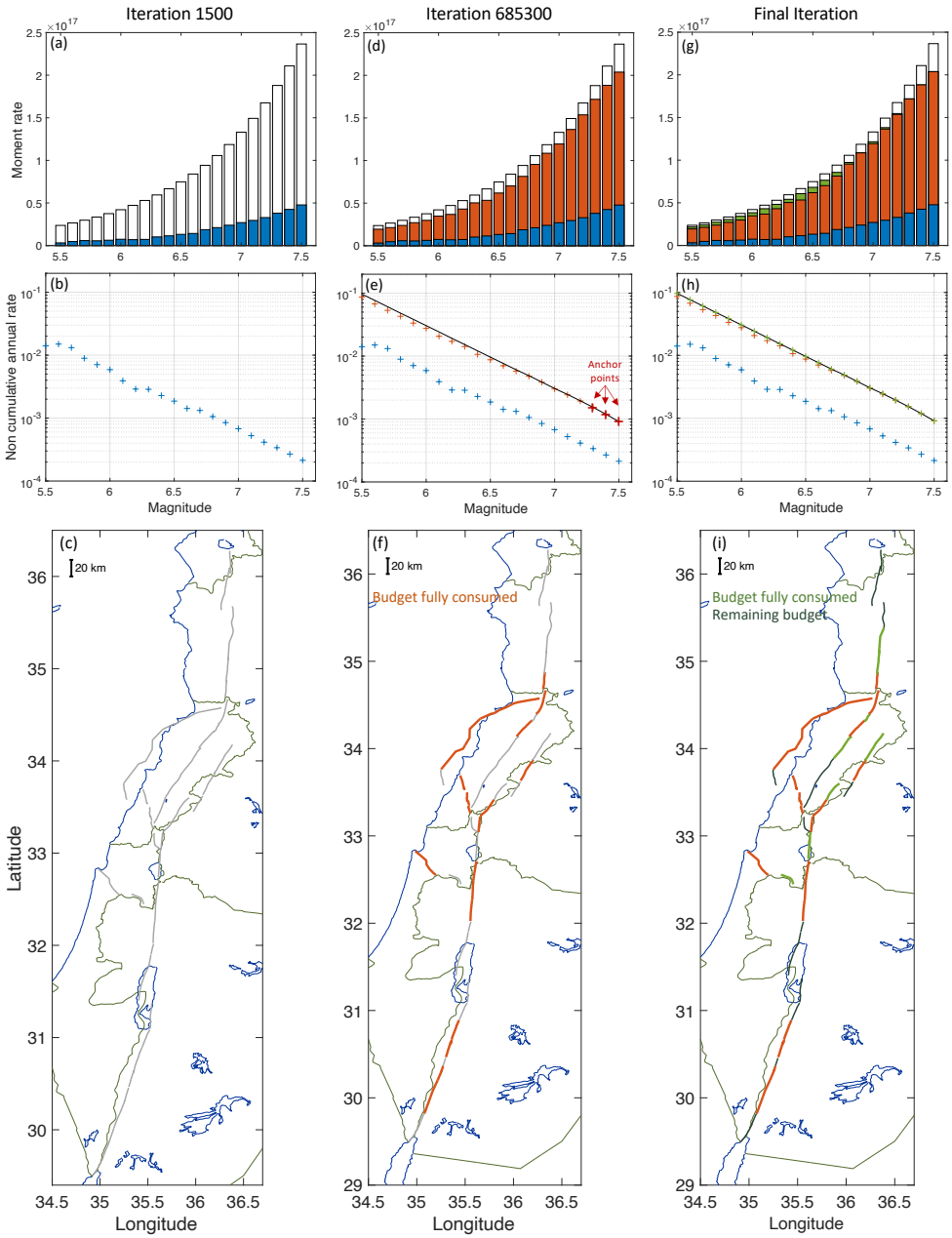

Fig. 4. 4 Illustration of the iterative process in SHERIFS, at 2 intermediary steps (1st and 2nd column) and final step (3rd column). First row: distribution of the moment rate per magnitude bin (black: total budget available, in color: budget spent). Second row: seismic rates spent over the fault system. Third row: fault segments that still have some budget to spent (gray), segments with slip budget exhausted (red, then green), segments with part of the slip budget converted into aseismic slip (black, end of the process). See the text.

4.3.2 Results: distribution of magnitude rates in space, stability

SHERIFS' algorithm delivers a set of segments and segments' combinations (ruptures) with associated magnitudes and occurrence rates. In PSHA calculation, for a given site, ground-motion exceedance rates are calculated by multiplying rates of ruptures with the probabilities that the ruptures produce an exceedance of the ground-motion levels at the site. The exact distribution in magnitude and in space of the ruptures control the hazard levels. Figure 4.5 (1st row) displays for every segment the annual rates of occurrence obtained for its participation to magnitude M_w5.5, M_w6.5 and M_w7.5 ruptures. Rates are normalized by the segment area in order to be comparable throughout the system. The distribution obtained is not homogeneous in space and may vary strongly depending on the segment. For magnitudes 5.5 and 6.5, the highest rates are obtained on the southern half of the Yammouneh fault, southern segments of Jordan Valley fault, and northern and southern segments of Araba Fault. These segments are those participating the least to the large ruptures (Fig. 4.4f); part of their slip rate is not spent into earthquakes (Fig. 4.4i). For magnitudes 7.5, we observe the opposite, the highest rates are obtained along the JVF north of the Dead Sea, and along the northern segments of the Yammouneh fault.

To understand the distribution of seismic rates in space, we analyze the set of possible ruptures defined at the beginning of the process. Figure 4.5 (2nd row) displays the number of ruptures a given segment may be involved in. As expected, every segment can host a magnitude M_w5.5 rupture. The segments involved in the largest number of M_w6.5 ruptures are those connecting the Yammouneh and Jordan Valley faults; whereas the segments involved in the largest number of M_w7.5 ruptures belong to the Yammouneh fault and Jordan Valley Fault north of the Dead Sea. During the iterative process, owing to the shape of the pdf used (Fig. 4.3), SHERIFS algorithm is more likely to pick magnitudes in the upper magnitude range than in the lower magnitude range. The segments most frequently selected to host the largest magnitudes have their slip rates exhausted more rapidly (Fig. 4.4f). Once the rates in the upper magnitude range are fixed, the remaining budget is distributed over moderate magnitudes on the segments that still have some slip budget.

Besides, we have checked the stability of the results. Rates for three different runs are displayed in the Electronic Supplement (Fig. 4.S1). For the three magnitudes considered, the participation rates are approximately stable from one run to the other. We also checked the stability of the resulting system MFD, and found that the obtained seismic rates are identical over the magnitude range from one run to the other. Segments responsible for limiting the rates in the upper magnitude range (anchor points of the system MFD), i.e. segments with the slip rate budget exhausted that prevent further maximum magnitudes to be sampled, are very similar from one run to the other.

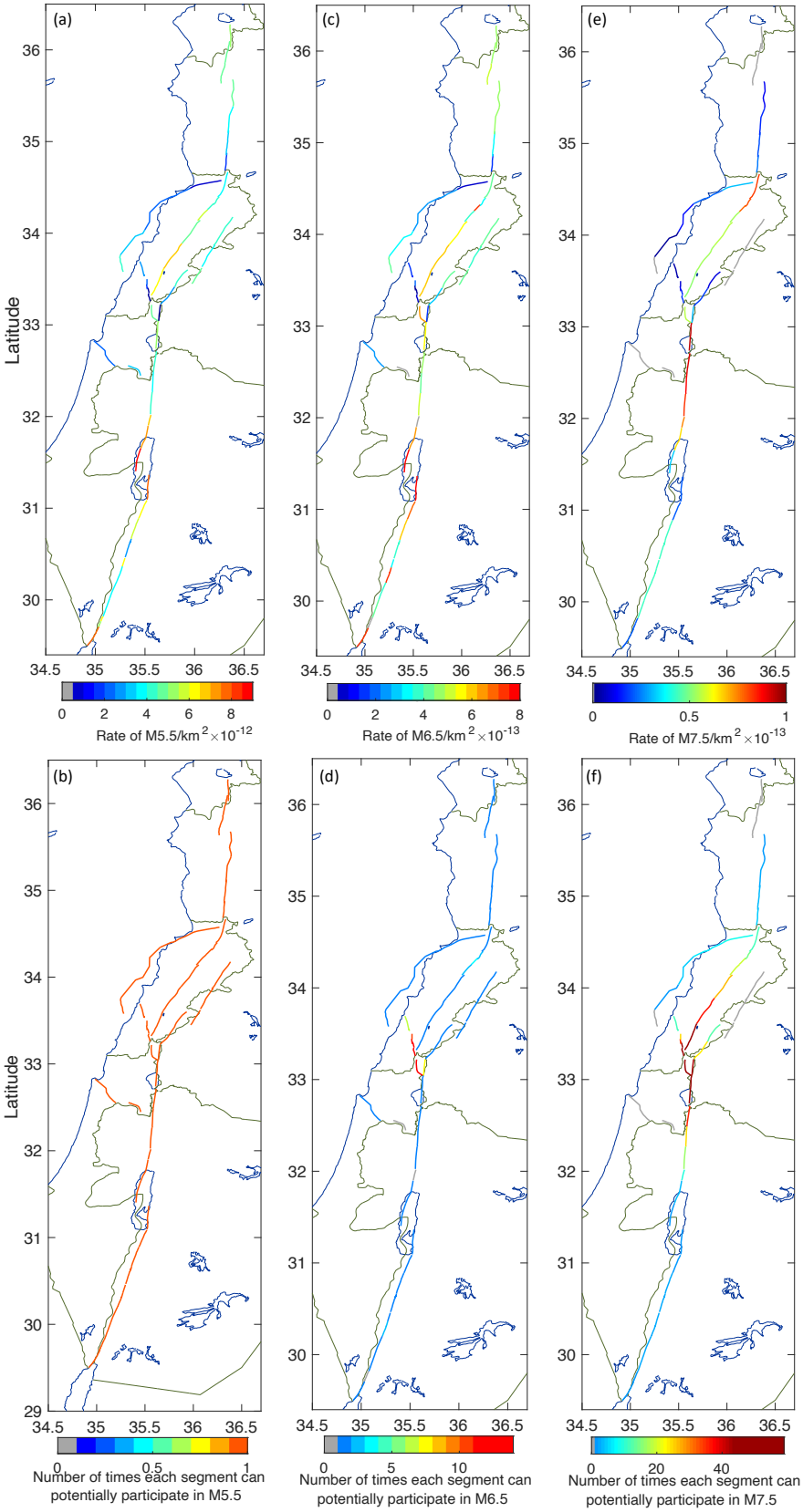

Fig. 4. 5 First row: obtained fault model in terms of annual rates of earthquakes (for magnitudes M_w 5.5, 6.5, and 7.5), normalized per square kilometer. Second row: number of times a fault segment can potentially participate in a given magnitude rupture (M_w 5.5, 6.5, and 7.5).

4.3.3 Magnitude-frequency distribution obtained at the scale of the fault system: comparison with the classical implementation of faults

The moment budget available for earthquakes relies on the slip rates of fault segments and is the same as in the classical implementation of faults. However, the distribution of this moment budget over earthquake ruptures is not similar, as the interconnected fault model includes much more rupture possibilities between segments than the classical implementation. In the interconnected fault model (with maximum jump 10km), ruptures can combine e.g. segments from both the Missyaf and Yammouneh faults, or segments from both the Missyaf and Mount Lebanon fault. Also, segments that belong to the Roum fault can break with segments on Yammouneh, Rachaya, and/or the Jordan Valley faults. In figure 4.6a, we compare the fault-system MFD obtained with SHERIFs with the fault-system MFD that corresponds to the classical implementation (i.e. the sum of individual Gutenberg-Richter MFDs). We observe that earthquake rates are slightly lower in the moderate magnitude range, and slightly higher in the upper magnitude range close to M_{max}. This can be understood by highlighting the segments that can participate e.g. in the maximum magnitude M_{max} (Figs. 4.6b and 4.6c, in blue): more segments can participate in a magnitude 7.5 in the interconnected model than in the classical (rigid) implementation. There is more moment rate available for the upper-magnitude range, as the model is moment-balanced there is slightly less moment rate available for earthquakes in the moderate-magnitude range.

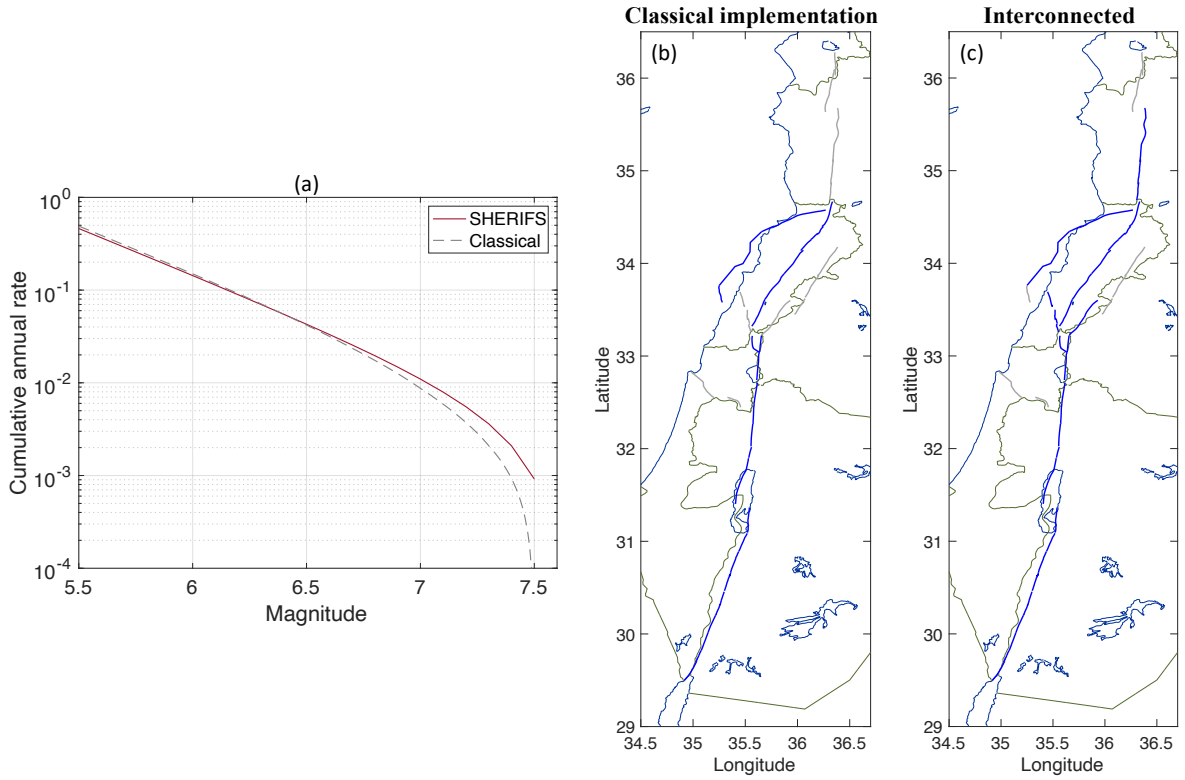

Fig. 4. 6 Comparison between the classical implementation of faults, and the interconnected model. (a) Magnitude-frequency distributions at the scale of the whole fault system (assumption M_{max} 7.5), both distributions are moment-balanced using the fault slip rate. (b) Classical and (c) Interconnected fault model, segments that can participate in a maximum magnitude M_{max} 7.5 rupture (more segments can participate in the interconnected fault model, so more moment rate is available for the upper magnitude range).

4.3.4 Increasing the maximum magnitude and the connectivity of the fault system

Reviewing other major strike-slip fault systems worldwide and the largest earthquakes they have generated (e.g. the M_W 7.8 1906 earthquake on the San Andreas, Yeats et al. 1997; 2002 M_W 7.9 Earthquake along the Denali fault in Alaska, Eberhart-Phillips et al. 2003 ; or the recent 2023 M_W 7.8 earthquake on the East Anatolian fault), we believe magnitudes larger than 7.5 could occur along the Levant fault system. We must build source models that include the possibility for larger events, therefore we test two other potential maximum magnitudes: 7.9 and 8.1.

We run the algorithm with the same parametrization except for the maximum magnitude that is set to 7.9. Results are displayed in Figures 4.7 and 4.8. Using a maximum jump of 10km, segments on the Araba, Serghaya and Ghab faults cannot participate in the maximum magnitude 7.9 earthquake (Fig. 4.7a). Many segments are left with more than 50% of the slip rate not used (Fig. 4.7b). Seventy-two percent of the total slip rate is not spent into earthquakes (Fig. 4.7b). Such a high percentage of aseismic slip is not realistic.

We increase the maximum jump for ruptures from 10 to 12 km and run a new calculation. Ruptures can now jump over the Ghab pull-apart as well as over Mount Hermon jog. All segments can now participate in a magnitude 7.9 earthquake, except for segments on the Araba fault (Fig. 4.7c). Only a few end-fault segments are left with more than half of the slip rate not used. Thirty percent of the total slip rate is not spent into earthquakes (Fig. 4.7d). At last, we increase the maximum jump to 18km, the fault system is now entirely connected, ruptures can jump over all major discontinuities. All segments can participate in the maximum magnitude earthquake (Fig. 4.7e) and 14% of the total slip rate is considered aseismic slip. This is the order of magnitude expected for aseismic deformation on the LFS.

Figure 4.8 displays the distribution of the moment rate spent in earthquakes as well as the fault-system MFDs obtained for the three different runs. Applying a maximum jump of 10km leads to a model that is not realistic, only a small part of the moment rate budget is spent into earthquakes (Fig. 4.8a, light grey histogram). The reason lies in the way the SHERIFs algorithm fixes the rates at the level of the fault system. Low rates in the upper magnitude range (light grey crosses in Fig. 4.8b) lead to low rates over the whole magnitude range, as these anchor points control the fault-system MFD (dash-dotted line). Increasing the connectivity, more segments can participate in the largest magnitude earthquakes, the rates of the anchor points increase, and the rates of the system MFD increase (Fig. 4.8b).

To our knowledge, no earthquake of magnitude larger or equal to 8.0 has occurred on a strike-slip fault system, but we cannot exclude such a scenario. Figure 4.9 displays the system MFD obtained increasing the maximum magnitude to 8.1, considering a fully connected fault system. A magnitude 8.1 requires a rupture length of approximately 730 km, i.e. more than half of the entire fault system must break. As expected, for a given moment budget, increasing the maximum magnitude leads to a decrease of the rates in the moderate magnitude range. Nearly a quarter of the total slip rate budget is not converted into earthquakes and thus considered aseismic deformation, which is not realistic. The size of the fault system prevents such a large magnitude from being tested. The fault system would need to be extended to the North and to the South.

At last, we also perform a run assuming that the magnitude-frequency at the scale of the system follows a characteristic shape (Youngs and Coppersmith, 1985). Assuming a magnitude 7.9 and a fully

interconnected fault model, a quarter of the total slip rate budget is not converted into earthquakes (Table 4.2), which is not realistic.

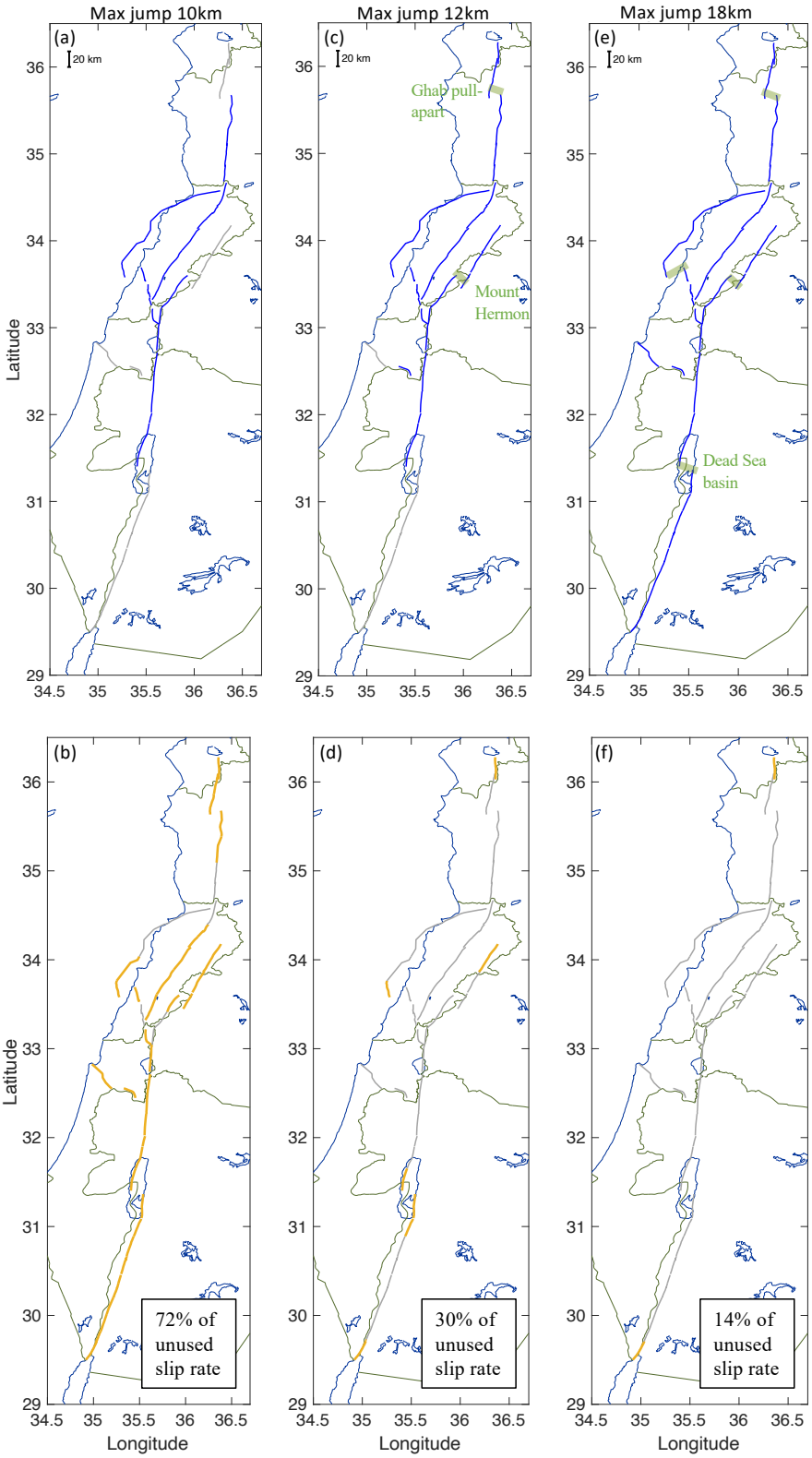

Fig. 4. 7 Increasing the connectivity in a fault model with M_{max} 7.9, 1st column: jump up to 10km allowed, 2nd column: jump up to 12km, 3rd column: up to 18km (entirely connected). 1st row: segments that can participate in

a M_{max} 7.9 rupture (blue). 2nd row: segments that are left with more than 50% of unused slip rate (orange), the percentage of the slip rate not used at the scale of the fault system is indicated.

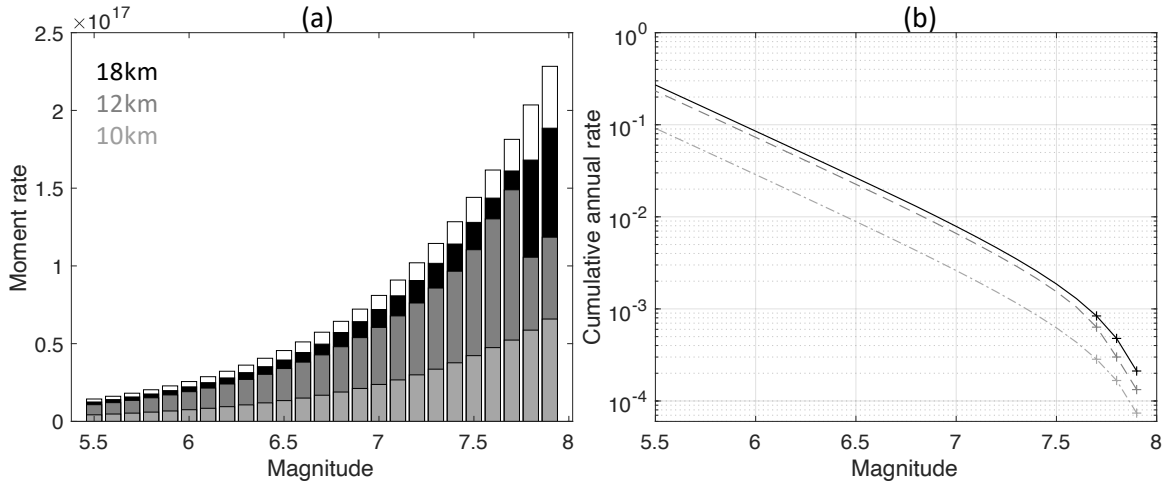

Fig. 4. 8 Increasing the connectivity in a fault model with M_{max} 7.9, (a) distribution of the moment rate spent per magnitude bin and (b) magnitude-frequency distribution, at the scale of the fault system. Light gray: ruptures cannot jump more than 10km, gray: maximum jump for ruptures of 12km, they can jump over Mount Hermon and Ghab pull apart, black: maximum jump 18km, system is entirely connected. See Figure 4.7.

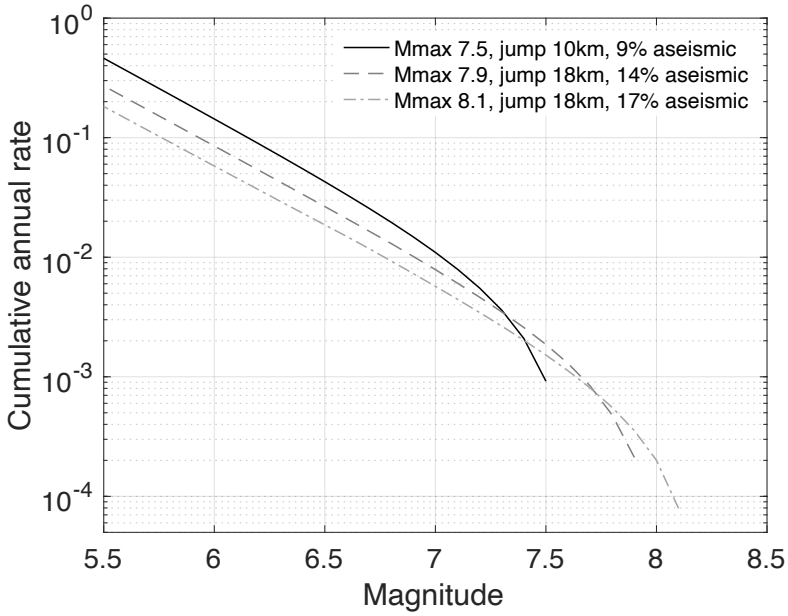

Fig. 4. 9 Magnitude-frequency distribution obtained at the scale of the fault system, for three runs of SHERIFs: assumption M_{max} 7.5 and the major discontinuities act as barriers; assumption M_{max} 7.9 and the system is entirely connected; assumption M_{max} 8.1 and the system is entirely connected. All models are moment-balanced, but the percentage of slip rate that has not been used varies with the model (respectively 9, 14 and 24%). Our preferred model is the fully interconnected model with M_{max} 7.9 (see the text).

4.4 Comparison of the modeled rates with the available observations

4.4.1 Observed earthquake rates

The fault model built for PSHA is made of earthquake ruptures and associated annual rates of occurrence. Slip rate estimates have been used to infer earthquake frequencies, with the constraint that the magnitude-frequency distribution at the scale of the fault system follows a Gutenberg-Richter shape. Both the earthquake catalog of the region and the available paleoseismic data were not used to derive the model; these observations can be compared with the earthquake forecast.

Brax et al. (2019) published a catalog of historical earthquakes for the Levant Fault System within latitudes 31.5° and 35.5°. For every earthquake, the authors reviewed the literature associated to evaluate the information available from written historical accounts, as well as the macroseismic intensity dataset produced and its interpretation in terms of epicentral location and magnitude estimate. Earthquakes whose existence is attested but for which it was not possible to find a solution relying on clearly identified historical sources and intensity data have not been included (see Electronic Supplement 2 in Brax et al. 2019). For the period before 1900, we used the Brax et al. (2019) catalog, supplemented south of latitude 31.5° and north of latitude 35.5° by earthquake solutions from the EMME earthquake catalog (Zare et al. 2014), resulting in 23 earthquakes in total (Fig. 4.2).

We used global instrumental catalogs over the period 1900 to 2020, within the spatial window 34.5° to 37° in longitude, and 29° to 37° in latitude. We consider the ISC-GEM (International Seismological Center - Global Earthquake Model, Version 10, Storchak et al., 2015), GCMT (Global Centroid Moment Tensors, Ekström et al., 2012) and ISC (International Seismological Centre, Storchak et al. 2020) catalogs. From the ISC catalog we include only earthquakes with an ISC location and a magnitude M_S or m_b (that we convert into M_w applying equations from Lolli et al. 2014). We obtain 35 instrumental events with magnitude M_w ranging from 4.1 to 6.1 (Fig. 4.2).

Figure 4.10 displays the earthquake catalog obtained, magnitudes versus event times. Destructive earthquakes with magnitudes larger or equal to ~7 occurred regularly in the last 2000 years in the region. The last one struck southern Lebanon in 1837. Magnitudes of historical earthquakes bear large uncertainties (see e.g. Brax et al. 2019), nonetheless such high magnitude levels are confirmed by the analysis of numerous paleoseismic trenches available along the LFS. The distribution of magnitudes 5.5-6.5 over time is particularly irregular and suspicious. In the instrumental period starting in 1900, the largest earthquake in the spatial window is the M_w6.1 1927 Jericho earthquake (magnitude from the ISC-GEM catalog). The instrumental catalog also bears significant uncertainties as only global data have been included. Brax et al. (2019) did include earthquake solutions from local networks in the region. Different magnitude types are provided and to merge the datasets, several conversions between magnitudes are required (see Electronic Supplement 3 in Brax et al. 2019). The dispersion observed in the magnitude comparisons is in most cases huge. In the present work, we prefer to use only global catalogs and ensure a certain level of homogeneity in the magnitude estimate, at the cost of a higher magnitude of completeness.

Earthquake rates are estimated considering a magnitude interval of 0.5. The analysis of the catalog in terms of completeness is not straightforward. Based on cumulative number of events versus time plots, we evaluate that magnitudes larger or equal to 7.1 are complete since 363, magnitudes larger or equal to 6.6 since 1170, magnitudes larger or equal to 4.6 since 1981 and larger or equal to 4.1 since 2003

(Fig. 4.10). For the magnitude interval 5.6-6.6, there are too few earthquakes to estimate the period of completeness. We estimate periods from the ISC-GEM catalog at the global scale: magnitudes larger or equal to 5.6 are considered complete since 1965, and magnitudes larger or equal to 6.1 since 1925. Additionally, to get a rough estimation of the impact of magnitude uncertainties on rates, we generated 100 synthetic catalogs from the original one, sampling the magnitude of each earthquake from a gaussian distribution centered on the original magnitude with a standard deviation of 0.3 for historical events and 0.1 for instrumental events.

Cumulative annual rates are displayed in Fig. 4.11, superimposed to the magnitude-frequency distribution obtained with SHERIFS for the fault system (M_{max} 7.5 and 7.9). The MFDs are consistent with the rates of magnitudes 7.1+ estimated over ~1660 years, but in the magnitude range 4-6 these MFDs forecast more earthquakes than observed in the last ~40 years. Is this 40-years period representative of long-term seismic activity? Is it possible that a few centuries ago, at the time sequences of large earthquakes struck the Levant Fault system, the background seismic activity could have been much higher than in the recent past? Are we missing the long aftershock sequences that these large earthquakes may have produced (e.g. Stevens & Avouac 2017)? We don't know. The MFD corresponding to the characteristic Youngs and Coppersmith (1985) model is also displayed. THe model forecasts lower rats for magnitudes M6+ than observed.

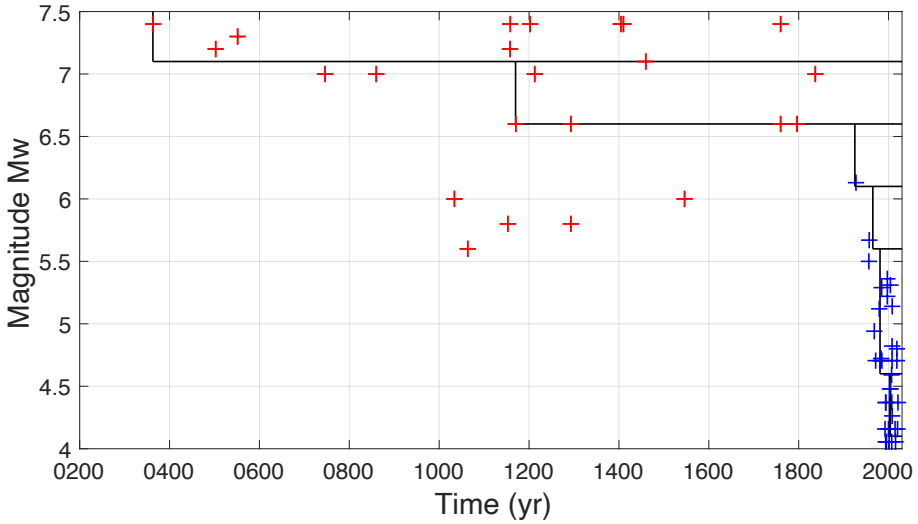

Fig. 4. 10 Earthquake catalog used (same as in Fig. 4.2), magnitude versus time, historical (red) and instrumental (blue) events. Periods of completeness per magnitude interval are indicated (straight lines).

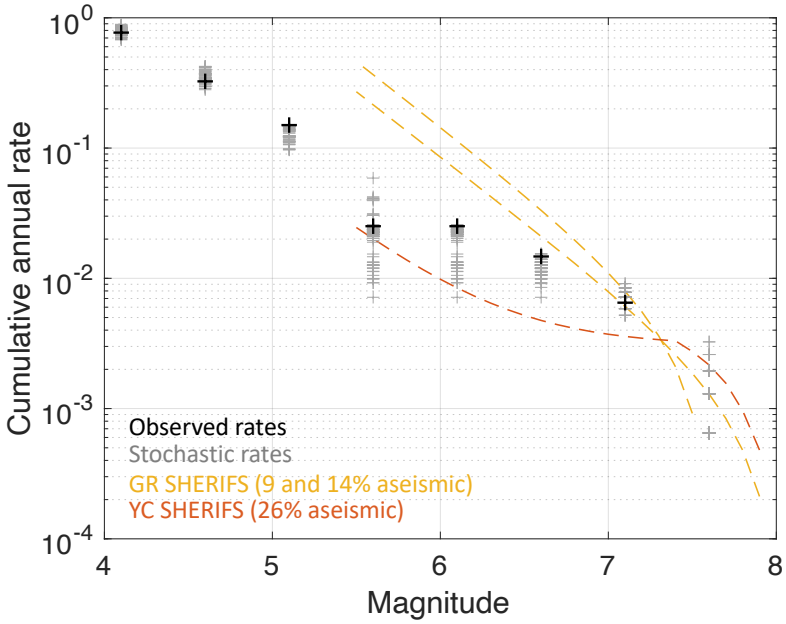

Fig. 4. 11 Magnitude-frequency distributions compared to observed rates. Black crosses: observed annual rates estimated from the earthquake catalog considered, grey crosses: annual rate from synthetic earthquake catalogs obtained by sampling magnitudes in PDFs centered on the original magnitude (standard deviation 0.1 for the instrumental catalog and 0.3 for the historical one). Orange dashed curves: fault system MFDs, assumption Gutenberg-Richter, model with M_{max} 7.5, model with M_{max} 7.9. Red dashed curves: fault system MFDs, assumption Youngs and Coppersmith, model with M_{max} 7.5, model with M_{max} 7.9.

4.4.2 Earthquake rates from paleoseismic trenches

Paleoseismic studies provide information on earthquakes that occurred before historical times and thus extend the observation time window available. Several trenches have been excavated along the Levant Fault System, they deliver key data on the size and on the timing of the earthquakes that ruptured the fault at the trench site. From the fault model built with SHERIFS, we can extract the set of ruptures passing through the trench site, with associated rates, and compare this forecast with the paleoseismic data.

Daeron et al. (2007) analyzed in detail a trench across the Yammouneh basin. They identified ten to thirteen paleo-events extending back more than ~12kyr, and they were able to provide reliable age bounds for half of these events. In the historical period, the most recent event is the 1202 destructive earthquake (magnitude estimate 7–7.8, according to Ambraseys and Jackson, 1998). They also identified in the trench an earthquake that occurred between 30 B.C. and A.D. 469. We consider these two earthquakes in the historical period, as well as 6 prehistoric earthquakes that occurred in a period extending over ~5600 years starting ~12kyrs ago (record considered complete over the period, events S7 to S12, see Daeron et al. 2007). Estimates for six inter-event times are thus available. To take into account the uncertainty on the age of these events, we generate synthetic earthquake sequences by sampling the age of each event within a pdf defined by the minimum and maximum age bounds (following Ellsworth et al. 1999). For each synthetic sequence, a mean interevent time is calculated. We use 1000 synthetic sequences to produce a distribution for the mean interevent time. In Fig. 4.12, this distribution is superimposed to the rates of ruptures passing through the site, as forecasted by our preferred fault model (M_{max} 7.9, entirely connected). We also display the rates forecasted by the fault

model relying on a Youngs and Coppersmith MFD. Daeron et al. (2007) evaluated a characteristic coseismic slip of about 5.5m, which according to Leonard (2014) corresponds to an interval of magnitude 7.4 to 8 (extension of the grey box on the graphic). The paleoseismic rates are compatible with the earthquake forecasts.

Lefevre et al. (2018) conducted trench excavation at the Taybeh site, situated on the Wadi Araba fault revealing evidence of twelve surface-rupturing earthquakes spanning the last 8000 years. To build the distribution of mean inter-event times, we use the most complete and reliable part of this earthquake sequence, i.e. the period starting with the 31 BC earthquake that includes 5 earthquakes. To provide a magnitude range for these earthquakes, we use the rupture lengths estimated in Lefevre et al. (2018) by correlating the information at different trench sites (grey box in Figure 4.12). Our fault model forecasts less earthquakes than "observed" at the Taybeh site. More work is required to evaluate rates of earthquakes from the different trenches available along the southern part of the LFS.

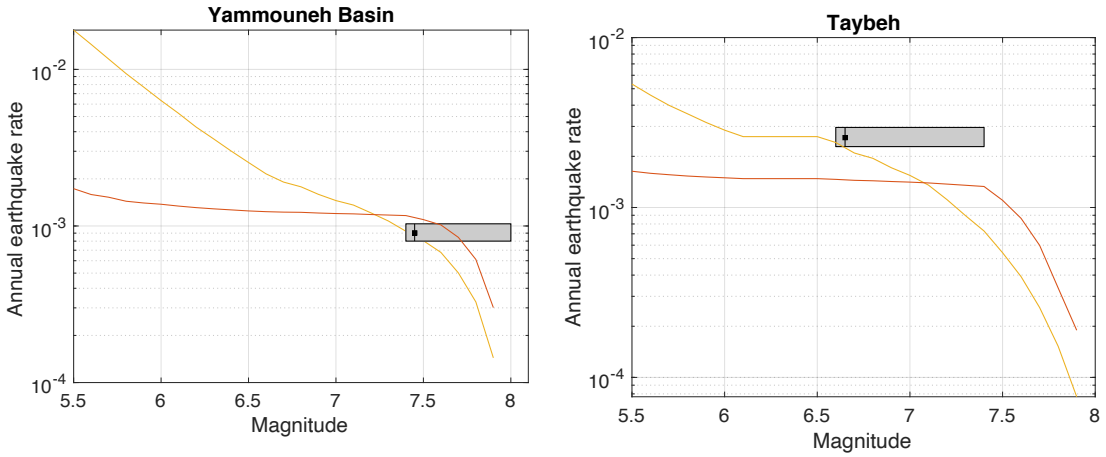

Fig. 4. 12 Comparison of the earthquake forecast with rates of earthquakes based on paleoseismic data, at two sites along the LFS. Solid lines: rates of ruptures passing through the site, as forecasted by the fault model built (also called "participation rates"); orange: fully interconnected model with M_{max} 7.9 and Gutenberg-Richter system MFD; red: fully interconnected model with M_{max} 7.9 and Youngs and Coppersmith system MFD. Rectangle: distribution for the mean inter-event time between large earthquakes, inferred from the paleoseismic data, taking into account the uncertainty on the ages. Trench in Yammouneh Basin located along segment S41; Taybeh site on segment S8 on Wadi Araba (see Fig.4.1).

4.5 Seismic hazard levels

4.5.1 PGA at 475 yrs - comparison between the interconnected model (maximum jump 10km) and the classical implementation – M_{max} 7.5

We run two hazard calculations, one based on the classical fault implementation, and the other one on the interconnected fault model. In both models, the maximum magnitude in the system is 7.5 (Fig. 4.13). Two seismic hazard maps for the PGA at 475 years return period are produced (Fig. 4.13, generic rock site with V_{S30} = 760 m/s), by combining each fault model with a set of ground-motion models. Following El Kadri et al. (2023), we use Chiou and Youngs (2014), Akkar et al. (2014) and Kotha et al. (2020) equally weighted. The three models predict ground motions for shallow crustal earthquakes.

Overall, using the interconnected fault model, the hazard levels decrease along the main strand (from ~0.7 to ~0.5g), but increase along the secondary faults (from 0.4 to 0.5g), with respect to the classical implementation. In the interconnected calculation, hazard estimates are highest along the southern half of Yammouneh fault, as well as along the southern segments of JVF, northern and southern segments of Araba fault, corresponding to the segments with remaining slip budget at the end of the iterative process (Fig. 4.4i). Once the system MFD is anchored to the upper magnitude rates, the moderate magnitudes that can still be distributed are preferably associated to these segments; moderate magnitudes control hazard estimates at 475 years return period.

At sites along the Serghaya fault, the interconnected model delivers hazard values that are ~0.1g higher than in the classical implementation. To understand these results, we need to compare the seismic rates associated to the Serghaya fault in both models (Fig. 4.14). The interconnected fault model includes larger rates in the moderate magnitude range (contributing the most at 475 yrs return period), and lower rates in the upper magnitude range. For sites above the Mount Lebanon Thrust dipping plane, hazard values decrease slightly in the northern part (from 0.5 to 0.4g) and increase significantly in the southern part (from 0.4 to 0.6g). The northern segments of Mount Lebanon Thrust are involved in more large magnitude ruptures than its southern segments, as they may break with segments from the Missyaf as well as Yammouneh faults.

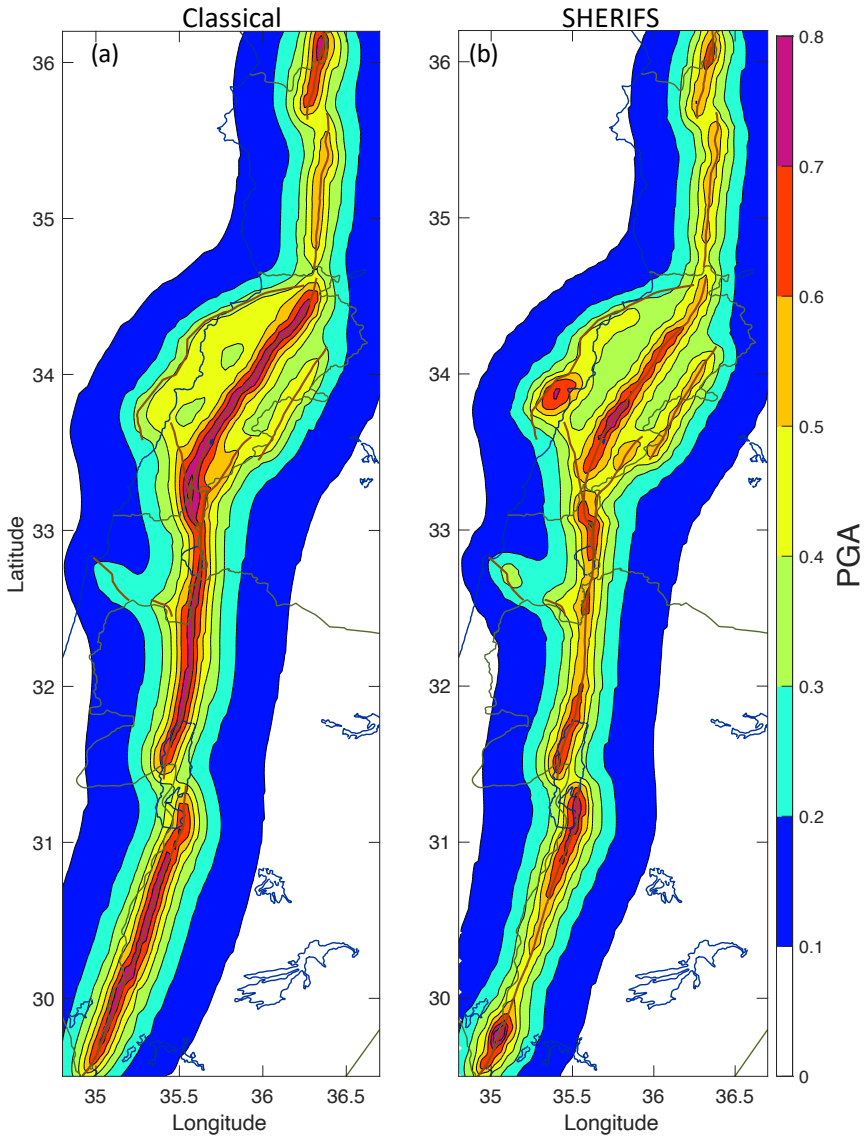

Fig. 4. 13 Seismic hazard map for the PGA at 475 years return period (a) based on the classical implementation of faults, assuming that the maximum magnitude is M_{max} 7.5, (b) based on the interconnected model assuming M_{max} 7.5 (maximum jump 10km, ruptures cannot jump major discontinuities).

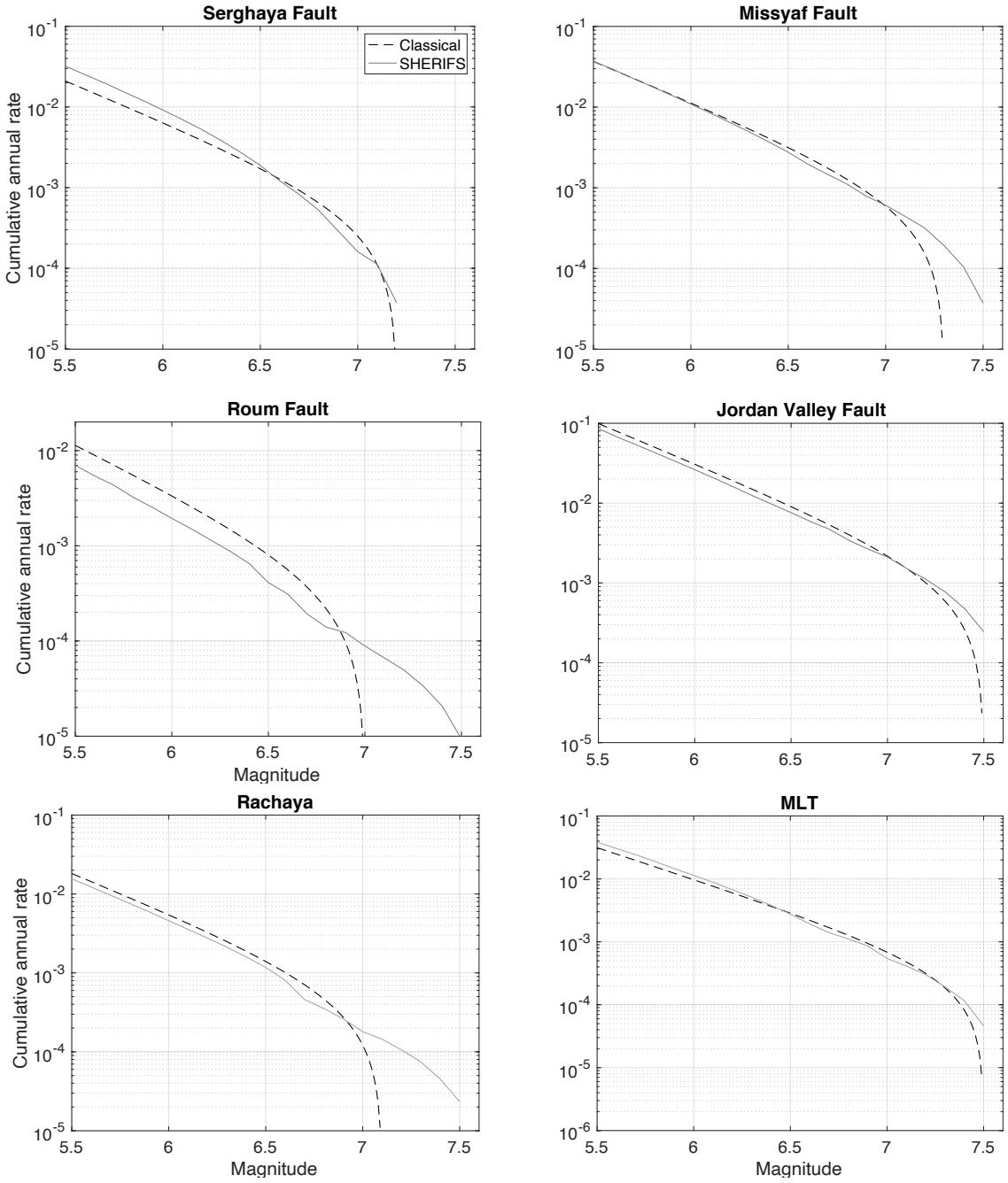

Fig. 4. 14 Magnitude-frequency distributions for faults in the classical implementation (dashed lines), compared to participation rates obtained with SHERIFS (solid lines). Assumption M_{max} 7.5. Interconnected model with maximum jump 10km. Participation rates: seismic rates associated to the segments are summed, some ruptures may involve segments that do not belong to the fault.

4.5.2 PGA at 475 yrs: M_{max} 7.9 fully interconnected model

We believe that magnitudes larger than 7.5 may occur within the Levant Fault System, and we show in Section 3.4 that for a model with M_{max} 7.9 to be meaningful (realistic percentage of aseismic slip), the system must be entirely connected (maximum jump 18km, ruptures can jump all major discontinuities). Figure 4.15 displays the seismic hazard map obtained combining this M_{max} 7.9 model with the ground-motion logic tree. As in any moment-balanced source model, the increase of the maximum magnitude leads to a decrease of seismic rates in the moderate magnitude range, and hence a decrease of seismic

hazard levels at 475 years return period. Applying the SHERIFS algorithm on the Levant fault system, the assumption of a maximum magnitude 7.9 delivers hazard levels larger or equal to 0.3g at sites within 20km of all fault segments. Values larger than 0.4g are found along most of the main strand. Hazard levels larger than 0.5g are obtained on the Araba fault as well as on the southern part of Mount Lebanon Thrust, due to a larger density of moderate magnitude ruptures at these locations. The seismic hazard map for the return period 2475 years is also displayed. Hazard levels are larger than 0.8g along all fault segments.

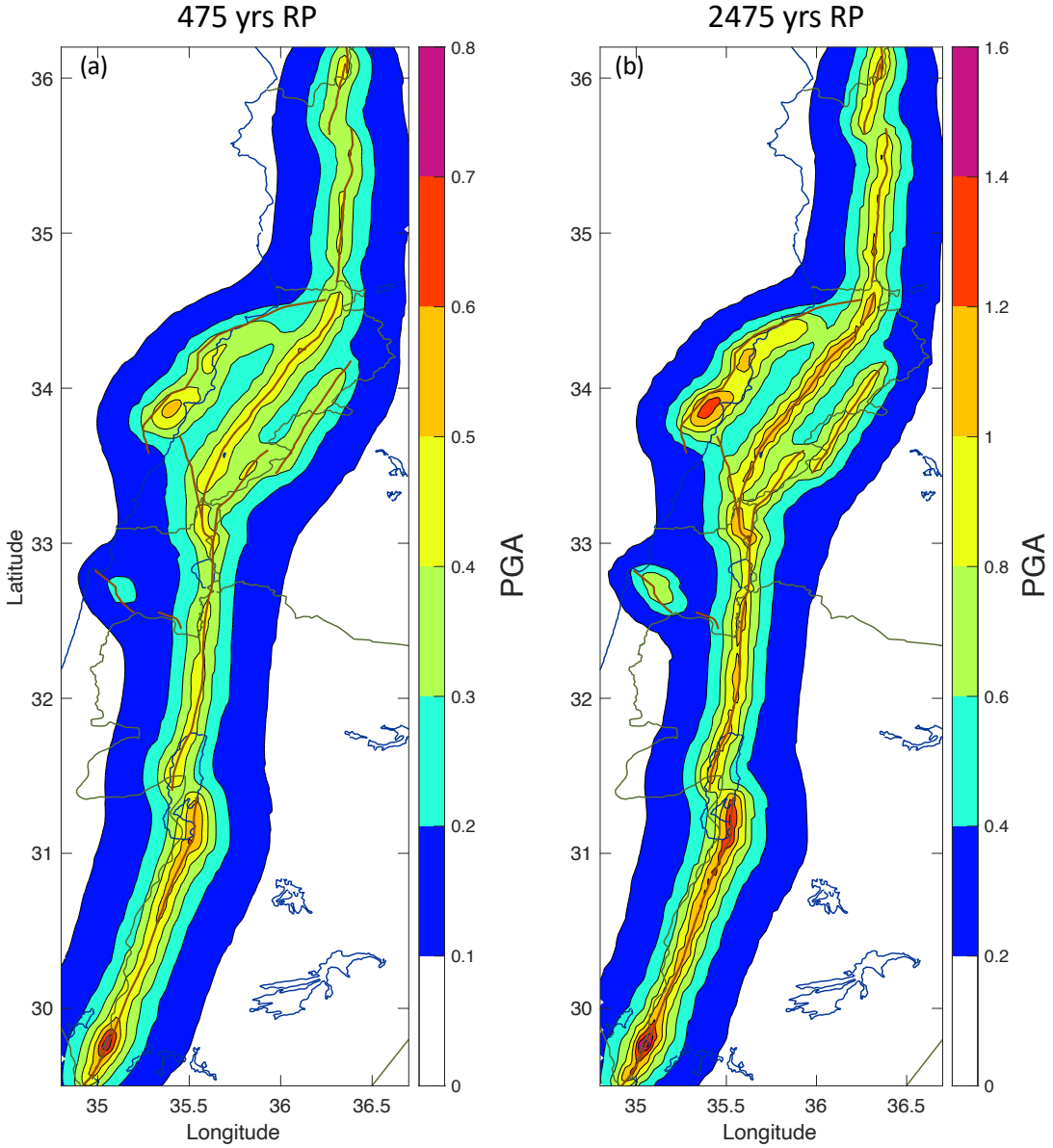

Fig. 4. 15 Seismic hazard map for the PGA based on a fully interconnected model assuming M_{max} 7.9. (a) Return period 475 yrs, (b) return period 2475 yrs.

4.6 Discussion and conclusions

The classical way of implementing faults in PSHA, considering separate faults that cannot interact, is not realistic. In the future, fault models in PSHA must account for complex ruptures, but there is no standard method yet. A few algorithms have been proposed to distribute the moment rate over the

physically possible ruptures, SHERIFS (Chartier et al. 2017, 2019) is one of them. This algorithm is being increasingly used (e.g. Gomez Novell et al. 2020 ; Cheng et al. 2021; Moratto et al. 2023), however none of the works published up to now analyze the distribution of seismic rates in magnitude and in space (that controls hazard levels), nor analyze the results in light of the classical implementation of faults (the bulk of PSHA studies at present). The aim of this manuscript is to address these issues.

We show how the algorithm distributes the seismic rates over the fault system, applying rules for defining which segments can break together. We show how some key decisions impact the seismic rates, such as the decision on the maximum magnitude the system can produce, or the maximum distance ruptures can jump between segments. The conversion of the slip rates into earthquakes is far from straightforward, we display seismic rates maps that help understand the process. Our tests show that the seismic rates associated with a given segment depend strongly on the precise location of the segment within the fault system, and on the segment combinations it can be involved in. Hence, hazard levels are directly related to the implementation of the fault system, its segmentation, and the decision on which segments may break together.

In the SHERIFS iterative process, magnitudes are picked in a pdf at each iteration and associated to a combination of segments (with area matching the magnitude, applying a scaling relationship). At the scale of the system, seismic rates follow a Gutenberg-Richter magnitude-frequency distribution (or another MFD shape). However, the set of ruptures and associated rates does not constitute a synthetic catalog, which is maybe the trickiest issue (see the bell shape of the distribution of magnitudes picked while building the M_{max} 7.5 and M_{max} 7.9 fault models, Fig. 4.S2 in Electronic Supplement).

We perform a comparison of a classical fault model implementation with an interconnected fault model, in terms of the distribution in space of seismic rates for different magnitude levels, and in terms of seismic hazard levels. Both models are moment-balanced taking into account fault slip rates. We find that hazard levels may decrease or increase, with respect to the classical implementation, depending on the location of the segment within the system (main strand, secondary strand, segment combinations). For the Levant Fault System, hazard values at 475 yrs return period decrease along the main strand (~4-5 mm/yr), and increase along the secondary faults (~1-2 mm/yr). One main difference between the models is that the distribution in space of seismic rates is not homogeneous in the interconnected model, even for moderate magnitude earthquakes (M5.5). These moderate magnitude earthquakes control hazard levels at 475 yrs return period. We find highest hazard levels along segments with the highest seismic rates in the moderate magnitude range.

Among the fault models tested, our preferred model is based on a maximum magnitude 7.9 and a fully interconnected fault system. Nine percent of the slip rate is not spent into earthquakes, which is a reasonable amount for aseismic creep along the LFS. Combined with a set of ground-motions valid for the region, hazard levels have been estimated. At 475 years return period, we find PGA values larger than 0.2g over most of the Lebanese territory; and values larger than 0.3g within 20km of all fault segments considered. At 2475 yrs return period, values larger than 0.4g are obtained over most of the Lebanese territory, with highest hazard around 1g for sites on the faults.

Table 4. 1 List of the Faults, Segments, and Sections geometry and the slip rate assigned to each section

*From Leonard 2014 (A in km^2):

Fault	**Segment** (Tectonic segmentation)	**Section** (SHERIFS segmentation)	**Dip (°)**	**Length (km)**	**Width (km)**	**Mean Slip rate (mm/yr)**	**Mean maximum magnitude (Leo2014)**	
							At the level of each section	At the level of the whole fault (Classically)
Araba	1	5	90	30.1	18	4.5	6.7	7.5
	2	6		23			6.6	
	3	7		25.8			6.6	
	4	8		22.9			6.6	
	5	9		10.4			6.0	
	6	10		18.9			6.5	
	7	11		22.4			6.6	
		12		21.9			6.6	
	8	1		6.5			5.6	
	9	2		5.3			5.4	
	10	3		4.3			5.3	
	11	4		25.3			6.6	
Jordan Valley	1	15	90	33.7	18	4.5	6.8	7.5
	2	16		25.2			6.6	
		17		24.4			6.6	
	3	18		27.1			6.7	
	4	19		13			6.2	
	5	20		28.1			6.7	
		21		28.1			6.7	
Carmel Gilboa	1	46	60	36.5	28	0.5	6.8	6.8
	2	47		16.8			6.4	6.4
Yammouneh	1	13	90	20.2	18	4.5	6.5	7.5
	2	39		35.1			6.8	
		40		34.2			6.8	
	3	41		32.8			6.8	
	4	42		16.1			6.4	
	5	43		9.5			5.9	
	6	44		11			6.1	
	7	45		31.4			6.7	
Rachaya	1	14	90	19.7	18	1.4	6.5	7.1
	2	29		24.8			6.6	
		30		23.8			6.6	
Serghaya	1	36	90	21	18	1.4	6.6	7.2

	2	37		29.1			6.7	
	3	38		39.1			6.8	
Roum	1	31	90	9.9	18	0.9	6.0	7
	2	32		7.1			5.7	
	3	33		6			5.5	
	4	34		6.9			5.7	
	5	35		16			6.4	
Mount Lebanon	1	48	45	20.7	20	1.5	6.6	7.5
	2	49		37.9			6.9	
		50		37			6.9	
	3	51		31.8			6.8	
		52		30.5			6.8	
Missyaf	1	22	90	21.4	18	2.2	6.6	7.3
	2	23		29.7			6.7	
	3	24		32.8			6.8	
		25		32.4			6.7	
Ghab	1	26	90	26	18	2.2	6.7	7
		27		25.9			6.7	
	2	28		27.7			6.7	

Strike Slip: Mmax_mean = log10(A) - 2.0087
Reverse: Mmax_mean = log10(A) - 2.0013

Table 4. 2 Different parameterizations tested in the application of the SHERIFs algorithm on the Levant fault system. Slip rate increment (dsr) used: 0.0001 mm/yr. Seismogenic depth considered: 18km for the strike-slip segments (width of ruptures), 14km for segments on the Mount Lebanon Thrust

Model	Maximum jump distance	Reccurence model	M_{max}	Length of maximum rupture (km)	Number of rupture combinations	Unused slip rate (%)
1	10	GR	7.5	182	532	9
2	10	GR	7.9	458	3690	72
3	12	GR	7.9	460	8452	30
4	18	GR	7.9	464	18864	14
5	18	GR	8.1	732	119327	24
6	18	YC	7.9	464	18864	26

4.7 Electronic Supplement

Implementation of an interconnected fault system in PSHA, example on the Levant fault (in prep)

Sarah El Kadri, Céline Beauval, Marlène Brax, Yann Klinger

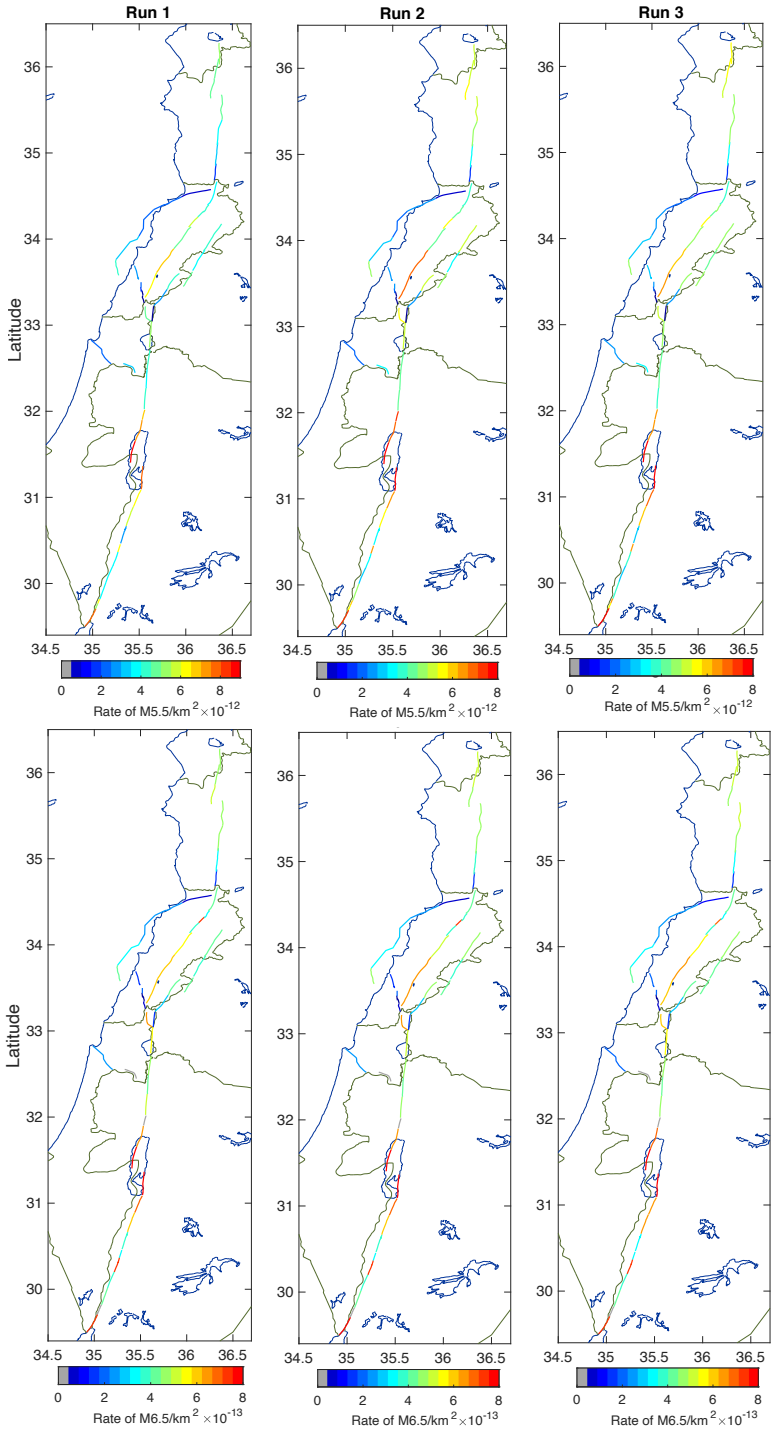

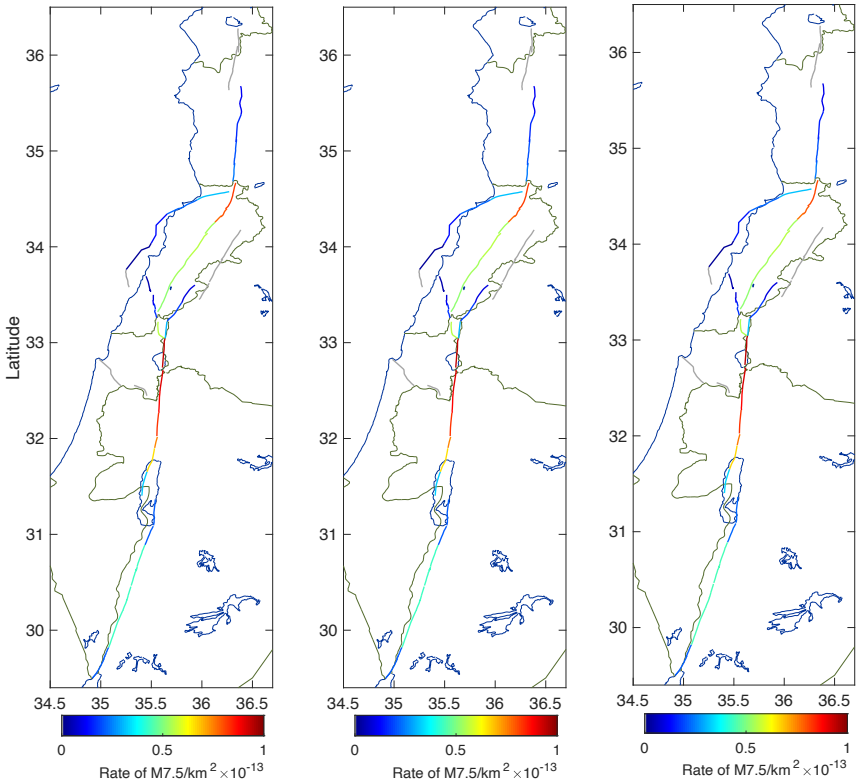

Fig. 4.S1 Obtained fault model in terms of annual rates of earthquakes for 3 different runs, first row for M_w5.5, second row for M_w6.5, third row for M_w7.5, normalized per square kilometer.

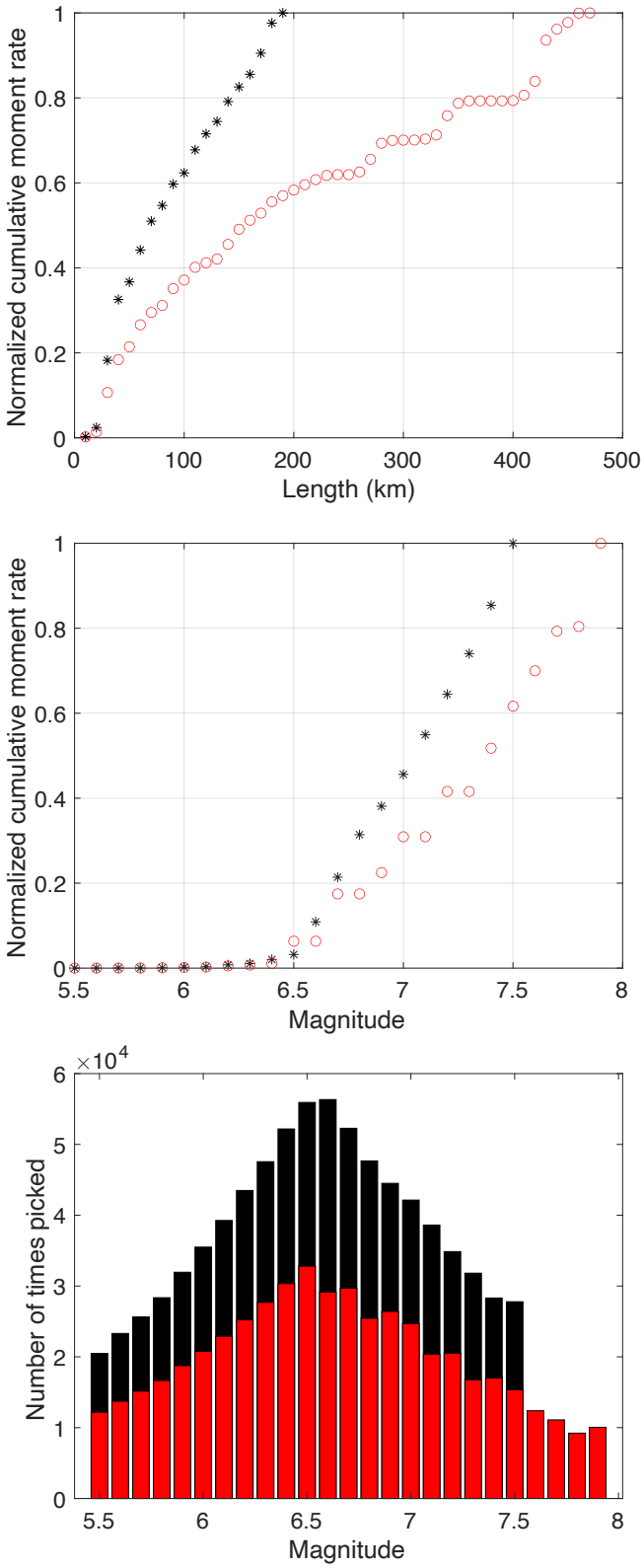

Fig. 4.S2 Normalized cumulative moment rate of each model; Black: SHERIFS calculation model 1, red: SHERIFS calculation model 4 (see Table 4.2), as a function of (a) the length of the rupture combinations, (b) the magnitude, (c) Number of times each magnitude bin has been picked during the calculation

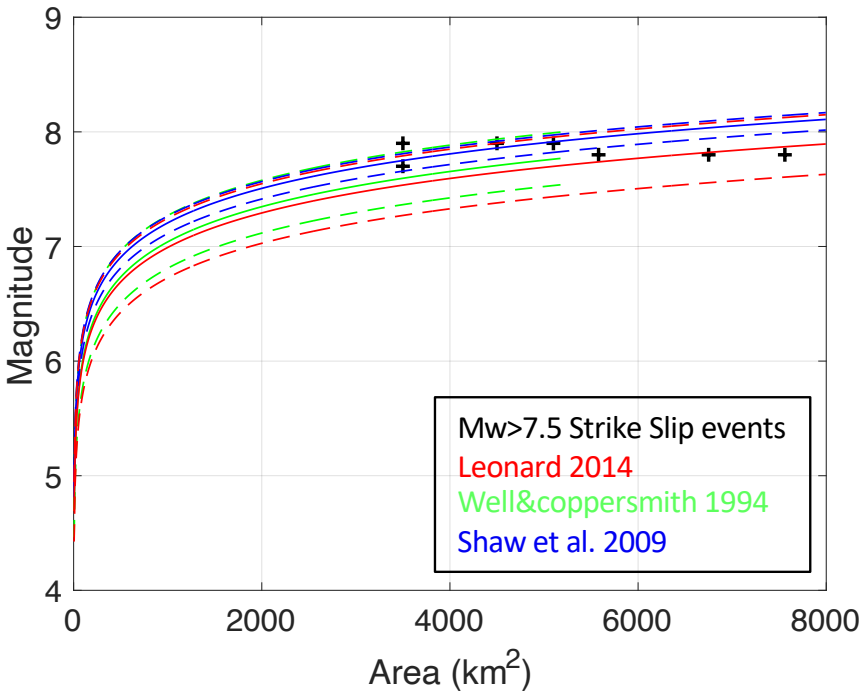

Fig. 4.S3 The regressions between moment magnitude Mw and rupture area A(km^2) for strike slip events; solid lines correspond to the linear magnitude-area relation and the dashed lines are $\pm\sigma$ uncertainties. The observed M>7.5 strike slip earthquakes represented in black crosses are described in Table S1.

Table 4.S1 Global events occurred along strike slip plate boundary faults associated with their rupture characteristics (estimated magnitude, length of rupture, width of the fault, slip rate)

Fault system	Slip rate(mm/yr)	Date	Magnitude	Length(km)	width(km)	Reference
East Anatolian Fault	10.6-12	06-02-2023	Mw 7.8	310	18	Barbot et al. (2023)
Erzincan segment (North Anatolian Fault)	20(east)-25(west)	26-12-1939	Mw 7.9	360	12.5 ± 3.5	Barka (1996); Gürsoy et al. (2013); bohnhoff et al. (2015)
Ladik segment (North Anatolian Fault)		26-11-1943	Mw 7.7	280		
Denali Fault in Alaska	8-13	03-11-02	Mw 7.9	340	15	Eberhart-Phillips et al. (2003)
San Francisco	35	18-04-1906	Mw 7.8	432	15-20	Yeats et al. (1997)
Fort Tejon - SAF	35	09-01-1857	Mw 7.9	350	10	Zielke et al. (2010;2012)
Kunlun Fault in China - Kokoxili earthquake	11.5 ± 2	14-11-2001	Mw 7.8	450	10 in most places and 20 in the region of highest slip	Robinson et al. (2006); Bihong Fu et al. (2005)

General conclusions

The primary goal of this PhD thesis was to perform a comprehensive fault-based seismic hazard analysis for Lebanon, incorporating quantitative data derived from geologic, paleoseismic and geodetic studies. This conclusion begins by summarizing the key findings from each chapter. Following that, it addresses certain challenges uncovered in the research and offers potential pathways for future exploration.

Conclusions on the work done

The third chapter details the comprehensive work undertaken to develop probabilistic seismic hazard maps for Lebanon. This involved constructing a source model integrating a smoothed seismicity model with magnitude-frequency distributions based on an earthquake catalog. Additionally, fault source models were incorporated, employing recurrence models derived from geological or geodetic slip rates. Two distinct sets of alternative moment-balanced earthquake recurrence models were formulated for faults: one assuming an exponential Gutenberg-Richter model and another based on a characteristic Youngs and Coppersmith (1985) model. Throughout this process, uncertainties in parameters and decisions made during the construction of the source model were meticulously traced and quantified.

To assess seismic hazard levels, the source model logic tree was combined with three equally weighted ground-motion models (Akkar et al. 2014; Chiou and Youngs 2014; Kotha et al. 2020) to account for epistemic uncertainty in predicting ground motion within the region. The analysis revealed that uncertainties related to slip rate estimates, minimum magnitude and maximum magnitude potential? on faults (M_{max}), and the choice of recurrence model significantly influenced earthquake frequencies on faults and consequently impacted hazard estimations. On the other hand, the smoothed seismicity model, representing off-fault seismicity, exhibited minimal contribution to hazard for return periods equal to or larger than 475 years. Hazard maps have been produced for different spectral accelerations and return periods. Notably, for PGA at 475 years return period, values exceeding 0.3 g covered more than two-thirds of the country, with the highest hazard values (> 0.5 g) concentrated along the primary strand of the Levant fault. A specific study focusing on Beirut, the capital city, revealed that hazard levels were predominantly influenced by the Mount Lebanon thrust Fault situated beneath the city.

In the fourth chapter, our objective was to enhance the assessment of seismic hazard along the LFS (Levant Fault System) by integrating fault interaction. In classical hazard models, ruptures can occur along segments within predefined faults, ruptures cannot break segments that belong to distinct faults. To address this limitation, we employed the SHERIFS algorithm, which adopts an iterative approach to estimate earthquake rates on faults, distributing the slip rate budget over the possible segments' combinations. Going down to the scale of the tectonic segment was crucial for replicating realistic ruptures as closely as possible. We included the possibility for ruptures to jump over significant discontinuities and barriers, such as pull-apart basins and compressional jogs. However, the application of the methodology to the Levant fault system has shown the strong dependence of earthquake frequencies and hazard estimates on specific input decisions. Factors like the definition of the segment extensions, the discontinuities that may act as rupture barriers, the maximum magnitude for the system, and the shape of the Magnitude-Frequency Distribution (MFD) play pivotal roles.

Hazard maps were generated for the PGA at a 475-year return period. Results based on the interconnected fault model were compared to results based on the classical approach, applying similarly the scaling relationship (mean magnitude inferred from area). While the interconnected model allows for longer ruptures with higher magnitudes, hazard levels decrease along the rapid main strand, and increase on the slower secondary faults. The results show that hazard levels are significantly influenced by the precise location of the segment within the fault system, and on the segment combinations it can be involved in.

In conclusion, although the implementation of a rigid configuration for faults, where segments are represented as independent structures that cannot interact with each other, fail to mimic what could happen in reality, the implementation of an interconnected model doesn't entirely solve the issue. Based on our work, it is not straightforward to construct a realistic model, SHERIFS algorithm enables to include complex ruptures into the fault model, but it requires a number of parameters and decisions bearing large uncertainties.

In summary, employing a rigid configuration for faults, where segments are portrayed as isolated structures with no interaction, fails to replicate real-world events. The use of an interconnected model to build a realistic model is a promising concept, but its implementation is not straightforward. To accurately depict potential occurrences in the LFS or in any seismically active region, additional efforts are required to account for segment connectivity and introduce more physical constraints in the modeling of earthquake rates for seismic hazard assessment.

Appendix A: A time-dependent model for the Yammouneh Fault

Contents

List of Figures

This chapter is a very preliminary version of a future article co-authored in collaboration with Batul Nemer (Master student, work done during her master thesis), Celine Beauval, and Marleine Brax. Its focuses specifically on the Yammouneh fault, chosen for its comprehensive characterization in comparison to other faults. The aim is to conduct a time-dependent analysis aimed at refining the assessment of seismic hazard in the Lebanese region.

A time-dependent model for the Yammouneh Fault

B. Nemer[(1)] , S. El Kadri[(1,2)] , C. Beauval[(2)] and M. Brax[(1)]

[(1)] National Council for Scientific Research, CNRS-L P.O. Box 16-5432 Achrafyeh 1100-2040, Beirut, Lebanon

[(2)] Univ. Grenoble Alpes, Univ. Savoie Mont Blanc, CNRS, IRD, Univ. Gustave Eiffel, ISTerre, 38000 Grenoble, France

A.5.1 Introduction

Traditional seismic hazard assessments often consider poissonian occurrence of earthquakes, where the likelihood of an earthquake occurring is independent of the time elapsed since the previous one. However, earthquakes' occurrence and behavior can change over time due to various factors. Time-dependent models account for this variability, enhancing the accuracy of seismic hazard predictions. Incorporating time-dependent models helps identify regions that might experience changes in seismic activity or have an increased likelihood of significant earthquakes. This targeted approach ensures that mitigation efforts, emergency planning, and infrastructure development focus on areas where the hazard is heightened.

The elastic rebound theory of Reid 1911 postulates that the probability of an earthquake occurrence is small after an event, and it increases gradually as tectonic stresses rebuild on the fault (Matthews et al, 2002; Field 2015; Wong & Thomas 2022). This time-dependent behavior contrasts with the constant probability assumption of the traditional Poissonian model (Merz & Cornell, 1973).

A time-independent PSHA has already been conducted in Lebanon by El Kadri et al. (2023), which is a reasonable assumption in regions where the available data are sufficient to provide only an estimate of the average recurrence rate of earthquakes (Cornell 1968). However, we seek to advance the standards in PSHA by transitioning towards a time-dependent hazard assessment in regions where recurrence and timing information are available (Wong & Thomas 2022).

Moreover, studies along the LFS have revealed a pattern where significant earthquakes tend to occur in clusters (Lefevre et al. 2018). For instance, there was a sequence spanning from the eleventh to the thirteenth century along the main strand, encompassing events such as those in 1033, 1170, and 1202. Understanding how these clusters of substantial seismic events influence seismic hazard assessment remains an ongoing challenge. However, it's becoming increasingly evident that time-dependent models considering fault interactions are essential to comprehensively address this clustering phenomenon in seismic hazard assessments. These models could potentially shed light on the mechanisms behind such event clusters and their implications for seismic risk assessment.

Moving from time-independent to time-dependent PSHA represents our objective to grasp the genuine dynamics of earthquake occurrences. This shift aims to enhance our comprehension of seismic hazard in Lebanon, enabling us to offer more precise and reliable assessments. It's worth noting that in this study, the calculation of time-dependent probability is relatively straightforward. It relies on a probability density function of inter-event times and is contingent on the time elapsed since the last earthquake.

In this study, we focused on the Yammouneh fault due to its detailed characterization, offering well-defined dates for characteristic earthquakes derived from extensive paleoseismic and geomorphologic studies (Daeron et al. 2007; Nemer et al. 2008). The Brownian passage time model is used (Matthews et al. 2002). A Monte Carlo analysis is conducted on the age ranges of past paleo events along this fault. This analysis aims to ascertain the Mean Recurrence Time (MRT) and the aperiodicity. We calculate conditional probabilities, tracking uncertainties related to parameter choices (MRT, aperiodicity) to gauge their influence on the likelihood of occurrence. By manipulating influential parameters, we strive to comprehend the factors governing seismic hazard related to this fault. Our findings highlight that the characteristic magnitude significantly impacts hazard levels, while factors such as the probability of occurrence and fault geometry contribute to a lesser extent.

A.5.2 Brownian Passage Time (BPT)

Abaimov et al. (2007) introduced several probability models employed to characterize earthquake recurrence statistics. These models encompass the Weibull distribution (Hagiwara 1974), the Lognormal distribution (Nishenko & Buland 1987), and the Brownian Passage Time (Inverse-Gaussian) distribution (Matthews et al. 2002). The latter was utilized in earthquake hazard assessment within the San Francisco area (WGCEP, 2003). Considering its presumed ability to adequately represent earthquake distribution, we will also incorporate the BPT model in our time-dependent analysis (Ellsworth et al. 1999).

The probability density function of a BPT model is defined by Matthews et al. (2002) as:

$$f(t;\mu,\alpha) = \left(\frac{\mu}{2\pi\alpha^2 t^3}\right)^{1/2} exp\left\{-\frac{(t-\mu)^2}{2\mu\alpha^2 t}\right\} \quad (1)$$

where μ is the mean recurrence time (MRT), α is the aperiodicity (or coefficient of variation), which is the ratio of the standard deviation of recurrence times to the mean recurrence time. This parameter describes how regularly or irregularly characteristic earthquakes are expected to occur on any fault (Akinci et al. 2017), and its choice is significant in terms of the resulting earthquake occurrence probability calculation (Parsons 2005; Akinci et al. 2010).

Since the BPT model treats the mean as a pure scale parameter, adjusting the value of α allows for a comprehensive exploration of the entire spectrum of potential distribution shapes (Matthews et al. 2002). Fig.1 shows the probability density function of the BPT model for different values of α. It is noticeable that lower values of α result in symmetric distributions with a distinct central tendency around the mean. Conversely, higher values of α lead to distributions that are heavily skewed to the right and exhibit a sharp peak to the left of the mean value.

The BPT model given by Matthews et al. (2002) requires two essential parameters: the mean recurrence time of earthquakes along a fault and the time elapsed since the last earthquake on a fault, which is information rarely found for the majority of earthquakes around the world (Cramer et al., 2000; Wong & Thomas, 2020).

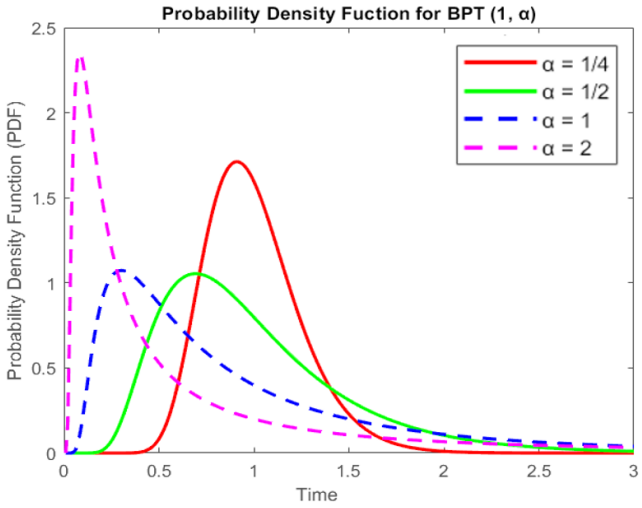

Fig. 1 Probability density function for the BPT (1, α), α = ¼, ½, 1, 2. Time represents "Normalized Time", in which each individual recurrence sequence is divided by the sample mean interval between events.

A.5.2.1 Parameter Estimation for the BPT Model

We center our attention on the Yammouneh fault, the principal fault crossing the Lebanese restraining bend. Daëron et al. (2005) conducted an analysis of paleo-seismological trenches in lacustrine deposits and presented evidence of coseismic slip on the fault corresponding to the A.D. 1202 earthquake, which was estimated to have a magnitude of M_S 7-7.8 according to Ambraseys & Jackson (1998). The study also revealed that this particular segment of the fault has remained locked since then. This suggests that significant strain has accumulated along the fault over time, raising the potential for future seismic activity in the region.

It is worth noting that the fact that this fault segment has been locked since the A.D. 1202 earthquake serves as an additional incentive for conducting a time-dependent analysis. The essence of such analysis underscores how the probability of earthquake occurrence increases with the time elapsed since the last earthquake on the fault (Matthews et al. 2002). In this context, we are talking about a remarkable span of 821 years. According to Elias (2015), the occurrence of a major earthquake on this fault should not come as a surprise.

Daeron et al. (2007) combined historical data with new paleoseismic data to estimate the mean recurrence time of the main Lebanese segment of the LFS, by expanding the trench work across the Yammouneh paleolake. Ten to thirteen paleo-events of magnitudes M~7.5 were identified, which provide a robust dataset for the estimation of the parameters (μ and α) of the BPT model.

Mean Recurrence Time (MRT)

Out of the 13 events identified by Daeron et al. (2007), only 8 to 9 were considered due to their reliability in providing data crucial for estimating the parameters of the BPT model. The remaining events were

excluded from the analysis due to issues related to poor detection, including scarcity of radiocarbon data and unresolved age constraints..

The most recent events (S1, S2 and S3) were classified into a historical sequence, while the rest of the identifiable events (S7 till S12) were grouped into a prehistoric sequence. Daeron et al. (2007) estimated that if S2 is combined with S1, the historical MRT is between 733 to 1230 years. If they are separate events, the historical MRT is between 366 to 615 years. However, they lean towards thinking that the breaks in S2 were actually caused by S1. To further constrain the MRT, the prehistorical sequence appears to have an MRT of 1127 ± 135 years.

The uncertainty associated with this parameter is notably high due to the inherent uncertainty in the event dates. Nevertheless, Nemer et al. (2008) conducted a study on the YF utilizing remote imagery, geomorphology, and paleoseismology. Their aim was to investigate the seismic characteristics of the YF and its connection to the development of strike-slip 'pull-apart' basins. They trenched 175 meters south of the location investigated by Daeron et al. (2007) (refer to Fig. 2 for the trench location). The close proximity facilitated the correlation of trench findings between both studies. Nemer et al. (2008) associated five events with the initial five events identified by Daeron et al. (2007). However, as the events identified by Nemer et al. (2008) did not supplement the findings of Daeron et al. (2007), this study will depend on the results of Daeron et al. (2007) since they identify a greater number of earthquakes than Nemer et al. (2008).

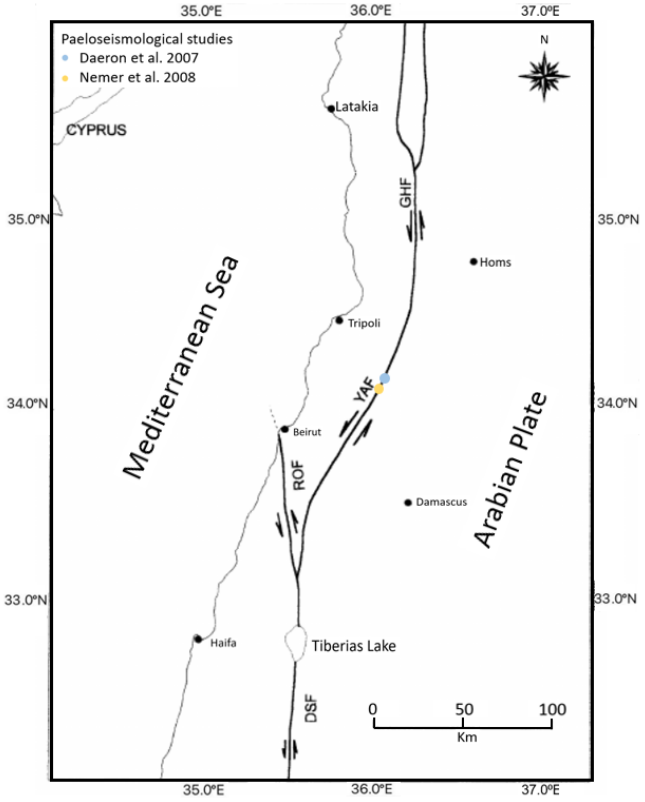

Fig. 2 Map indicating the location of the paleoseismic trenches of Daëron et al. (2007) and Nemer et al. (2008).

Aperiodicity α

The aperiodicity describes the regularity or irregularity of earthquakes occurrences on a fault, and the higher it is, the more random the occurrence becomes. Field (2015) suggests that the aperiodicity can be related to the magnitude, as higher magnitude events occur more periodically (smaller α) than lower magnitude earthquakes that occur quite frequently (larger α).

Ellsworth et al. (1999) generated synthetic earthquake sequences to evaluate the validity of the mean and aperiodicity inferred from short earthquake sequences. Not only do short sequences produce large uncertainties, but this uncertainty is further compounded by the dating of the events themselves. To analyze this problem, Ellsworth et al. (1999) performed a Monte Carlo analysis in order to explore the range of α as a function of earthquake magnitude and tectonic style. Their global dataset comprised repeating microearthquakes, moderate earthquakes, historically documented sequences of large-magnitude events, and sequences inferred from paleoseismic investigations; a total of 35 sequences were considered suitable for analysis. The results showed that:

1) the limited worldwide earthquake recurrence interval data have a Brownian Passage Time model shape factor (basically the covariance of the distribution) of 0.46 ± 0.32,

2) the 35 recurrence interval sequences examined are compatible with a shape factor of 0.50,

3) the 35 earthquake sequences had no systematic differences when grouped by tectonic style.

Referring to this paper, many studies chose to use the average value of α = 0.5 with an uncertainty of ± 0.2, such as WGCEP (2003) in California, WGUEP (2016) in the Wasatch Front Zone, Peruzza et al. (2010) in Italy, Akinci et al. (2017) in Calabria, Italy, and Chan et al. (2017) in Taiwan. Cramer et al. (2000) also suggest the use of this central value unless a fault-specific α is available. However, other studies, such as that of Parsons (2008), chose their parameters by performing a Monte Carlo analysis based on their paleoseismic data.

In this study, we believe we have enough data to proceed with a bootstrap analysis and a Monte Carlo analysis, which will be described in the following sections.

A.5.2.2 Bootstrap Analysis

Despite the conventional approach of data resampling in traditional bootstrap analysis, we follow the definition provided by Ellsworth et al. (1999), in which synthetic earthquake series are drawn a 100 times from a BPT distribution, with predefined μ and α values. It is worth noting that series containing 3 to 10 events are not sufficient to provide a good estimate for the BPT parameters (Ellsworth et al., 1999), which is where most of the real-world seismic observations lie, and particularly our earthquake observations for the Yammouneh Fault (6 earthquake series for Daeron et al. 2007)

The parameters used for the analysis are the following: μ = 1100, derived from the recurrence calculation by Daeron et al. (2007) of ~1127 years. As for the aperiodicity, we choose α = 0.5 because it is the value mostly used (as stated previously, section A.5.2.1). As the sequences are generated, we

record their associated mean recurrence times and aperiodicities, as is shown in the histogram of Fig. 3. Then, we compute the mean values of the generated parameters. Upon a quick glance at the histograms, a clear pattern emerges: the average values of the generated parameters consistently fall below the initial values employed in the bootstrap analysis. For the aperiodicity values, the calculated mean lingers around 0.4. This is notably lower than the original value of 0.5 that was set. Similarly, when it comes to the mean recurrence time, the computed average lies around 827 years, which is also smaller than the original value of 1100 years that we started with. This inherent uncertainty echoes precisely what Ellsworth et al. (1999) hinted at: the challenge of confidently estimating parameters when working with sequences that contain just 3 to 10 events. The natural consequence of dealing with shorter sequences is the noticeable variability in aperiodicity values, leading to a wide spectrum of outcomes. To address this issue, they performed a Monte Carlo analysis, as described in the next section.

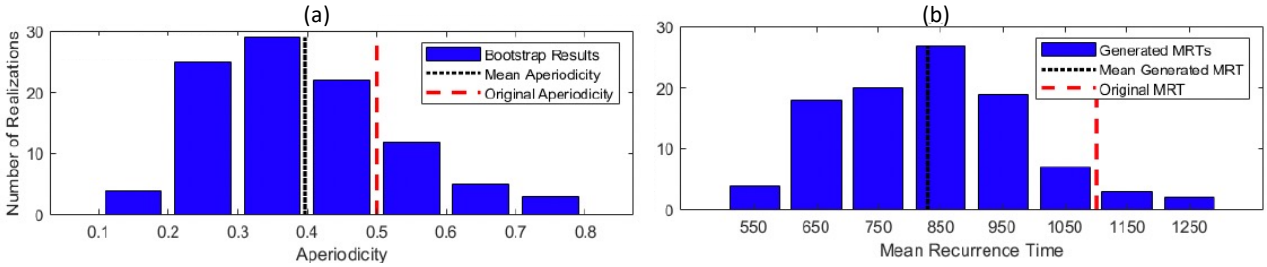

Fig. 3 Histogram of Bootstrap Results performed for the earthquake series from Daeron et al. (2007). (a) Aperiodicity values (b) Mean Recurrence Times. Black lines represent the mean of the generated parameters. Red lines represent the values of the original parameters.

A.5.2.3 Monte Carlo Analysis

Following the steps of Ellsworth et al. (1999), we conduct a Monte Carlo analysis. We begin by plotting the uniform Probability Density function (pdf) for the events of Daeron et al. (2007). This uniform pdf distribution is used to account for the uncertainty in dating, meaning we acknowledge the range of possible ages for each earthquake. Sampling the pdf, an event could happen anywhere within the given age constraint. Next, we generate 1000 realizations of the earthquake dates drawn at random from those distributions, where each realization represents one possible sequence of dates for all of the earthquakes in that series. We analyze each generated sequence individually to determine μ and α. This is achieved by calculating the time intervals between the dates in each realization, which allows the computation of the needed parameters.

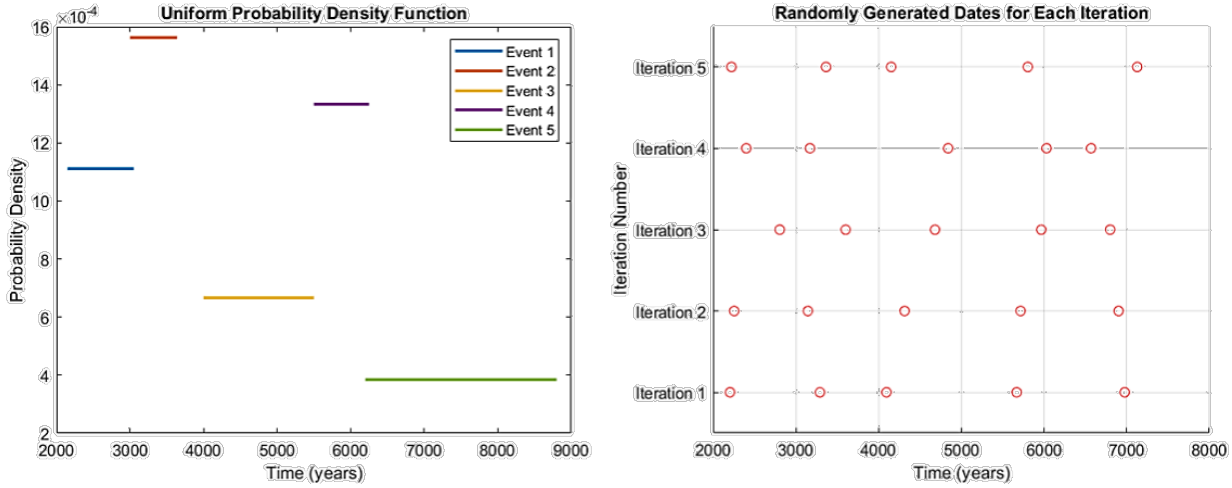

Fig. 4 Illustration of the Monte Carlo estimation procedure applied to the five paleoseismic earthquake sequences identified by Nemer et al. (2008). Probability density distributions of the five events are plotted on the left, and five earthquake series drawn at random from those distributions are shown on the right.

This process is illustrated in Fig. 4 for the five events identified by Nemer et al. (2008). The uniform pdfs are accounted for and five examples of earthquake series are drawn at random from those distributions. By computing the inter-event times between the dates of each iteration (a total of 4 inter-event times here), we can compute μ (the mean of inter-event times) and α (the ratio of the standard deviation of recurrence times to the mean recurrence time).

Distributions of the MRT, aperiodicity, and 50-year conditional probability (see next section) can be derived from this procedure (see Fig. 5). The uncertainty in the MRT has already been covered in a previous section (See "Mean Recurrence Time"), so we can shift our focus to the results of the aperiodicity.

The estimated aperiodicity for the events of Daeron et al. (2007) is around 0.49. Despite employing a Monte Carlo analysis, it is important to acknowledge the impact of short sequences in producing a diverse range of aperiodicity values. However, the 68% confidence interval of the aperiodicity, lies between 0.3 and 0.7, which is the range estimated by Ellsworth et al. (1999).

With regard to the aperiodicity, we'll adopt the range we established, aligning with the framework of Ellsworth et al. (1999), and used by numerous studies mentioned previously, which stands at 0.5 ± 0.2.

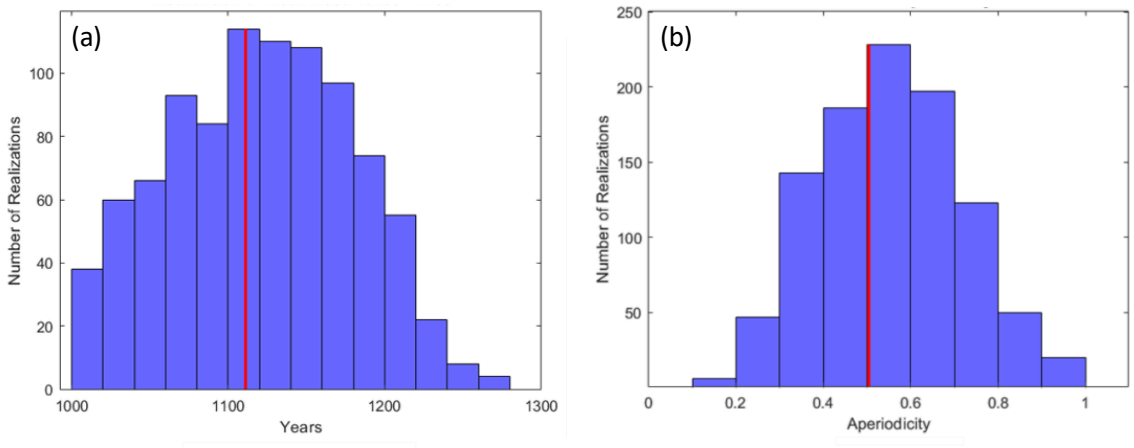

Fig. 5 (a) Distributions of Mean Recurrence Time using events S1, S3 and S7 to S12 from Daeron et al. (2007), (b) Aperiodicity for the MC Analysis. Red lines represent the mean of the observed results.

A.5.3 Conditional probability calculation

The conditional probability is defined by the WGCEP (2003) as the probability of an earthquake happening on a specific rupture source within a defined time interval (e.g. the 50-year period from 2023 to 2073), given that no earthquake has occurred on that source prior to the year 2023. It is also known as the probability of occurrence (poe) of the next earthquake on a fault. It is given by the following formula:

$$P(T \leq t \leq T + \Delta T \mid t > T) = \frac{F(T) - F(T+\Delta T)}{F(T)} \tag{2}$$

$$\text{Where, } F(T) = \int_T^{\infty} f(t)dt \tag{3}$$

F(T) is the cumulative density function (CDF), also known as the integration of the PDF over a specific time, T is the time elapsed since the last characteristic earthquake on the fault, (here it is the 1202 event, so 821 years have elapsed since then), and ΔT is the desired future time interval of reference (e.g. 50 years). Graphically, the conditional probability is given by the hachured area in Fig. 6.

With all the parameters readily available, we conduct calculations using a diverse range of mean recurrence times and aperiodicities, within the estimated uncertainty, allowing us to thoroughly examine their impact on the overall conditional probability calculations. In this work, we have specifically selected certain values for discussion purposes. These values include mean recurrence times of 923, 1020, 1100, and 1175 years, and aperiodicity values of 0.1, 0.2, 0.3, 0.4, and 0.5. Note: The MRT values of 1020 and 1175 were obtained from the work of Nemer et al. (2008). Moreover, the MRT of 923 years was determined by dividing the duration of Daeron et al.'s (2007) observations, spanning 12,000 years, by the number of identified events, amounting to 13.

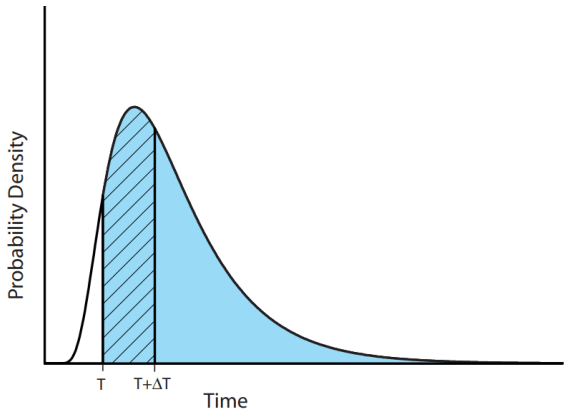

Fig. 6 Conditional Probability calculation from a Probability Density Function. The time interval of interest (exposure time) is from T (the present time) to T+ΔT (hachured area). The survivor function at time T is equal to the shaded area. The conditional probability is the ratio of these two areas. Source: WGCEP (2003)

A.5.3.1 Influence of Mean Recurrence Time on Probability of Occurrence

Fig. 7 shows the influence of the MRT on the 50-year conditional probability (poe) calculation, for α = 0.3. It becomes evident that the probabilities decrease as the MRTs increase. However, it is important to note that none of the probabilities exceed or even reach the 30% value, indicating a relatively limited increase in the probabilities across the range of MRT values.

Considering a characteristic recurrence model for the sources capable of rupturing the entire fault segment with a single event of maximum magnitude, Akinci et al. (2017) also observe a similar trend for the Calabria region in Italy, where the lowest probabilities are associated with sources characterized by recurrence times (MRT) much larger than the time elapsed (Te) since the last characteristic event (e.g., source ITIS011 in Akinci et al. (2017): MRT = 1000 and Te = 232, resulting in poe < 10% probability for the occurrence of an earthquake on the fault within the next 50 years). The probabilities are higher when the elapsed time becomes approximately equal to the mean recurrence time, and even higher when the elapsed time is twice the mean recurrence interval (e.g., ITCS016: MRT = 115 and Te = 235, resulting in poe ~ 55%).

It's worth noting that Akinci et al. (2017) concentrated their analysis on events with magnitudes ranging from 5.5 and above. In contrast, our study is specifically confined to larger magnitude events (Mw > 7). This distinction is essential in understanding our observed lower probabilities, despite the similarities in the behaviour of the probabilities. Our earthquake sequence in the Yammouneh is characterized by long recurrence intervals, resulting in lower probabilities of occurrence within the next 50 years.

To further illustrate this, we perform another exercise with a mean recurrence time of 500 years (green curve in Fig. 7), confirming what happens when the recurrence time becomes smaller than the elapsed time of 821 years. An increase in the time elapsed – mean recurrence time (Te/MRT) ratio leads to higher probabilities. For instance, when this ratio equals 1.64 (50 years from now, with MRT = 500 years), the probability reaches approximately 35%.

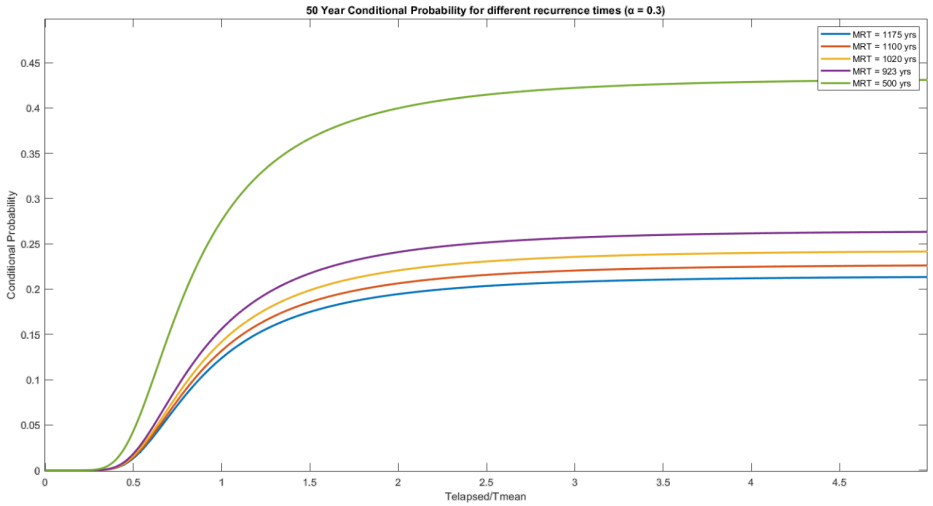

Fig. 7 Testing the influence of the mean recurrence time (MRT or Tmean) on the 50-year conditional probability calculation, for a fixed α = 0.3 and a fixed elapsed time. Telapsed: time elapsed since the 1202 AD event, in 2023 = 821 years

A.5.3.2 Influence of Aperiodicity on Probability of Occurrence

Now we test the impact of the aperiodicity parameter on the calculation of the probability of occurrence. Smaller aperiodicity values lead to higher probabilities, as expected. The selection of the aperiodicity value, as guided by Peruzza et al. (2010), Ellsworth et al. (1999), and Pantosti et al. (2008), is influenced by epistemic errors that encompass uncertainties in paleoseismic event dates or possibly missed events. Therefore, it is crucial to explore multiple aperiodicity values before drawing conclusions.

As Peruzza et al. (2010) mention, the reference value of α = 0.1 represents periodic or quasi-periodic sequences, resulting in a probabilities that reach 90%. Lower values, such as 0.2 to 0.5, generate probabilities that increase less rapidly with the time elapsed. Our main focus lies within the 0.5 ± 0.2 range, and specifically the central value of 0.5, as it was the resultant value of our Monte Carlo analysis.

For comparison, we introduce a Poisson model with mean recurrence time of 1100 years. This model features a constant probability value of 4.44%, calculated as follows:

$$P(T) = 1 - e^{-\lambda \Delta t} \tag{4}$$

Where λ is the average rate of earthquake occurrence, with $\lambda = \frac{1}{1100}$.

Transitioning to a time-dependent model, for example, 50 years from now, considering the same mean recurrence time of 1100 years and we vary the aperiodicity, the probabilities of occurrence would be: 7.6% (α = 0.3) and 7.2% (α = 0.5). Consequently, the probability decreases when transitioning from quasi-periodic to more stationary processes. Furthermore, as Field (2015) highlighted, large-magnitude earthquakes tend to exhibit lower aperiodicity values due to their rhythmic nature and lack of randomness.

.

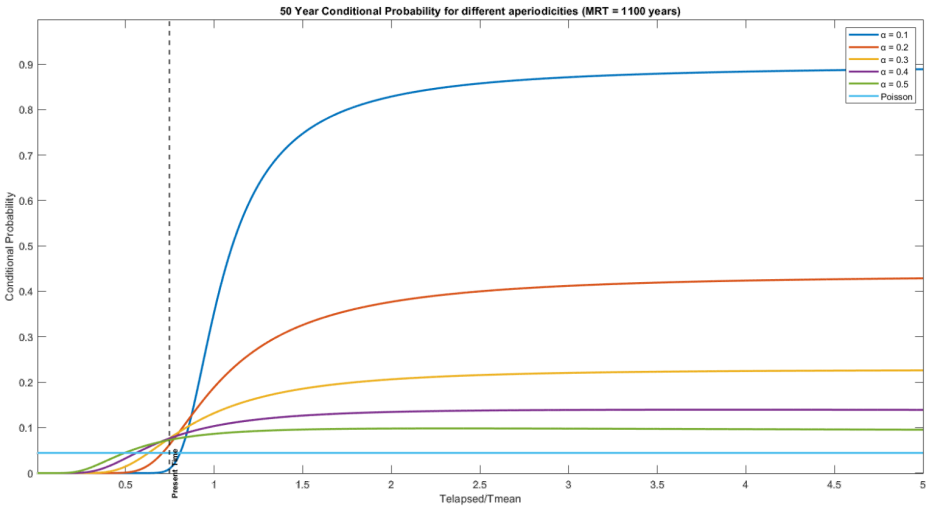

Fig. 8 Test on the influence of the aperiodicity α on the 50-year conditional probability, for a mean recurrence time of 1100 years. The graph compares a Poisson model (light blue) with time-dependent models. In a Poisson model, probabilities remain constant over time. In contrast, in the BPT (Brownian Passage Time) models, the probability increases with time. Lower aperiodicity values indicate more regular (periodic) behavior, resulting in higher probabilities over time.

A.5.4 Influence of source model uncertainties on hazard estimates

A.5.4.1 Identification of key parameters/key decisions

Once the probability of occurrence over the future time window is calculated, assessing hazard along the desired fault becomes feasible. However, selecting a set of Ground Models (GMMs) that best suits the region is crucial. As highlighted by El Kadri et al. (2023), the scarcity of ground-motion records in Lebanon poses a challenge in choosing an appropriate model for predicting ground motions. Compounded by the fact that all sites in Lebanon are situated within 20 km of seismic faults—either strike-slip faults inland or thrust faults offshore—the proximity to seismic sources introduces complexities to ground-motion assessments. To address this, we opt for three ground-motion models derived from shallow crustal earthquakes, each derived from distinct datasets. This approach aims to encompass the epistemic uncertainty associated with predicting ground motions, utilizing the models of Chiou and Youngs (2014), Akkar et al. (2014), and Kotha et al. (2020).

For the Yammouneh fault, we consider a simple source model with a unique fault and a unique earthquake occurring on the fault, denoted as a characteristic earthquake (M_C). As for the rest of the faults, because we don't have sufficient information, it might be more suitable to represent them using time-independent models. Earthquake recurrence models associated for these faults are the same used in the study by El Kadri et al. (2023). Uncertainties on the source model parameters for the Yammouneh fault, such as, aperiodicity, mean recurrence time, geometry of the fault and the characteristic magnitude are taken into consideration by adopting a logic tree in order to understand which parameters or decisions, impact hazard estimates (Fig. 9).

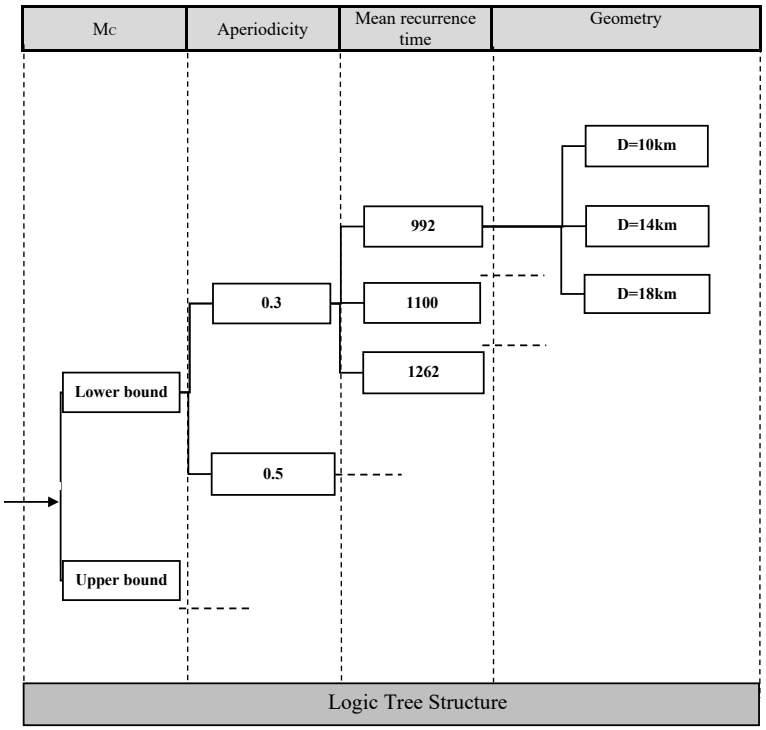

Fig. 9 Source model logic tree for Yammouneh fault. All branches are equally weighted, delivering 2x3x3x3= 54 different branches combinations, combined with 3 ground-motion models, resulting in 162 hazard results.

Hazard calculations are conducted by setting a maximum distance limitation of 150 km, utilization of the Leonard (2014) scaling relationship for generating extended rupture planes, and truncation of the Gaussian distribution predicted by ground-motion models at 3 standard deviations above the mean. To perform these calculations, we employed the OpenQuake engine, developed by the Global Earthquake Model Foundation, as detailed by Pagani et al. (2014).

Fig. 10 display the results for Zahle site, close to the Yammouneh Fault (longitude and latitude : 35.9°, 33.8°), for the PGA and for the spectral period (2s) at 475 years return period, considering generic rock site conditions (V_{S30} = 760 m/s).

The black distribution is derived from sampling the full logic tree, involving 54 source models (2x3x3x3), combined with 3 GMMs, resulting in a total of 162 hazard estimates. In the Zahle site, situated near the YF fault, the PGA obtained is 1.04g. To assess the influence of the uncertainty on the characteristic magnitude (M_C), the 162 values are separated into two distinct distributions. One is based on the lower bound (light blue, 81 values), and the other relies on the upper bound of M_C (dark blue, 81 values). The disparity in the mean values between these two distributions signifies the impact of M_C uncertainty on hazard. Likewise, the effects of uncertainties on other parameters, such as mean recurrence time, aperiodicity, and the geometry of the faults (seismogenic depth, see El Kadri et al. 2023 for further explanation), can be analyzed in a similar manner.

This analysis shows that the choice of the characteristic magnitude on the Yammouneh fault is the decision that impacts the most the hazard values, as well the mean recurrence time has a little impact. However, the uncertainty on the aperiodicity or geometry has a negligible impact on hazard.

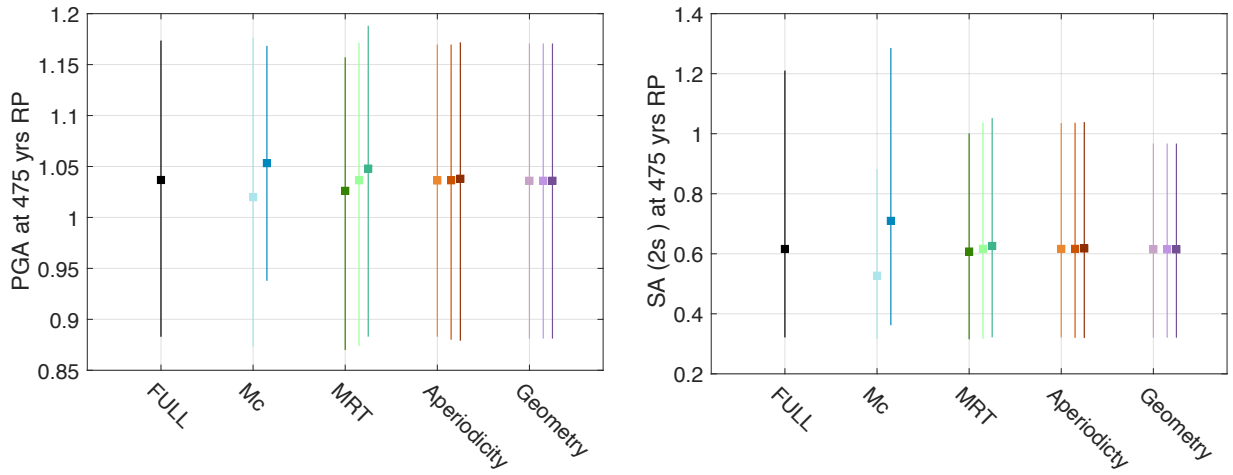

Fig. 10 Hazard level distributions, exploring the source model logic tree, at 475 years return period, at Zahle site. Mean value (square), percentiles 16th and 84th (vertical bar). 'FULL': full logic tree (162 values). 'Mc': choice of characteristic magnitude on faults, lower bound (light blue, 81 values), upper bound (dark blue, 81 values). 'MRT': Mean recurrence time, dark to light (1262,1100,992). 'Aperiodicity': light to dark (0.3, 0.4,0.5). 'Geometry': 3 alternative fault geometries, light to dark purple (depths 10,14,18 km).

A.5.5 Perspectives and Conclusion

In this study, we have undertaken an analysis of seismic hazard assessment focusing on the Yammouneh Fault located inside the Lebanese region. By utilizing a time-dependent approach, we aimed to reveal the potential seismic hazard associated with this fault.

The fundamental parameters of the Brownian Passage Time model, mean recurrence time (MRT), and aperiodicity (α), play an essential role in shaping the seismic hazard calculations. The mean recurrence time, as estimated through paleoseismic analysis, captures the time intervals between characteristic earthquake occurrences. It has been observed that, for a fixed elapsed time since the last earthquake, the conditional probabilities increases when the mean recurrence time decreases.

Similarly, the aperiodicity (α) parameter, representing the regularity of earthquake occurrence, demonstrates a significant influence on the calculation of the probability of occurrence. Smaller aperiodicity values suggest more regular seismic activity and lead to higher probabilities, while larger aperiodicity values result in a more Poisson-like distribution, lowering probabilities. Careful selection of aperiodicity values is essential for obtaining meaningful hazard assessments.

This analysis reveals that the primary factor influencing hazard levels along the Yammouneh Fault is the selection of the characteristic magnitude. Subsequently, at a secondary level, the mean recurrence time exhibits a minor influence on hazard. However, parameters like aperiodicity or fault geometry, on the other hand, have a negligible impact on hazard levels.

References

Abaimov, S. G., Turcotte, D. L., & Rundle, J. B. (2007). Recurrence-time and frequency-slip statistics of slip events on the creeping section of the San Andreas fault in central California. Geophysical Journal International, 170(3), 1289–1299. https://doi.org/10.1111/j.1365-246X.2007.03479.x

Abou Elenean K. Seismotectonics of Egypt in relation to the mediterranean and red seas tectonics. Egypt: Ain Shams Univ.; 1997. PhD Thesis

Abou Romieh, M,Westaway R, Daoud M, Radwan Y,Yassminh R, Khalil A,al-Ashkar A , Louglin , S, Arrell K & Bridgeland D, (2009). Active crustal shortening in NE Syria revealed by deformed terraces of the River Euphrates, Terra Nova, 21, 427–437.

Adams, J., & Atkinson, G. (2003). Development of seismic hazard maps for the proposed 2005 edition of the National Building Code of Canada. *Canadian Journal of Civil Engineering*, *30*(2), 255-271.

Akkar, S., & Bommer, J. J. (2010). Empirical equations for the prediction of PGA, PGV, and spectral accelerations in Europe, the Mediterranean region, and the Middle East. *Seismological Research Letters*, *81*(2), 195-206.

Akkar S, Sandikkaya MA, Bommer JJ (2014) Empirical ground-motion models for point- and extendedsource crustal earthquake scenarios in Europe and the Middle East. Bull Earthq Eng 12(1):359–387

Alchalbi A, Daoud M, Gomez F et al. (2010) Crustal deformation in northwestern Arabia from GPS measurements in Syria: Slow slip rate along the northern Dead Sea Fault. Geophys J Int 180(1):125–135. https://doi.org/10.1111/j.1365-246X.2009.04431.x

Al-Tarazi, E.: 1992, Investigation and Assessment of Seismic Hazard in Jordan and Its Vicinity, PhD. thesis, Institute of Geophysics, Ruhr-University Bochum, Germany.

Al-Tarazi, E. (1994). Seismic hazard assessment in Jordan and its vicinity. *Natural Hazards*, *10*, 79-96.

Al-Tarazi, E. 1999. Regional Seismic Hazard Study for the Eastern Mediterranean (Trans-Jordan, Levant and Antakia) and Sinai Region, J. of African Earth Sciences, 28 (3): 743-750.

Al-Tarazi, E., & Sandvol, E. (2007). Alternative models of seismic hazard evaluation along the Jordan–Dead Sea transform. *Earthquake Spectra*, *23*(1), 1-19.

Al Tarazi E, Abu Rajab J, Gomez F, Cochran W, Jaafar R and Ferry M (2011) GPS measurements of nearfield deformation along the southern Dead Sea Fault System. Geochem Geophys Geosyst 12:Q12021. https://doi.org/10.1029/2011GC003736

Akinci, A., Perkins, D., Lombardi, A., & Basili, R. (2010). Uncertainties in the estimation of the probability of occurrence of strong earthquakes from individual seismological sources in the Apennines, Italy. Journal of Seismology, 14, 95–117.

Akinci, A., Vannoli, P., Falcone, G., Taroni, M., Tiberti, M. M., Murru, M., Burrato, P., & Mariucci, M. T. (2017). When time and faults matter: Towards a time-dependent probabilistic SHA in Calabria, Italy. Bulletin of Earthquake Engineering, 15(6), 2497–2524. https://doi.org/10.1007/s10518-016-0065-7

Allen, T. I., Griffin, J. D., Leonard, M., Clark, D. J., & Ghasemi, H. (2020). The 2018 national seismic hazard assessment of Australia: Quantifying hazard changes and model uncertainties. *Earthquake Spectra*, *36*(1_suppl), 5-43.

Allen, T. I., Adams, J., & Halchuk, S. (2015). The seismic hazard model for Canada: Past, present and future. In *Proceedings of the Tenth Pacific Conference on Earthquake Engineering* (p. 8).

Ambraseys NN, Barazangi M (1989) The 1759 earthquake in the Bekaa Valley: implications for earthquake hazard assessment in the Eastern Mediterranean region. J Geophys Res: Solid Earth 94(B4):4007–4013

Ambraseys, N. N., Melville, C. P., & Adams, R. D. (1994). The Seismicity of Egypt, Arabia and the Red Sea. Cambridge Univ. Press; 1994. p. 1–137.

Ambraseys N.N., Simpson K.A. and Bommer J.J.; 1996: Prediction of horizontal response spectra in Europe. Earthq. Eng. Struct. Dyn., 25, 371-400.

Ambraseys, N., & Jackson, J. (1998). Faulting associated with historical and recent earthquakes in the Eastern Mediterranean region. Geophysical Journal International, 133(2), 390–406.

Ambraseys NN (2006) Comparison of frequency of occurrence of earthquakes with slip rates from longterm seismicity data: the cases of Gulf of Corinth, Sea of Marmara and Dead Sea Fault Zone. GeophysJ Int 165:516–256. https://doi.org/10.1111/j.1365-246X.2006.02858.x

Ambraseys NN (2009) Earthquakes in the Mediterranean and Middle East: a multidisciplinary study of seismicity up to 1900. Cambridge University Press, Cambridge, United Kingdom, 968 pp. https://doi.org/10.1017/CBO9781139195430

AMEC (2012) Lebanon Litani risver basin management support program, seismic deformation analysis of Qaraoun Dam, 147 pages (http://www.litani.gov.lb/wp/wp-content/uploads/LRBMS/028-LRBMS-SEISMIC%20DEFORMATION%20ANALYSIS%20OF%20QARAOUN. pdf)

Andrews, D. J., & Schwerer, E. (2000). Probability of rupture of multiple fault segments. Bulletin of the Seismological Society of America, 90(6), 1498-1506.

Ang, A. H.-S. and Tang, W. H. (1975). Probability concepts in engineering planning and design Vol. 1, Vol. 1,. Wiley, New York; London.

Arango MC and Lubkowski ZA (2012) Seismic hazard assessment and design requirements for Beirut, Lebanon. In: 15th World Conference on Earthquake Engineering, Lisboa, pp 10

Arieh, E., Rotstein, Y., (1985) A note on the seismicity of Israel (1900-1982). *Bulletin of the Seismological Society of America* 1985;; 75 (3): 881–887. doi: https://doi.org/10.1785/BSSA0750030881

Arieh, E., & Rabinowitz, N. (1989). Probabilistic assessment of earthquake hazard in Israel. *Tectonophysics*, *167*(2-4), 223-233.

Atkinson, G. M., & Boore, D. M. (2003). Empirical ground-motion relations for subduction-zone earthquakes and their application to Cascadia and other regions. *Bulletin of the Seismological Society of America*, *93*(4), 1703-1729.

Baker, J. W. (2013). An introduction to probabilistic seismic hazard analysis. *White paper version*, *2*(1), 79.

Bankston III, C. L., Barnshaw, J., Bevc, C., Capowich, G. E., Clarke, L., Das, S. K., Donato, K. M., Dynes, R. R., Eargle, L. A., Elliott, J. R., et al. (2010). The sociology of Katrina: Perspectives on a modern catastrophe. Rowman & Littlefield Publishers.

Beauval, C., & Bard, P. Y. (2021). History of probabilistic seismic hazard assessment studies and seismic zonations in mainland France. *Comptes Rendus. Géoscience*, 353(S1), 413-440. https://doi.org/10.5802/crgeos.95

Bender, B., & Perkins, D. M. (1987). *SEISRISK III: a computer program for seismic hazard estimation* (No. 1772). US Government Printing Office.

Ben-Menahem, A., 1979. A new earthquake catalogue for the Middle East, 92 B.C.-1979 A.D. Boll. Geofis. Teoret. Appl., 21: 245-310

Ben-Menahem, A., Vered, M., & Brooke, D. (1982). Earthquake risk in the Holy Land. *Boll. Geofis. teor. appl*, *24*(95), 175-187.

Bommer, J. J. (2002). Deterministic vs. probabilistic seismic hazard assessment: an exaggerated and obstructive dichotomy. Journal of Earthquake Engineering, 6(spec01), 43-73.

Boore, D. M., & Joyner, W. B. (1997). Site amplifications for generic rock sites. *Bulletin of the seismological society of America*, *87*(2), 327-341.

Boore, D. M., & Atkinson, G. M. (2008). Ground-motion prediction equations for the average horizontal component of PGA, PGV, and 5%-damped PSA at spectral periods between 0.01 s and 10.0 s. *Earthquake spectra*, *24*(1), 99-138.

Brax M, Albini P, Beauval C, Jomaa R, Sursock A (2019) An earthquake catalog for the Lebanese region. Seismol Res Lett 90(6):2236-2249. https://doi.org/10.1785/0220180292

Briais, A., Singh, S.C., Tapponnier, P.E., Elias, A., Sursock, A., Jomaa, R., Carton, H., Daeron, M., King, G. and Jacques, E. (2004). Neogene and active shortening offshore the reactivated Levant margin in Lebanon; results of the SHALIMAR cruise. AGU 2004 fall meeting. EOS Trans. Am. Geophys. Union, 85(47, suppl.), @Abstract T53B-0490.

Campbell, K. W. (1997). Empirical near-source attenuation relationships for horizontal and vertical components of peak ground acceleration, peak ground velocity, and pseudo-absolute acceleration response spectra. *Seismological research letters*, *68*(1), 154-179.

Campbell, K. W., & Bozorgnia, Y. (2008). NGA ground motion model for the geometric mean horizontal component of PGA, PGV, PGD and 5% damped linear elastic response spectra for periods ranging from 0.01 to 10 s. *Earthquake spectra*, *24*(1), 139-171.

Campbell, K. W., & Bozorgnia, Y. (2014). NGA-West2 ground motion model for the average horizontal components of PGA, PGV, and 5% damped linear acceleration response spectra. *Earthquake Spectra*, *30*(3), 1087-1115.

Carton H, Singh SC, Tapponnier P, Elias A, Briais A, Sursock A, Jomaa R, King GCP, Daeron M, Jacques E, Barrier E (2009) Seismic evidence for Neogene and active shortening offshore of Lebanon (Shalimar cruise). J Geophys Res 114:B07407. doi:10.1029/2007JB005391

Chaimov, T. A., Barazangi, M., Al-Saad, D., Sawaf, T., & Gebran, A. (1990). Crustal shortening in the Palmyride fold belt, Syria, and implications for movement along the Dead Sea fault system. *Tectonics*, *9*(6), 1369-1386.

Chan, C., Wang, Y., Wang, Y., & Lee, Y. (2017). Seismic-Hazard Assessment over Time: Modeling Earthquakes in Taiwan. Bulletin of the Seismological Society of America, 107(5), 2342–2352. https://doi.org/10.1785/0120160278

Chan, C.-H., Ma, K.-F., Shyu, J. B. H., Lee, Y.-T., Wang, Y.-J., Gao, J.-C., et al. (2020). Probabilistic seismic hazard assessment for Taiwan: TEM PSHA2020. *Earthquake Spectra*, 36(1_suppl), 137–159. https://doi.org/10.1177/8755293020951587

Chartier, T., Scotti, O., Lyon-Caen, H., & Boiselet, A. (2017). Methodology for earthquake rupture rate estimates of fault networks: Example for the western Corinth rift, Greece. *Natural Hazards and Earth System Sciences,17*(10), 1857–1869. https://doi.org/10.5194/nhess-17-1857-2017.

Chartier T, Scotti O, Lyon-Caen H. (2019). SHERIFS: Open-source code for computing earthquake rates in fault systems and constructing hazard models. Seismol Res Lett, 90: 1678–1688

Cheng, J., Xu, X., Ren, J., Zhang, S., & Wu, X. (2021). Probabilistic multi-segment rupture seismic hazard along the Xiaojiang fault zone, southeastern Tibetan Plateau. *Journal of Asian Earth Sciences*, *221*, 104940.

Chiou, B. S. J., & Youngs, R. R. (2014). Update of the Chiou and Youngs NGA model for the average horizontal component of peak ground motion and response spectra. Earthquake Spectra, 30(3), 1117-1153.

Cmt. Centroid moment tensor catalog. http://www.seismology.harvard.edu; 2019.

Cornell, C. A. (1968). Engineering seismic risk analysis. Bulletin of the Seismological Society of America, 58(5):1583–1606.

Courtillot, V., Armijo, R., & Tapponnier, P. (1987). Kinematics of the Sinai triple junction and a two-phase model of Arabia-Africa rifting. *Geological Society, London, Special Publications*, *28*(1), 559-573.

Cramer, C. H., Petersen, M. D., Cao, T., Toppozada, T. R., & Reichle, M. (2000). A Time-Dependent Probabilistic Seismic-Hazard Model for California. Bulletin of the Seismological Society of America, 90(1), 1–21. https://doi.org/10.1785/0119980087

Daeron M, Benedetti L, Tapponnier P, Sursock A, Finkel RC (2004) Constraints on the post~ 25-ka slip rate of the Yammouneh fault (Lebanon) using in situ cosmogenic 36Cl dating of offset limestone clast fans. Earth Planet Sci Lett 227(1–2):105–119. https://doi.org/10.1016/j.epsl.2004.07.014

Daeron M, Klinger Y, Tapponnier P, Elias A, Jacques E, Sursock A (2005) Sources of the large AD 1202 and 1759 Near East earthquakes. Geology 33(7):529–532. https://doi.org/10.1130/G21352.1

Daeron M, Klinger Y, Tapponnier P, Elias A, Jacques E, Sursock A (2007) 12,000-year-long record of 10 to 13 paleoearthquakes on the Yammouneh fault, Levant fault system, Lebanon. Bull Seismol Soc Am 97(3):749–771. https://doi.org/10.1785/0120060106

Danciu L, Sesetyan K, Demircioglu MB, Gülen L, Zare M, Basili R, Elias A, Adamia S, Tsereteli M, Yalçin H, Utkucu M, Khan MA, Sayab M, Hessami K, Rovida A, Stucchi M, Burg JP, Karakhanyan A, Babayan H, Avanesyan M, Mamadli T, Al-Qaryouti M, Kalafat D, Erdik M, Giardini D (2018) The 2014 earthquake model of the Middle East: seismogenic sources. Bull Earthq Eng. https://doi.org/10.1007/s10518-017-0096-8

Danciu L, Kale O, Akkar S (2016) The 2014 Earthquake Model of the Middle East: ground motion model and uncertainties. Bull Earthq Eng (2016). doi:10.1007/s10518-016-9989-1

Danciu, L., Nandan, S., Reyes, C., Basili, R., Weatherill, G., Beauval, C., Rovida, A., Vilanova, S., Sesetyan, K., Bard, P-Y., Cotton, F., Wiemer, S., Giardini, D. (2021). The 2020 update of the European Seismic Hazard Model: Model Overview. EFEHR Technical Report 001, v1.0.0, https://doi.org/10.12686/a15.

Darawcheh, R., Sbeinati, M. R., Margottini, C., & Paolini, S. (2000). The 9 July 551 AD Beirut earthquake, eastern Mediterranean region. *Journal of Earthquake Engineering*, *4*(04), 403-414.

Di Giacomo, D., Bondár, I., Storchak, D. A., Engdahl, E. R., Bormann, P., & Harris, J. (2015). ISC-GEM: Global Instrumental Earthquake Catalogue (1900–2009), III. Re-computed MS and mb, proxy MW, final magnitude composition and completeness assessment. Physics of the Earth and Planetary Interiors, 239, 33-47.

Eberhart-Phillips, D., P. J. Haeussler, J. T. Freymueller, A. D. Franckel, C. M. Rubin, P. Craw, N. A. Ratchkovski, G. Anderson, G. A. Carver, A. J. Crone, T. E. Dawsson, H. Fletcher, R. Hansen, E. L. Harp, R. A. Harris, D. P. Hill, S. Hreinsdottiir, R. W. Jibson, L. M. Jones, R. Kayen, D. K. Keefer, C. F. Larsen, S. C. Moran, S. F. Personius, G. Plafker, B. Sherrod, K. Sieh, N. Sitar, and W. K. Wallace (2003). The 2002 Denali fault earthquake, Alaska: a large magnitude, slip-partitioned event, Science 300, 1113–1118.

EC8; CEN European Standard ENV 1998-1-1/2/3, Eurocode 8: Design Provisions for Earthquake Resistance of Structures—Part I: General Rules. Technical Committee 250/SC8. Technical Committee: Brussels, Belgium, 2004.

Ekström, G., Nettles, M., & Dziewoński, A. M. (2012). The global CMT project 2004–2010: Centroid-moment tensors for 13,017 earthquakes. *Physics of the Earth and Planetary Interiors*, *200*, 1-9.

Elias, A., P. Tapponnier, S. C. Singh, G. C. P. King, A. Briais, M. Daëron, H. Carton, A. Sursock, E. Jacques, R. Jomaa, and Y. Klinger (2007), Active thrusting offshore Mount Lebanon: Source of the tsunamigenic A.D. 551 Beirut-Tripoli earthquake, *Geology*, 35, 755–758, doi:710.1130/G2363A.

Elias, A. (2015). Notes on Earthquake Hazard in Lebanon. https://doi.org/10.13140/RG.2.1.3763.4004

El-hadidy M. Seismotectonics and seismic hazard studies in and around Egypt. PhD Thesis. Egypt: Ain Shams Univ.; 2012.

Elhadidy, M., Abdalzaher, M. S., & Gaber, H. (2021). Up-to-date PSHA along the Gulf of Aqaba-Dead Sea transform fault. Soil Dynamics and Earthquake Engineering, 148, 106835.

El-Isa, Z. H., Merghelani, H. M., & Bazzari, M. A. (1984). The Gulf of Aqaba earthquake swarm of 1983 January–April. *Geophysical Journal International*, *78*(3), 711-722.

El Kadri, S., Beauval, C., Brax, M., Bard, P. Y., Vergnolle, M., & Klinger, Y. (2023). A fault-based probabilistic seismic hazard model for Lebanon, controlling parameters and hazard levels. *Bulletin of Earthquake Engineering*, *21*(7), 3163-3197.https://doi.org/10.1007/s10518-023-01631-z

Ellenblum, R., Marco, S., Agnon, A., Rockwell, T., & Boas, A. (1998). Crusader castle torn apart by earthquake at dawn, 20 May 1202. Geology, 26(4), 303-306.

Ellsworth, W. L., Matthews, M. V., Nadeau, R. M., Nishenko, S. P., Reasenberg, P. A., & Simpson, R. A. (1999). A physically-based earthquake recurrence model for estimation of long-term earthquake probabilities. US Geological Survey.

EMSC. Eastern mediterranean seismological center. http://www.emsc-csem. org/#2; 2019.

Erdik, M. (1984). Report on the Turkish earthquake of October 30, 1983. *Earthquake Spectra*, *1*(1), 151-172.

Erdik M, Şeşetyan K, Demircioğlu MB, Harmandar E (2014) Assessment of site-specific earthquake hazard for Bisri Dam, Lebanon. Report for the Council for development and reconstruction of the Republic of Lebanon, 44 p

Esteva, L. (1967, July). Criteria for the construction of spectra for seismic design. In Third Panamerican Symposium on Structures, Caracas, Venezuela (Vol. 1082).

Esteva L (1968) Bases para la formulacion de decisiones de dise.o sismico. Thesis and Report 182, Universidad Autonoma Nacional de Mexico (in Spanish)

Esteva, L., & Villaverde, R. (1973). Seismic risk, design spectra and structural reliability. In *Proceedings of Fifth World Conference on Earthquake Engineering* (Vol. 2, pp. 2586-2596).

Esteva L.: 1974, Geology and probability in the assessment of seismic risk, *Proc. at the 2nd International Congress of the International Association of Engineering Geologists*, Sao Paolo, p. 14.

Ferry M, Meghraoui M, AbouKaraki N, Al-Taj M, Amoush H, Al-Dhaisat S, Barjous M (2007) A 48-kyr-long slip rate history for the Jordan Valley segment of the Dead Sea fault, Earth Planet. Sci Lett 260:394–406

Ferry M, Meghraoui M, Abou Karaki N, Al-Taj M, Khalil L (2011) Episodic behavior of the Jordan Valley section of the Dead Sea fault inferred from a 14-ka-long integrated catalog of large earthquakesepisodic behavior of the Jordan Valley section of the Dead Sea fault. Bull Seismol Soc Am101(1):39–67. https://doi.org/10.1785/0120100097

Field, E. H., & Page, M. T. (2011). Estimating earthquake-rupture rates on a fault or fault system. Bulletin of the Seismological Society of America, 101(1), 79-92.

Field, E. H., Arrowsmith, R. J., Biasi, G. P., Bird, P., Dawson, T. E., Felzer, K. R., Jackson, D. D., Johnson, K. M., Jordan, T. H., Madden, C., Michael, A. J., Milner, K. R., Page, M. T., Parsons, T., Powers, P. M., Shaw, B. E., Thatcher, W. R., Weldon, R. J., Zeng, Y., (2014). Uniform California earthquake rupture forecast, version 3

(UCERF3)—The time-independent model. *Bulletin of the Seismological Society of America*, *104*(3), 1122-1180. doi: https://doi.org/10.1785/0120130164

Field, E. H. (2015). Computing Elastic-Rebound-Motivated Earthquake Probabilities in Unsegmented Fault Models: A New Methodology Supported by Physics-Based Simulators. Bulletin of the Seismological Society of America, 105(2A), 544–559. https://doi.org/10.1785/0120140094

Field, E., G. Biasi, P. Bird, T. Dawson, K. Felzer, D. Jackson, K. Johnson, T. Jordan, and C. Madden (2015). Long-term time-dependent probabilities for the Third Uniform California Earthquake Rupture Forecast (UCERF3), Bull. Seismol. Soc. Am.105, no. 2A, 511–543

Fletcher, J., Teran, O. J., Rockwell, T. K., Oskin, M. E., Hudnut, K. W., Mueller, K. J., et al. (2014). Assembly of a large earthquake from a complex fault system: Surface rupture kinematics of the 4 April 2010 El Mayor-Cucapah (Mexico) M_w 7.2 earthquake. *Geosphere*, 10, 797–827. https://doi.org/10.1130/ges00933.1

Freund, R., Zak, I. and Garfunkel, Z., (1968). On the age and rate of the sinistral movement along the Dead Sea rift. Nature, 220: 253-255

Freund, R., Garfunkel, Z., Zak, I., Goldberg, M., Weissbrod, T. and Derin, B., (1970). The shear along the Dead Sea rift. Philos. Trans. R. Sot. London, Ser. A, 267: 105-127.

Fu, B., Awata, Y., Du, J., Ninomiya, Y., & He, W. (2005). Complex geometry and segmentation of the surface rupture associated with the 14 November 2001 great Kunlun earthquake, northern Tibet, China. *Tectonophysics*, *407*(1-2), 43-63.

Fujiwara, H., Kawai, S., Aoi, S., Morikawa, N., Senna, S., Kudo, N., Ooi, M., Hao, K. X., Wakamatsu, K., Ishikawa, Y., Okumura, T., Ishii, T., Matsushima, S., Hayakawa, Y., Toyama, N. and Narita, A. (2009). Technical reports on national seismic hazard maps for Japan, Technical Note of the National Research Institute for Earth Science and Disaster Resilience, No. 336, 512 pp.

Fujiwara, T., Kodaira, S., No, T., Kaiho, Y., Takahashi, N., Kaneda, Y., (2011). The 2011 Tohoku-Oki earthquake: Displacement reaching the trench axis. *Science* **334**, 1240.

Gardner JK, Knopoff L (1974) Is the sequence of earthquakes in Southern California, with aftershocks removed, Poissonian? Bull Seismol Soc Am 64(5):1363–1367

Garfunkel, Z. (1981). Internal structure of the Dead Sea leaky transform (rift) in relation to plate kinematics. *Tectonophysics*, *80*(1-4), 81-108.

Geist, E. L., & ten Brink, U. S. (2021). Earthquake magnitude distributions on northern Caribbean faults from combinatorial optimization models. *Journal of Geophysical Research: Solid Earth*, *126*(10), e2021JB022050.

Gerges, A., Porcu, M. C., & Vielma Pérez, J. C. (2023). A Contribution to Facilitate the Seismic Design in Lebanon Using Short-Length Spectrum-Consistent Earthquakes. *Applied Sciences*, *13*(24), 12990.

Giardini, D., (1999). The global seismic hazard assessment program (GSHAP)-1992/1999.

Giardini, D., Grünthal, G., Shedlock, K. M. and Zhang, P.: The GSHAP Global Seismic Hazard Map. In: Lee, W., Kanamori, H., Jennings, P. and Kisslinger, C. (eds.): International Handbook of Earthquake & Engineering Seismology, International Geophysics Series 81 B, Academic Press, Amsterdam, 1233-1239, 2003.

Gomez, F., M. Meghraoui, A. N. Darkal, F. Hijazi, M. Mouty, Y. Suleiman,R. Sbeinati, R. Darawcheh, R. Al-Ghazzi, and M. Barazangi (2003),Holocene faulting and earthquake recurrence along the Serghaya branchof the Dead Sea fault system in Syria and Lebanon,Geophys. J. Int.,153,658–674, https://doi.org/10.1046/j.1365-246X.2003.01933.x

Gomez, F., G. Karam, M. Khawlie, S. McClusky, P. Vernant, R. Reilinger, R. Jaafar, C. Tabet, K. Khair, and M. Barazangi (2007a), Global Positioning System measurements of strain accumulation and slip transfer through

the restraining bend along the Dead Sea fault system in Lebanon, *Geophys. J. Int.*, 168(3), 1021–1028, doi:10.1111/j.1365-246X.2006.03328.x.

Gomez, F., Nemer, T., Tabet, C., Khawlie, M., Meghraoui, M., & Barazangi, M. (2007b). Strain partitioning of active transpression within the Lebanese restraining bend of the Dead Sea Fault (Lebanon and SW Syria). *Geological Society, London, Special Publications*, *290*(1), 285-303.

Gomez, F., Cochran, W. J., Yassminh, R., Jaafar, R., Reilinger, R., Floyd, M., et al. (2020). Fragmentation of the Sinai Plate indicated by spatial variation in present-day slip rate along the Dead Sea Fault system. *Geophysical Journal International*, 221(3), 1913–1940. https://doi.org/10.1093/gji/ggaa095

Gómez-Novell O, García-Mayordomo J, Ortuño M, Masana E and Chartier T (2020) Fault System-Based Probabilistic Seismic Hazard Assessment of a Moderate Seismicity Region: The Eastern Betics Shear Zone (SE Spain). Front. Earth Sci. 8:579398. doi: 10.3389/feart.2020.579398

Grünthal, G., Bosse, C., Sellami, S., Mayer-Rosa, D., & Giardini, D. (1999). Compilation of the GSHAP regional seismic hazard for Europe, Africa and the Middle East.

Grünthal, G., Stromeyer, D., Bosse, C., Cotton, F., and Bindi, D. (2018). The probabilistic seismic hazard assessment of Germany—version 2016, considering the range of epistemic uncertainties and aleatory variability. Bulletin of Earthquake Engineering, 16(10):4339–4395.

Guidoboni, E., Traina, G., & Comastri, A. (1994). Catalogue of ancient earthquakes in the Mediterranean sea up to the 10th century.

Guidoboni, E., and A. Comastri (2005). Catalogue of Earthquakes and Tsunamis in the Mediterranean Area from the 11th to the 15th Century, INGV-SGA, Bologna, Italy.

Gutenberg B, Richter CF (1944) Frequency of earthquakes in California*. Bull Seismol Soc Am 34(4):185–188

Hagiwara, Y. (1974). Probability of earthquake occurrence as obtained from a Weibull distribution analysis of crustal strain. Tectonophysics, 23, 323–328.

Hamiel Y, Piatibratova O, Mizrahi Y (2016) Creep along the northern Jordan Valley section of the Dead Sea Fault. Geophys Res Lett 43(6):2494–2501. https://doi.org/10.1002/2016GL067913

Hamiel, Y., Masson, F., Piatibratova, O., & Mizrahi, Y. (2018). GPS measurements of crustal deformation across the southern Arava Valley section of the Dead Sea Fault and implications to regional seismic hazard assessment. *Tectonophysics*, *724*, 171-178.

Hamiel, Y., & Piatibratova, O. (2021). Spatial variations of slip and creep rates along the southern and central Dead Sea Fault and the Carmel–Gilboa Fault System. *Journal of Geophysical Research: Solid Earth*, *126*(9), e2020JB021585.

Harajli, M., Sadek, S., & Asbahan, R. (2002). Evaluation of the seismic hazard of Lebanon. *Journal of seismology*, *6*, 257-277.

Hariri, A.: 1991, Seismotectonic study, seismic hazard assessment and zonation of the Syrian Arab Republic, M.S. Thesis, Institute of Earthquake Engineering and Engineering Seismology University 'Kiril and Metodij' Skopje, Macedonia.

Hatcher, R.D., Jr., Zeitz, I., Regan, R.D.&Abu-Ajamieh,M., (1981). Sinistral strike-slip motion on the Dead Sea Rift: confirmation from new magnetic data, Geology, 9, 458–462.

Haynes, J. M., Niemi, T. M., & Atallah, M. (2006). Evidence for ground-rupturing earthquakes on the Northern Wadi Araba fault at the archaeological site of Qasr Tilah, Dead Sea Transform fault system, Jordan. *Journal of seismology*, *10*, 415-430.

He, L., Feng, G., Xu, W., Wang, Y., Xiong, Z., Gao, H., & Liu, X. (2023). Coseismic kinematics of the 2023 Kahramanmaras, Turkey earthquake sequence from InSAR and optical data. Geophysical Research Letters, 50(17), e2023GL104693.

Headquarters for Earthquake Research Promotion (HERP) (2014) The National Seismic Hazard Map 2014 version—with an overview on the ground motion hazard of the whole country. Technical report, Headquarters for Earthquake Research Promotion (in Japanese). Available at: https://www.jishin.go.jp/evaluation/seismic_hazard_map/shm_report/shm_report_2014/ (last accessed June 2020).

Hofstetter, R., Klinger, Y., Amrat, A. Q., Rivera, L., & Dorbath, L. (2007). Stress tensor and focal mechanisms along the Dead Sea fault and related structural elements based on seismological data. *Tectonophysics*, *429*(3-4), 165-181.

Hough, S. E., & Avni, R. (2009/2010). The 1170 and 1202 CE Dead Sea Rift earthquakes and long-term magnitude distribution of the Dead Sea Fault Zone. *Israel Journal of Earth Sciences*, *58*.

Huijer, C., Harajli, M. & Sadek, S. (2010). Implications of the recent mapping of the offshore thrust fault system on the seismic hazard of Lebanon. Research Report submitted to the Lebanese National Council for Scientific Research (LNCSR), 100. Also, MS thesis presented by the first author to the CEE Department, American University of Beirut, available upon request from http://library.aub.edu.lb/record=b1454788.

Huijer, C., Harajli, M., & Sadek, S. (2011). Upgrading the seismic hazard of Lebanon in light of the recent discovery of the offshore thrust fault system. *Lebanese Science Journal*, *12*(2), 67.

Huijer C, Harajli M, Sadek S (2016) Re-evaluation and updating of the seismic hazard of Lebanon. J Seismolog 20(1):233–250. https://doi.org/10.1007/s10950-015-9522-z

Husein Malkawi, A. I. and Fahmi, Kb.: 1995, Empirically derived earthquake ground motion attenuation relations for Jordan and conterminous areas, Int. J. Eng. Geol., in press.

IBC. International Building Code; Ch.16 S.13 Earthquake Loads; International Code Council: Washington, DC, USA, 1997.

Inbal, A., Ziv, A., Lior, I., Nof, R. N., & Eisermann, A. S. (2023). Non-Triggering and Then Triggering of a Repeating Aftershock Sequence in the Dead Sea by the 2023 Kahramanmaraş Earthquake Pair: Implications for the Physics of Remote Delayed Aftershocks. *Geophysical Research Letters*, *50*(18), e2023GL104908.

Jiménez, M. J., Giardini, D., & Grünthal, G., (2001). SESAME-Working. Group, 3-18.

Jiménez, M. J., Giardini, D., & Grünthal, G. (2003). The ESC-SESAME unified hazard model for the European-Mediterranean region. *csem-emsc Newsletter*, *19*, 2-4.

Jiménez M.J.; 2006: Cooperation in seismic hazard mapping of the Dead Sea region. UNESCO workshop report, Barcelona, Spain, 19 – 21 December 2006.

Jimenez, M., Al-Nimry, H., Khasawneh, A., Al-Hadid, T., & Kahhaleh, K. (2008). Seismic hazard assessment for Jordan and neighbouring areas. *Bollettino di Geofisica Teorica ed Applicata*, *49*(1), 17-36.

Joyner, W. B., & Boore, D. M. (1981). Peak horizontal acceleration and velocity from strong-motion records including records from the 1979 Imperial Valley, California, earthquake. *Bulletin of the seismological Society of America*, *71*(6), 2011-2038.

Karcz, I. (2004). Implications of some early Jewish sources for estimates of earthquake hazardin the Holy Land. *Annals of Geophysics*.

Khair, K., Karakaisis, G. F., & Papadimitriou, E. E. (2000). Seismic zonation of the Dead Sea transform fault area.

Kim, D.C., Kim, K.O., Pelinovsky, E., Didenkulova, I. and Choi, B.H., (2013). Three-dimensional tsunami runup simulation for the port of Koborinai on the Sanriku coast of Japan. *Journal of Coastal Research* 2 January 2013; (65 (10065)): 266–271. doi: https://doi.org/10.2112/SI65-046.1

Kijko, A. and M. A. Sellevoll (1989). Estimation of earthquake hazard parameters from incomplete data files. Part I. Utilization of extreme and complete catalogs with different threshold magnitudes, Bull. Seism. Soc. Am. 79, 645-654.

KIJKO , A. and SELLEVOLL, M.A. (1992), Estimation of Earthquake Hazard Parameters from Incomplete Data Files. Part II, Incorporation of Magnitude Heterogeneity, Bull. Seismol. Soc. Am. 82, 120–134.

Kirkpatrick, S., C. D. Gelatt, and M. P. Vecchi (1983). Optimization by simulated annealing, Science 220, no. 4598, 671–680, doi: 10.1126/science.220.4598.671.

Klinger, Y., Rivera, L., Haessler, H., & Maurin, J. C. (1999). Active faulting in the Gulf of Aqaba: new knowledge from the Mw 7.3 earthquake of 22 November 1995. *Bulletin of the Seismological Society of America*, *89*(4), 1025-1036.

Klinger, Y., Avouac, J. P., Dorbath, L., Karaki, N. A., & Tisnerat, N. (2000). Seismic behaviour of the Dead Sea fault along Araba valley, Jordan. *Geophysical Journal International*, *142*(3), 769-782.

Klinger, Y., Etchebes, M., Tapponnier, P., & Narteau, C. (2011). Characteristic slip for five great earthquakes along the Fuyun fault in China. Nature Geoscience, 4(6), 389-392.

Klinger, Y., Le Béon, M., & Al-Qaryouti, M. (2015). 5000 yr of paleoseismicity along the southern Dead Sea fault. *Geophysical Journal International*, *202*(1), 313-327.

Klinger, Y., Okubo, K., Vallage, A., Champenois, J., Delorme, A., Rougier, E., Lei, Z., Knight, E. E., Munjiza, A., Satriano, C., Baize, S., Langridge, R., & Bhat, H. S. (2018). Earthquake damage patterns resolve complex rupture processes. *Geophysical Research Letters*, 45, 10,279–210,287. https://doi.org/10.1029/2018GL078842

Kotha SR, Weatherill G, Bindi D, Cotton F (2020) A regionally-adaptable ground-motion model for shallow crustal earthquakes in Europe. Bull Earthq Eng 18(9):4091–4125. https://doi.org/10.1007/s10518-020-00869-1

Kramer, S. L. (1996) Geotechnical Earthquake Engineering, Prentice Hall.

Krinitzsky, E. L. (1993) “Earthquake probability in engineering - Part 2: Earthquake recurrence and limitations of Gutenberg-Richter b-values for the engineering of critical structures," Engrg. Geol. 36, 1-52.

Kulkarni, R. B., Youngs, R. R., & Coppersmith, K. J. (1984). Assessment of confidence intervals for results of seismic hazard analysis. In Proceedings of the Eighth World Conference on Earthquake Engineering (Vol. 1, pp. 263-270).

Kurtz, R., Klinger, Y., Ferry, M., & Ritz, J. F. (2018). Horizontal surface-slip distribution through several seismic cycles: The Eastern Bogd fault, Gobi-Altai, Mongolia. Tectonophysics, 734, 167-182.

Le Beon, M. L., Y. Klinger, A. Q. Amrat, A. Agnon, L. Dorbath, G. Baer, J.-C. Ruegg, O. Charade, and O. Mayyas (2008), Slip rate and locking depth from GPS profiles across the southern Dead Sea Transform, *J. Geophys. Res.*, 113, B11403, doi:10.1029/2007JB005280.

Le Beon M, Klinger Y, Al-Qaryouti M, Meriaux AS, Finkel RC, Elias A, Mayyas O, Ryerson FJ, Tapponnier P (2010) Early Holocene and Late Pleistocene slip rates of the southern Dead Sea fault determined from Be-10 cosmogenic dating of offset alluvial deposits. J Geophys Res Solid Earth 115(B11414):24

Le Béon, M., Klinger, Y., Mériaux, A. S., Al-Qaryouti, M., Finkel, R. C., Mayyas, O., & Tapponnier, P. (2012). Quaternary morphotectonic mapping of the Wadi Araba and implications for the tectonic activity of the southern Dead Sea fault. *Tectonics*, *31*(5).

Lefevre, M., Klinger, Y., Al-Qaryouti, M., Le Béon, M., & Moumani, K. (2018). Slip deficit and temporal clustering along the Dead Sea fault from paleoseismological investigations. *Scientific reports*, *8*(1), 4511.

Leonard M (2014) Self-consistent earthquake fault-scaling relations: update and extension to stable continental strike-slip faults. Bull Seismol Soc Am 104(6):2953–2965. https://doi.org/10.1785/0120140087

Li, X., Jonsson, S., Liu, S., Ma, Z., Castro-Perdomo, N., Masson, F., Klinger, Y. (2024, in press). Resolving the Slip-Rate Inconsistency along the Northern Dead Sea Fault.
Lin, P. S., & Lee, C. T. (2008). Ground-motion attenuation relationships for subduction-zone earthquakes in northeastern Taiwan. Bulletin of the Seismological Society of America, 98(1), 220-240.

Malkawi, A., Liang, R., Nusairat. K. and Al-Homoud, A. 1995. Probabilistic Seismic Hazard Zonation of Syria, Natural Hazards, 12: 139-151.

Marco S, Rockwell TK, Heimann A, Frieslander U, Agnon A (2005) Late Holocene activity of the Dead Sea Transform revealed in 3D palaeoseismic trenches on the Jordan Gorge segment. Earth Planet Sci Lett 234(1-2):189–205

Masson, F., Hamiel, Y., Agnon, A., Klinger, Y., & Deprez, A. (2015). Variable behavior of the Dead Sea Fault along the southern Arava segment from GPS measurements. *comptes rendus geoscience*, *347*(4), 161-169.

Matthews, M. V., W. L. Ellsworth, and P. A. Reasenberg (2002), A Brownian model for recurrent earthquakes, *Bull. Seismol. Soc. Am.*, 92, 2233–2250, doi:10.1785/0120010267.

McCalpin, J. P., (2009). Application of paleoseismic data to seismic hazard assessment and neotectonic research. *International Geophysics*, *95*, 1-106.

McCue, K. (1999). Seismic hazard mapping in Australia, the southwest Pacific and southeast Asia.

McGuire, R. K. (1976): "Fortran computer program for seismic risk analysis", US. Geol. Surv., Open - File Rept 76-67, 90 p.

McGuire, R. K. (1978). *FRISK: computer program for seismic risk analysis using faults as earthquake sources* (No. 78-1007). US Geological Survey.

McGuire, R. K. (2001). Deterministic vs. probabilistic earthquake hazards and risks. *Soil Dynamics and Earthquake Engineering*, *21*(5), 377-384.

McQuarrie, N., Stock, J.M., Verdel, C. & Wernicke, B.P., (2003). Cenozoic evolution of Neotethys and implications for the causes of plate motions, Geophys. Res. Lett., 30, doi: 10.1029/2003GL017992.

Meghraoui M, Gomez F, Sbeinati R et al. (2003) Evidence for 830 years of seismic quiescence from palaeoseismology, archaeoseismology and historical seismicity along the Dead Sea fault in Syria. Earth Planet Sci Lett 210(1–2):35–52. https://doi.org/10.1016/S0012-821X(03)00144-4

Meghraoui, M. (2015). Paleoseismic history of the Dead Sea fault zone.

Meletti C, Marzocchi W, D'Amico V, Lanzano G, Luzi L, Martinelli F, Pace B, Rovida A, Taroni M, Visini F (2021) The new Italian seismic hazard model (MPS19). Ann Geophys 64(1):SE112. https://doi.org/10.4401/ag-8579

Merz, H., & Cornell, C. A. (1973). Seismic risk analysis based on a quadratic magnitude-frequency law. Bulletin of the Seismological Society of America, 63, 1999–2006.

Montalva, G. A., Bastías, N., & Rodriguez-Marek, A. (2017). Ground-motion prediction equation for the Chilean subduction zone. Bulletin of the Seismological Society of America, 107(2), 901-911.

Moratto, L., Santulin, M., Tamaro, A., Saraò, A., Vuan, A., & Rebez, A. (2023). Near-source ground motion estimation for assessing the seismic hazard of critical facilities in central Italy. *Bulletin of Earthquake Engineering*, *21*(1), 53-75.

Musson R.; 1999: Probabilistic seismic hazard maps for the North Balkan region. Annali Geofis., 42, 1109-1124.

Nemer T, Meghraoui M (2006) Evidence of coseismic ruptures along the Roum fault (Lebanon): a possible source for the AD 1837 earthquake. J Struct Geol 28(8):1483–1495. https://doi.org/10.1016/j.jsg.2006.03.038

Nemer T, Meghraoui M, Khair K (2008) The Rachaya-Serghaya fault system (Lebanon): evidence of coseismic ruptures, and the AD 1759 earthquake sequence. J Geophys Res: Solid Earth 113(5):1–12. https://doi.org/10.1029/2007JB005090

Nemer, T., Gomez, F., Al Haddad, S., & Tabet, C. (2008). Coseismic growth of sedimentary basins along the Yammouneh strike-slip fault (Lebanon). Geophysical Journal International, 175(3), 1023–1039. https://doi.org/10.1111/j.1365-246X.2008.03889.x

Nicol, A., Pettinga, J., Clark, K., & Jacobs, K. (2012). National Seismic Hazard Model for New Zealand: 2010 update. *Bulletin of the Seismological Society of America*, 102(4), 1514–1542. https://doi.org/10.1785/0120110170

Nishenko, S. P., & Buland, R. (1987). A generic recurrence interval distribution for earthquake forecasting. Bulletin of the Seismological Society of America, 77, 1382–1399.

NL:135. Ministry of Industry. The Lebanese Standards Institution (LIBNOR): Beirut, Lebanon, 2012.

Pagani, M., Monelli, D., Weatherill, G., Danciu, L., Crowley, H., Silva, V., Henshaw, P., Butler, L., Nastasi, M., Panzeri, L., Simionato, M., & Vigano, D. (2014). OpenQuake Engine: An Open Hazard (and Risk) Software for the Global Earthquake Model. Seismological Research Letters, 85(3), 692–702. https://doi.org/10.1785/0220130087

Pagani, M., Silva, V., & Simionato, M. (2023). OpenQuake Engine Manual—GEM Foundation. https://docs.openquake.org/manuals/OpenQuake%20Manual%20(latest).pdf

Page, M. T., Field, E. H., Milner, K. R., & Powers, P. M. (2014). The UCERF3 grand inversion: Solving for the long-term rate of ruptures in a fault system. *Bulletin of the Seismological Society of America*, *104*(3), 1181-1204.

Palano, M., Imprescia, P., & Gresta, S. (2013). Current stress and strain-rate fields across the Dead Sea Fault System: Constraints from seismological data and GPS observations. *Earth and Planetary Science Letters*, *369*, 305-316.

Pantosti, D., Pucci, S., Palyvos, N., De Martini, P. M., D'Addezio, G., Collins, P. E. F., & Zabci, C. (2008). Paleoearthquakes of the Düzce fault (North Anatolian Fault Zone): Insights for large surface faulting earthquake recurrence. Journal of Geophysical Research, 113(B1), B01309. https://doi.org/10.1029/2006JB004679

Papaioannou C. and Papazachos C.; 2000: Time-Independent and Time-Dependent Seismic Hazard in Greece based on Seismogenic Sources. Bull. Seism. Soc. Am., 90, 22-33.

Parsons, T. (2005). Significance of stress transfer in time-dependent earthquake probability calculations. Journal of Geophysical Research, 110(B5), B05S02. https://doi.org/10.1029/2004JB003190

Parsons, T. (2008). Monte Carlo method for determining earthquake recurrence parameters from short paleoseismic catalogs: Example calculations for California. US Geological Survey, 113(B3), B03302. https://doi.org/10.1029/2007JB004998

Peruzza, L., Pace, B., & Cavallini, F. (2010). Error propagation in time-dependent probability of occurrence for characteristic earthquakes in Italy. Journal of Seismology, 14(1), 119–141. https://doi.org/10.1007/s10950-008-9131-1

Peruzza, L., Pace, B., Lavecchia, G., & Boncio, P. (2007). Reply to "Comment on 'Layered Seismogenic Source Model and Probabilistic Seismic-Hazard Analyses in Central Italy' by B. Pace, L. Peruzza, G. Lavecchia, and P. Boncio" by W. Marzocchi. Bulletin of the Seismological Society of America, 97(5), 1766–1768. https://doi.org/10.1785/0120070043

Petersen, M. D., M. P. Moschetti, P. M. Powers, C. S. Mueller, K. M. Haller, A. D. Frankel, Y. Zeng, S. Rezaeian, S. C. Harmsen, O. S. Boyd, N. Field, R. Chen, K. S. Rukstales, N. Luco, R. L. Wheeler, R. A. Williams, and A. H. Olsen (2014). Documentation for the 2014 update of the United States National Seismic Hazard Maps, U.S. Geological Survey Open-File Report 2014–1091, 243 pp, doi: 10.333/ofr20141091.

Plassard, J. and Kogaj, B.: 1981, Seismicity of Lebanon, A Catalogue of felt earthquakes (in French, Observatoire de Ksara (Lebanon) Annals, Memoirs, Tore. IV, Cahier 1, Conseil National de la Recherche Scientiflque, Beirut, Lebanon.

PS92; Règles PS Applicables aux Bâtiments, Dites Règles PS92. NF P 06-013/DTU Règles PS92. AFNOR: Paris, France, 1995.

Quennell, A. M. (1958). The structural and geomorphic evolution of the Dead Sea Rift. *Quarterly Journal of the Geological Society*, *114*(1-4), 1-24.

Quennell, A.M., 1984. The Western Arabia rift system, in The Geological Evolution of the Eastern Mediterranean, pp. 775–788, eds Dixon, J.E. & Robertson, A.H.F., Blackwell Scientific.

Reid, H.F., 1911. The elastic rebound theory of earthquakes, Bull. Dep. Geol. Univ. Calif., 6, 412–444.

Reiter, L. (1990) Earthquake Hazard Analysis: Issues and Insights, Columbia University Press.

Richter, Charles F., (1935). An instrumental earthquake magnitude scale. *Bulletin of the Seismological Society of America* 1935;; 25 (1): 1–32. doi: https://doi.org/10.1785/BSSA0250010001

Sadeh, M., Hamiel, Y., Ziv, A., Bock, Y., Fang, P., & Wdowinski, S. (2012). Crustal deformation along the Dead Sea Transform and the Carmel Fault inferred from 12 years of GPS measurements. *Journal of Geophysical Research: Solid Earth*, *117*(B8).

Saleh, M., & Becker, M. (2015). New constraints on the Nubia–Sinai–Dead Sea fault crustal motion. *Tectonophysics*, *651*, 79-98.

Sadigh, K., Chang, C. Y., Egan, J. A., Makdisi, F., & Youngs, R. R. (1997). Attenuation relationships for shallow crustal earthquakes based on California strong motion data. *Seismological research letters*, *68*(1), 180-189.

Sbeinati, M. R., Meghraoui, M., Suleyman, G., Gomez, F., Al Najjar, H., & Al-Ghazzi, R. (2009). Timing of Earthquake Ruptures at the Al Harif Aque duct (Dead Sea Fault) from Archaeoseismology, Paleo seismology and Tufa Cores. In *Intern. Workshop on Active Tectonic Studies and Earthquake Hazard Assessment in Syria* (p. 78).

Sbeinati MR, Meghraoui M, Suleyman G et al. (2010) Timing of earthquake ruptures at theAl Harif Roman aqueduct (Dead Sea fault, Syria) from archaeoseismology and paleoseismology. Anc Earthq 243. https://doi.org/10.1130/2010.2471(20)

Schwartz, D. P., and Coppersmith, K. J., (1984), Fault behavior and characteristic earthquakes: Examples from the Wasatch and San Andreas Fault Zones, *J. Geophys. Res.*, 89(B7), 5681–5698, doi:10.1029/JB089iB07p05681.

Scotti, O., Clement, C., and Baumont, D. (2014). Seismic hazard for design and verification of nuclear installations in france: regulatory context, debated issues and ongoing developments. Bollettino Di Geofisica Teorica Ed Applicata, 55(1):135–148.

Sesetyan, K., Demircioglu, M. B., Duman, T. Y., Çan, T., Tekin, S., Azak, T. E., & Fercan, Ö. Z. (2018). A probabilistic seismic hazard assessment for the Turkish territory—part I: the area source model. *Bulletin of Earthquake Engineering*, *16*, 3367-3397.

Shapira, A., 1981. Assessment of the potential earthquake risk in Israeland adjacent areas. IsraelJ. Earth Sci.,30: 135--141.

Shapira, A., 1983a. A probabilisticapproach for evaluating earthquake risks,with application to the Afro-Eurasian junction. Tectonophysics, 91: 321--334.

Shapira, A., 1983b. Potential earthquake risk estimations by application of a simulation process. Tectonophysics, 95: 75--89.

Shedlock, K. M., & Tanner, J. G. (1999). Seismic hazard map of the western hemisphere.

Stevens, V. L., & Avouac, J. P. (2017). Determination of Mmax from background seismicity and moment conservation. *Bulletin of the Seismological Society of America*, *107*(6), 2578-2596.

Stirling, M., McVerry, G., Gerstenberger, M., Litchfield, N., Van Dissen, R., Berryman, K., Barnes, P., Wallace, L., Villamor, P., Langridge, R., Lamarche, G., Nodder, S., Reyners, M., Bradley, B., Rhoades, D., Smith, W., Nicol, A., Pettinga, J., Clark, K., & Jacobs, K. (2012). National Seismic Hazard Model for New Zealand: 2010 update. *Bulletin of the Seismological Society of America*, 102(4), 1514–1542. https://doi.org/10.1785/0120110170

Storchak, D. A., Di Giacomo, D., Engdahl, E. R., Harris, J., Bondár, I., Lee, W. H. K., et al. (2015). The ISC-GEM global instrumental earthquake catalogue (1900–2009): Introduction. Physics of the Earth and Planetary Interiors, 239, 48–63. https://doi.org/10.1016/j.pepi.2014.06.009

Storchak, D. A., Harris, J., Brown, L., Lieser, K., Shumba, B., & Di Giacomo, D. (2020). Rebuild of the Bulletin of the International Seismological Centre (ISC)—part 2: 1980–2010. *Geoscience Letters*, *7*(1), 1-21.

Silva, V., Akkar, S., Baker, J., Bazzurro, P., Castro, J. M., Crowley, H., Dolsek, M., Galasso, C., Lagomarsino, S., Monteiro, R., Perrone, D., Pitilakis, K. & Vamvatsikos, D. (2019). Current challenges and future trends in analytical fragility and vulnerability modeling. *Earthquake Spectra*, *35*(4), 1927-1952.

Thingbaijam, K. K. S., Mai, P. M., & Goda, K. (2017). New empirical earthquake source-scaling laws. *Bulletin of the Seismological Society of America*, *107*(5), 2225-2246.

Turcotte, T. and Arieh, E., 1986. Catalog of earthquakes in and around Israel 31BC-1984 AD. Prepared for the Isr. Electr. Corp., 96 pp.

UBC. Uniform Building Code. In Proceedings of the International Conference of Building Officials, Whittier, CA, USA; 1997.

Uhrhammer R (1986) Characteristics of northern and southern California seismicity. Earthq Notes 57:21

Van Stiphout T, Zhuang J, Marsan D (2012) Seismicity declustering. Community Online Resource for Statistical Seismicity Analysis (CORSSA). doi:10.5078/corssa-52382934. http://www.corssa.org

Vered, M., & Striem, H. L. (1977). A macroseismic study and the implications of structural damage of two recent major earthquakes in the Jordan Rift. *Bulletin of the Seismological Society of America*, *67*(6), 1607-1613.

Visini, F., Valentini, A., Chartier, T., Scotti, O., & Pace, B. (2020). Computational tools for relaxing the fault segmentation in probabilistic seismic hazard modelling in complex fault systems. *Pure and Applied Geophysics*, *177*, 1855-1877.

Wang, Y. J., Chan, C. H., Lee, Y. T., Ma, K. F., Shyu, J. B. H., Rau, R. J., & Cheng, C. T. (2016). Probabilistic seismic hazard assessment for Taiwan. *Terr. Atmos. Ocean. Sci*, *27*(3), 325-340.

Wechsler N, Rockwell TK, Klinger Y, Štěpančíková P, Kanari M, Marco S, Agnon A (2014) A paleoseismic record of earthquakes for the Dead Sea transform fault between the first and seventh centuries CE:nonperiodic behavior of a plate boundary fault. Bull Seismol Soc Am 104(3):1329–1347. https://doi.org/10.1785/0120130304

Wechsler, N., Rockwell, T. K., & Klinger, Y. (2018). Variable slip-rate and slip-per-event on a plate boundary fault: The Dead Sea fault in northern Israel. *Tectonophysics*, *722*, 210-226.

Wells DL, Coppersmith KJ (1994) New empirical relationships among magnitude, rupture length, rupture width, rupture area, and surface displacement. Bull—Seismol Soc Am 84(4):974–1002

WGCEP, W. G. on C. E. P. (2003). Earthquake probabilities in the San Francisco Bay Region. US Geological Survey, 2002–2031.

WGUEP. (2016). Estimating the probabilities of future large earthquakes along the Wasatch Front. Utah Geological Survey Miscellaneous Publication, 16(3), 164.

Wong, I., & Thomas, P. (2020). Implementing time-dependent seismic hazard in seismic design and building codes: It's Time. In 17th World Conference on Earthquake Engineering Proceedings.

Wong, I. G., Thomas, P. (2022). An Argument for Time-dependent National Seismic Hazard Maps. 2022 Annual Meeting of the Seismological Society of America, 19-23 April, Bellevue.

Yeats, R. S.; Sieh, K. E.; Allen, C. R. 1997: The geology of earthquakes. New York, Oxford University Press. 568 p.

Youngs, R. R., & Coppersmith, K. J. (1985). Implications of fault slip rates and earthquake recurrence models to probabilistic seismic hazard estimates. *Bulletin of the Seismological society of America*, *75*(4), 939-964.

Youngs, R. R., Chiou, S. J., Silva, W. J., & Humphrey, J. R. (1997). Strong ground motion attenuation relationships for subduction zone earthquakes. *Seismological research letters*, *68*(1), 58-73.

Yücemen, M. S. (1992). Seismic hazard maps for Jordan and vicinity. *Natural Hazards*, *6*, 201-226.

Yücemen M.S.; (1995): Assessment of seismic hazard for Jordan considering the uncertainty in the location of seismic sources. In: Proceedings of the International Conference on Earthquake Engineering, Amman, Jordan, Vol. 1, pp. 135-144.

Yücemen, M. S., Ozturk, N. Y., Deniz, A. Y. K. U. T., & Muaz, S. (2005). Assessment of seismic hazard for Jordan. In *Proceedings of The International Earthquake Engineering Conference, Jordan, Paper* (Vol. 3).

Zare M, Amini H, Yazdi P, Sesetyan K, Demircioglu MB, Kalafat D, Erdik M, Giardini D, Khan MA, Tsereteli N (2014) Recent developments of the Middle East catalog. *Journal of Seismology* 18: 749–772.

Zhang, P., Yang, Z. X., Gupta, H. K., Bhatia, S. C., & Shedlock, K. M. (1999). Global seismic hazard assessment program (GSHAP) in continental Asia.

Zhang, Y., Tang, X., Liu, D., Taymaz, T., Eken, T., Guo, R., Zheng, Y., Wang, J., and Sun, H. Geometric controls on cascading rupture of the 2023 Kahramanmaraş earthquake doublet. Nature Geo-science, Oct. 2023. doi:10.1038/s41561-023-01283-3

Zohar, M., Salamon, A., & Rubin, R. (2016). Reappraised list of historical earthquakes that affected Israel and its close surroundings. Journal of Seismology, 20, 971-985.